



**DETERMINATION OF THE ROLE OF
NANOPARTICLE ACTIVE SITES IN
CATALYTIC HYDROGENATION REACTIONS
BY CYCLIC VOLTAMMETRY AND
NOVEL IN-SITU SURFACE SPECTROSCOPY**

**A thesis submitted to
Cardiff University
For the degree of
Philosophiae Doctor**

By

Shaoliang GUAN M.Sc.

**School of Chemistry
Cardiff University**

December 2014

DEDICATION

With all my love to my parents and wife who support me constantly. Nothing is more important than sharing the life happiness with them.

ABSTRACT

Cyclic Voltammetry, Surface Enhanced Raman Spectroscopy and Shell-Isolated Nanoparticle-Enhanced Raman Spectroscopy (SHINERS) have been used to investigate two types of heterogeneously catalysed hydrogenation reactions – hydrogenation of selected alkynes and the Orito reaction. Using a spectro-electrochemical flowcell, which is designed and built in-house, the selectivity and reactivity of the reactions on platinum surfaces have been truly discovered.

By studying hydrogenation of a range of alkyne molecules, including 2-butyne-1,4-diol, 2-pentyne, 4-octyne, propargyl alcohol and 2-methyl-3-butyn-2-ol, on different platinum surfaces, it was found that alkyne adsorption on Pt defect sites produces a long-lived di-sigma/pi-alkene complex which may undergo further hydrogenation to produce alkane. This complex may form on different surfaces with various orientations. However, depending on the specific molecules, the intermediate may not survive on some surfaces due to the steady state conditions arising from the catalytic reaction whereby adsorption of alkyne and hydrogenative desorption of reaction intermediates determines the overall surface coverage of intermediate as a function of potential. Alkene selectivity can be increased by blocking defect sites, using polyvinylpyrrolidone or bismuth, leaving only platinum{111} terraces available for catalysis.

By studying ethyl pyruvate (EP) adsorption on different surfaces of platinum and palladium, it was found that EP half-hydrogenated state (HHS) is a critical intermediate of the hydrogenated product which only forms on the step sites of the platinum surface at the hydrogen evolution reaction potential. However, another new intermediate adsorbate, which is believed to be a η^1 species and is believed to be a precursor of the HHS only forms on the terraces of the surface.

By studying the surface intermediates formed during hydrogenation of EP at palladium modified platinum single crystal electrodes, it was found that there was no unequivocal evidence for bands pertaining to EP adsorption on palladium could be identified under hydrogenating conditions due to the reconstruction of the palladium adlayer to reveal Pt subsurface sites.

ACKNOWLEDGEMENTS

I would like to thank those who walked into my PhD life during the last three years and played different roles in the show of my life.

Without Mujib, Peter, Ashley, Charlie, Katherine and Ollie, I would've not enjoyed the time in the lab or office. They are the ones whom I can constantly and instantly share the laughter and academic success with.

Without all the friends I have made in Cardiff, including SGI members, Cardiff Chinese football team, Cardiff Chinese PhD group, and Cardiff University Chinese Society, my life would've not been as colourful as it is.

Without the funding from National Physical Laboratory and Dr. Andy Wain's support, my PhD project would've not been possible.

Without Prof. Mike Bowker, Dr. Dave Willock and Prof. Phil Davis, my PhD project and my career would've not been going smoothly.

Especially, without Prof. Gary Attard, I would've not been trained as a person with specialties which are beneficial to my future. Because of his meticulous care and non-stopping guidance, I have achieved so far. He has spent so much time in helping me with his firsthand experience in every possible way. It has been an honour to be his student.

Finally, without my wife Masami, my father and mother, and my wife's whole family, I would've not been motivated and encouraged to conquer this challenge. I want to be a better person for all of them.

PUBLICATIONS

- 1) G. A. Attard, J. A. Bennett, I. Mikheenko, P. Jenkins, S. Guan, L. E. Macaskie, J. Wood and A. J. Wain. *Faraday Discussion*, 2013, **162**, 57.

CONTENTS

List of Symbols	i
Chapter 1 Introduction	
1.1 Perspectives in Catalysis.....	1
1.2 Surface Chemistry	13
1.2.1 Electroanalytical techniques.....	15
1.2.2 Raman and Surface enhanced Raman spectroscopy.....	16
1.2.3 Nanoparticle synthesis for Raman spectroscopy and catalysis	19
1.2.4 Growth and Epitaxy	23
1.2.5 Chirality.....	28
1.2.6 Catalysts in electrochemistry - electrocatalysts.....	32
1.3 An Overview of Catalytic Hydrogenation	36
1.3.1 Alkyne hydrogenation.....	36
1.3.2 Alkyl pyruvate hydrogenation.....	40
1.3.2.1 The Orito reaction	40
1.3.2.2 Proposed models for enantioselective induction by the chiral alkaloid...44	
1.4 Project Aims.....	46
1.5 References	47
Chapter 2 Theoretical Background	
2.1 Surface Structure	56
2.1.1 Geometrical Structure	56
2.1.1.1 The structure of bulk metal surfaces	56

2.1.1.2 The structure of single crystal metal surfaces – the Miller index system	57
2.1.2 Electronic Structure	62
2.2 The Electrical Double Layer	64
2.3 Cyclic Voltammetry	69
2.3.1 CV of polycrystalline platinum surfaces	72
2.3.2 CV of platinum single crystal electrodes	76
2.4 Spectroscopy	77
2.4.1 Molecular vibrations	79
2.4.1.1 Vibrations of diatomic molecules	79
2.4.1.2 Vibrations of polyatomic molecules	81
2.4.2 The Absorption Process	85
2.4.3 Light Scattering	87
2.4.4 Raman Spectroscopy	89
2.4.5 Surface Enhanced Raman Spectroscopy	95
2.4.5.1 The electromagnetic enhancement theory for SERS	96
2.4.5.2 Surface selection rules	98
2.4.5.3 The charge transfer theory for SERS	99
2.4.5.4 Applications	100
2.5 References	101

Chapter 3 Experimental

3.1 Introduction	104
3.2 The Spectro-electrochemical Flowcell	104
3.3 Preparation of Surfaces for SERS Analysis	107
3.3.1 Au@Pt Core-shell Nanoparticles	108
3.3.2 Au@SiO ₂ Core-shell Nanoparticles	109
3.4 Cyclic Voltammetry	113

3.4.1 Single Crystal Measurements	113
3.4.2 CV Measurements of Pt Single Crystals decorated with Au@SiO ₂ NPs	116
3.4.3 <i>In situ</i> Measurements of CV and SERS	117
3.5 Metal Deposition on Single Crystal Electrodes	122
3.6 Raman Spectrophotometer and Microscope	123
3.6.1 The Raman Experiment	125
3.6.2 Data Processing and Analysis	126
3.7 Running a SERS Experiment	128
3.8 Water Purification System	129
3.9 Chemical Reagents	129
3.10 References	130

Chapter 4 Hydrogenation of Alkynes at Nanoparticle and Single Crystal Platinum Surfaces

4.1 Introduction	132
4.2 Results and Discussions	133
4.2.1 Studies of butynediol adsorption at Pt surfaces	133
4.2.1.1 CV of butynediol adsorption on Pt{ <i>hkl</i> } single crystal electrodes	133
4.2.1.2 SERS of butynediol adsorption at a polycrystalline Pt surface	138
4.2.1.3 SHINERS of butynediol adsorption at Pt{111} single crystal electrode	143
4.2.1.4 SERS of butenediol adsorption on Au@Pt NPs surface	145
4.2.2 Studies of 2-pentyne and 4-octyne adsorption at Pt surfaces	146
4.2.2.2 <i>In situ</i> SERS studies of 2-pentyne and 4-octyne adsorption at polycrystalline Pt surface	149
4.2.2.3 <i>In situ</i> SHINERS studies of 2-pentyne and 4-octyne adsorption on Pt{ <i>hkl</i> } single crystal electrodes	151
4.2.3 Discussion	157

4.3 Conclusion	160
4.4 References	160

Chapter 5 Steric Effects in Hydrogenation of Alkynes and the Role of PVP in Promoting Selectivity

5.1 Introduction	162
5.2 Results and Discussions	163
5.2.1 CV studies of alkyne adsorption on Pt surfaces	163
5.2.1.1 CV of propargyl alcohol adsorption on Pt{ <i>hkl</i> } single crystal surfaces	163
5.2.1.2 CV of 2-methyl-3-butyn-2-ol adsorption on Pt{ <i>hkl</i> } single crystal surfaces	167
5.2.2 <i>In situ</i> SERS studies of propargyl alcohol adsorption on Pt surfaces	169
5.2.2.1 Polycrystalline Pt surface	169
5.2.2.2 Pt{ <i>hkl</i> } single crystal surfaces	171
5.2.3 <i>In situ</i> SERS studies of 2-methyl-3-butyn-2-ol adsorption on Pt surfaces ...	175
5.2.3.1 Polycrystalline Pt surface	175
5.2.3.2 Pt{ <i>hkl</i> } single crystal surfaces	177
5.2.3.3 PVP modified Pt surface	181
5.3 Conclusion	188
5.4 References	189

Chapter 6 Adsorption of Ethyl Pyruvate on Platinum Surfaces

6.1 Introduction	190
6.2 Results and Discussions	192
6.2.1 CV of ethyl pyruvate adsorption on Pt{ <i>hkl</i> } single crystal surfaces	192
6.2.2 Raman spectra of ethyl pyruvate and its product ethyl lactate	197
6.2.3 SER spectra of EP hydrogenation on Au@Pt NPs surface	198

6.2.4 SER spectra of EP adsorption on the surface of Pt{ <i>hkl</i> } single crystal electrodes	202
6.2.4.1 Pt{111}	202
6.2.4.2 Pt{100}	204
6.2.4.3 Pt{110}	206
6.2.4.5 The influence of the potential on EP adsorption on the Pt{111} surface	208
6.2.5 Discussion	214
6.3 Conclusion	218
6.4 References	219

Chapter 7 Adsorption of Ethyl Pyruvate on Palladium Surfaces

7.1 Introduction	221
7.2 Results and Discussion	221
7.2.1 CVs of palladium deposited on Pt{ <i>hkl</i> } single crystal electrodes	221
7.2.2 SERS of EP adsorption on palladium surfaces	226
7.2.2.1 Polycrystalline palladium surfaces of Au@Pd NPs	226
7.2.2.2 Pd on Pt{110} <i>Palladium multilayer</i>	229
7.2.2.3 Pd on Pt{111} <i>Palladium multilayer</i>	230
7.2.2.4 Pd on Pt{100} <i>Palladium multilayer</i>	233
7.2.2.5 Pd on Pt{110} <i>Palladium monolayer</i>	235
7.2.2.6 Pd on Pt{111} <i>Palladium monolayer</i>	236
7.2.2.7 Pd on Pt{100} <i>Palladium monolayer</i>	238
7.3 Conclusion	240
7.4 References	241

Chapter 8 Conclusion

8.1 Introduction.....	243
8.2 Hydrogenation of Alkynes.....	243
8.3 Hydrogenation of Ethyl Pyruvate.....	245
8.4 Future Work.....	246
8.5 References.....	248

List of Symbols

English

Symbol	Description	Units
A	Area/absorbance	$\text{cm}^2/-$
b	Path length	cm
c	Speed of light through a vacuum	$2.9979 \times 10^8 \text{ m s}^{-1}$
\bar{c}	Concentration of absorbing species	mol dm^{-3}
C	Capacitance	F, C V ⁻¹
C_o	Concentration of electroactive species	mol cm^{-3}
D_o	Diffusion co-efficient	$\text{cm}^2 \text{ s}^{-1}$
D_e	Dissociation energy	kJ mol^{-1}
e^-	Charge on one electron	$-1.602 \times 10^{-19} \text{ C}$
E	Energy/ Applied potential	eV, J, J mol ⁻¹ /V
E_a	Activation energy	eV, J, J mol ⁻¹
\bar{E}	Electric field	V m ⁻¹
E_F	Fermi energy	eV
E_{vac}	Vacuum energy	eV
F	Faraday constant	$9.649 \times 10^4 \text{ C mol}^{-1}$
H_f	Heat of formation	kJ mol^{-1}
h	Planck's constant	$6.626 \times 10^{-34} \text{ J s}$
i	Current	A
K	Boltzmann constant	$1.381 \times 10^{-23} \text{ J K}^{-1}$
K	Rate constant	
l	Bond length	Å, nm
M	Mass	g
n	Number of electrons	-
N_A	Avogadro's constant	$6.022 \times 10^{23} \text{ mol}^{-1}$
P	Pressure	Pa, $\text{kg m}^{-1} \text{ s}^{-2}$
Q	Charge	C
R	Gas constant/resistance	$8.314 \text{ J K}^{-1} \text{ mol}^{-1}/\Omega$
t	Time	s

T	Temperature	K
v	Energy states	-
ν	Scan rate	$V s^{-1}$
V	Potential/Volume	V/m^3

Greek

Symbol	Description	Units
α	Polarisability	$C \cdot m^2 \cdot V^{-1}$
δ	Bending vibration mode	-
δ	Charge	V
ε	Absorptivity co-efficient	$M^{-1} cm^{-1}$
θ	Isotherm	-
λ	Wavelength	m
μ	Dipole moment/Reduced mass	Debye/g
ν	Stretching vibration mode	-
ν	Frequency	s^{-1}
$\tilde{\nu}$	Wavenumber	cm^{-1}
σ	Hammett parameter	-
σ_c	Cross section	cm^2
σ_d	Charge density	$\mu C cm^{-2}$
Φ	Work function	eV
Ω	Solid angle	Steradians

Abbreviations

CD	Cinchonidine
CN	Cinchonine
CS-NP	Core-shell nanoparticle
CT	Charge transfer (SERS theory)
CTAB	Cetyltrimethylammonium bromide
CV	Cyclic Voltammetry/cyclic voltammogram
DFT	Density Functional Theory

ee	Enantiomeric excess
EM	Electromagnetic (SERS theory)
EP	Ethyl pyruvate
EL	Ethyl lactate
EtOH	Ethanol
HER	Hydrogen evolution reaction
HHS	Half hydrogenated state
HMMP	High molecular mass product
H OPD	Hydrogen overpotential deposition
H UPD	Hydrogen underpotential deposition
KPL	Ketopantolactone
MeBuOH	2-Methyl-3-butyn-2-ol
MP	Methyl pyruvate
ML	Methyl lactate
NPs	nanoparticles
ORC	Oxidation reduction cycle
PA	Propargyl alcohol
PTFE	Polytetrafluoroethylene (Teflon®)
Q	Quinoline
QD	Quinidine
QN	Quinuclidine
SERS	Surface Enhanced Raman Scattering
SHINERS	Shell-isolated nanoparticle enhanced Raman spectroscopy
XPS	X-ray photoelectron spectroscopy

CHAPTER ONE

Introduction

1.1 Perspectives in Catalysis

The phenomenon of catalysis had been studied broadly since the early 19th century. Berzelius in 1836 was first to introduce the term ‘catalysis’ (meaning ‘loosening down’ in Greek) by endowing catalysts with some mysterious force.¹ A few classic examples have proven that people around the world were trying to discover the powerful quality of catalysts at the same time. For instance, in 1812, Kirchhoff² recorded the catalysed hydrolysis of starch by acid, which is now considered as a typical example of homogeneous catalysis.³ Then in 1817, Humphry Davy explored how by introducing a hot platinum wire into a mixture of air and coal gas, the metal became white hot.⁴ Also in 1824, Henry⁵ reported that ethylene inhibited the reaction between hydrogen and oxygen on platinum, which was regarded as the first example of poisoning of a catalyst.⁶

In 1834, Michael Faraday produced gaseous hydrogen and oxygen by the electrolysis of water and recombined them with platinum plates. Then Grove in 1845 proved that a hot platinum filament may decompose water vapour into hydrogen and oxygen. A few decades later, Philips used platinum to oxidise sulphur dioxide to sulphur trioxide with air.⁷ During the test, he discovered that the loss of catalytic activity was because the metal surface was poisoned by other reactants. All the above examples demonstrated that platinum was already known to possess excellent catalytic qualities even by the middle of the nineteenth century.

In 1877, Lemoine proved that the decomposition of hydriodic acid to hydrogen and iodine reached the same equilibrium point (19%) at 350 °C no matter if the reaction took place homogeneously in the gas phase or heterogeneously in the presence of platinum metal.⁸ Also, Bertholet further confirmed that the catalyst did not affect the equilibrium when he was trying to work on the acid-catalysed esterification of organic acids and hydrolysis of esters in 1879.⁶ Such observations helped crystallise our understanding of the key features of catalysis.

The 2nd of July in 1909 was regarded as a landmark day in the history of catalysis since it was when at Karlsruhe, Fritz Haber successfully prepared abundant quantities of ammonia with nitrogen and hydrogen as the gaseous reactants using reduced magnetite (Fe_3O_4) as the catalyst.⁹ Subsequently, scientists in BASF labs optimised this process on an industrial scale

and the production of fertilisers and explosives using ammonia changed the world forever.¹⁰ Again in Germany, the Fischer-Tropsch process¹¹ was invented to convert syn-gas to hydrocarbons and alcohols using cobalt or iron catalysts (apartheid South Africa manufactured petrol by this process for many years in order to circumvent the trade embargoes placed on it during this period). Soon, by selective oxidation of methanol, naphthalene and benzene, production on an industrial scale of formaldehyde, phthalic anhydride and maleic anhydride respectively allowed for the plastics industry to expand on an unprecedented scale.⁶

Catalytic cracking became important in the late 1930s.¹² This refers to the breaking of C-C bonds from large petroleum hydrocarbon molecules into smaller hydrocarbon fragments suitable for fuelling motor cars, aeroplanes and other major transport infrastructure. The most frequently used catalyst in this context was clay of the montmorillonite treated with acid. Around the same time, another development which needs to be drawn attention to was the oligomerisation of gaseous alkenes using 'silicophosphoric' acid and studied by Ipatieff and Pines.¹³ Later this too became an important industrial chemical reaction.¹

After World War II, due to their lack of stability, acid-treated clays were gradually replaced by amorphous, synthetic silica-alumina catalysts. These not only remained stable for longer, but gave better product distributions. The synthesis of zeolite, a representative catalyst from this family, was first reported by Rabo *et al.* in 1960.¹⁴ They showed that it was a really active and selective catalyst for isomerising hydrocarbons in particular. Now, it is widely used to catalyse a variety of reactions, such as hydrocracking, shape-selective conversions and reforming.¹⁵ Other large-scale heterogeneously catalysed reactions originating from the 1960s included the dehydrogenation of butane and ethylbenzene to generate butene and styrene monomer respectively, which were regarded as perfect examples of selective oxidation.⁶

Since the 1980s, applied catalysis has spread much more widely into natural environment protection, pure research institutions and fine chemicals.^{1, 16} Platinum-rhodium bimetallic particles supported on high-area ceric oxide-alumina mixed oxides can turn undesirable automobile exhaust species (CO and NO) into harmless products (CO₂ and N₂) and this single development has had an enormous impact in banishing the terrible smog that often accumulated in cities due to reactions of sunlight with automotive exhaust fumes.¹⁷ Another target of research involves obtaining high efficiency of fuel production from inexpensive

precursors using solar energy. Scientists are intensively studying catalytic reduction reactions driven by light absorption, for example conversion of water to hydrogen¹⁸ or carbon dioxide to methanol¹⁹. Hence, heterogeneous catalysis may be seen as an overriding and crucial human endeavour for the benefit of mankind. The development of both energy efficient and atom-efficient chemical transformations through catalysis for the production of fuels, pharmaceuticals and plastics, environmental protection and economic growth is one of the greatest intellectual challenges facing science in the 21st century. It is the aim of the present study to examine a small portion of this vast area of research in order to understand fundamentally, the processes allowing for the enantioselective hydrogenation of prochiral molecules.

1.1.1 Heterogeneous catalysis

The focus of this study is catalytic hydrogenation whereby two hydrogen atoms are added across a double or triple bond. Such hydrogenation reactions can include addition across alkenes, alkynes, carbonyls and nitrile bonds for example.²⁰ When hydrogenation is carried out using a catalyst that speeds up the rate of a chemical reaction yet itself is contained in a different phase to the reactant, it is referred to as heterogeneous catalysis. Moreover, a simple description of a catalyst as a substance that speeds up both the rate of the forward and reverse reaction (i.e. brings the system closer to equilibrium) without itself being consumed or chemically changed affords a qualitative description of a catalyst. Catalysis is a significant phenomenon for our modern industrial economy and an essential technology facilitating added value to chemical feedstocks. Nearly 90% of all our chemicals and materials are produced using catalysis at one stage or another.¹ Many developed countries are net exporters of such chemicals and thus rely on catalysis for the health of their economies.

In a catalytic reaction, catalysts neither consume themselves, nor change the extent of a reaction. Generally, catalysts react with one or more reactants to form intermediates and give the final reaction products subsequently. In the whole process, they are regenerated and not consumed at the end. With a catalyst, less free energy of activation is needed to reach the transition state, but the total free energy change from reactants to products remains the same. As mentioned earlier, a catalyst has no effect on the position of chemical equilibrium because the rate of both the forward and the reverse reaction are accelerated simultaneously.

Figure 1.1 illustrates these points by showing the reaction energy profile for a prototypical chemical reaction in which reactants X and Y are continuously converted to product Z along the ‘reaction progress’ on the x-axis. From **Figure 1.1**, one can conclude that with the presence of the catalyst, the reaction undergoes a different pathway (shown in red) with lower activation energy. Therefore, both the forward and reverse reactions are accelerated. This means that under different conditions of temperature and pressure, good hydrogenation catalysts may also act as good dehydrogenation catalysts!

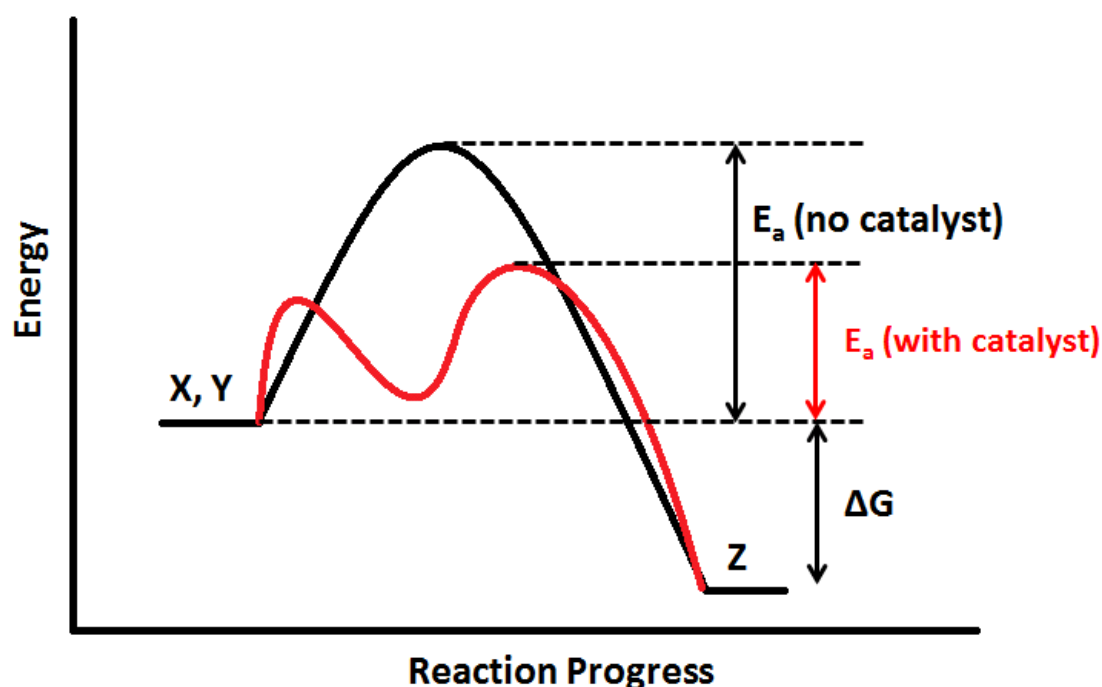


Figure 1.1 Generic potential energy diagram showing the effect of a catalyst in a hypothetical exothermic chemical reaction $X + Y$ to give Z .

As described above, a catalyst is a substance that increases the rate at which a chemical reaction reaches equilibrium without being consumed in the process.^{16, 21} In heterogeneous catalysis, the reactants diffuse to the catalyst surface and adsorb onto it by forming chemical bonds. At the end of the reaction, the products desorb from the surface and diffuse away. The reaction rate enhancement therefore takes place at an interface between the catalyst and the reactants. Here, the interphase may not only include single component solid, liquid or gas, but also multi-component immiscible liquids, such as water and oil. Solids are in the majority among practical heterogeneous catalysts, while gases and liquids are major reactants.

For solid heterogeneous catalysts, surface area is critical as it determines the availability of catalytic sites. Gas reactions catalysed by solid materials may take place both in the exterior and interior surfaces of a catalyst. The rate is determined by both the ‘availability’ of the surface area to impinging gas or liquid molecules (here pore size is fundamental together with the tortuosity of the pores¹⁶) and the magnitude of the surface area itself. In order to create a large surface area which is fully accessible, metal catalysts are usually dispersed throughout the whole surface of a suitable porous support. When the pores of the catalyst materials are wide enough so that they won’t obstruct the passage of reactants and products, the rate of conversion (from reactants to products) is proportional to the specific surface area. Otherwise, narrower pores will limit the reaction rate and then the rate is either proportional to the square root of the specific surface area or independent of it (depending on the mode of diffusion).²²

1.1.2 Reaction Rate

The reaction rate is defined as how fast a reaction takes place. For a chemical reaction occurring in a closed system, the rate is determined by the change in concentration or partial pressure (for gas phase reaction) of the reactant(s), r , and/or the product(s), p :

$$\text{rate} = -\frac{d[r]}{dt} = \frac{d[p]}{dt} = k(T)[r]^m \quad (\text{Eq. 1.1})$$

and is dependent on the concentration of r to the power of its reaction order (denoted by superscript m in this case). Since the rate of a reaction is always positive, a negative sign indicates the reactant(s) concentration is decreasing. The rate constant, k , at a fixed temperature is defined by the Arrhenius equation:

$$k = Ae^{-E_a/RT} \quad (\text{Eq. 1.2})$$

where A is the pre-exponential factor representing the collision frequency of the reactants, E_a is the activation energy for the reaction, R is the universal gas constant and T is the absolute temperature in K. The units of k are dependent on m . As is shown in **Figure 1.1**, by lowering E_a , a catalyst can increase the rate constant and so the reaction rate at a fixed temperature. In order to achieve maximum rate enhancement by optimising the reduction of E_a without diluting the reaction mixture, the amount of catalyst is usually controlled. Therefore, the rate values are normalised to the amount of catalyst $\text{mol}\cdot\text{dm}^{-3}\cdot\text{g}^{-1}\cdot\text{s}^{-1}$ to give the specific rate.

Alternatively, if the quantity of reaction sites is known, the rate values can be regarded as the number of product molecules generated per site per second (turnover frequency, s^{-1}).

For a heterogeneously catalysed reaction, the rate values may be normalised to the surface area of catalyst ($\text{mol}\cdot\text{dm}^{-3}\cdot\text{m}^{-2}\cdot\text{s}^{-1}$). There are other kinetic factors that may affect the reaction rate. Considering the whole process of the reaction, these factors are: (1) diffusion of the reactant to the catalyst surface; (2) adsorption of the reactant onto the surface; (3) diffusion of the adsorbate across the surface to the active site; (4) reaction of the reactant-catalyst complex; (5) desorption of product from the active site; and (6) diffusion of product away from the surface. Therefore the reaction rate is dependent not only on the catalyst's ability to lower E_a , but also the kinetic factors that control A .¹⁶

1.1.3 Molecular Adsorption on Metal Surfaces

In all heterogeneously catalysed processes, there is always at least one reactant that attaches to the surface of the solid catalyst for a period of time. The mechanisms for the catalytic reactions are of extreme importance and can be categorised into two distinct pathways called Langmuir-Hinshelwood and Eley-Rideal. The former proposes that both species adsorb on the surface and subsequently they both undergo a bimolecular reaction whilst still bonded to the surface. In the latter reaction mechanism, only one of the reactant molecules is bound to the surface. The surface complex thus formed then reacts with other reactant molecules impinging directly onto the surface from the gas phase.

Catalysis at solid surfaces is often explained in terms of the *Sabatier principle*. It states that interactions between the substrate and the catalyst are 'just right': either too weak or too strong an interaction will impede the catalytic process. This is because when the interaction is too weak, the substrate and the catalyst will fail to bind together and result in no reaction taking place. Conversely, if the interaction between adsorbate and surface is too strong, the catalytic sites will be blocked by the adsorbed species and render the surface complex formed incapable of dissociation. Therefore, it is considered beneficial to the activation of the reactant molecules to achieve the highest possible coverage of surface intermediates (requiring a strong interaction with the surface) but at the same time high diffusion and product desorption rates (weak surface interaction) so that conversion into useful products will be optimal.

When considering molecules forming surface complexes, it is helpful to distinguish between different types of adsorption. Let us consider catalytic oxidation as an example. In this process, the initial adsorption of oxygen gas molecules is usually followed by dissociation to form adsorbed oxygen atoms. The adsorption of the oxygen atoms on the catalyst surface is referred to as chemisorption. Chemisorption involves the rearrangement of electrons between the adsorbate and surface, resulting in breaking a chemical bond and forming new ones. The enthalpy changes corresponding to chemisorption usually exceed $30 \text{ kJ}\cdot\text{mol}^{-1}$ and in the case of oxidation referred to above can reach $400 \text{ kJ}\cdot\text{mol}^{-1}$. The larger the adsorption enthalpy, the greater is the extent of interaction and hence, the coverage of the surface with the oxygen atoms. Nevertheless, it's not beneficial at all when the interaction becomes too great, since it will be very difficult for these strongly chemisorbed atoms to react with other surface adsorbed molecules. Also, other molecules will find it difficult to chemisorb at sites that are already occupied by strongly bound oxygen. Therefore the Sabatier principle suggests that the best heterogeneous catalysts will be those in which the chemisorption of molecular species is sufficient to 'activate' these molecules, but not so great that subsequent surface diffusion, surface reaction and surface desorption of products are completely quenched. This means that when rates of reaction for different metal catalysts (catalytic rate) are plotted versus adsorption enthalpy of a reactant, the plot often exhibits a 'volcano curve' trend with optimal activity being exhibited by those surfaces satisfying the Sabatier principle.

A volcano plot, introduced by Baladin, for the decomposition of formic acid using different metal catalysts is shown in **Figure 1.2**. Studies show that the reaction intermediate is a surface formate, hence, the heat of formation (ΔH_f) of the metal formate is plotted on the x axis. The y axis (plotted in reverse to maintain the traditional 'volcano' shape) is used for the temperature at which the reaction reaches a specific rate. At both low and high values of ΔH_f , the reaction rate (as measured by the temperature required to sustain a particular rate) is slow. This is because at low values of ΔH_f , the rate of adsorption is the rate-limiting step whereas for high values of the ΔH_f , the rate of desorption becomes rate-limiting. It is seen that the maximum catalytic rate is observed for the platinum group metals. These exhibit intermediate values of ΔH_f and so catalytic rate is manifested as a balance between an 'optimised' rate of adsorption and surface diffusion and product desorption.

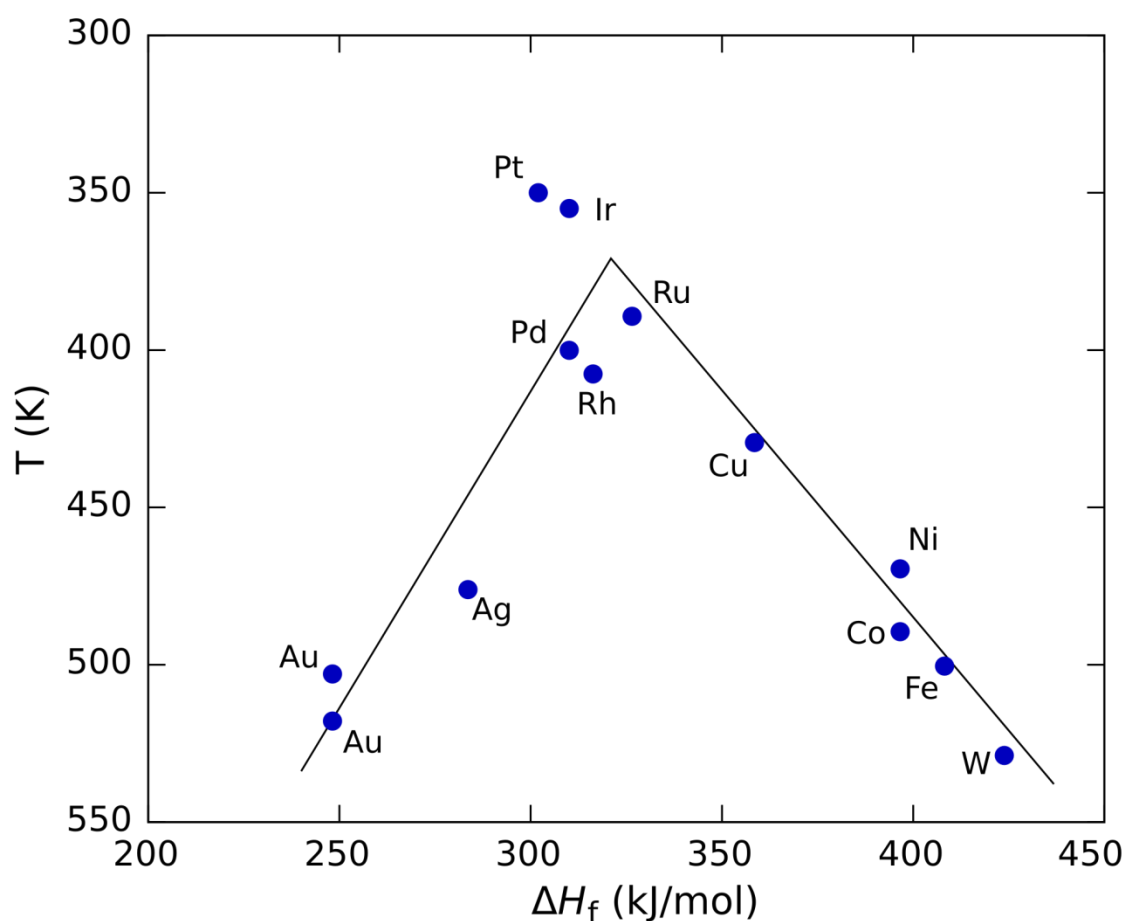


Figure 1.2 A typical volcano plot for the decomposition of formic acid on transition metal surfaces. The temperature necessary to maintain a specific rate of reaction is plotted against enthalpy of formation of the metal formates.

The formation of the chemical bond in chemisorption can further be classified as either *non-dissociative* or *dissociative* depending on whether or not molecular dissociation of the adsorbate occurs. In non-dissociative chemisorption the adsorbate is stable and does not break up into smaller molecular fragments. Carbon monoxide adsorption on platinum surfaces is a classic example of non-dissociative chemisorption.²³ However, dissociative adsorption involves decomposition of the adsorbate with most if not all of the fragments bound to the surface. Examples include oxygen adsorption on most metals at room temperature (as mentioned above) or dissociation of H_2 on platinum to form adsorbed hydrogen atoms.²⁴

Chemisorption is associated with highly directional chemical bonds. Hence, with certain position and orientation, chemisorbed adsorbates bind specific sites where there is a strong

interaction between them and the substrate. On metals, chemisorbed atoms tend to adsorb at the sites of highest coordination. For example, oxygen atoms bind in the fcc three-fold hollow sites of Pt{111} with a bond energy of $\sim 370 \text{ kJ}\cdot\text{mol}^{-1}$.²⁵

Strong chemisorption usually leads to ordered overlayers. The symmetry of the substrate may facilitate the chemisorbed overlayer to make well-ordered arrays of the adsorbate possible. The lateral interactions between the adsorbate may also improve the order of the overlayer. However, the temperature of the substrate can manipulate the symmetry of the overlayer if it is high enough to allow the adsorbate to move laterally across the surface. Then, in this situation, any adsorbate-adsorbate interaction can result in the formation of *islands*. These are localised areas of high coverage separated by clean areas or areas of low coverage.²⁶

Another important interaction is so-called physisorption, which is characterised by an electrostatic interaction between the surface and an adsorbate. In this process, the electronic structure of the molecule is barely perturbed since bonding occurs through Van der Waals type forces. There is only redistribution of the electrons within the molecule to form a polarised state at the surface. Therefore, no electrons are exchanged between the surface and the adsorbed molecule. The adsorption strength is considered to be weaker than in chemisorption with enthalpy changes of less than $30 \text{ kJ}\cdot\text{mol}^{-1}$. These ‘precursor states’ play an important role in catalysis because they allow a reactant to rapidly diffuse across the surface of the solid until it locates an ‘active site’ and undergoes chemisorption.²⁷

Most inert gases or substrates may only undergo physisorption, hence the coverage is strongly dependent on substrate temperature. The adsorption-desorption process is usually reversible with higher temperatures causing desorption and lower temperatures giving higher coverages (universal physisorption occurring at 0 K). Van der Waals interactions can also occur between the physisorbates and occur laterally to generate ordered overlayers or islands. Since the physisorbates do not interact strongly or directionally, there is usually very little adsorption site specificity. Therefore, the overlayers tend to be incommensurate rather than following any order or symmetry imposed by the underlying substrate.

1.1.4 Adsorption Isotherms

The term *adsorption isotherm* is used to describe the equilibrium of molecules between a surface and the bulk phase with surface bound and unbound molecules adsorbing and

desorbing from a surface at constant temperature as a function of pressure. Considering the situation in which only a single adsorbate can bind on each surface site, the equilibrium fractional surface coverage θ can be calculated using the isotherm with respect to the number of sites,

$$\theta = \frac{N_A}{N} \quad (\text{Eq. 1.3})$$

where N_A is the number of adsorbates and N is the total number of adsorption sites. The Langmuir adsorption isotherm was the first attempt to describe the equilibrium and is based on the assumption that the number of gaseous molecules impinging on a surface is proportional to the pressure, P .²⁸ Therefore, the equilibrium will be achieved when the rate of adsorption (proportional to $P(1-\theta)$) and the rate of desorption (proportional to θ) are equal:

$$k_a P(1 - \theta) = k_d \theta \quad (\text{Eq. 1.4})$$

where k_a and k_d are the rate constants for the adsorption and desorption processes, respectively. After rearranging equation 1.4, the coverage is then described as a function of pressure:

$$\theta = \frac{KP}{1+KP} \quad (\text{Eq. 1.5})$$

where

$$K = \frac{k_a}{k_d} \quad (\text{Eq. 1.6})$$

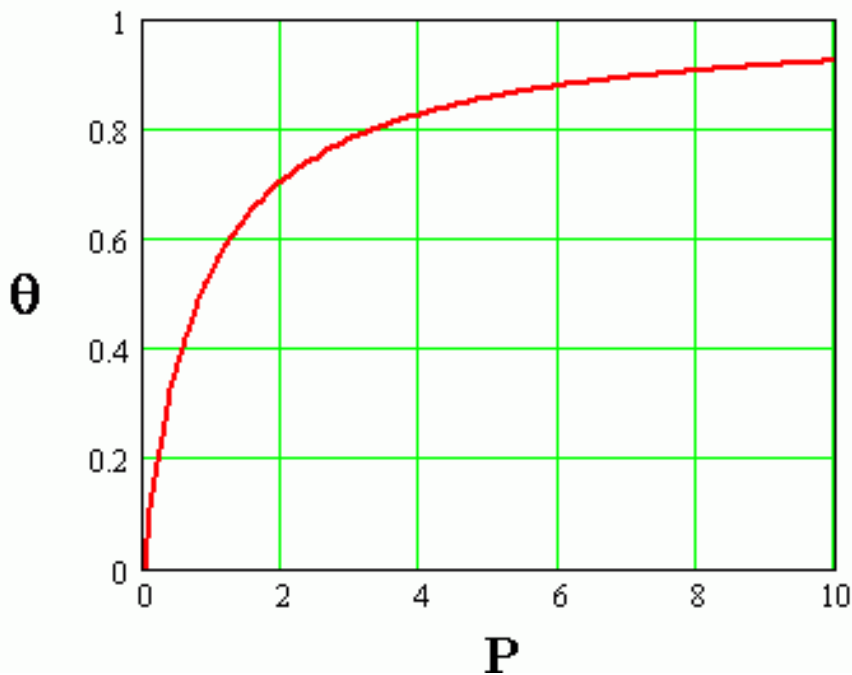


Figure 1.3 The Langmuir adsorption isotherm

Figure 1.3 shows a plot of the fractional adsorbate coverage against pressure for a Langmuir type equilibrium. Although this model is widely used to assess reaction kinetics, it fails to evaluate the adsorbate interactions. Therefore, the following assumptions are made:

1. The surface is uniform and contains equivalent adsorption sites capable of binding only one adsorbate molecule per site.
2. The adsorption is only led by a collision of a gas phase molecule with a vacant site on the surface. The molecule will desorb back into the gas phase if it collides with an occupied site.
3. The heat of adsorption is independent of coverage.

This last assumption is seldom correct as the heat of adsorption is usually observed to decrease (become less exothermic) as coverage increases. Factors causing this effect would include: 1) the repulsive forces of interaction between adsorbates; 2) a change in bonding type of the adsorbate at different levels of coverage; 3) an increase in the work function (energy required to remove an electron from the substrate) of the substrate; 4) heterogeneity of the surface (the opposite of assumption 1).¹

The Langmuir isotherm is only applicable to fractional coverages up to one monolayer. For multilayer adsorption in which physisorptive processes are involved, an alternative adsorption isotherm was conceived by Brunauer, Emmett and Teller (BET). It assumed that the multilayers are adsorbed consecutively with second layer adsorption beginning after the first layer is complete. During this process, each adsorbate provides a site of adsorption for the next layer.²⁹

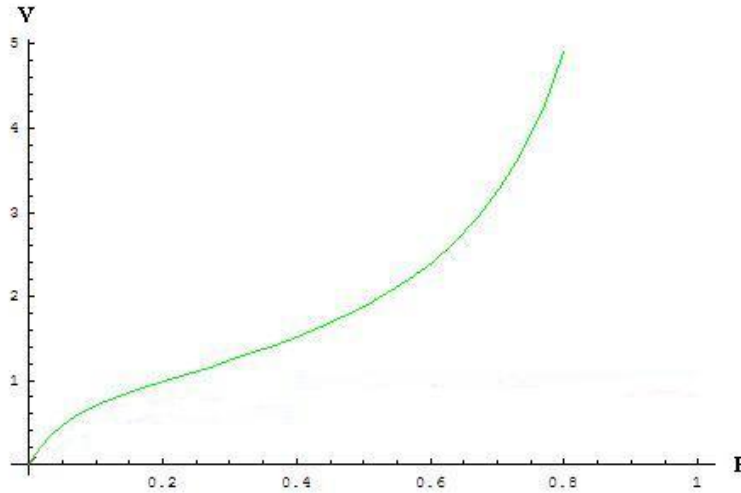


Figure 1.4 The BET adsorption isotherm

The BET isotherm successfully portrays the volume adsorbed against pressure as being an s-shaped curve in **Figure 1.4** due to multilayer physical adsorption. The assumptions by Langmuir concerning the absence of lateral adsorbate interactions and surface homogeneity are continued in the BET isotherm. The heat of adsorption in the second and subsequent layers are characterised by heats of adsorption equal to the latent heat of evaporation. The heat of adsorption of the first layer is taken up with a fixed heat of adsorption. Based on these assumptions, the BET equation is given as follows:

$$V = \frac{V_m c P}{(P_0 - P) \left\{ 1 + \frac{(c-1)P}{P_0} \right\}} \quad (\text{Eq. 1.7})$$

where V is volume of gas adsorbed, V_m is the maximum volume equivalent to an adsorbed monolayer, P is pressure of gas and P_0 is the saturated vapour pressure of the liquid at the operating temperature. The BET constant c is given by:

$$c = \exp \left(\frac{Q_a - Q_l}{RT} \right) \quad (\text{Eq. 1.8})$$

with $Q_a - Q_l$ being the difference between heat of adsorption on the first layer and heat of liquefaction of the gas phase molecule. This can be rearranged to:

$$\frac{P}{V(P_0 - P)} = \frac{1}{V_m c} + \frac{(c-1) P}{V_m c P_0} \quad (\text{Eq. 1.9})$$

A plot of $P/V(P_0 - P)$ against P/P_0 should be linear. The intercept on the y-axis is given by $1/V_m c$ and together with knowledge of the gradient of the graph gives the monolayer capacity together with constant c .

These two model isotherms mentioned above are mainly used for systems that are relatively simple. However, the major adsorption isotherms can be categorised into six types rather than just these two.³⁰ When more factors are taken into consideration such as lateral interactions, capillary condensation, porous adsorbents and non-porous surface, more complicated isotherm types can be derived.

1.2 Surface Chemistry

Techniques for the exploration of surfaces in electrochemistry remained quite different from those used in surface science for the majority of the last century.^{31, 32} In surface science, the achievement of ultra-high vacuum (UHV) conditions allowed for both the preparation of well-defined surfaces together with their maintenance as ostensibly clean over the time period necessary to complete a surface measurement. In addition, experimental methods involving X-rays and electrons impinging on the surface under UHV conditions afforded a truly surface sensitive approach to chemical analysis since electrons in the energy range 50-1000 eV escaping into vacuum as a result of these perturbations are characteristic of the first few atomic layers of solid only and analysis of their energies and spatial distributions may act as fingerprints of surface structure and composition.³³ However, in the case of electrochemistry, the presence of the electron-absorbing condensed phase (electrolyte) precluded explicit use of electron analysis in surface studies although X-ray diffraction and scattering using thin layers of electrolyte were possible using synchrotron radiation.³⁴ Hence, prior to the coupling of electrochemical cells to UHV systems to facilitate *ex situ* measurements, electron based physical techniques proved useless for studying the double layer. The situation could be alleviated somewhat by early pioneers such as Bewick³⁵ who measured reflection-IR properties of electrodes as a function of modulating the electrode potential and extracted

fundamental information regarding the vibrational properties of adsorbed intermediates³⁶. Hubbard³⁷ and Yeager³⁸ also made outstanding contributions to the coupling of surface science and electrochemical approaches to surface characterisation. Nonetheless, the delay in electrochemistry in relation to probing fundamental properties of solid electrode surfaces was only addressed towards the latter part of the century by two developments: 1. The invention of the scanning tunnelling microscope (STM) by G. Binnig and H. Rohrer of IBM in 1981³⁹ for which they received the Nobel prize and 2. the ‘flame-annealing’ technique developed mainly by Clavilier around the same time⁴⁰. Both of these contributions re-energised the study of the double layer and allowed electrochemistry to compete on an equal footing with the surface scientists to understand adsorption at solid surfaces. Of course electrochemical methods possess their own great advantages.

One can easily measure the rate of a charge transfer reaction occurring at a metal-solution interface as the electric current per unit area and in the first part of the 20th century, surface electrochemistry had been widely associated with kinetic data pertaining to electrocatalysis and examples of rates being measured in the ten millisecond range as a function of potential as far back as 1928 are reported.⁴¹ So-called Impedance Spectroscopy whereby the response of an electrochemical cell to alternating currents of variable frequency and time-scales may also reveal important properties regarding the kinetics of electron transfer, mass transport and bulk and surface structural transformations.⁴² Well-defined flow to and from an electrode surface as epitomised by methods such as rotating disc electrode (RDE)⁴³, rotating ring-disc electrode (RRDE)⁴⁴ and wall-jet studies⁴⁵ can contribute valuable information concerning the kinetics of electrocatalytic reactions.⁴⁶

Therefore, there are two different lines of experimentation for studying an electrode surface and the reactions occurring upon it. The first basic measurement in the historical view is a rate, which for a redox reaction is the number of electrons flowing across the surface per unit time per unit area (the current density). In this case, the variables may include potential, double-layer constituents, pressure and temperature. Second, spectroscopic techniques for chemical analysis for measuring the electrode *ex situ* using low energy electron diffraction (LEED)⁴⁷, thermal desorption spectroscopy (TDS)⁴⁸, X-ray photoelectron spectroscopy (XPS)³⁰ or indeed *in situ* (Fourier transform infra-red (FTIR)⁴⁹, surface-enhanced Raman spectroscopy (SERS))⁵⁰ hold out great promise for the future of the field.

1.2.1 Electroanalytical techniques

Electroanalytical techniques involve measurements of electrical quantities and their relationship with chemical parameters. A range of applications such as industrial quality control, environmental monitoring and biomedical analysis have flowed from such approaches.⁴⁶ Different from many chemical measurements involving homogeneous bulk solution, electrochemical processes take place at the electrode-solution interface and as such, instrumentation which is simple and can be miniaturised often makes these attractive analytical techniques.

Since electrochemistry more often involves the measurement of a parameter such as potential or current, a common approach is to use potential as the main controlling variable of the system and then to monitor the current. By setting a series of constant potential values, either positive to or negative of the reversible potential, the current density as a function of time to steady state may be observed. This method, called the *potential-step* method was pioneered after Hickling introduced an electronic feedback technique for maintaining a chosen electrode potential.⁵¹ The time constant of the circuit is given by $4CR$, where C is the double-layer capacitance, and R is the resistance of the double layer. Hence, if currents are at times much less than $4CR$, it will largely reflect charging of the double layer. At times above this transition time, diffusion control will intervene in observing the Tafel kinetics if the current density exceeds the limit.

In contrast '*Current-step*' methods set a series of constant current densities in order to record the potential-time relationship. According to Marchiano and Arvia⁵², the potential should be constant for a given current. This was the first transient method in electrochemical kinetics as exemplified by Bowden and Rideal in 1928.⁵³ Theoretically, the potential-step method is superior since the rate depends exponentially on potential. However, one cannot ignore the vast number of applications of current-step methods being made since the 1990s.⁵⁴

In order to determine the mechanism, one needs to determine the i - V relation in electrode kinetics whereby i is the electric current and V is the potential. The simplest way is to fix the potential at a series of values and observe the current-time relation at each given value. Ideally, after charging the double layer, the current should be constant and is the required parameter. One also needs the relaxation time for adsorbed intermediates to reach the steady state. However, unwanted side products might form and cause time variations.

One of the methods of obtaining i - V relations and related mechanistic data is the potential-sweep method. It is the most common electrochemical method in use, which provides an efficient and straightforward assessment of the redox behaviour of molecules on the electrode surface. The most basic potential sweep method is *linear sweep voltammetry* (LSV). In LSV, the potential of the working electrode is varied linearly with time between two values (usually the initial E_i and final E_f potentials). As the electrode potential increases or decreases constantly, the currents due to the capacitive charging of the electrode's double layer flow continuously. When the potential reaches a value at which the species in solution undergo electrochemical conversions, Faradaic current will also contribute to the current flow.⁵⁵

Cyclic voltammetry (CV) is another potential-sweep method which is based on the same principles as LSV. It was first reported in 1938 and described theoretically by Randles.⁵⁶ However, in contrast to LSV, in CV the potential of the working electrode inverts after reaching a chosen value. Then the current is measured and the data are plotted as current vs. potential. The sweep rate applied can vary from a few millivolts per second to hundreds of volts per second. The current measured during this process is often normalised to the electrode surface area and referred to as the current density. The current density is then plotted against the applied potential, and the result is referred to as a cyclic voltammogram. A peak in the measured current is seen at a potential that is characteristic of any electrode reaction taking place. The peak width and height for a particular process may depend on the sweep rate, electrolyte concentration and the electrode material.^{46, 57} The analyte that is studied by CV has to be redox active within the experimental potential window. It should also display a reversible wave which shows its ability to be reduced (oxidised) on a forward scan and then reoxidised (rereduced) predictably on the return scan.

1.2.2 Raman and Surface enhanced Raman spectroscopy

When Sir Chandrasekhra Venkata Raman first discovered the phenomenon that bears his name in 1928, the 'instrumentation' was crude, because he used sunlight as the source and a telescope as the collector.⁵⁸ The scattering was detected by his eyes, which was most remarkable. Later, much effort was expended in trying to improve the components of Raman instrumentation in every possible way. In the early stages, the development of better excitation sources was paramount. Different kinds of lamps which contained helium, bismuth, or lead were invented, but were found unsatisfactory due to the low light intensities until mercury lamp sources were designed for Raman use in the 1930s. These were then

modified by Hibben using a mercury burner.⁵⁹ Spedding and Stamm⁶⁰ used a version of this design with a cooled version in 1942 and these developments were further progressed by Rank and McCartney⁶¹ in 1948. The Raman instrument became commercial thanks to the development of the mercury excitation system, which consisted of four lamps surrounding the Raman tube, by Hilger Co. In 1952, Welsh *et al.* improved the Hilger lamp by introducing one with a four-turn helix of Pyrex tubing.⁶² The practicality of using different elements for coloured materials was tested in the next decade before laser sources were developed for use in Raman spectroscopy in 1962. Eventually, Ar⁺ and Kr⁺ lasers became available and the Nd-YAG laser superseded these.⁶³

The detection systems for Raman measurements have also made astonishing progress in their sensitivity. From the original measurements using photographic plates, to the first photoelectric Raman instrument reported in 1946 by Rank and Wiegand⁶⁴, to the usage of a cooled photomultiplier in 1950, scientists who had ambitions for Raman spectroscopy had never given up on improving the instrument. Developments in the optical train started in the early 1960s. After discovering the efficiency of removal of stray light with a double monochromator rather than a single one, a triple one was also introduced. Now, Raman spectra can also be obtained by Fourier transform (FT) spectroscopy.⁶⁵

However, the upper limit of differential Raman scattering sections for molecules is about 10^{-29} cm⁻²·sr⁻¹, which means, the corresponding Raman intensity for a monolayer of an adsorbate is less than 1 count per second (cps) with traditional Raman spectrometer systems.⁶⁶ Therefore, it was out of the detection limit of all Raman spectrometers for most adsorbates since Raman intensities from molecules adsorbed on surfaces were so low.

Then the extensive study of the structure and dynamics of molecules adsorbed on surfaces using Raman spectroscopy began... by accident! In 1974, surface enhanced Raman scattering (SERS) from pyridine adsorbed on electrochemically roughened silver was first reported by Martin Fleischmann *et al.* at the Department of Chemistry in the University of Southampton in the UK.⁶⁷ This initial publication has been cited more than 2100 times. Later in 1977, there were two groups who independently discovered that neither the surface area nor the concentration of the adsorbed species could account for so much of the enhanced signal as believed by Fleischmann *et al.*⁶⁷. Jeanmaire and Van Duyne proposed an electromagnetic enhancement theory,⁶⁸ while Albrecht and Creighton proposed a charge-transfer theory,⁶⁹ both of which will be introduced in detail in section 2.4.5.

Although the exact mechanism of the enhancement effect of SERS is still a matter of debate, it has never impeded its exploration and application. Since then, the effect of surface enhanced intensity from molecules on other metal surfaces has been found including lithium, sodium and potassium.^{70,71} The coinage metals, namely silver, copper and gold gave rise to the strongest and most reliable SERS activity because of their special optical properties.⁷² Because of its high sensitivity, SERS is a useful probe for studies of *in situ* gas-solid and liquid-solid interfaces at the molecular level.⁷³⁻⁷⁶ Robust research activities have expanded from an electrochemical environment to air and indeed UHV conditions.⁷⁷ All possible metallic morphologies, such as smooth surfaces, sphere segment void structure, films coated on roughened substrates, colloids and powders, and even catalysts supported on insulator granules became the challenging targets and were conquered one by one.^{76, 78-91} However, only the few coinage metals mentioned above could provide great enhancement of the Raman effect. Due to this particular restriction, Raman spectroscopy was not used as widely as IR spectroscopy in surface science and electrochemistry and certainly never for single crystal electrodes other than the coinage metals.

Nevertheless, researchers had never given up on expanding the application of Raman spectroscopy to the study of other metallic and even non-metallic surfaces. Some of these workers spent much effort in studies of electrocatalytically interesting transition metals in particular by coating SERS-active Ag or Au electrodes with ultrathin films of Ni, Co, Fe, Pt, Pd, Rh and Ru.⁹²⁻⁹⁷ By either electrochemical deposition or laser ablation, SERS spectra of adsorbed species on these films could be obtained thanks to the long range effect of the electromagnetic enhancement created by the SERS-active substrate.⁹⁰ Although it provided a new way to explore different metal surfaces and gain information on various interfaces, the enhancement effect could be weakened if the coated film was too thick. Therefore, only a few atomic layers of the film thickness would give rise to the strongest effect. A problem often encountered however was incomplete coverage of the SERS active metal support resulting in 'pin holes' of high SERS activity dominating the spectrum rather than the coating metal. Hence, it was not possible to avoid the adsorbate binding to the exposed substrate and generating strong signals. This difficulty of preparing pinhole free, ultrathin films with good stability limited the wider application of SERS.

Once these difficulties were overcome however, studies over a wide range of different metals and potentials became more and more realistic.^{76, 98} Nowadays, SERS has become a general

technique for researchers to study as many reactions as possible occurring at the electrified interface at a molecular level.

1.2.3 Nanoparticle synthesis for Raman spectroscopy and catalysis

Compared to metal films deposited onto a roughened electrode either electrochemically or in vacuum, there are several advantages in using nanoparticles (NPs) as SERS active substrates. Because the dimensions of the surface morphologies produced via electrochemical roughening are crucial to the observation of SERS,⁹⁹ it is often difficult to generate such 'roughness' uniformly across a macroscopic surface leading to inhomogeneity in the intensities of SERS bands (one often refers to the presence of hotspots giving rise to exceptional SERS activity in localised regions of a sample). However, if all NPs are of equal diameter and of optimal size to generate a maximal SERS response, simply coating a substrate with such NPs will immediately render it SERS active with uniform homogeneity across the whole electrode surface. Also, using NPs in this way does not require the use of expensive vacuum evaporation chambers to produce a SERS active film and so reduces cost and makes such substrates available to all.

Usually, nanoparticles are created with sizes between 2 and 100 nm since SERS phenomena only happen on metal surfaces containing surface morphological features lying within these ranges. In particular, metal NPs with sizes between 10 and 100 nm possess special surface plasmon resonance properties which results in great enhancement of the Raman signal for molecules adsorbed on (or close to) their surfaces.^{100, 101} Hence, the design and preparation of metal nanoparticle substrates has become the main focus in order to achieve strong signal intensity and reproducibility. Metal NP colloids are the most commonly used SERS substrate because their manufacture usually involves simple experimental steps such as mixing of liquid solutions, heating and separation. Another great advantage of NPs is that they can be used as catalytic components of technical catalysts. Colloidal metal nanoparticles have been synthesised with controlled sizes and shapes to meet various requirements in catalysis researches.¹⁰²⁻¹⁰⁵ Here, the preparation of spherical metal NPs, aggregation of metal NPs, bimetallic NPs and metal NPs with other kinds of shapes will be discussed. Their influence on the SERS signals in terms of the size and shape and the excitation wavelength will be noted as well.

Wet chemistry methods have been developed mainly for the preparation of metal NP colloids, such as chemical reduction, laser ablation and photoreduction. The development of the shape of the NPs is no longer limited to spheres but rather, with the addition of suitable modifiers NPs of various shapes and size distributions have emerged.^{103, 105} Moreover, the composition of the NPs may now range from a single component to multiple components (or alloys). No matter what kind of shape or composition, the aggregation step during the preparation process is regarded as a key stage with respect to obtaining better SERS signals by presenting 'hot spots' to the probe laser beam of uniform intensity and distribution.¹⁰⁶ Gradually, new types of metal NPs have been designed according to the fact that the SERS intensity depends on the excitation wavelength and the strength of the plasmons propagating on the surface of the metal NPs. These kinds of core-shell metal NPs and dimers of NPs can generate enhancement factors as high as 10^6 .¹⁰⁷ This exquisite control of particle shape, size and composition both for tailoring the SERS activity and the catalytic activity/selectivity of NPs has brought enormous attention from scientists worldwide.

Colloidal spherical particles are the oldest class of NPs reported. In 1979, Creighton used ice-cold NaBH_4 solution to reduce AgNO_3 and KAuCl_4 to obtain silver and gold NPs respectively. He chose pyridine as the probe to investigate the SERS activity of these metal NPs and discovered a strong dependence on the excitation wavelength.¹⁰⁸ Typical methods of preparing these kinds of Ag NPs involved reduction of AgNO_3 by sodium citrate under reflux.^{109, 110} The size of the Ag NPs was usually between 60 and 80 nm. These are also the simplest and most common methods of synthesising spherical metal NPs. The reducing agents include sodium citrate¹¹¹, sodium borohydride¹¹², hydrazine¹¹³ and hydroxylamine hydrochloride^{114, 115}. Then by adjusting the parameters such as the reaction temperature, pH of the solution and the kind of metal salt, the size and the aggregation state of metal NPs would be controlled. For instance, a very stable silver colloid exhibiting a particle size between 40-70 nm was prepared by Nickel *et al.*¹¹⁶ by reducing aqueous silver nitrate with hydrazine dihydrochloride in a weakly alkaline solution. These Ag NPs were reported to show a high SERS signal with the dye molecule Nile Blue A. Also, Li *et al.* prepared 17 nm in diameter spherical Ag NPs with mercaptoacetic acid as capping agent and noted that the SERS signal was determined by the particle sizes and degree of aggregation.¹¹⁷ The preparation of gold NPs was developed by Frens¹¹⁸, who used a similar method to reduce chloroauric acid using sodium citrate. The particle sizes produced were in the range of 20-100 nm. Peter *et al.* prepared Au NPs based on the seed-mediated growth method in which

HAuCl_4 was reduced with sodium acrylate and subsequently refluxed for 30 min.¹¹⁹ Schwartzberg and his co-workers utilized the template method to manufacture hollow, spherical Au NPs and obtained strong SERS signals from 4-mercaptobenzoic acid adsorbed on the NP surfaces due to the homogeneous structure.¹²⁰ Besides the commonly used synthesis of NPs in aqueous solutions, NP preparation involving organic solvents was invented by Shen et al.¹²¹ In this report, the monodisperse noble-metal NPs with SERS effect were synthesised in a direct reaction of the metal salt with oleylamine in toluene.

Apart from the wet chemistry methods mentioned above, laser ablation and photoreduction are also the most used methods to prepare SERS active NPs. The big advantage for the NPs prepared by these methods, which are considered as 'chemically pure', is that they avoid the influence of residual ions on the SERS signal during the chemical reaction. The typical procedure for laser ablation includes using a pulse laser (1064 nm from a Nd:YAG laser) to ablate metal plates or foils in distilled water or a NaCl solution.^{122, 123} Reproducible SERS spectra can be obtained from the metal colloids with optimised size distribution after taking the parameters, such as laser pulse energy, the time of ablation and the laser beam focussing into account. Meanwhile, the general procedure for the photoreduction method involves using light (gamma or UV laser irradiation) to reduce the metal salt.¹²⁴⁻¹²⁷ For instance, Ahern *et al.* observed the SERS signals of pyridine and biotin using Ag colloids prepared by laser irradiation.¹²⁸

As mentioned, there is a strong relationship between the size of the metal NPs and their SERS activity. It has been proved that the variation of the localised surface plasmon with NP size plays an important role in affecting the SERS activity.¹²⁹⁻¹³³ Jang *et al.* discovered that the SERS enhancement of 4-biphenylmethanethiolate on Au NPs was very weak for the size of 11 nm and much better for larger particles (43 and 97 nm).¹³⁴ On the other hand, Nie *et al.* explored the relationship between the optical excitation wavelength and particle size by studying the SERS activity on different sizes of Ag NPs with different laser lines (488, 568 and 647 nm).⁷⁸ **Figure 1.5** clearly shows that the SERS enhancement obtained from the NPs is strongly dependant on the size of the particles and the excitation wavelength. Therefore, in order to obtain the best SERS signal, one needs to decide the size of the NPs and the preferential wavelength to excite surface plasmon resonance on them.

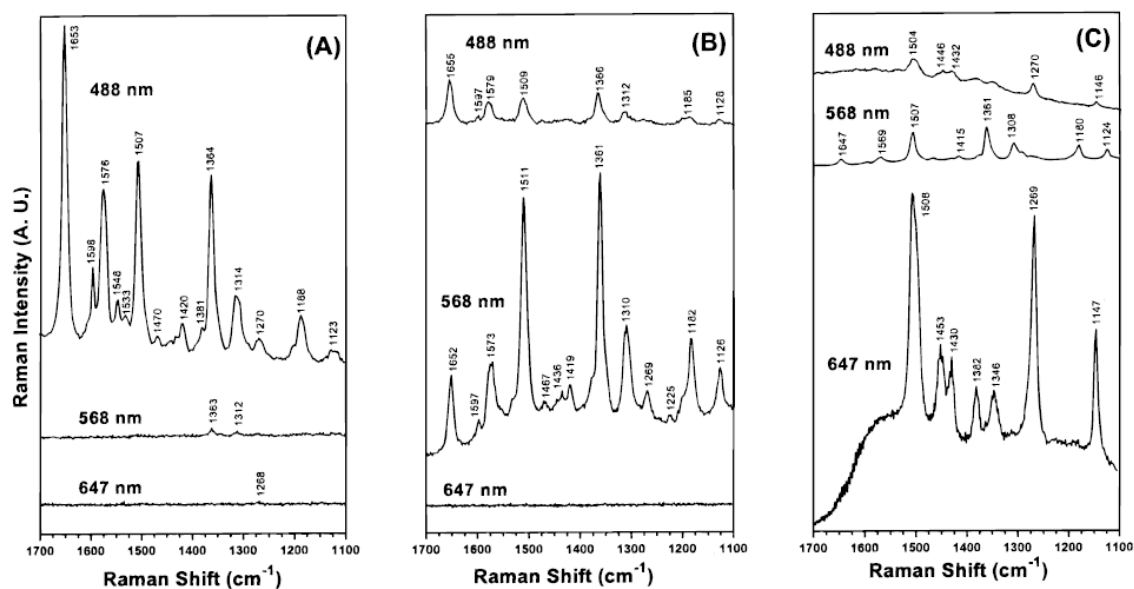


Figure 1.5 SER spectra of spatially isolated single Ag NPs, which were selected by wide-field screening for maximum enhancement at (a) 488 nm, (b) 567 nm and (c) 647 nm. Reprinted from reference 78.

The stability of the metal NPs colloidal system is another important factor to be considered for various applications. Those prepared by the traditional citrate reducing methods are known to be very stable over a long time. However, the chemical properties of the surface will change remarkably after several days, resulting in loss of consistency and intensity of the SERS signal. Hence, addition of stabilizers, such as poly(vinyl alcohol), poly(vinylpyrrolidone) and sodium dodecyl sulphate, to prevent aggregation was utilised and so improve the stability of the colloids.¹³⁵⁻¹³⁷ Nevertheless, the disadvantages of the stabilizer would include generating interfering signals as a consequence of the added polymer together with increasing the electrostatic barrier, resulting in a reduction of the ability of analytes to adsorb. Hence, to avoid using polymers that are difficult to remove post synthesis, alternative methods of stabilising NPs have been developed including silica or bovine serum albumin (BSA) coatings.^{138, 139}

In order to obtain much stronger SERS signals, aggregation of the metal colloids is an essential step. It has been indicated experimentally and theoretically that, when single NPs form aggregates of two or more NPs, a stronger enhancement can be generated due to the coupling of the electromagnetic field around the vacant interstices separating the particles.^{76, 140-144} Therefore, to facilitate aggregation, hydrosol activation is induced by adding inorganic salts, surfactants, organic amines or mineral acids to the colloids.¹⁴⁵⁻¹⁴⁷ For example, the Ag

colloids with evident SERS activity prepared by reduction with hydrazine and aggregation of the NPs by Cl^- was reported by Nickel and his co-workers.¹¹³ It was found that Cl^- can improve the enhancement greatly because of the increase of electromagnetic field induced by the anion and the reorientation of the molecules on the NPs. Also, the analyte itself was reported to cause aggregation of the NPs and show different enhancements by Heard *et al.*¹³⁶ They found that the addition of cetylpyridinium and cetylquinolinium salts changed the colour of the solution due to the aggregation of the metal NPs into clusters. This aggregation, which produces strong enhancement of Raman signal, proved that it plays an important role for the observation of enhanced Raman scattering from an adsorbed species.

Besides silver or gold NPs with a single composition, bimetallic or core-shell bimetal NPs which combine the SERS activities of both metals and generate greater enhancement have been developed.¹⁴⁸⁻¹⁵⁰ By changing the ratio between the two metals or the shell thickness of these NPs, it will cause a shift of the resonance frequency. Fang *et al.* first attempted to simply mix the prepared Ag and Au NP colloids and explored SERS of them coated with dye.¹⁴⁸ They found that a certain ratio of mixed Ag and Au colloids induces a specific aggregation and results in stupendous increase in the SERS activity. However, in order to achieve better SERS enhancement with the proper control of the metal NPs, the most common method for making bimetallic NPs is using a chemical reaction as reported in the literature.¹⁴⁹⁻¹⁵² Later, core-shell NPs with the composite either Au@Ag or Ag@Au were also fabricated and utilised for single molecule detection.^{153, 154} Recently, Tian *et al.* proposed the 'borrowing SERS enhancement' concept and chemically synthesised Au NPs coated with ultra-thin shells of different transition metals. By the long-range effect of the enhanced electromagnetic field created by the Au core, the non SERS active transition metals remarkably improve their Raman effect.¹⁰⁶ It has been widely used since its invention for the study of various catalytic reactions on the transition metal surfaces.

1.2.4 Growth and Epitaxy

The adsorption of one monolayer or less seems to be a simple case. But when the coverage exceeds a single monolayer, what will happen? It has been shown that strong chemisorption usually leads to ordered overlayers. However, adsorbates may or may not take on structures related to the substrate at high coverage. They may resemble much more the bulk adsorbate structure and this tension between substrate and adsorbate properties leads to concepts such as *surface strain* and *surface stress* determining the overall film morphology.²⁶ Intimately

connected with both of these is the *surface energy* which is related to the surface tension in the case of a liquid. Hence, several factors may influence the order of a monolayer, such as the strength of the adsorption interaction and lateral interactions, the relative strength between them, and so on. Subsequently, different modes of layer growth will be encountered. However, it will not be quantified in the present study. Interested readers may refer the literature (reference26) for a more detailed coverage.

As an example, let us consider what happens when two Si{111} surfaces are brought in contact. In this case, because of a perfect match, new bonds between the two surfaces will be formed so that the interface will be indistinguishable from the rest of the crystal. In contrast, if two unreconstructed (111) surfaces of Si and Ge are brought in contact, they will not match because of the difference of their lattice constants. Forcing them to form bonds will intensively perturb the atomic distances in the interface from those in the bulk. Whether or not such a perturbation will result in a stable interface after relaxation needs to be explored. The region of a surface or interface in which properties are distinguishable from either of the two bulk phases forming the interface is called the selvedge. The selvedge of metal surfaces in UHV often shows an oscillatory relaxation of the interplanar spacing moving from vacuum to the bulk due to imbalances in forces between surface and bulk atoms.²⁶

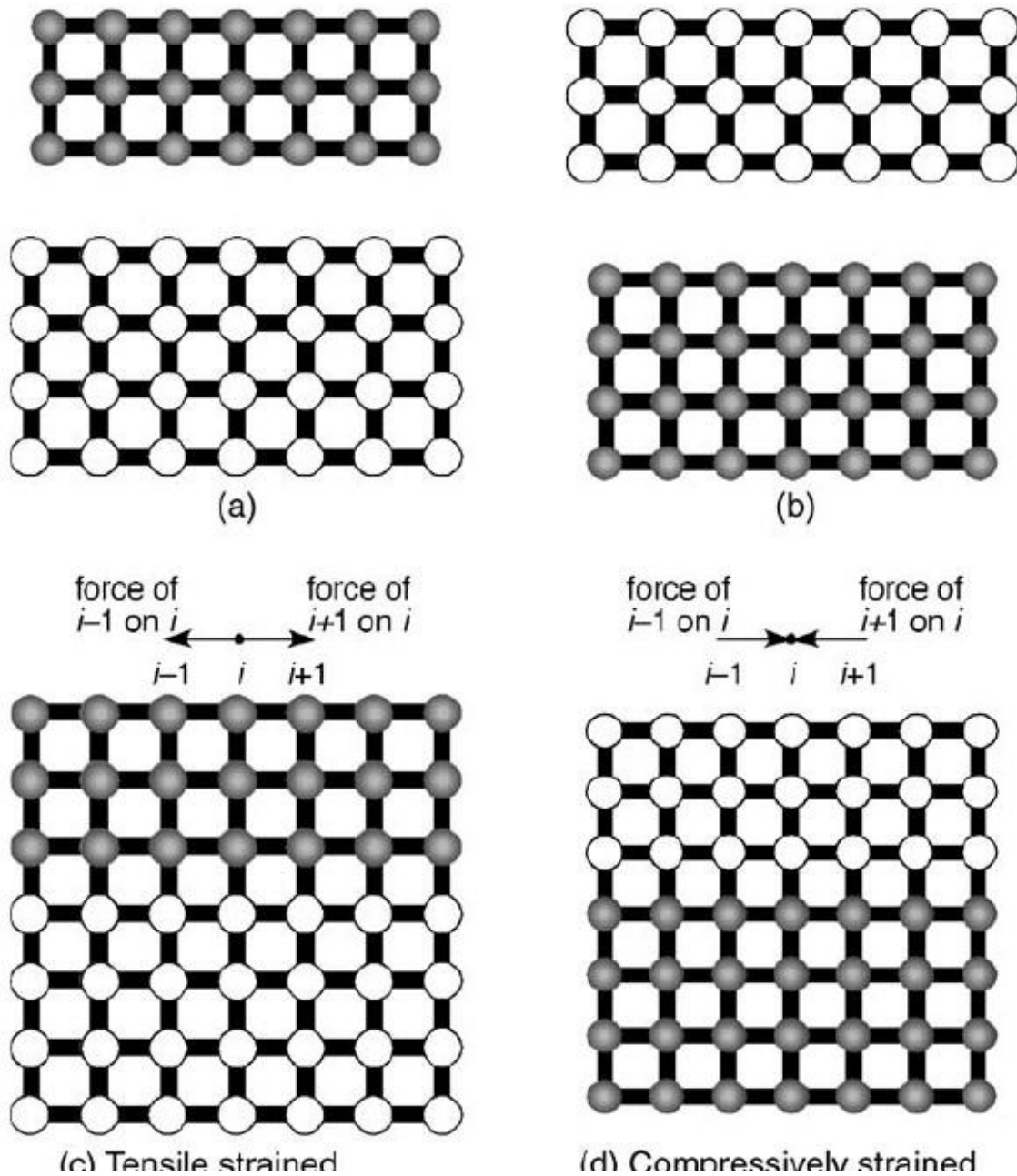


Figure 1.6 Stress and strain in pseudomorphic layers in cross-sectional view. (a) The substrate has a larger lattice spacing than the film. (b) The substrate has a smaller lattice spacing. (c) The film expands to the lattice spacing of the substrate and is under tension. (d) The film contracts upon attachment and is under compression. The net force vanishes in both cases with different directions. Reprinted from reference 26.

Two types of growth, namely *homoepitaxy* and *heteroepitaxy*, are involved in the above two cases (**Figure 1.6**). In the first case, the growth is simplified since the growing layer has the same atomic dimensions and lattice structure as the substrate. While in the second growth process, the dissimilar layers have to share the same structures as the substrate, which lead to

different bonding and phenomena. Therefore, strain is introduced to determine growth characteristics and define the electrical characteristics. For example, strain can reduce the band gap of GeSi layers grown on Si and make them useful for high-speed switches manufacturing. A *pseudomorphic layer* is then used to describe the layer that has assumed the structure of the substrate instead of exhibiting in the bulk material.³⁰ **Figure 1.6** illustrates stress and strain.

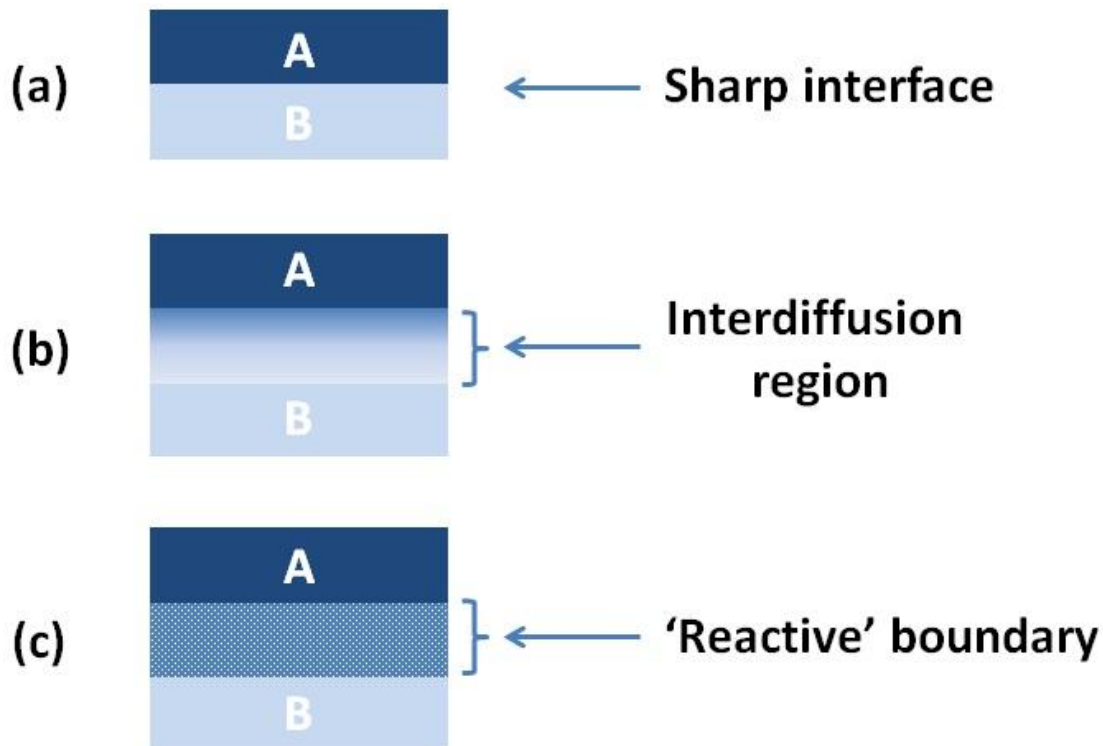


Figure 1.7 Three types of interfaces formed between two materials: (a) sharp interface; (b) nonabrupt interface; and (c) reactive interface.

Several types of interfaces could be formed when the effect of strain relaxation is taken into consideration. As shown in **Figure 1.7**, the simplest situation is the *sharp interface* formation when there is no mixing of the two materials. However, the other two forms of *nonabrupt interface* involve the mixing. If one of the materials is soluble in the other, a region of variable composition will be created due to its diffusion into the other. If they form a new compound which stabilises between the two pure phases, a so-called *reactive interface* will be formed.

The type of interface not only depends on the materials, but also on the fashion in which growth is performed. The balance between kinetics and thermodynamics has an impact on the

morphology and composition of the layered structures.²⁶ The reaction conditions and the rate of deposition are critical in interface growth. For example, high temperature favours surface diffusion and promotes interdiffusion between layers. Another important parameter that affects layer structure is the layer thickness. The introduction of *defects* (misfit dislocations) at the interface, which generally occurs at the overlayer with a value greater than the *critical thickness*, supports one mechanism of *strain relief*. Otherwise, the upper surface of the overlayer would relax the interfacial strain through roughening. Both of them may appear together with interdiffusion in either a cooperative or competitive way.

Since the sites at a surface exhibit different strength of interaction with adsorbates and these sites are present in ordered arrays, it is expected for adsorbates to bind in well-defined sites. Interactions between adsorbates can enhance the order of the overlayer; indeed, these interactions can also lead to a range of phase transitions in the overlayer.

Since the materials involved in growth vary, growth modes can be either a simple process without stress or a rather complicated one. In the case of thin liquid layers growing on a solid substrate, only the balance of forces at the liquid-gas (lg), solid-gas (sg) and solid-liquid (sl) needs to be considered, while gravity is neglected. There are only two growth modes which are *wetting* (2D layer-by-layer) and *nonwetting* (3D island formation). Meanwhile, three growth modes, named after their original investigators, were revealed for solid-on-solid growth, as shown in **Figure 1.8**. Due to the strain caused by lattice mismatch, this type of growth became more complicated.

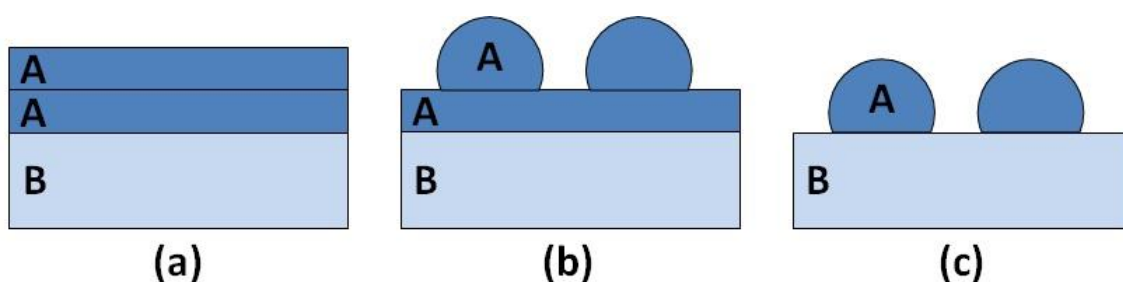


Figure 1.8 The thermodynamically controlled solid-on solid growth modes in the presence of a gas (or fluid or vacuum). (a) Frank-van der Merwe (FM) layer-by-layer growth of two lattice matched materials; (b) Stranski-Krastanov (SK) layer-plus-island growth; and (c) Volmer-Weber (VW) island growth.

Figure 1.8a depicts Frank-van der Merwe (FM) growth in which the deposited metal grows in a layer-by-layer fashion with the second layer starting only after the completion of the first. The second mode is Stranski-Krastanov (SK) growth, which describes a situation where three-dimensional islands start forming on top of the first one or two completed monolayers (**Figure 1.8b**). Dislocations are not occurring at any interface of the strained layer. However, the islands continuously relax with a lattice distortion in the growth direction. The last one called Volmer-Webber (VW) growth occurs with three dimensional islands forming at all stages of metal deposition (**figure 1.8c**). There are dislocations at the interface between the lattice mismatched materials.^{30, 155, 156}

Two thermodynamic properties of the materials control the growth of one of them on the surface of another. The first is the instability free energy of the film, which is the sum of the surface free energy of the growing film on the substrate ($\gamma_{F/S}$) and the interfacial energy between the film and the substrate (γ_I). The second is the surface free energy of the substrate (γ_S). The difference between the two values of these two free energies decides the growth modes. FM (Pseudomorphic) growth occurs when the instability free energy ($\gamma_{F/S} + \gamma_I$) is smaller than the substrate free energy γ_S at all stages of metal deposition. VW growth takes place when ($\gamma_{F/S} + \gamma_I$) is always greater than γ_S . SK growth combines the above two conditions at different stages. FM growth happens at least for one single monolayer when ($\gamma_{F/S} + \gamma_I$) is smaller than γ_S , then followed by VW growth ($(\gamma_{F/S} + \gamma_I) > \gamma_S$).³⁰

The validity of these models in predicting the growth mode also depends on the local surface equilibrium and kinetic factors. Since overlayer growth is a dynamic process, the growth mode can change with substrate temperature or crystallographic orientation of the substrate. Hence, kinetic factors sometimes could dominate thermodynamic features. If kinetic limitations prevent the growth from achieving equilibrium, it will be inappropriate to invoke the classical ‘thermodynamic’ description.^{157, 158}

1.2.5 Chirality

The French physicist Francois Arago discovered the power of rotatory polarisation exhibited by quartz back in 1811. He passed a polarised light beam through a quartz crystal and found the plane of the light was rotated.¹⁵⁹ Then in 1835, Jean-Baptiste Biot also observed a similar phenomenon by replacing the quartz crystal with sugar solutions.¹⁶⁰ This unusual observation could not be explained until 1848 when the difference between the tartaric acid crystals

gained from wine production and those obtained via chemical synthesis was noted by Louis Pasteur.¹⁶¹ According to him, only the crystals obtained from chemical synthesis could rotate polarised light whereas those derived from wine production could not. Ingeniously, using his own eyes and a pair of tweezers, he managed to separate out two different types of ammonium sodium tartrate crystals into two piles. He noted that the crystals collected in one pile were mirror images of those in the other. Save for the visual differences of the crystals noted, almost all other physical properties (density, boiling point, solubility, hardness, etc.) were the same. Upon re-dissolving each set of crystals to form two ostensibly ‘identical’ solutions, Pasteur discovered that one solution rotated the plane of polarised light in a clockwise way (known as dextrorotatory), while the other rotated the light in an anti-clockwise fashion (known as levorotatory). This property was called optical activity. The commercially sourced form of tartaric acid did not rotate polarised light in this way since both types of left- and right-handed crystal were present with equal amounts. The ‘asymmetry’ between the two forms described by Pasteur was later termed ‘chirality’ by Lord Kelvin in 1893. Based on these observations, van’t Hoff managed to rationalise the basis of the chirality in organic molecules by assuming a tetrahedral arrangements of different atoms or groups around a central carbon atom.¹⁶² These discoveries relating to the subject of molecular and structural shape were later to become one of the most important topics in modern science.¹⁶³ In this context, the present study will investigate the adsorption of molecules at solid surfaces in order to clarify the mechanism by which chiral auxiliary molecules steer the chiral outcome of prochiral alpha-ketoester hydrogenation in heterogeneous enantioselective catalysis.

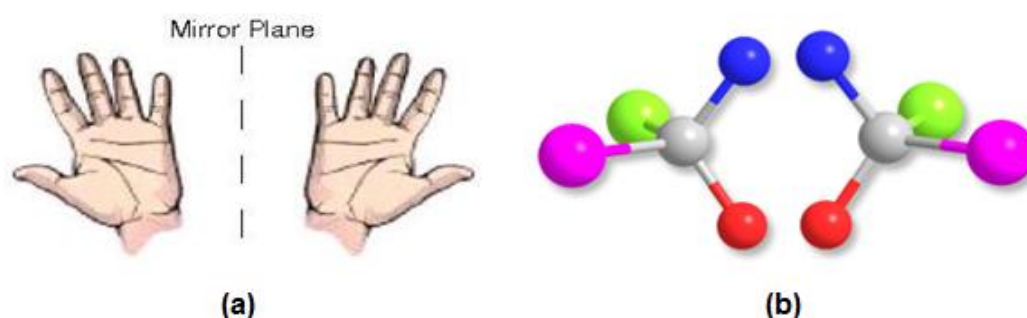


Figure 1.9 Examples of chiral objects: (a) hands and (b) an sp^3 hybridised carbon atom bonded to four different constituents.

Like a hand, an object which is chiral is non-superimposable on its mirror image (**Figure 1.9**). In molecular terms, such objects are usually composed of a series of stereoisomers

called optical isomers (also enantiomers), each being a mirror image of the other. A molecule with the central carbon atom bonded to four different atoms or groups is therefore considered chiral. The atoms or groups bonded to the centre carbon are assigned a priority according to their mass and labelled 1-4 in descending order by using the Cahn-Ingold-Prelog system.¹⁶⁴ Hence, enantiomers are named and labelled in this way. As shown in **Figure 1.10**, the enantiomer is viewed with the fourth atom/group with the lowest mass pointing away. If groups 1-3 in preference run in a clockwise way, the enantiomer will be noted with the prefix *R*- (rectus) or *S*- (sinister) if 1-3 groups run anti-clockwise.

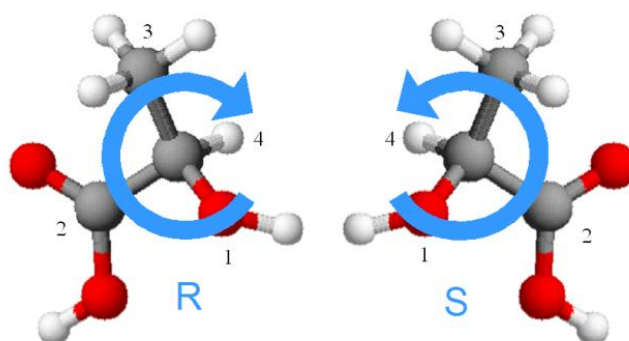


Figure 1.10 Enantiomers being described using the Cahn-Ingold-Prelog system of nomenclature.

Non-superimposable stereoisomers usually containing more than one stereocentre are termed *diastereoisomers*. They are not mirror images of one another. Compounds containing two or more stereocentres but in themselves are not chiral are termed *meso-compounds*, which in this case are superimposable on their mirror images (**Figure 1.11**).¹⁶⁵

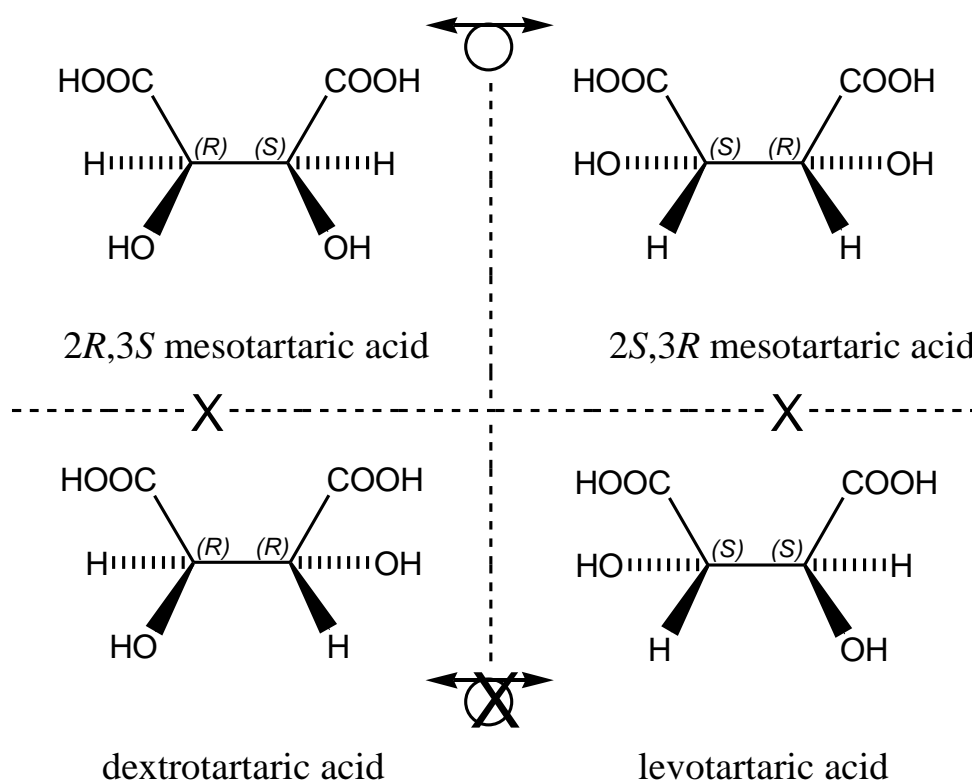


Figure 1.11 The meso-compounds are equivalent as they are superimposable on each other. Dextrotartaric acid is the enantiomer of levotartaric acid. The meso-compounds are diastereoisomers of dextro- and levotartaric acid. Reprinted from reference 165.

Since enantiomers possess this specific feature, their interaction with other chiral molecules or light has become an important area of research. Manufacturing pure enantiomeric compounds that contain exclusively only one type of handedness is the primary target in industry since such centres are crucial to all aspects of biochemistry with applications in fine chemicals including fragrances¹⁶⁶, pharmaceuticals¹⁶⁷, flavours¹⁶⁸, and agrochemicals¹⁶⁹.

A mixture of equal amounts of two enantiomers is called a *racemate*. If one enantiomer is in excess, the excess can be quantified as a percentage of the total mixture. The so-called enantiomeric excess (*ee*) is quantified in the following equation:

$$ee = \frac{[R]-[S]}{[R]+[S]} \times 100\% \quad (\text{Eq. 1.10})$$

where [R] is the concentration of the *R*-enantiomer and [S] the concentration of the *S*-enantiomer. The numerator will be [S] – [R] if calculating the *S*-enantiomer percentage.

It is often expensive to produce enantiomerically pure substances on a large scale. However, for a small quantity of racemate, the enantiomers can be separated by chiral chromatography.¹⁷⁰ Also, using an enantioselective reaction can produce two chemically different diastereoisomers. Since each diastereoisomer will be chemically and physically distinct, they may be separated using classical methods of separation such as fractional distillation.¹⁷¹ When each separated diastereoisomer is subsequently treated chemically to regenerate the enantiomer, the resulting mixture will contain only a single enantiomer which may be further separated by standard means. Another method of separation of a racemic mixture into its individual enantiomers would be a kinetic resolution whereby a chemical such as an enzyme reacts preferentially with one of the enantiomers.¹⁷² In this way, the racemate becomes enriched in a single enantiomer although of course, ultimately 50% of the initial sample will be destroyed in the process!

Since it is not easy to separate enantiomers, more efficient synthetic methods were developed to directly produce a single pure enantiomer.¹⁷³ Enantioselective catalysis is applied to target the industrial problems of manufacturing enantiopure chemicals. A Nobel prize was awarded to Knowles, Noyori and Sharpless in 2001 for their use of homogeneous catalysts in enantioselective compounds production.¹⁷⁴ However, three major difficulties were raised due to the usage of homogeneous catalysts if the enantiopurity needed to reach $\geq 99\%$ *ee*. It includes the separation of both catalyst and product from the reaction mixture, limited chance of catalyst re-use, and high sensitivity to normal ambient conditions (such as with oxygen/water vapour being present). Many of these problems could be overcome if an enantioselective heterogeneous catalysts could be designed for similar purposes. This is because, simple filtration may remove the solid catalyst from the reaction mixture and regeneration by controlled heating in an oxygen or hydrogen ambient may often restore optimal catalytic behaviour.¹

1.2.6 Catalysts in electrochemistry - electrocatalysts

The goal of exploring electrode materials with better performance and higher efficiency can be achieved with knowledge of the basic science behind the electrocatalytic processes itself. Therefore, in order to study the structure and composition of solid electrode surfaces, the reduction/oxidation state of surface atoms, the adsorbate bonding capability, surface coverages and lifetimes on the surface of reaction intermediates become key questions. These can be addressed taking a macroscopic viewpoint of the experiment and varying parameters

such as electrolyte composition, applied electrical potential, pressure, temperature, *etc.*, under control.¹⁷⁵ Combining these approaches with surface sensitive probes based on photon, electron, and ion spectroscopies aids enormously the exploration of electrochemical surface chemistry.^{176, 177}

Usually, based on surface science and electrochemical kinetic measurements, electrocatalysts with high efficacy may be designed. A wide variety of materials, including single metals, alloys, carbons, oxides, amorphous materials, polymers, enzymes and so on, are used as materials in fuel cell applications. Those consisting of inorganic catalysts are relative simple to manufacture.¹ Their anodes are usually made of single metals such as platinum or occasionally (to help with CO tolerance), Ru may be added supported on graphite¹⁷⁸. The anode is supplied with the fuel (hydrogen or methanol for example) whilst the cathode (again usually Pt or a Pt alloy) is supplied with oxygen/air. Separating both of these electrodes will be a semi-permeable hydrated membrane usually consisting of the polyelectrolyte Nafion[®] which facilitates proton transport but prevents diffusion of fuel from anode to cathode.¹⁷⁹ During the overall fuel cell reaction, energy is produced in the form of electric current as well as water and/or carbon dioxide. More complex fuel cells involving enzymes and living organisms are also becoming more popular in order to replace the expensive precious metals as electrocatalysts together with a drive to look for more environmentally friendly processes. Some typical electrocatalysts will be introduced according to their chemical nature as electrocatalytic systems.¹⁸⁰

Firstly, dispersed and rough metal electrodes are the most widely utilised. From nanometer to micrometer, the size of crystalline metal clusters varies in the electrocatalyst dispersions.¹⁸¹ In heterogeneous reactions, the particle size and shape plays a significant role in the behaviour of the electrocatalyst.^{182, 183} The discovery of changes of electrocatalytic activity with time in aged fuel cell electrode electrocatalysts has been ascribed to both catalyst particle sintering and corrosion which decreases the overall surface area of the electrocatalyst.¹⁸⁴ Corrosion of the graphite support has also been noted as an extensive problem in optimal fuel cell performance. Therefore, when new catalysts with improved performance (activity) and multi-functionality (selectivity) are designed, their size, shape, surface structure and environmental characteristics are taken into consideration. The preparation involves a wide range of processing, such as rough palladium nanoparticles and nanowires formed on highly ordered graphite (HOPG) by electrodeposition, fractal surface

formation and highly rough palladium or platinum electrodes produced from electrochemical roughening by cyclic potential techniques.¹⁸⁵⁻¹⁸⁷

Secondly, dispersed metal-carbon electrodes are of special interest due to their unique electronic properties. These carbon materials exhibit electrical properties ranging from an essentially metallic material in disordered graphite or glassy carbon to a semi-metallic behaviour in high surface area carbons.¹⁸⁸ Carbon surfaces are largely inert to electrochemical processes over a wide potential range although as mentioned earlier, prolonged exposure to electrooxidising conditions can result in slow degradation of the material. Hence, carbon electrodes are often used for manufacturing chemically modified electrodes. However, the surface chemistry of carbons is very complex since there are a range of surface defects present.^{189, 190} Also, some functional groups containing O- and OH- usually take part in the processes of physisorption and chemisorption.¹⁹¹ Due to their physicochemical properties for inhibiting the agglomeration of metal nanoparticles, carbon blacks are still used. Vulcan carbon is one of the well-known power source carbon supports, which contains 0.5 wt% of thiophene-like sulphur.¹⁹² The supported platinum electrocatalyst is not poisoned by the sulphur as the oxide layer on the surface of Pt NPs protects it by desulphurising the carbon whilst making membrane electrodes for fuel cells.¹⁹³ Its large surface area ($\sim 250 \text{ m}^2 \cdot \text{g}^{-1}$) with micropores allows Pt NPs to readily distribute themselves equally through the material. Therefore, the requirement of maximising Pt surface accessibility to fuel is met. Since the contact between Pt and carbon is considered of great importance for tethering the particles, work has been undertaken trying to incorporate platinum nanoclusters during the synthesis of porous structures of conductive carbons.¹⁹⁴ Furthermore, the surface chemistry and morphology of the carbon support must sustain its high dispersion over time.

Nowadays, a lot of researchers are focusing on electrocatalysis in low temperature proton exchange membrane fuel cells (PEMFC).¹⁹⁵ In order to achieve the desired reaction rate in fuel cells, the electrocatalyst usually needs to be a precious metal such as platinum although metal thrifiting is more and more being used to reduce the total amount of Pt necessary to maintain a particular power output by combining a thin layer of platinum on top of a 'cheaper' metal.¹⁹⁶ Usually, platinum metal NPs are supported on electronically conductive carbons but recently, carbon nanotubes (CNTs) have become attractive alternatives to graphite¹⁹⁷. The observation of the decomposition of hydrazine being more effective for

iridium NPs supported on CNTs instead of graphite points to superior properties afforded by CNT supports.¹⁹⁸ This is already impacting significantly in choosing the support material for hydrazine-fuelled space vehicles.¹⁹⁹

Besides, metals such as Raney nickel for molecular hydrogen electrochemical oxidation²⁰⁰, metal alloys including platinum-tin for methanol electrooxidation²⁰¹⁻²⁰³, and platinum-chromium for oxygen electrochemical reduction reaction (OERR)²⁰⁴, are typical electrocatalysts used in fuel cells. Finding the most active sites of the nanoscale materials and controlling their amorphousness and disorder and relating this to the catalytic activity is a key issue.²⁰⁵ It was discovered that the activity of Pt catalyst in the direct methanol fuel cell (DMFC) was improved by adding tin, in which methanol oxidation in sulphuric acid took place on carbon-supported Pt-Sn electrodes.^{49, 206} It has also been proved that platinum-based alloys, such as Pt_α-Ru_β for methanol oxidation and Pt_α-Cr_β for the OER, are more efficient than pure platinum.²⁰⁷ Both of their interfacial domains are highly disordered. Since there are many choices of transition metals (and their oxides) which can be potential alloy materials, scientists are working extensively testing alternative alloy catalyst combinations with both lower costs and greater resilience.

Finally, there is another kind of chemically modified electrodes which can also meet certain requirements with specific electrocatalytic activities. By anchoring chemical functional groups, the catalytic properties of conducting substrates can be modified. The electrode surface formed would be more complex due to the interactions between the functional groups and the substrate. However, molecular complexes grafted onto the support can help electrochemically convert reactants to products by accelerating the electron transfer processes or immobilising oxidation-reduction couples.^{208, 209} They can be prepared by various conventional methods, such as adsorption (functionalised vinyl compounds on platinum)^{210, 211}, chemical reactions (metal porphyrin film covering an activated carbon electrode)²¹², polymerisation (pyrolytic graphite modified by polyvinylpyridine)²¹³, and so on. Furthermore, new nanostructured materials with novel functions and special optical, magnetic, and catalytic properties have been designed and utilised for electrode assemblage and appear to hold out great potential.²¹⁴⁻²²³

1.3 An Overview of Catalytic Hydrogenation

Paul Sabatier, a French chemist, introduced catalytic hydrogenation with his seminal work in the 19th century.²²⁴ His perception of the surface phenomena occurring was remarkable. Wilhelm Normann from Germany also played a key role in founding catalytic hydrogenation. He used nickel powder to convert oils and waxes into edible foodstuffs.²²⁵

Hydrogenation is an important chemical reaction to the food, pharmaceutical, petrochemical and fine chemical industries. In its most elementary sense, the term hydrogenation refers to the addition reaction of molecular hydrogen to an unsaturated carbon-carbon, carbon-nitrogen or carbon-oxygen bond.²²⁶ It is a chemical reaction between molecular hydrogen and another molecule, usually in the presence of a catalyst. However, molecular hydrogen does not readily react with organic molecules. It always requires a catalyst, which is not consumed or part of the final product, to facilitate the chemical reaction. Non-catalytic hydrogenation takes place only at very high temperatures. In all of the above industrial fields, the production of most important chemicals involves catalysis. In environmental science, catalytic converters in automobiles have been playing a significant role in controlling air pollution for nearly four decades.²²⁷ In green chemistry, catalytic reactions are preferred due to the reduced amount of waste generated. In the food industry, the largest scale application of hydrogenation is for the processing of vegetable oils. In the petrochemical industry, petroleum refining makes intense use of catalysis for alkylation,²²⁸ catalytic cracking,²²⁹ naphtha reforming and steam reforming, etc. There is also a side effect of incomplete hydrogenation for human health, which is the isomerisation of the remaining unsaturated carbon bonds. In the unprocessed fats in most edible fat sources, although the *cis* configuration of the double bonds predominates, incomplete hydrogenation may partially convert those molecules to *trans* isomers, which have been implicated in circulatory diseases. Moreover, since the conversion from *cis* to *trans* is more favourable because the latter configuration has lower energy, it is most important to control the isomer ratio via food legislation.

1.3.1 Alkyne hydrogenation

Because of its exceptional synthetic use and special versatility, the acetylenic group has attracted many researchers to explore its ability to form carbon-carbon bonds with retention of the double bond. The triple bond may be considered a pseudo *cis* double bond in stereoselective synthesis in which semi-hydrogenation of the triple bond is required (**Figure**

1.12). Therefore, it is of great importance to demand catalyst to exhibit both bond selectivity and stereoselectivity.

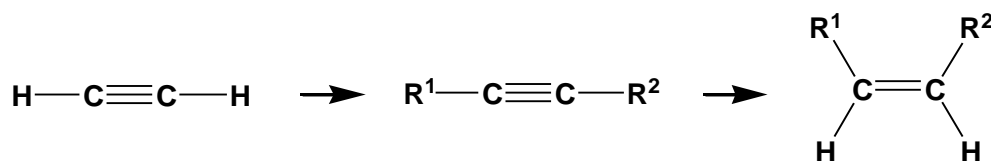


Figure 1.12 The triple bond considered as a pseudo *cis* double bond

In 1874, de Wilde noted that acetylene was reduced to ethane with a platinum catalyst.²³⁰ However, the first semi-hydrogenation reaction was discovered by Sabatier and Senderens in 1899.²³¹ They found that, instead of using platinum catalysts, palladium or nickel can reduce acetylene to ethylene. Later, Paal recorded the stereoselective nature of the addition in his report of partial reduction of phenylpropionic acid over colloidal palladium giving *cis*-cinnamic acid.²³² Unsupported colloid was used in most semi-hydrogenation reactions over palladium before the 1930s.²³³ Since then, almost all work has involved palladium on some kind of support such as charcoal, calcium carbonate and barium sulphate.²³⁴

The catalytic semi-hydrogenation (partial hydrogenation) of alkynes is of special interest in the fine chemical industries because of its efficiency in producing alkenes.²³⁵ Many processes and applications in the petrochemical, pharmaceutical and agrochemical industries are based on this kind of selective hydrogenation of carbon-carbon triple bonds using heterogeneous catalysis. The conventional process involves a so-called Lindlar catalyst, which is quinoline-promoted CaCO₃ supported palladium poisoned with lead.^{236, 237} Despite the attempt to enhance its selectivity by deactivating the Pd sites using quinoline and lead, its application to alkyne hydrogenation still has problems, such as limited catalyst robustness, overhydrogenation to alkanes, impossibility of reuse due to deactivation and potential toxicity if leaching of lead occurs.²³⁸ Therefore, the process design of alkyne hydrogenation has been paid particular attention by researchers for many years. A variety of heterogeneous catalysts, including palladium, platinum, rhodium and nickel, have been the targets which are usually modified for improved selectivity by addition of other metals and /or amines and sulphides.²³⁹

Due to its remarkable activity and selectivity, palladium is the most widely used catalyst compared to the other metals from Group VIII, such as Pt, Ru, Rh and Ni. There are a couple of methods to adjust its catalytic performance. Reduction of selectivity can be achieved by adding other metal salts. High reaction rates and adjustable selectivity can also be attained by

introduction of modifiers. The main characteristic of Pd-based catalysts is their strong double bond isomerisation activity leading to unwanted side-products in stereoselective reductions.^{240, 241}

Especially, for alkyne hydrogenation, catalyst selectivity is more important than reactivity.²⁴² In order to improve the ability of Pd to yield alkenes by selective hydrogenation, promoters and additives are used. The addition of a second metal to obtain bimetallic catalysts is helpful in obtaining better catalyst selectivity. Transition metals, such as Ag, Rh, Au, Cu, Cr, Zn along with alkali metals were proved to be quite effective to achieve this.²⁴³ Moreover, quinoline or piperidine can be used in Lindlar's catalyst in the semi-hydrogenation of alkynes. Side reactions that affect the selectivity of the catalytic hydrogenation include cis/trans equilibration and double bond migration. Both isomerisation reactions may occur with Pd and Ni catalysts. However, they may be suppressed by adding Rh or Pt or nitrogen bases. Due to the increased reactivity and stronger adsorption of alkynes compared to alkenes, partial hydrogenation of the C≡C triple bond to generate olefins is the preferred reaction pathway. Semi-hydrogenation of the diene to the monoalkene is also the preferred pathway compared to complete saturation.^{235, 241}

The alternative way of improving the selectivity of the catalysts is to explore the structure effect of the catalyst on the reaction. The idea of a structure sensitive reaction has been demonstrated by Crespo-Quesada *et al.*,²⁴⁴ who compared the selectivity of cubic, octahedral and cuboctahedral particles of platinum in the hydrogenation of 2-methyl-3-butyn-2-ol. The different proportions of terraces and edges/corners present on the three different types of NP led to distinct selectivity in the hydrogenation. The results of Crespo-Quesada *et al.* indicated two distinct active sites were present on the particles; semi-hydrogenation of the alkyne occurred preferentially on terraces whereas further hydrogenation to the alkane occurred over edges. A similar study was conducted by Schmidt *et al.*, who used cubic, octahedral and cuboctahedral platinum particles in ethyl pyruvate enantioselective hydrogenation.²⁴⁵ The reaction was found to be shape selective, with increasing Pt{111}/Pt{100} terrace ratio leading to an increase in both rate and enantiomeric excess.

Lee *et al.* demonstrated structure sensitivity in the *cis-trans* isomerisation of 2-butene, where Pt{111} single crystals favoured *trans-* to *cis-* isomerisation.²⁴⁶ The opposite selectivity was observed over Pt{100} facets. They used colloidal techniques to prepare cubic and tetrahedral particles of platinum, which exposed only {100} and {111} facets respectively. The catalyst

composed of {111} surfaces not only favoured the isomerisation of *trans*- to *cis*- alkene but also gave higher alkene hydrogenation selectivity.²⁴⁷

The above investigations required the synthesis of metal particles of a specific shape. An alternative route for exploring the reactivities of different surface types is to use a selective-poison to block a particular group of heterogeneous sites on the catalyst surface. Adsorbates such as bismuth and sulphur adsorb preferentially upon specific sites, preventing or limiting any reactions which prefer those sites.^{248, 249} This approach of selectively ‘decorating’ particular surface sites with inert site blockers was used previously by Anderson *et al.*,²⁵⁰ who utilised bismuth and lead as selective poisons for palladium catalysts in the hydrogenation of 1- and 2-hexyne. Bismuth blocked surface defect sites, suppressing the double bond-shift of terminal to internal alkenes, which occurs rapidly at these sites. Lead preferentially adsorbed on terraces and caused a reduction in the degree of *cis-trans* isomerisation. Since then, more recent work has demonstrated the importance of surface modification in the surface chemistry of alkynes.²⁵¹⁻²⁵⁵

Previous work by Attard *et al.* has also investigated the effect of selective surface poisons on catalytic properties.^{51, 249} A study on 2-butyne-1,4-diol (butynediol) demonstrated that 2-butene-1,4-diol (butenediol) selectivity could be substantially improved, at the cost of reaction rate, by increasing surface coverage of bismuth on platinum.²⁵⁶ Since bismuth is known to preferentially adsorb at defect sites,²⁴⁸ these sites were associated with unselective alkyne to alkane transformations whereas Pt{111} sites facilitated selective hydrogenation of the alkyne to alkene, in agreement with conclusions drawn by Crespo-Quesada and co-workers.²⁴⁴ The rates of *cis*- to *trans*- isomerisation were not affected in these studies, indicating that these reactions took place over Pt terraces in agreement with Lee *et al.*²⁴⁶ In addition, organic fragments left over after cleaning of Pt nanoparticles grown in the bacterium were shown to increase the selectivity towards semi-hydrogenation products using 2-butyne-1,4-diol as substrate.²⁵⁶ The location of such fragments at defect sites was shown to be responsible for this type of behaviour. A striking feature of this work was the elimination of toxic heavy metals from the catalyst whilst maintaining selectivity.

1.3.2 Alkyl pyruvate hydrogenation

1.3.2.1 The Orito reaction

In 1979, Orito and co-workers first observed the enantioselective hydrogenation of a prochiral activated ketone to the corresponding alcohol catalysed by platinum with added chiral modifier.²⁵⁷ Specifically, they used the chiral alkaloid cinchonidine (CD) to modify a carbon supported platinum catalyst to convert methyl pyruvate (MP, dissolved in dichloromethane) to *R*-methyl lactate (ML) to a high *ee* (**Figure 1.13**). It was also shown that, when using cinchonine (CN, an epimer of CD) as the modifier, *S*-ML was obtained with similar enantioselectivity. The structures of CD and CN are shown in **Figure 1.14**. Both can be divided into three parts. The aromatic quinoline (Q) ring system is considered to be responsible for anchoring the alkaloid to the metallic surface. Meanwhile, the quinuclidine (QN) ring is a system containing a tertiary nitrogen which facilitates complexation with the reactant. The last section is the chiral centre determining the chirality of the product.

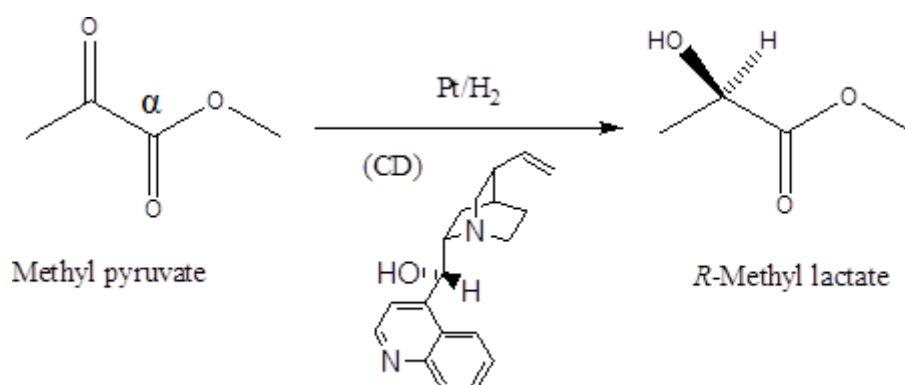


Figure 1.13 Orito's reaction scheme for the enantioselective hydrogenation of MP.

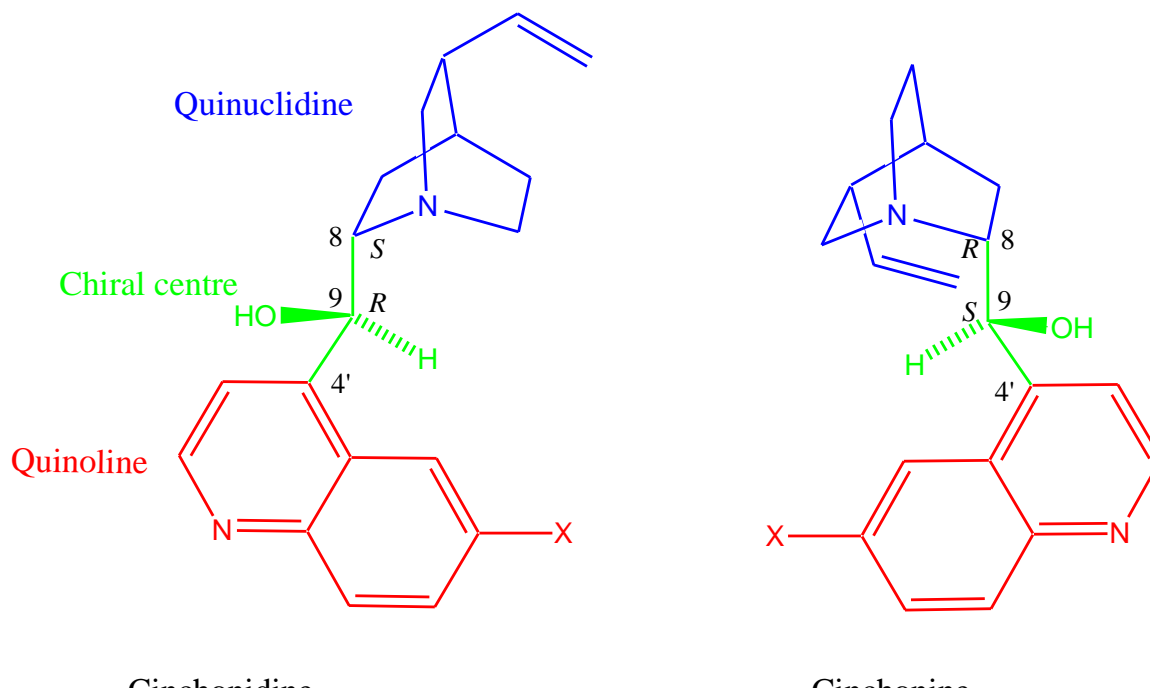


Figure 1.14 Structures of the cinchona alkaloids used in the Orito reaction. The functional group X is a hydrogen for CD and CN and a methoxy group for quinine and quinidine respectively.

In the Orito reaction, the carbonyl group to be hydrogenated is usually activated by an electron withdrawing group in the alpha position.²⁵⁷ As shown in **Figure 1.13**, the ester group is the electron withdrawing group in MP. Hence, the stability of the ketone towards hydrogenation is reduced. When MP reacts with hydrogen, a chiral alcohol will be formed. Ethyl pyruvate (EP) has a similar structure to MP except for the difference of one carbon in the length of the ester alkyl chain. Both MP and EP give a high reaction performance in terms of rate and final *ee*.²⁵⁸ Therefore, in order to understand the mechanism of the Orito reaction, it is essential to study how hydrogen, CD and MP/EP interact with the surface of the platinum catalyst. Although enantiopure methyl and ethyl lactate are rarely used commercially, the racemate is used in products such as electronics, adhesives, printing, paints, textile, and polar solvent in cleaners.²⁵⁹ However, as one of the first examples of a heterogeneously catalysed enantioselective reaction discovered, it provides a bench mark by which many other enantioselective reactions can be understood.

Until recently, information concerning the orientation of EP on Pt was scarce. Hence, much reliance was placed upon previous surface science studies of simpler carbonyl compounds such as acetone. Using Electron Energy Loss Spectroscopy (EELS), acetone adsorbed on

Pt{111} suggested two possible adsorption modes, both involving σ -bonding with the surface. One is an η^1 lone pair bond between the oxygen of the carbonyl group and the Pt surface, which is an end-on mode as shown in **Figure 1.15a**. The other, called η^2 -mode, involves both oxygen and carbon from the keto carbonyl bonding with the metal surface (**Figure 1.15b**).^{260, 261}

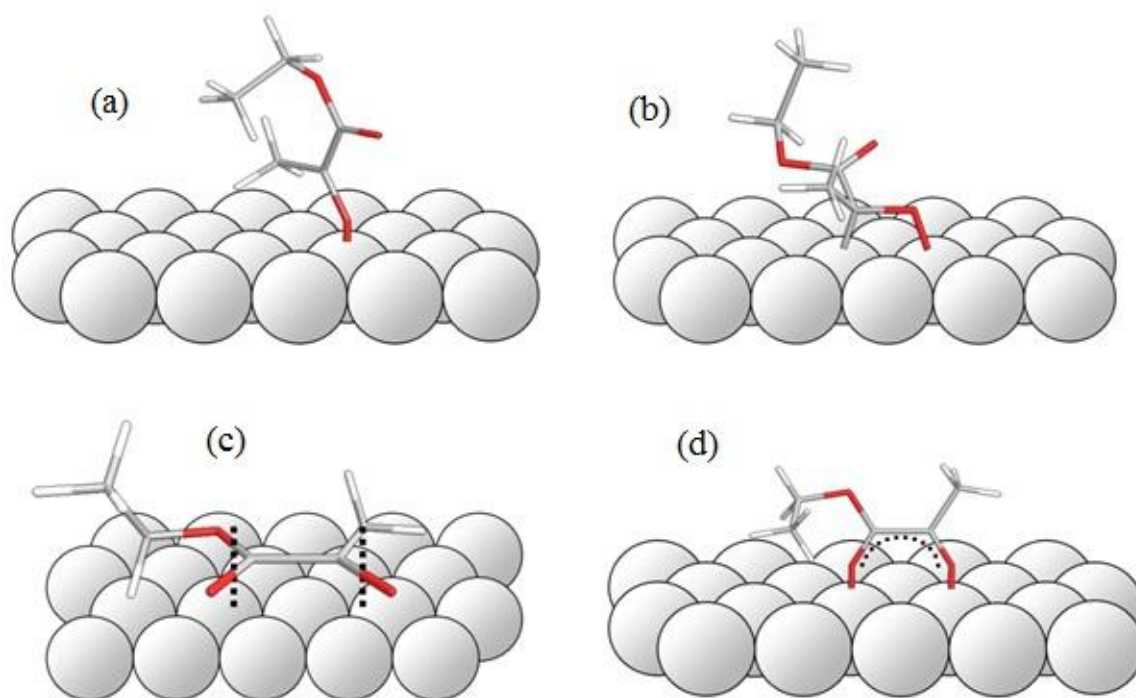


Figure 1.15 EP adsorption modes; (a) η^1 , (b) η^2 , (c) π -bonded, and (d) enediolate. Reprinted from reference 165.

Later, X-ray Absorption Near Edge Structure (XANES) was utilised to explore EP adsorption on Pt{111}.²⁶² It was discovered that only the η^1 -mode was formed on the surface with an oxygen lone pair bond. There was no evidence of η^2 -type configuration. However, as shown in **Figure 1.15c**, a new orientation of EP with the molecular plane lying parallel to the surface plane was suggested. This absorption mode indicates the π -orbitals of the two carbonyl groups interacting with the Pt surface. Although both of these modes may co-exist on the metal surface, an introduction of hydrogen gas could cause a tilt of the molecular plane of the η^1 -mode closer to the surface plane. Hence, the η^1 -mode was proposed to be a precursor of the flat configuration mode, which corresponded to previous studies concerning the mechanism of catalytic hydrogenation.²⁶³ Later, the same authors also explored the binding energy of core shell and valence shell electrons using X-ray Photoelectron Spectroscopy

(XPS) and Ultra-Violet Photoelectron Spectroscopy (UPS).²⁶⁴ A stabilisation of the highest occupied molecular orbital (HOMO) upon adsorption was observed. This lone-pair orbital is associated with both C=O groups on EP. Hence, the keto carbonyl was definitely involved in the chemisorption to the surface according to these workers but the possible involvement of ester carbonyl could not be ruled out. Angle-resolved measurements suggested an upright or tilted surface configuration for EP under UHV conditions at low temperature in accordance with results for similar molecules.²⁶²

However, a study of MP adsorption on Pt{111} using Density Functional Theory (DFT) suggested that the most energetically stable mode was the η^2 -, not the η^1 - mode.²⁶⁵ Since the π -bond of the carbonyl was believed to rehybridise upon adsorption in the η^2 -mode, it would now present a more σ -bond like feature which was supported by the observation of an extension in the C-O bond length in the η^2 -configuration compared to the η^1 -mode. This was suggested as a possibly reason for the increasing rate of the hydrogenation reaction on platinum because the carbonyl bond was strongly activated and that the real rate may actually depend on the ratio of the η^1 - and η^2 -modes at the surface. It should be noted that the rate acceleration over and above the intrinsic hydrogenation rate facilitated by CD/CN is due to quite a different effect (see later).²⁶⁶

Reflection-Absorption Infra-Red Spectroscopy (RAIRS) also confirmed the presence of the η^1 - and η^2 - configurations of MP adsorbed on a Pt surface as a function of temperature.²⁶⁷ Furthermore, another adsorption mode with both the keto and ester carbonyl oxygen lone pairs bonding to the surface were identified (**Figure 1.15d**). This so-called enediolate configuration possesses a delocalised π system across the O-C-C-O framework.²⁶⁷ Nevertheless, it only survives at very low temperatures (110 K).

In order to discover alternatives to platinum for the catalytic hydrogenation reaction, UHV studies of MP adsorption on copper{111}²⁶⁸ and nickel{111}²⁶⁹ have also been carried out. Although it was shown that a η^2 - configuration was dominant in the adsorption of EP on Cu{111}, copper does not dissociate hydrogen as readily as platinum. Hence, it is not a potential candidate as a hydrogenation catalyst. Meanwhile, nickel{111} was found to stabilise a cis-bidentate adsorption type of MP, which is similar to the enediolate configuration on Pt but with no delocalisation.²⁶⁹ Theoretical investigations based on a single nickel atom (not a plane) suggested the existence of an η^1 -mode of adsorption.²⁷⁰ However, since nickel is known to be inactive in the hydrogenation of α -ketoesters and may yield

different fragments due to decomposition, the relevance of EP studies on nickel in relation to the Orito reaction is doubtful.^{271, 272}

Although enantiopure EL is not a commercially valuable compounds, other analogous alcohols with optical feature may be quite useful organic synthons.²⁷³ *R*-pantolactone is one of the alcohols which is usually used in the synthesis of vitamin B₅ and co-enzyme.²⁷⁴ Its ketone precursor, ketopantolactone (KPL), has a cyclic ring structure. Therefore, the degree of enantioselectivity of the reaction is affected slightly, with 79% *ee* compared to >95% for EP under optimal conditions.²⁷⁵ However, since Pt/Al₂O₃ catalysts modified by CD caused an excess of *R*-pantolactone to form, the sense of enantioselectivity remains unchanged compared to EP and hence, a similar chiral induction mechanism was suggested.^{274, 275}

1.3.2.2 Proposed models for enantioselective induction by the chiral alkaloid

The interesting aspect of the Orito reaction is that not only are very higher *ee* values observed for the reaction, but also enantioselectivity is accompanied by rate enhancement of up to 40 times.²⁷⁴⁻²⁷⁶ This is really unusual since it would be expected that CD adsorption on Pt sites might actually decrease hydrogenation rate since Pt sites are blocked so the effective surface area is reduced. Moreover, it appears that rate enhancement and *ee* are coupled, the higher the rate enhancement, the greater is the *ee*.²⁷⁵ Hence, any explanation of the mechanism of the Orito reaction must explain not only the enantiodifferentiation observed, but also the rate enhancement. Three mechanisms for inducing enantioselectivity in the Orito reaction have been proposed, which are referred to as the 'shielding model', the 'template model' and the '1:1 interaction model'.²⁷⁷ Only the 1:1 model can rationalise rate enhancement (see later).²⁷⁸

The shielding model was proposed by Margitfalvi *et al.* and focused on interactions of the modifier with the reactant *in the solution phase* before adsorption.²⁷⁹ Based on this assumption, the modifier is changed to the 'closed' conformation after interacting with the reactant in solution. It is believed that the enantioselective step is obtained via the π - π orbitals overlapping between the delocalised π system of the quinoline ring and the conjugated double bond of the carbonyl on the pyruvate molecule together with the tertiary nitrogen of the quinuclidine ring. It was suggested that the formation of the complex in the liquid phase is the key step to induce enantio-diferentiation on the surface of the platinum catalyst since only one face of the impinging solution carbonyl complex is presented to the Pt surface due to 'shielding' by the surrounding CD molecule.²⁷⁹ Since it lacks a reasonable explanation for the

observed high enantioselectivities at very low modifier concentrations (mass transport limited diffusion of the complex to the surface is therefore active), the shielding model was discounted.

The second proposal was based on ordered arrays of the modifier adsorbed on the platinum surface forming templates resulting in 'exposed' chiral ensembles of platinum atoms.²⁸⁰ Wells *et al.* attempted to explain the enantiodifferentiation by building templates on the platinum surface with modifiers. For example, if CD was the choice of modifier, the α -ketoester reactant in the energetically favoured *s-trans* conformation would be favoured to adsorb *Si*-face down in the exposed chiral ensembles of platinum atoms and subsequently form an *R*-hydroxyester.²⁸⁰ However, they discarded their template model later, based on a series of surface science experiments that showed no evidence of ordered arrays of CD on Pt{111} surfaces.²⁸¹

The final model involves the assumption of a 1:1 interaction between EP and CD, which was first addressed by Blaser *et al.* who reported that alkylation of the tertiary nitrogen may lead to complete loss of enantioselectivity.²⁷⁸ It was proposed that the tertiary nitrogen could either undergo a nucleophilic attack on the carbon of the keto or an electrophilic attack on the keto oxygen when it is protonated.²⁸² In so doing, the hydrogen bonding would activate the carbonyl still further towards hydrogenation and it is well known that in homogeneous catalysis, such interactions do lead to rate enhancement.²⁶⁵ It was believed that the modifier was adsorbed on the platinum surface with the quinoline ring lying flat against it. Hence, an interaction between the aromatic π states and unoccupied metal valence states allowed for 'tethering' of CD to the surface and if the quinoline ring is subsequently hydrogenated, it should be expected that *ee* would be lost since the hydrogenated CD would tether much more weakly to the Pt surface and indeed this effect has been observed experimentally.²⁷⁸ At the same time, the nitrogen in the quinuclidine was supposed to point towards the surface and pick up a hydrogen atom from the Pt surface and transfer this to the activated carbonyl.²⁷⁸ However, the exact interaction between CD and EP on Pt is still controversial. This is exemplified by recent work by McBreen and co-workers who, although agreeing with the 1:1 model disagreed with Baiker in terms of which hydrogen bonding interactions were important.^{278,283} In McBreen's model, adsorption of CD on Pt activates the C-H bonds of the quinolone system towards hydrogen bonding. Hence, rather than just a N-H...O=C- interaction affording enantioselection, both keto and ester carbonyls interact with C-H bonds

via hydrogen bonding.²⁸³ Detailed STM studies of the molecules adsorbed on Pt confirmed that these interactions were occurring.

1.4 Project Aims

Using cyclic voltammetry and surface enhanced Raman spectroscopy which are highly surface sensitive analytical techniques, the hydrogenation reactions of various alkynes on platinum surfaces are firstly investigated with the following experimental plans:

- To apply SERS active Au@Pt core-shell NPs on a platinum working electrode housed in a spectro-electrochemical flowcell.
- To investigate the interaction of 2-butyne-1,4-diol, 2-pentyne, 4-octyne, methyl butynol and propargyl alcohol on the polycrystalline platinum surface and co-adsorbed with hydrogen.
- To investigate the adsorption behaviour of the alkynes mentioned above on well define platinum surfaces.
- To prepare SERS active platinum single crystals with Au@SiO₂ NPs.
- To investigate the interaction of the alkynes listed above on the surfaces of Pt{*hkl*} single crystal electrodes and co-adsorbed with hydrogen.

Then, using the same techniques, the Orito reaction is to be investigated with the following experiments:

- To investigate the interaction of ethyl pyruvate on the surfaces of Pt{*hkl*} single crystal electrodes and co-adsorbed with hydrogen.
- To investigate the interaction of the chiral modifier CD on platinum co-adsorbed with EP and hydrogen.
- To grow palladium with monolayer or multilayer coverages on well-defined platinum surfaces.
- To make the palladium surfaces SERS active with the distribution of Au@SiO₂ NPs.
- To investigate the interaction of ethyl pyruvate on the surfaces of Pd/Pt{*hkl*} single crystal electrodes and co-adsorbed with hydrogen.

The advantage of using cyclic voltammetry is that the hydrogen atmosphere can be turned on and off easily with the control of electrode potentials. Therefore, the hydrogenation reaction

can be monitored and compared with and without the presence of hydrogen. The aims of the investigations listed above are to explore the reaction mechanisms of the selective hydrogenation of alkynes to alkenes and the enantioselective hydrogenation of the activated ketone to the alcohol. By understanding the reaction mechanisms, catalysts can be optimised in order to acquire better selectivities.

Some of the work has been published in Faraday Discussion (listed before contents) and adapted into Chapter Four and Chapter Five.

1.5 References

1. J. M. Thomas and W. J. Thomas, *Principles and practice of heterogeneous catalysis*, VCH, 1997.
2. G. Kirchhoff, *Scheigger's Journal*, 1812, **4**, 108.
3. A. J. J. Straathof and P. Adlercreutz, *Applied Biocatalysis*, Taylor & Francis, 2000.
4. H. Davy, *Philosophical Transactions of the Royal Society*, 1817, **97**, 45.
5. M. D. F. R. S. Henry, *Philosophical Magazine*, 1825, **65**, 269.
6. I. Fecheté, Y. Wang and J. C. Védrine, *Catalysis Today*, 2012, **189**, 2-27.
7. P. Phillips, *Journal of the Franklin Institute*, 1831, **11**, 180.
8. G. Lemoine, *Ann. Chim. phys.*, 1877, **12**, 145.
9. D. Stoltzenberg, *Fritz Haber: Chemist, Nobel Laureate, German, Jew*, Chemical Heritage Press, 2004.
10. M. Appl, in *Ullmann's Encyclopedia of Industrial Chemistry*, Wiley-VCH Verlag GmbH & Co. KGaA, Editon edn., 2000.
11. F. Fischer and H. Tropsch, *Brennst.-Chem.*, 1923, **4**, 276.
12. J. G. Speight, *The Chemistry and Technology of Petroleum, Fourth Edition*, CRC Press, 2006.
13. V. N. Ipatieff and H. Pines, *Ind. and Engin.Chem.*, 1935, **27**, 1364.
14. J. A. Rabo, in *Zeolite Chemistry and Catalysis*, ed. J. A. Rabo, Am. Chem. Soc., Washington D.C., USA, Editon edn., 1976, pp. 332-349.
15. S. Bhatia, *Zeolite Catalysts: Principles and Applications*, Taylor & Francis, 1989.
16. J. M. Thomas and W. J. Thomas, *Introduction to the principles of heterogeneous catalysis*, Academic Press, 1967.
17. L. L. Hegedus and J. J. Gumbleton, *Chemtech.*, 1980, 630.
18. X. Wang, K. Maeda, A. Thomas, K. Takanebe, G. Xin, J. M. Carlsson, K. Domen and M. Antonietti, *Nat Mater*, 2009, **8**, 76-80.
19. E. E. Barton, D. M. Rampulla and A. B. Bocarsly, *Journal of the American Chemical Society*, 2008, **130**, 6342-6344.
20. R. A. W. Johnstone, A. H. Wilby and I. D. Entwistle, *Chemical Reviews*, 1985, **85**, 129-170.
21. E. K. Rideal, *Catalysis in theory and practice*, Macmillan and Company, Limited, 1919.
22. L. L. Latour, R. L. Kleinberg, P. P. Mitra and C. H. Sotak, *Journal of Magnetic Resonance, Series A*, 1995, **112**, 83-91.
23. A. I. Boronin, P. A. Zhdan and V. P. Khruschev, *Reaction Kinetics and Catalysis Letters*, 1982, **18**, 181-185.
24. A. F. Innocente and A. C. D. Ângelo, *Journal of Power Sources*, 2006, **162**, 151-159.
25. R. M. Watwe, R. D. Cortright, M. Mavrikakis, J. K. Nørskov and J. A. Dumesic, *The Journal of Chemical Physics*, 2001, **114**, 4663.
26. K. W. Kolasinski, *Surface Science: Foundations of Catalysis and Nanoscience*, Wiley, 2012.

27. A. W. Gauger and H. S. Taylor, *Journal of the American Chemical Society*, 1923, **45**, 920-928.
28. I. Langmuir, *Journal of the American Chemical Society*, 1918, **40**, 1361-1403.
29. S. Brunauer, P. H. Emmett and E. Teller, *Journal of the American Chemical Society*, 1938, **60**, 309-319.
30. K. K. Kolasinski, *Surface Science: Foundations of Catalysis and Nanoscience*, Wiley, 2012.
31. A. T. Kuhn, *Techniques in electrochemistry, corrosion, and metal finishing: a handbook*, Wiley, 1987.
32. G. Southampton Electrochemical, *Instrumental Methods in Electrochemistry*, John Wiley & Sons, Incorporated, 1987.
33. P. van der Heide, *X-ray Photoelectron Spectroscopy: An Introduction to Principles and Practices*, Wiley, 2011.
34. D. T. Bowron and S. Diaz Moreno, *Coordination Chemistry Reviews*, 2014, **277–278**, 2-14.
35. A. Bewick, K. Kunimatsu, B. S. Pons and J. W. Russell, *Journal of Electroanalytical Chemistry and Interfacial Electrochemistry*, 1984, **160**, 47-61.
36. B. Beden, A. Bewick and C. Lamy, *Journal of Electroanalytical Chemistry and Interfacial Electrochemistry*, 1983, **148**, 147-160.
37. N. Batina, B. E. Kahn, C.-H. Lin, J. W. McCargar, G. N. Salaita and A. T. Hubbard, *Electroanalysis*, 1989, **1**, 213-221.
38. P. Horsman, B. E. Conway and E. Yeager, *Comprehensive Treatise of Electrochemistry*, Springer, 1984.
39. G. Binnig, H. Rohrer, C. Gerber and E. Weibel, *Physical Review Letters*, 1982, **49**, 57-61.
40. J. Clavilier, R. Durand, G. Guinet and R. Faure, *Journal of Electroanalytical Chemistry and Interfacial Electrochemistry*, 1981, **127**, 281-287.
41. F. P. Bowden and E. K. Rideal, *Proceedings of the Royal Society of London. Series A*, 1928, **120**, 59-79.
42. E. Barsoukov and J. R. Macdonald, *Impedance Spectroscopy: Theory, Experiment, and Applications*, Wiley, 2005.
43. F. Opekar and P. Beran, *Journal of Electroanalytical Chemistry and Interfacial Electrochemistry*, 1976, **69**, 1-105.
44. Y. V. Pleskov and V. Y. Filinovskii, *The Rotating Disc Electrode*, Plenum Publishing, New York, 1976.
45. W. J. Albery and C. M. A. Brett, *Journal of Electroanalytical Chemistry and Interfacial Electrochemistry*, 1983, **148**, 201-210.
46. A. J. Bard and L. R. Faulkner, *Electrochemical Methods: Fundamentals and Applications*, Wiley, 2000.
47. C. J. Barnes, M. Lindroos and D. A. King, *Surface Science*, 1988, **201**, 108-128.
48. B. E. Nieuwenhuys, D. I. Hagen, G. Rovida and G. A. Somorjai, *Surface Science*, 1976, **59**, 155-176.
49. T. Iwasita, F. C. Nart and W. Vielstich, *Berichte der Bunsengesellschaft für physikalische Chemie*, 1990, **94**, 1030-1034.
50. S. K. Doorn and J. T. Hupp, *Journal of the American Chemical Society*, 1989, **111**, 1142-1144.
51. G. A. Attard, K. G. Griffin, D. J. Jenkins, P. Johnston and P. B. Wells, *Catalysis Today*, 2006, **114**, 346-352.
52. S. Marchiano and A. J. Arvia, in *Comprehensive Treatise of Electrochemistry*, eds. E. Yeager, J. O. M. Bockris and S. Sarangapani, Plenum Press, New York, Editon edn., 1983, vol. 6, p. 133.
53. M. Ahn and J. Kim, *The Journal of Physical Chemistry C*, 2013, **117**, 24438-24445.
54. M. F. Viegas, L. M. Abrantes and J. Lecoeur, *Journal of Materials Science: Materials in Medicine*, 1990, **1**, 105-109.
55. F. A. Settle, *Handbook of Instrumental Techniques for Analytical Chemistry*, Prentice Hall PTR, 1997.
56. J. E. B. Randles, *Transactions of the Faraday Society*, 1948, **44**, 327-338.

57. E. Gileadi, E. Kirowa-Eisner and J. Penciner, *Interfacial electrochemistry: an experimental approach*, Addison-Wesley Pub. Co., Advanced Book Program, 1975.
58. C. V. Raman, *Indian Journal of Physics*, 1928, **2**, 387-398.
59. J. H. Hibben, *The Raman Effect and Its Chemical Applications*, Reinhold Publishing Corporation, 1939.
60. F. H. Spedding and R. F. Stamm, *The Journal of Chemical Physics*, 1942, **10**, 176.
61. D. H. Rank and J. S. McCartney, *Journal of the Optical Society of America*, 1948, **38**, 279-279.
62. H. L. Welsh, M. F. Crawford, T. R. Thomas and G. R. Love, *Canadian Journal of Physics*, 1952, **30**, 577-596.
63. J. R. Ferraro, *Introductory Raman Spectroscopy*, Elsevier Science, 2003.
64. D. H. Rank and R. V. Wiegand, *Journal of the Optical Society of America*, 1946, **36**, 325-330.
65. D. B. Chase, *Journal of the American Chemical Society*, 1986, **108**, 7485-7488.
66. H. W. Schrötter and H. W. Klöckner, in *Raman Spectroscopy of Gases and Liquids*, ed. A. Weber, Springer Berlin Heidelberg, Editon edn., 1979, vol. 11, pp. 123-166.
67. M. Fleischmann, P. J. Hendra and A. J. McQuillan, *Chemical Physics Letters*, 1974, **26**, 163-166.
68. D. L. Jeanmaire and R. P. Van Duyne, *Journal of Electroanalytical Chemistry and Interfacial Electrochemistry*, 1977, **84**, 1-20.
69. M. G. Albrecht and J. A. Creighton, *Journal of the American Chemical Society*, 1977, **99**, 5215-5217.
70. P. A. Lund, D. E. Tevault and R. R. Smardzewski, *The Journal of Physical Chemistry*, 1984, **88**, 1731-1735.
71. W. Schulze, B. Breithaupt, K. P. Charlé and U. Kloss, *Berichte der Bunsengesellschaft für physikalische Chemie*, 1984, **88**, 308-310.
72. A. Kudelski and J. Bukowska, *Vibrational Spectroscopy*, 1996, **10**, 335-339.
73. M. Moskovits, *Reviews of Modern Physics*, 1985, **57**, 783-826.
74. A. Otto, in *Light Scattering in Solids IV*, eds. M. Cardona and G. Güntherodt, Springer Berlin Heidelberg, Editon edn., 1984, vol. 54, pp. 289-418.
75. M. Abdelsalam, P. N. Bartlett, A. E. Russell, J. J. Baumberg, E. J. Calvo, N. G. Tognalli and A. Fainstein, *Langmuir*, 2008, **24**, 7018-7023.
76. V. C. Bassetto, A. E. Russell, L. T. Kubota and P. N. Bartlett, *Electrochimica Acta*, 2014, **144**, 400-405.
77. E. A. Pozzi, M. D. Sonntag, N. Jiang, N. Chiang, T. Seideman, M. C. Hersam and R. P. Van Duyne, *The Journal of Physical Chemistry Letters*, 2014, **5**, 2657-2661.
78. S. R. Emory, W. E. Haskins and S. Nie, *Journal of the American Chemical Society*, 1998, **120**, 8009-8010.
79. M. Kahl and E. Voges, *Physical Review B*, 2000, **61**, 14078-14088.
80. V. M. Shalaev and A. K. Sarychev, *Physical Review B*, 1998, **57**, 13265-13288.
81. M. Moskovits, D. P. DiLella and K. J. Maynard, *Langmuir*, 1988, **4**, 67-76.
82. S. Franzen, J. C. W. Folmer, W. R. Glomm and R. O'Neal, *The Journal of Physical Chemistry A*, 2002, **106**, 6533-6540.
83. L. Cao, P. Diao, L. Tong, T. Zhu and Z. Liu, *ChemPhysChem*, 2005, **6**, 913-918.
84. J. F. Arenas, M. S. Woolley, J. C. Otero and J. I. Marcos, *The Journal of Physical Chemistry*, 1996, **100**, 3199-3206.
85. R. F. Aroca, R. A. Alvarez-Puebla, N. Pieczonka, S. Sanchez-Cortez and J. V. Garcia-Ramos, *Advances in Colloid and Interface Science*, 2005, **116**, 45-61.
86. M. J. Banholzer, J. E. Millstone, L. Qin and C. A. Mirkin, *Chemical Society Reviews*, 2008, **37**, 885-897.
87. G. Baker and D. Moore, *Analytical and Bioanalytical Chemistry*, 2005, **382**, 1751-1770.
88. T. Vo-Dinh, *TrAC Trends in Analytical Chemistry*, 1998, **17**, 557-582.
89. O. S.J., W. S.L., A. R.D. and H. N.J., *The Journal of Chemical Physics*, 1999, **111**, 4729-4735.

90. J. Hu, S. Chen, R. P. Johnson, X. Lin, Z. Yang and A. E. Russell, *The Journal of Physical Chemistry C*, 2013, **117**, 24843-24850.
91. F. M. Huang, D. Wilding, J. D. Speed, A. E. Russell, P. N. Bartlett and J. J. Baumberg, *Nano Letters*, 2011, **11**, 1221-1226.
92. S. Zou, M. J. Weaver, X. Q. Li, B. Ren and Z. Q. Tian, *The Journal of Physical Chemistry B*, 1999, **103**, 4218-4222.
93. P. Gao, D. Gosztola, L.-W. H. Leung and M. J. Weaver, *Journal of Electroanalytical Chemistry and Interfacial Electrochemistry*, 1987, **233**, 211-222.
94. M. Fleischmann, Z. Q. Tian and L. J. Li, *Journal of Electroanalytical Chemistry and Interfacial Electrochemistry*, 1987, **217**, 397-410.
95. M. Fleischmann and Z. Q. Tian, *Journal of Electroanalytical Chemistry and Interfacial Electrochemistry*, 1987, **217**, 385-395.
96. L.-W. H. Leung and M. J. Weaver, *Journal of Electroanalytical Chemistry and Interfacial Electrochemistry*, 1987, **217**, 367-384.
97. L. W. H. Leung and M. J. Weaver, *Journal of the American Chemical Society*, 1987, **109**, 5113-5119.
98. K. Kneipp, M. Moskovits and H. Kneipp, *Surface-Enhanced Raman Scattering: Physics and Applications*, Springer Berlin Heidelberg, 2006.
99. G. Mengoli, M. M. Musiani, M. Fleischman, B. Mao and Z. Q. Tian, *Electrochimica Acta*, 1987, **32**, 1239-1245.
100. J. T. Krug, G. D. Wang, S. R. Emory and S. Nie, *Journal of the American Chemical Society*, 1999, **121**, 9208-9214.
101. M. P. Cline, R. K. Chang and P. W. Barber, *Journal of the Optical Society of America B*, 1986, **3**, 15-21.
102. L. Guo, Q. Huang, X.-y. Li and S. Yang, *Physical Chemistry Chemical Physics*, 2001, **3**, 1661-1665.
103. Y. Xiong, J. M. McLellan, J. Chen, Y. Yin, Z.-Y. Li and Y. Xia, *Journal of the American Chemical Society*, 2005, **127**, 17118-17127.
104. Y. Xia, P. Yang, Y. Sun, Y. Wu, B. Mayers, B. Gates, Y. Yin, F. Kim and H. Yan, *Advanced Materials*, 2003, **15**, 353-389.
105. J.-L. Yao, J. Tang, D.-Y. Wu, D.-M. Sun, K.-H. Xue, B. Ren, B.-W. Mao and Z.-Q. Tian, *Surface Science*, 2002, **514**, 108-116.
106. Z.-Q. Tian, B. Ren, J.-F. Li and Z.-L. Yang, *Chemical Communications*, 2007, **0**, 3514-3534.
107. J.-F. Li, Z.-L. Yang, B. Ren, G.-K. Liu, P.-P. Fang, Y.-X. Jiang, D.-Y. Wu and Z.-Q. Tian, *Langmuir*, 2006, **22**, 10372-10379.
108. J. A. Creighton, C. G. Blatchford and M. G. Albrecht, *Journal of the Chemical Society, Faraday Transactions 2: Molecular and Chemical Physics*, 1979, **75**, 790-798.
109. K. Faulds, R. E. Littleford, D. Graham, G. Dent and W. E. Smith, *Analytical Chemistry*, 2003, **76**, 592-598.
110. Y. Wang, D. Li, P. Li, W. Wang, W. Ren, S. Dong and E. Wang, *The Journal of Physical Chemistry C*, 2007, **111**, 16833-16839.
111. P. C. Lee and D. Meisel, *The Journal of Physical Chemistry*, 1982, **86**, 3391-3395.
112. G. C. Weaver and K. Norrod, *Journal of Chemical Education*, 1998, **75**, 621.
113. U. Nickel, K. Mansyreff and S. Schneider, *Journal of Raman Spectroscopy*, 2004, **35**, 101-110.
114. M. V. Cañamares, J. V. Garcia-Ramos, J. D. Gómez-Varga, C. Domingo and S. Sanchez-Cortes, *Langmuir*, 2005, **21**, 8546-8553.
115. N. Leopold and B. Lendl, *The Journal of Physical Chemistry B*, 2003, **107**, 5723-5727.
116. U. Nickel, A. zu Castell, K. Pöppel and S. Schneider, *Langmuir*, 2000, **16**, 9087-9091.
117. X. Li, J. Zhang, W. Xu, H. Jia, X. Wang, B. Yang, B. Zhao, B. Li and Y. Ozaki, *Langmuir*, 2003, **19**, 4285-4290.
118. G. Frens, *Nature Physical Science*, 1973, **241**, 20.

119. P. N. Njoki, I. I. S. Lim, D. Mott, H.-Y. Park, B. Khan, S. Mishra, R. Sujakumar, J. Luo and C.-J. Zhong, *The Journal of Physical Chemistry C*, 2007, **111**, 14664-14669.
120. A. M. Schwartzberg, T. Y. Oshiro, J. Z. Zhang, T. Huser and C. E. Talley, *Analytical Chemistry*, 2006, **78**, 4732-4736.
121. C. Shen, C. Hui, T. Yang, C. Xiao, J. Tian, L. Bao, S. Chen, H. Ding and H. Gao, *Chemistry of Materials*, 2008, **20**, 6939-6944.
122. M. Procházka, P. Mojzeš, J. Štěpánek, B. Vlčková and P.-Y. Turpin, *Analytical Chemistry*, 1997, **69**, 5103-5108.
123. J. Nedderson, G. Chumanov and T. M. Cotton, *Applied Spectroscopy*, 1993, **47**, 1959-1964.
124. R. Sato-Berrú, R. Redón, A. Vázquez-Olmos and J. M. Saniger, *Journal of Raman Spectroscopy*, 2009, **40**, 376-380.
125. A. Torreggiani, Z. Jurasekova, M. D'Angelantonio, M. Tamba, J. V. Garcia-Ramos and S. Sanchez-Cortes, *Colloids and Surfaces A: Physicochemical and Engineering Aspects*, 2009, **339**, 60-67.
126. L.-P. Ding and Y. Fang, *Applied Surface Science*, 2007, **253**, 4450-4455.
127. S. Tan, M. Erol, A. Attygalle, H. Du and S. Sukhishvili, *Langmuir*, 2007, **23**, 9836-9843.
128. A. M. Ahern and R. L. Garrell, *Analytical Chemistry*, 1987, **59**, 2813-2816.
129. C. S. Seney, B. M. Gutzman and R. H. Goddard, *The Journal of Physical Chemistry C*, 2008, **113**, 74-80.
130. J. D. S. dos Santos, R. A. Alvarez-Puebla, J. O. N. Oliveira and R. F. Aroca, *Journal of Materials Chemistry*, 2005, **15**, 3045-3049.
131. J.-A. Wang, T. Zhu, X. Zhang and Z.-F. Liu, *Acta Phys. -Chim. Sin.*, 1999, **15**, 476-480.
132. G. Glaspell, C. Zuo and P. Jagodzinski, *Journal of Cluster Science*, 2005, **16**, 39-51.
133. S. Praharaj, S. Jana, S. Kundu, S. Pande and T. Pal, *Journal of Colloid and Interface Science*, 2009, **333**, 699-706.
134. S. Jang, J. Park, S. Shin, C. Yoon, B. K. Choi, M.-s. Gong and S.-W. Joo, *Langmuir*, 2004, **20**, 1922-1927.
135. O. Siiman, L. A. Bumm, R. Callaghan, C. G. Blatchford and M. Kerker, *The Journal of Physical Chemistry*, 1983, **87**, 1014-1023.
136. S. M. Heard, F. Grieser and C. G. Barraclough, *Chemical Physics Letters*, 1983, **95**, 154-158.
137. P. C. Lee and D. Meisel, *Chemical Physics Letters*, 1983, **99**, 262-265.
138. X. Su, J. Zhang, L. Sun, T.-W. Koo, S. Chan, N. Sundararajan, M. Yamakawa and A. A. Berlin, *Nano Letters*, 2004, **5**, 49-54.
139. S. P. Mulvaney, M. D. Musick, C. D. Keating and M. J. Natan, *Langmuir*, 2003, **19**, 4784-4790.
140. S. Mahajan, R. M. Cole, B. F. Soares, S. H. Pelfrey, A. E. Russell, J. J. Baumberg and P. N. Bartlett, *The Journal of Physical Chemistry C*, 2009, **113**, 9284-9289.
141. M. E. Abdelsalam, S. Mahajan, P. N. Bartlett, J. J. Baumberg and A. E. Russell, *Journal of the American Chemical Society*, 2007, **129**, 7399-7406.
142. J. F. Li, Y. F. Huang, Y. Ding, Z. L. Yang, S. B. Li, X. S. Zhou, F. R. Fan, W. Zhang, Z. Y. Zhou, Y. Wu de, B. Ren, Z. L. Wang and Z. Q. Tian, *Nature*, 2010, **464**, 392-395.
143. J. D. Speed, R. P. Johnson, J. T. Hugall, N. N. Lal, P. N. Bartlett, J. J. Baumberg and A. E. Russell, *Chemical Communications*, 2011, **47**, 6335-6337.
144. R. P. Johnson, S. Mahajan, M. E. Abdelsalam, R. M. Cole, J. J. Baumberg, A. E. Russell and P. N. Bartlett, *Physical Chemistry Chemical Physics*, 2011, **13**, 16661-16665.
145. L. Sun, Y. Song, L. Wang, C. Guo, Y. Sun, Z. Liu and Z. Li, *The Journal of Physical Chemistry C*, 2008, **112**, 1415-1422.
146. K. Kneipp and H. Kneipp, *Israel Journal of Chemistry*, 2006, **46**, 299-305.
147. S. E. J. Bell and N. M. S. Sirimuthu, *Journal of the American Chemical Society*, 2006, **128**, 15580-15581.
148. J. Fang, Y. Huang, X. Li and X. Dou, *Journal of Raman Spectroscopy*, 2004, **35**, 914-920.

149. R. G. Freeman, M. B. Hommer, K. C. Grabar, M. A. Jackson and M. J. Natan, *The Journal of Physical Chemistry*, 1996, **100**, 718-724.
150. L. Rivas, S. Sanchez-Cortes, J. V. García-Ramos and G. Morcillo, *Langmuir*, 2000, **16**, 9722-9728.
151. N. R. Jana, *Analyst*, 2003, **128**, 954-956.
152. K. Kim, K. L. Kim and S. J. Lee, *Chemical Physics Letters*, 2005, **403**, 77-82.
153. Y. Cui and R.-A. Gu, *Chem. J. Chin. U.*, 2005, **26**, 2090-2092.
154. S. Pande, S. K. Ghosh, S. Praharaj, S. Panigrahi, S. Basu, S. Jana, A. Pal, T. Tsukuda and T. Pal, *The Journal of Physical Chemistry C*, 2007, **111**, 10806-10813.
155. J. Venables, *Introduction to Surface and Thin Film Processes*, Cambridge University Press, 2000.
156. A. Pimpinelli and J. Villain, *Physics of Crystal Growth*, Cambridge University Press, 1998.
157. R. Kunkel, B. Poelsema, L. K. Verheij and G. Comsa, *Physical Review Letters*, 1990, **65**, 733-736.
158. R. Stumpf and M. Scheffler, *Physical Review Letters*, 1994, **72**, 254-257.
159. L. M. Dougherty and A. Dollfus, *Journal of British Astronomical Association*, 1989, **99**, 183-186.
160. J. B. Biot, *Bull. Soc. Philomath. Paris*, 1815, 190.
161. L. Pasteur, *C. R. Acad. Sci.*, 1848, **26**, 535.
162. J. H. van't Hoff, *Arch. Neerl. Sci. Exacts. Nat.*, 1874, **9**, 445.
163. E. L. Eliel and S. H. Wilen, *Stereochemistry of Organic Compounds*, Wiley India Pvt. Limited, 2008.
164. J. March, *Advanced Organic Chemistry: Reactions, Mechanisms, and Structure*, Wiley, 1992.
165. R. J. Taylor, Cardiff University, 2010.
166. A. M. Stalcup, K. H. Ekborg, M. P. Gasper and D. W. Armstrong, *Journal of Agricultural and Food Chemistry*, 1993, **41**, 1684-1689.
167. J. J. Partidge and B. L. Bray, in *Process Chemistry in the Pharmaceutical Industry*, ed. K. G. Gadamasetti, CRC Press, New York, Editon edn., 1999.
168. R. G. Berger, *Flavours and Fragrances: Chemistry, Bioprocessing and Sustainability*, Springer, 2007.
169. P. Wang, S. Jiang, D. Liu, H. Zhang and Z. Zhou, *Journal of Agricultural and Food Chemistry*, 2006, **54**, 1577-1583.
170. T. E. Beesley and R. P. W. Scott, *Chiral Chromatography*, Wiley, 1998.
171. S. Young, *Fractional Distillation*, HardPress, 2012.
172. G. Quinkert, E. Egert and C. Griesinger, *Aspects of Organic Chemistry: Structure*, Verlag Helvetica Chimica Acta, 1996.
173. H.-U. Blaser, *Chemical Communications*, 2003, 293-296.
174. W. S. Knowles, *Angewandte Chemie International Edition*, 2002, **41**, 1998-2007.
175. E. Santos and W. Schmickler, *Catalysis in Electrochemistry: From Fundamental Aspects to Strategies for Fuel Cell Development*, Wiley, 2011.
176. A. Al-Akl, G. Attard, R. Price and B. Timothy, *Physical Chemistry Chemical Physics*, 2001, **3**, 3261-3268.
177. M. J. Ball, C. A. Lucas, N. M. Marković, V. Stamenković and P. N. Ross, *Surface Science*, 2003, **540**, 295-302.
178. S. D. Lin, T.-C. Hsiao, J.-R. Chang and A. S. Lin, *The Journal of Physical Chemistry B*, 1998, **103**, 97-103.
179. K. A. Mauritz and R. B. Moore, *Chemical Reviews*, 2004, **104**, 4535-4586.
180. E. Reisner, J. C. Fontecilla-Camps and F. A. Armstrong, *Chemical Communications*, 2009, 550-552.
181. A. P. Alivisatos, *Science*, 1996, **271**, 933-937.
182. J. Chen, B. Lim, E. P. Lee and Y. Xia, *Nano Today*, 2009, **4**, 81-95.

183. F. Maillard, M. Eikerling, O. V. Cherstiouk, S. Schreier, E. Savinova and U. Stimming, *Faraday Discussions*, 2004, **125**, 357-377.
184. J. Wu, X. Z. Yuan, J. J. Martin, H. Wang, J. Zhang, J. Shen, S. Wu and W. Merida, *Journal of Power Sources*, 2008, **184**, 104-119.
185. T. Kessler, A. Visintin, A. E. Bolzan, G. Andreasen, R. C. Salvarezza, W. E. Triaca and A. J. Arvia, *Langmuir*, 1996, **12**, 6587-6596.
186. L. Vazquez, J. Gomez, A. M. Baro, N. Garcia, M. L. Marcos, J. Gonzalez Velasco, J. M. Vara, A. J. Arvia and J. Presa, *Journal of the American Chemical Society*, 1987, **109**, 1730-1733.
187. A. J. Arvia, R. C. Salvarezza and W. E. Triaca, *Electrochimica Acta*, 1989, **34**, 1057-1071.
188. J. L. Peng, X. D. Fan and L. A. Bursill, *International Journal of Modern Physics B*, 1996, **10**, 3875-3892.
189. J. L. Figueiredo, M. F. R. Pereira, M. M. A. Freitas and J. J. M. Órfão, *Carbon*, 1999, **37**, 1379-1389.
190. E. Bouleghimat, P. R. Davies, R. J. Davies, R. Howarth, J. Kulhavy and D. J. Morgan, *Carbon*, 2013, **61**, 124-133.
191. Z. Klusek, *Applied Surface Science*, 1998, **125**, 339-350.
192. J. McBreen, H. Olender, S. Srinivasan and K. V. Kordesch, *Journal of Applied Electrochemistry*, 1981, **11**, 787-796.
193. K. E. Swider and D. R. Rolison, *Journal of The Electrochemical Society*, 1996, **143**, 813-819.
194. N. L. Pocard, D. C. Alsmeyer, R. L. McCreery, T. X. Neenan and M. R. Callstrom, *Journal of Materials Chemistry*, 1992, **2**, 771-784.
195. J. Larminie and A. Dicks, *Fuel Cell Systems Explained*, J. Wiley, 2003.
196. M. Shao, *Electrocatalysis in Fuel Cells: A Non- and Low- Platinum Approach*, Springer, 2013.
197. Z. Liu, X. Lin, J. Y. Lee, W. Zhang, M. Han and L. M. Gan, *Langmuir*, 2002, **18**, 4054-4060.
198. K. P. De Jong and J. W. Geus, *Catalysis Reviews*, 2000, **42**, 481-510.
199. J. D. Clark, *Ignition!: An informal history of liquid rocket propellants*, Rutgers University Press, 1972.
200. M. Cooper and G. G. Botte, *Journal of The Electrochemical Society*, 2006, **153**, A1894-A1901.
201. T. Frelink, W. Visscher and J. A. R. van Veen, *Electrochimica Acta*, 1994, **39**, 1871-1875.
202. X. H. Xia and T. Iwasita, *Journal of The Electrochemical Society*, 1993, **140**, 2559-2565.
203. Y. Du, B. Su, N. Zhang and C. Wang, *Applied Surface Science*, 2008, **255**, 2641-2645.
204. S. Mukerjee, *Journal of Applied Electrochemistry*, 1990, **20**, 537-548.
205. J. W. Long, R. M. Stroud, K. E. Swider-Lyons and D. R. Rolison, *The Journal of Physical Chemistry B*, 2000, **104**, 9772-9776.
206. A. Hamnett, B. J. Kennedy and F. E. Wagner, *Journal of Catalysis*, 1990, **124**, 30-40.
207. N. M. Marković and P. N. Ross Jr, *Surface Science Reports*, 2002, **45**, 117-229.
208. R. S. Nicholson and I. Shain, *Analytical Chemistry*, 1964, **36**, 706-723.
209. S. Srinivasan and E. Gileadi, *Electrochimica Acta*, 1966, **11**, 321-335.
210. E. Laviron, *Journal of Electroanalytical Chemistry and Interfacial Electrochemistry*, 1980, **112**, 1-9.
211. M. Ahlers, W. Müller, A. Reichert, H. Ringsdorf and J. Venzmer, *Angewandte Chemie International Edition in English*, 1990, **29**, 1269-1285.
212. T. Matsue, M. Fujihira and T. Osa, *Journal of The Electrochemical Society*, 1979, **126**, 500-501.
213. F. Murray, in *Electroanalytical Chemistry*, ed. Dekker, New York, Editon edn., 1999, vol. Vol. 13.
214. M.-C. Daniel and D. Astruc, *Chemical Reviews*, 2003, **104**, 293-346.
215. K. L. Kelly, E. Coronado, L. L. Zhao and G. C. Schatz, *The Journal of Physical Chemistry B*, 2002, **107**, 668-677.
216. M. Bruchez, M. Moronne, P. Gin, S. Weiss and A. P. Alivisatos, *Science*, 1998, **281**, 2013-2016.
217. M. M. Alvarez, J. T. Houry, T. G. Schaaff, M. N. Shafiqullin, I. Vezmar and R. L. Whetten, *The Journal of Physical Chemistry B*, 1997, **101**, 3706-3712.

218. J. F. Hicks, D. T. Miles and R. W. Murray, *Journal of the American Chemical Society*, 2002, **124**, 13322-13328.
219. J. F. Hicks, F. P. Zamborini, A. J. Osisek and R. W. Murray, *Journal of the American Chemical Society*, 2001, **123**, 7048-7053.
220. S. Chen and R. W. Murray, *The Journal of Physical Chemistry B*, 1999, **103**, 9996-10000.
221. T. Trindade, P. O'Brien and N. L. Pickett, *Chemistry of Materials*, 2001, **13**, 3843-3858.
222. P. Schwerdtfeger, *Angewandte Chemie International Edition*, 2003, **42**, 1892-1895.
223. R. Gangopadhyay and A. De, *Chemistry of Materials*, 2000, **12**, 608-622.
224. *Nobel Lectures in Chemistry 1901-1921*, Elsevier Publishing Company, Amsterdam, 1966.
225. *UK Pat.*, 1903.
226. M. Hudlický, *Reductions in organic chemistry*, E. Horwood, 1984.
227. P. P. Company and E. M. Rosen, *The Petersen Automotive Troubleshooting & Repair Manual*, Grosset & Dunlap, 1975.
228. G. Stefanidakis and J. E. Gwyn, in *Chemical Processing Handbook*, ed. J. J. McKetta, CRC Press, Editon edn., 1993, pp. 80-138.
229. J. H. Gary and G. E. Handwerk, *Petroleum Refining: Technology and Econmoics*, 4th edn., CRC Press, 2001.
230. M. P. v. Wilde, *Berichte der deutschen chemischen Gesellschaft*, 1874, **7**, 352-357.
231. P. Sabatier and J. B. Senderens, *C. R. Acad. Sci., Paris Ser. C.*, 1899, **128**, 1173.
232. C. Paal and W. Hartmann, *Berichte der deutschen chemischen Gesellschaft*, 1909, **42**, 3930-3939.
233. C. Paal and H. Schiedewitz, *Berichte der deutschen chemischen Gesellschaft (A and B Series)*, 1930, **63**, 766-778.
234. R. J. Tedeschi and G. Clark, *The Journal of Organic Chemistry*, 1962, **27**, 4323-4326.
235. B. Chen, U. Dingerdissen, J. G. E. Krauter, H. G. J. Lansink Rotgerink, K. Möbus, D. J. Ostgard, P. Panster, T. H. Riermeier, S. Seebald, T. Tacke and H. Trauthwein, *Applied Catalysis A: General*, 2005, **280**, 17-46.
236. H. Lindlar and R. Dubuis, *Organic Synthesis*, 1966, **46**, 89.
237. J. G. Ulan, E. Kuo, W. F. Maier, R. S. Rai and G. Thomas, *The Journal of Organic Chemistry*, 1987, **52**, 3126-3132.
238. A. Jung, A. Jess, T. Schubert and W. Schütz, *Applied Catalysis A: General*, 2009, **362**, 95-105.
239. C. A. Brown and V. K. Ahuja, *Journal of the Chemical Society, Chemical Communications*, 1973, 553-554.
240. S. Nishimura, *Handbook of Heterogeneous Catalytic Hydrogenation for Organic Synthesis*, J. Wiley, 2001.
241. R. L. Augustine, *Heterogeneous Catalysis for the Synthetic Chemist*, Taylor & Francis, 1995.
242. P. Baumeister, M. Studer and F. Roessler, in *Handbook of Heterogeneous Catalysis*, eds. G. Ertl, H. Knözinger and J. Weitkamp, VCH, Editon edn., 1997, p. 2186.
243. L. Gucci and A. Sarkany, in *Catalysis: Volume 11*, eds. J. J. Spivey and S. K. Agarwal, The Royal Society of Chemistry, Editon edn., 1994, vol. 11, pp. 318-378.
244. M. Crespo-Quesada, A. Yarulin, M. Jin, Y. Xia and L. Kiwi-Minsker, *Journal of the American Chemical Society*, 2011, **133**, 12787-12794.
245. E. Schmidt, A. Vargas, T. Mallat and A. Baiker, *Journal of the American Chemical Society*, 2009, **131**, 12358-12367.
246. I. Lee, F. Delbecq, R. Morales, M. Albiter and F. Zaera, *Nature Materials*, 2009, **8**, 7.
247. I. Lee and F. Zaera, *Journal of Catalysis*, 2010, **269**, 359-366.
248. E. Herrero, V. c. Climent and J. M. Feliu, *Electrochemistry Communications*, 2000, **2**, 636-640.
249. D. J. Jenkins, A. M. S. Alabdulrahman, G. A. Attard, K. G. Griffin, P. Johnston and P. B. Wells, *Journal of Catalysis*, 2005, **234**, 230-239.
250. J. A. Anderson, J. Mellor and R. P. K. Wells, *Journal of Catalysis*, 2009, **261**, 208-216.
251. E. Gross and M. Asscher, *Langmuir*, 2010, **26**, 16226-16231.

252. M. Crespo-Quesada, F. Cárdenas-Lizana, A.-L. Dessimoz and L. Kiwi-Minsker, *ACS Catalysis*, 2012, **2**, 1773-1786.
253. S. G. Kwon, G. Krylova, A. Sumer, M. M. Schwartz, E. E. Bunel, C. L. Marshall, S. Chattopadhyay, B. Lee, J. Jellinek and E. V. Shevchenko, *Nano Letters*, 2012, **12**, 5382-5388.
254. M. Crespo-Quesada, R. R. Dykeman, G. Laurency, P. J. Dyson and L. Kiwi-Minsker, *Journal of Catalysis*, 2011, **279**, 66-74.
255. T. Mitsudome, Y. Takahashi, S. Ichikawa, T. Mizugaki, K. Jitsukawa and K. Kaneda, *Angewandte Chemie International Edition*, 2013, **52**, 1481-1485.
256. J. A. Bennett, G. A. Attard, K. Deplanche, M. Casadesus, S. E. Huxter, L. E. Macaskie and J. Wood, *ACS Catalysis*, 2012, **2**, 504-511.
257. Y. Orito, S. Imai and S. Niwa, *NIPPON KAGAKU KAISHI*, 1979, **1979**, 1118-1120.
258. X. Li, R. P. K. Wells, P. B. Wells and G. J. Hutchings, *Journal of Catalysis*, 2004, **221**, 653-656.
259. E. W. Flick, *Industrial Solvents Handbook*, Noyes Data Corporation, 1998.
260. N. R. Avery, W. H. Weinberg, A. B. Anton and B. H. Toby, *Physical Review Letters*, 1983, **51**, 682-685.
261. N. R. Avery, *Surface Science*, 1983, **125**, 771-786.
262. T. Bürgi, F. Atamny, A. Knop-Gericke, M. Hävecker, T. Schedel-Niedrig, R. Schlögl and A. Baiker, *Catalysis Letters*, 2000, **66**, 109-112.
263. O. Schwalm, B. Minder, J. Weber and A. Baiker, *Catalysis Letters*, 1994, **23**, 271-279.
264. T. Bürgi, F. Atamny, R. Schlögl and A. Baiker, *The Journal of Physical Chemistry B*, 2000, **104**, 5953-5960.
265. A. Vargas, T. Bürgi and A. Baiker, *Journal of Catalysis*, 2004, **222**, 439-449.
266. Z. Ma, I. Lee and F. Zaera, *Journal of the American Chemical Society*, 2007, **129**, 16083-16090.
267. S. Lavoie, M. A. Laliberté and P. H. McBreen, *Journal of the American Chemical Society*, 2003, **125**, 15756-15757.
268. C. Fleming, J. Johnston and M. Kadodwala, *Surface Science*, 2007, **601**, 5485-5491.
269. M. Castonguay, J. R. Roy, A. Rochefort and P. H. McBreen, *Journal of the American Chemical Society*, 2000, **122**, 518-524.
270. A. Rochefort and P. McBreen, *The Journal of Physical Chemistry A*, 2001, **105**, 1320-1325.
271. H. U. Blaser, H. P. Jalett, D. M. Monti, J. F. Reber and J. T. Wehrli, in *Studies in Surface Science and Catalysis*, ed. J. B. C. B. D. D. C. M. a. G. P. M. Guisnet, Elsevier, Editon edn., 1988, vol. Volume 41, pp. 153-163.
272. P. Wells and A. Wilkinson, *Topics in Catalysis*, 1998, **5**, 39-50.
273. S. Hanessian, *Total synthesis of natural products, the "Chiron" approach*, Pergamon Press, 1983.
274. E. Orglmeister, T. Mallat and A. Baiker, *Advanced Synthesis & Catalysis*, 2005, **347**, 78-86.
275. M. Schürch, O. Schwalm, T. Mallat, J. Weber and A. Baiker, *Journal of Catalysis*, 1997, **169**, 275-286.
276. D. Y. Murzin, *Journal of Molecular Catalysis A: Chemical*, 2008, **289**, 91-94.
277. A. Gellman, W. Tysoe and F. Zaera, *Catalysis Letters*, 2015, **145**, 220-232.
278. H. U. Blaser, H. P. Jalett, D. M. Monti, A. Baiker and J. T. Wehrli, in *Studies in Surface Science and Catalysis*, ed. R. K. G. a. A. W. Sleight, Elsevier, Editon edn., 1991, vol. Volume 67, pp. 147-155.
279. J. L. Margitfalvi, M. Hegedüs and E. Tfirst, *Tetrahedron: Asymmetry*, 1996, **7**, 571-580.
280. I. M. Sutherland, A. Ibbotson, R. B. Moyes and P. B. Wells, *Journal of Catalysis*, 1990, **125**, 77-88.
281. A. F. Carley, M. K. Rajumon, M. W. Roberts and P. B. Wells, *Journal of the Chemical Society, Faraday Transactions*, 1995, **91**, 2167-2172.
282. O. Schwalm, J. Weber, J. Margitfalvi and A. Baiker, *Journal of Molecular Structure*, 1993, **297**, 285-293.
283. S. Lavoie and P. H. McBreen, *The Journal of Physical Chemistry B*, 2005, **109**, 11986-11990.

CHAPTER TWO

Theoretical Background

2.1 Surface Structure

2.1.1 Geometrical Structure

2.1.1.1 The structure of bulk metal surfaces

Since the surface of a metal catalyst is crucial to any heterogeneous catalytic reaction, and different surface structures lead to different catalytic properties, it is essential to understand the physical and structural aspects of the metal surface.¹ When a metal solidifies from the molten state, a crystal is formed as the atoms arrange themselves into a three dimensional repeating pattern, known as the unit cell. The crystal consists of many small crystalline domains which are randomly distributed throughout the surface of the metal. The surface arrangement of atoms of this so called ‘polycrystalline’ metal must reflect the underlying bulk structure. Hence macroscopic measurements on polycrystalline surfaces cannot take into account events occurring at individual sites such as grain boundaries, steps² and vacancies³. This means that any measurement performed on such a surface should be considered as an average of all of these sites and the microscopic details have to be often ignored.⁴ The concern of this thesis is with events on both polycrystalline surfaces and well defined surfaces, which are derived from cutting single crystals. Therefore, the understanding of the macroscopic events and the particular structural relations between adsorption and surface sites has been examined.

The use of well-defined electrodes has yielded results on surface properties and composition determining the catalytic activity and the *chemisorption* and *physisorption* of species. Chemisorption is a kind of adsorption that involves a chemical reaction between the surface and the adsorbate, while physisorption leaves the chemical species of the adsorbate and surface intact. As shown in **Figure 2.1**, there is an activation energy barrier between these two types of adsorptions. Hence, variation of the adsorption site needs to be under the control of the experimentalist. Therefore, single crystal facets are employed since they exhibit the simplest adsorption behaviour of all surfaces because the variation in adsorption site is limited by the

geometry of the unit cell building the crystal. Greater complexity can be introduced to the surface structure by cutting a crystal surface at a particular angle to a given crystal plane, creating step and kinks sites on the surface.⁵

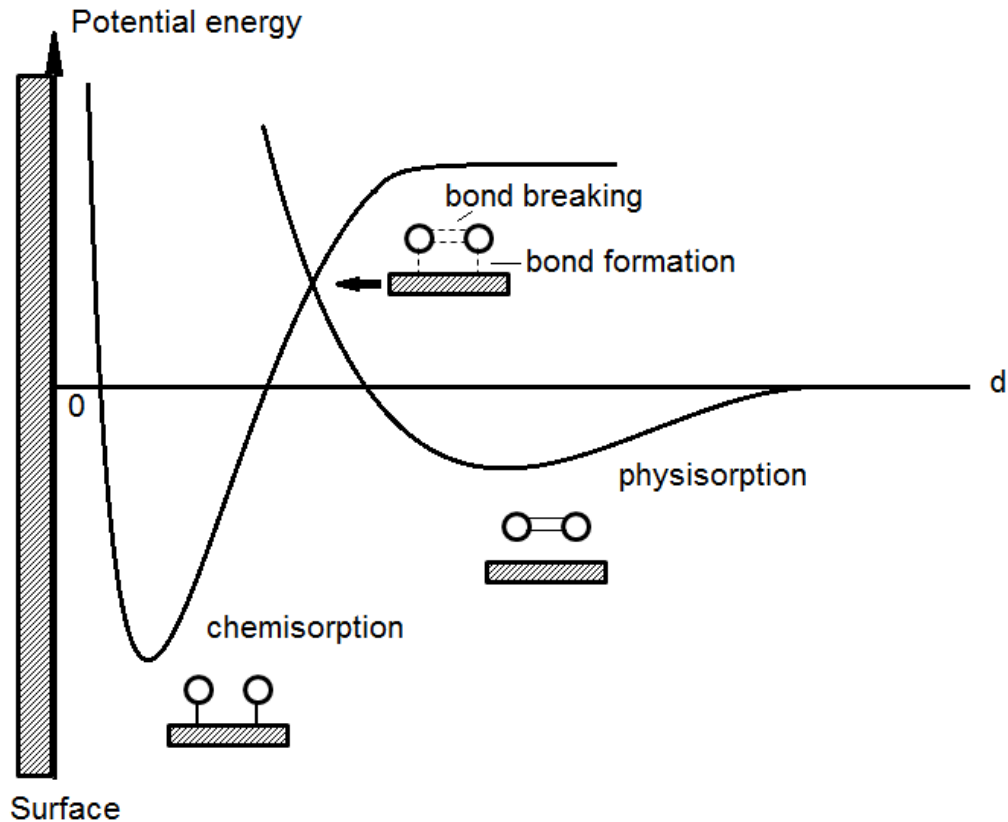


Figure 2.1 One-dimensional potential energy diagram for chemisorption and physisorption

2.1.1.2 The structure of single crystal metal surfaces – the Miller index system

Solid surfaces are usually found to consist of a mixture of flat regions (terraces) and defects (steps and kinks). It is well known that the local distribution of atoms around each of these surface sites is different. Hence, it is expected that their electronic properties will be distinguishable. In order to obtain the same reproducible result on a particular type of solid surface as another, it is important to precisely define the chemical and structural state of the solid substrate under investigation. Therefore, the most simplified surface systems, which contain a high ratio of terrace to defects and consist of just one type of atom, are first considered. Such a surface is referred as well-defined and single crystals possess this kind of surface. A single

crystal contains one repeating pattern of atoms extended throughout the material (the unit cell). The pattern is specific to the material. For metals, the most common atom packing arrangement is face-centred cubic (fcc), followed by body-centred cubic (bcc) and hexagonal close-packed (hcp). Platinum and gold, the transition metals to be studied in the present work, take up the fcc packing arrangement, as shown in **Figure 2.2**.

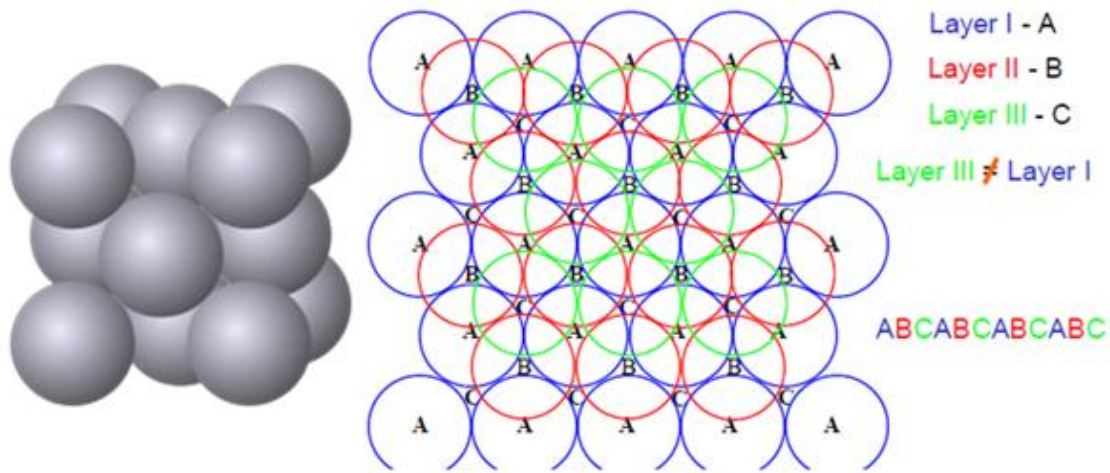


Figure 2.2 Arrangement of atoms in an fcc crystal structure⁶

For fcc metals, the arrangement of the hexagonal layers repeatedly builds up the crystal lattice every three layers (ABCABC) and it has the highest theoretical packing density that can be achieved by packing spheres. The lattice arrangement of hcp metals is very similar but the hexagonal layers are repeated every two layers, instead of three layers. Therefore, it is described as an ABAB arrangement.

The Miller index is a system that is used to describe a particular crystallographic plane. Cutting through the metal surface at a specific angle will produce a surface that has a particular surface arrangement of atoms. The periodicity of the plane is defined by its Miller index. The Miller indices for platinum are defined by using three vectors \vec{a} , \vec{b} and \vec{c} which represent the three axes of the unit cell. The distance from the origin to the intercept points in the crystal plane with vectors \vec{a} , \vec{b} and \vec{c} are defined as a , b and c respectively. Hence, the Miller indices h , k and l of a particular crystal plane are defined as:

$$h = |\vec{a}|/a \quad (\text{Eq 2.1})$$

$$k = |\vec{b}|/b \quad (\text{Eq 2.2})$$

$$l = |\vec{c}|/c \quad (\text{Eq 2.3})$$

If h , k or l are fractions, all of the three values are converted to the smallest integers but maintaining the original ratio of h to k to l by multiplying by a common factor. For example, one $\{hkl\}$ with the values of $\{1, 1/3, 1/6\}$ becomes $\{6, 2, 1\}$ by multiplying 6. If a negative intercept happens to appear, it will be indicated by placing a bar above the corresponding value of the index. The three most common low Miller index planes of fcc metals are $\{111\}$, $\{100\}$ and $\{110\}$. These three planes are schematically shown in **Figure 2.3** in relation to the fcc unit cell.⁷ These so called basal planes are commonly used for studies due to the irrelatively low surface free energies, high symmetries and stabilities.

If the plane of the fcc single crystal is not parallel to any of the three axes, then one of the $\{hkl\}$ values will be greater than 1. These surfaces, known as high Miller index planes, are usually produced by cutting a metal crystal in such a way that the resulting surface is rough on an atomic scale. This kind of surface contains either:

- Terraces of one of the three low Miller index planes separated by a monoatomic step. The width of the terrace is dependent on the cutting angle with respect to the low Miller index planes and is known as stepped surface.
- Or a combination of terraces, steps and kinks. This kind of surface is called a kinked surface.

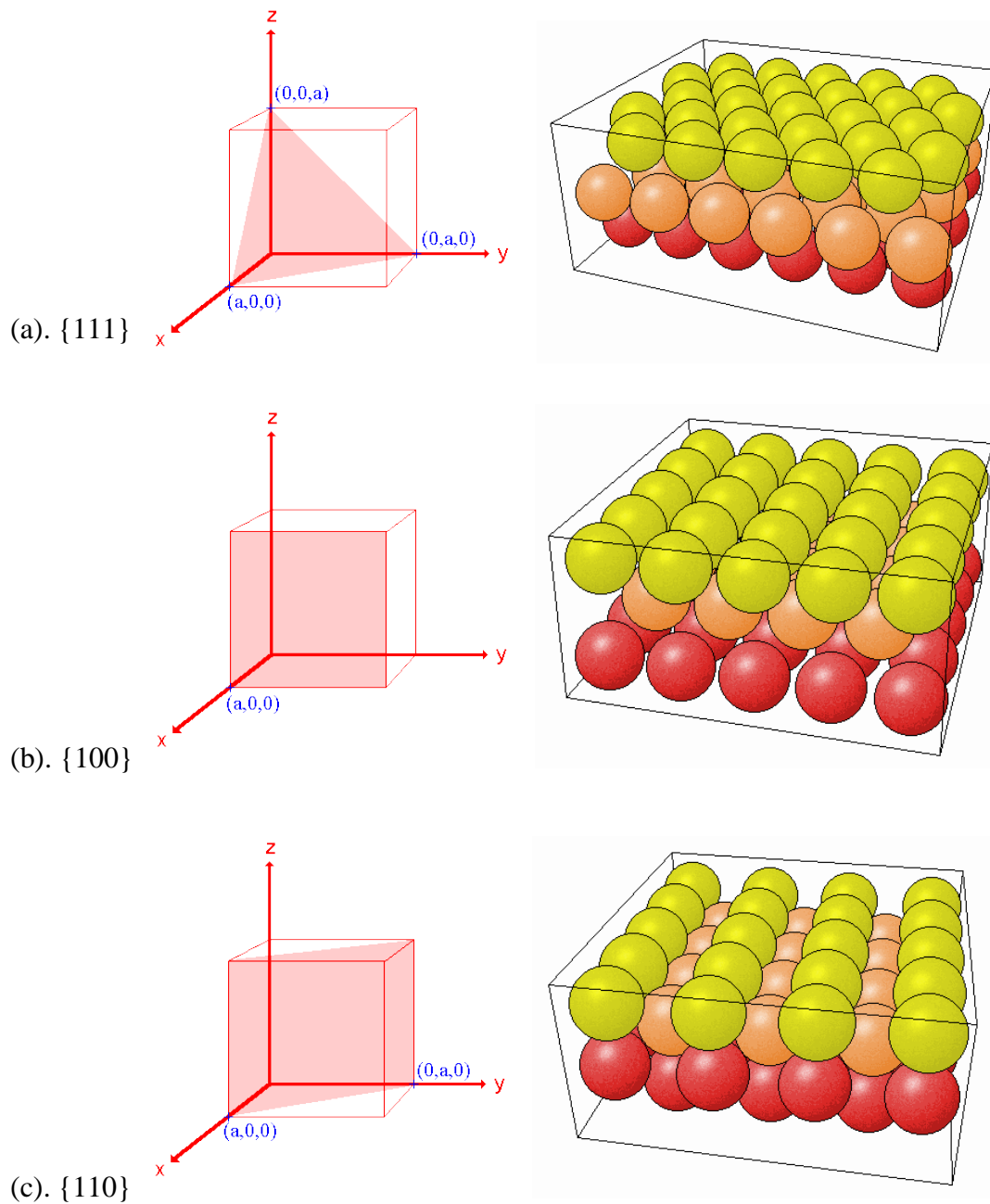


Figure 2.3 The fcc basal planes and corresponding unit cells, reprinted from reference 6.

The different stepped and kinked surfaces above exhibit specific geometric arrangements of atoms. Therefore, it results in different adsorption properties and chemical reactivity of each surface.

However, high Miller index planes can also be defined by microfacet notation. The stereographic triangle in **Figure 2.4** shows the relations between basal planes and stepped surface planes. Three basal planes are situated at the corners (poles) of the stereographic triangle. Between two poles, each side of the triangle (zone) represents the range of stepped surfaces associated with sites containing both poles. The equations of converting the microfacet notation to Miller index notation are given within the triangle. Taking the zone between fcc {100} and fcc {111} as an example, a surface which displays n atoms wide {100} terraces separated by a monatomic {111} step may be denoted $(2n-1,1,1)$. For example, a surface with a $3\{100\}\times\{111\}$ label in microfacet notation will have a Miller index of {511}.⁸ In each zone of the stereographic triangle, there is a point where n in the microfacet notation is 2, i.e. when a step which is two atoms in length turns up between every two atoms of terrace, hence the contributions from each basal plane is effectively equivalent. This point is called the *turning point* of the zone.

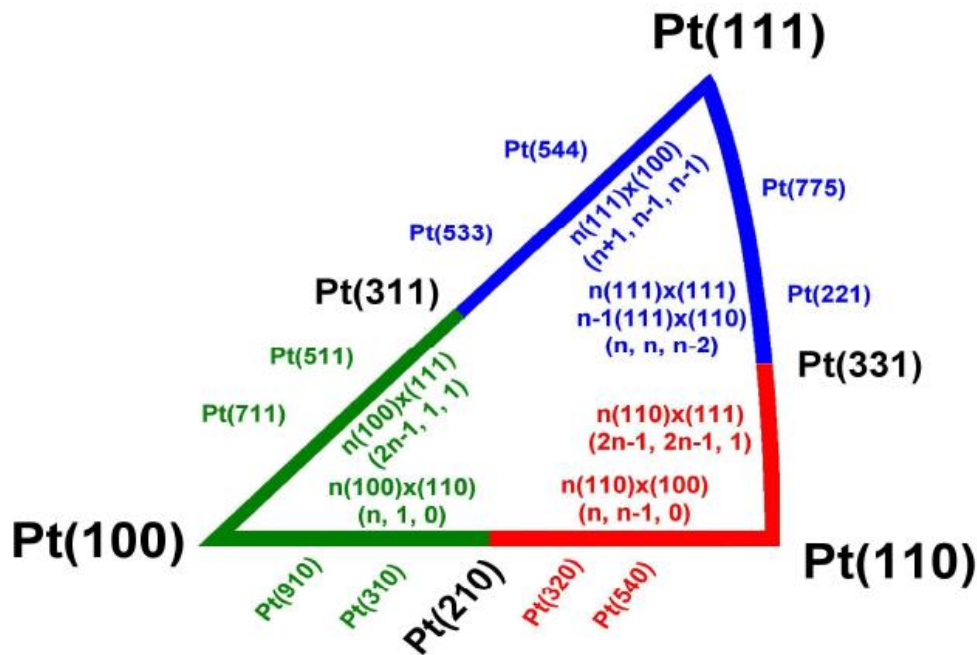


Figure 2.4 The stereographic triangle showing the relative positions and microfacet notations for a range of fcc single crystal surfaces (platinum in this case), reprinted from reference 7.

2.1.2 Electronic Structure

In a bulk solid, electrons in the atoms of the solid may broadly be classified as either core electrons or valence electrons. The core electrons are strongly bound to the nuclei and do not participate in electrical conduction or chemical bonding. The valence electrons are the most weakly bound electrons and exhibit the highest value of the principle quantum numbers. There are a large number of electronic states due to the great amount of electrons in a solid. In metals, the valence electrons form continuous bands of overlapping electronic states known as the valence band and the conduction band. It is the ability of the valence electrons to transverse between these two bands that determines electrical properties of the solid including its suitability for catalysis.¹ Usually, as shown in **Figure 2.5**, the density of states at the Fermi energy level is also utilised to illustrate variations in catalytic reactions of various kinds of metals.

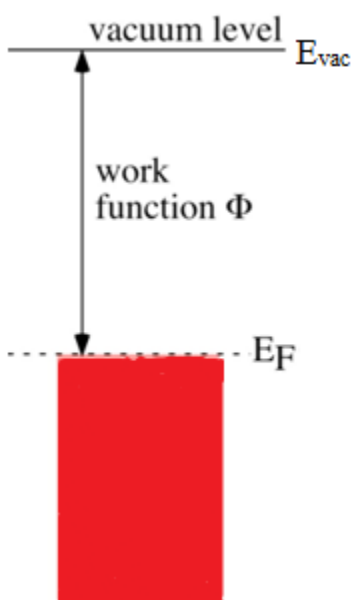


Figure 2.5 Fermi energy E_F , vacuum level E_{vac} and work function Φ of a metal. Shaded region signifies range of electronic states in the solid (valence band) that are filled.

In a metal, the valence band and conduction band are continuous and overlapped. Also, the conduction band is not fully occupied, so the electrical conductivity is high. Insulators and semi-conductors will have a band gap where no electronic state exists. In **Figure 2.5**, the valence band is shaded red and the conduction band is the area directly above the Fermi level. At absolute zero (0 K), the energy of the highest occupied electronic state in the conduction band is termed the

Fermi energy, E_F , where all states below are occupied and above are unoccupied and are related to the *work function*, Φ of the metal.

$$e\Phi = E_{vac} - E_F \quad (\text{Eq 2.4})$$

It means, at 0 K, the minimum energy required to remove one electron from the material into vacuum is the work function and can be described as the ionisation energy of the metal. The surface structure can greatly affect the work function of the metal. This is because the electrons distribution at the surface is different from the bulk. As the electron density does not end abruptly, instead, it oscillates near the surface to create an electrostatic dipole layer at the surface. Hence, the surface dipole contribution D needs to be entered into equation 2.4 and therefore the work function is highly dependent on surface properties, including the presence of surface defects and chemical impurities on the surface.

The energy of the crystal lattice at the surface is different to that in the bulk, due to the unsaturation of bonding in atoms at a surface.¹ As mentioned earlier, the surface atoms don't have the full coordination to neighbouring atoms and they form a higher energy configuration compared with those being located in the bulk. By changing their bonding geometry, such as bond length and angles, this higher energy state can be dissipated between layers in a process known as *relaxation*. For a metal, the result is often a shortening of the distance between the top layer of atoms and the second layer and the effect will even be passed down to 5-6 layers deep. This near surface region, distinguishable from the bulk, is called the *selvedge region*.⁹

Another way to minimise the surface energy is to change the periodicity of the surface atoms in a process known as *reconstruction*. In this process, the extra valence electrons are directed laterally, so that the bond length and angles between adjacent atoms have been changed. One of the most notable examples is that platinum{110} surface which when clean reconstructs from a (1×1) periodicity to (1×2) periodicity, commonly referred to as the missing row reconstruction,⁹ which is shown in **Figure 2.6**.

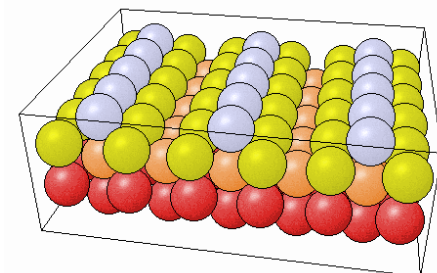


Figure 2.6 The reconstructed (1×2) Pt $\{110\}$ ‘missing row’ clean surface reconstruction.

Reconstruction can also be induced by chemisorption. Depending on the symmetry and energy of the electronic states, which is intimately related to the geometrical structure, a surface site is able to form a chemical bond with a potential adsorbate. When the chemical interactions are strong enough and the adsorbate coverage is high enough, the adsorbate can induce a reconstruction of the surface. An example of this phenomenon would be the alkali metal induced (1×2) surface reconstruction of Pd $\{110\}$, similar to the structure in **Figure 2.6**. Therefore, it is evident that, instead of being ‘static’, metal surfaces are constantly moving to compensate for energy differences between the bulk and surface of the metal. The ease with which electrons may be transferred to and from the metal surface often dictates the ability of the surface to activate chemical bonds. Hence, the ability to tune electronic structure in a systematic manner constitutes a powerful new approach to studying catalysis at solid surfaces.

2.2 The Electrical Double Layer

The *electrical double layer* (EDL) is an array of charged particles and/or orientated dipoles that exist in every material interface. With a characteristic potential distribution, it is formed in the interphase due to a non-uniform distribution of the charged particles. For the electrode/electrolyte interface, the EDL reflects the different ionic zones that are formed in solution to compensate for the excess charge at the electrode surface. A positively charged electrode will therefore attract a layer of negatively charged ions of the electrolyte and *vice versa*.

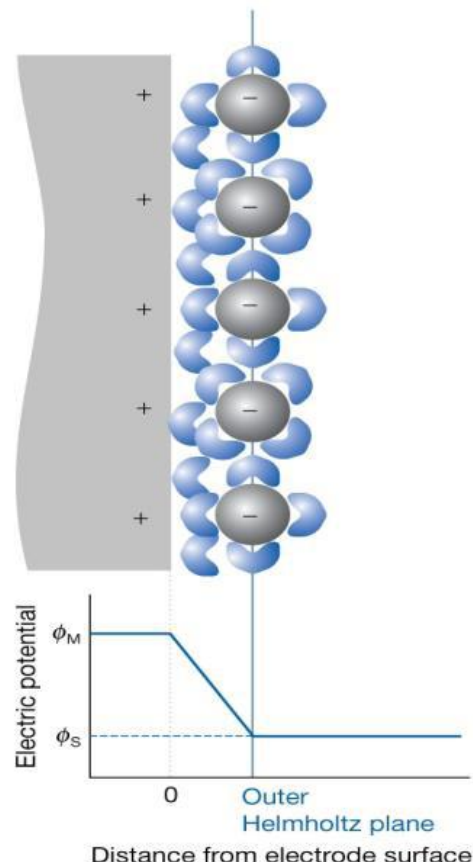


Figure 2.7 The Helmholtz model of the electrical double layer.¹⁰

The first model for the EDL was proposed by Helmholtz in the 1850s (**Figure 2.7**). Following the concepts of Helmholtz, the ions carrying the opposite charge to the charged electrode in the electrolyte will form a layer balancing the electrode charge. This layer is known as the Outer Helmholtz Plane (OHP).^{11, 12} The distance of approach of the OHP is assumed to be limited to the radius of the ion and a single sphere of solvation round each ion. The OHP is rigidly bound due to strong electrostatic bonds. In essence, ions from the electrolyte form a ‘parallel plate capacitor’ with the electrode. The EDL capacitance therefore depends on the charge separation distance and the value of the dielectric constant of the medium between the plates.

Thermal motion of the ions in the EDL was considered by Gouy and Chapman, who later proposed the diffuse double layer model.¹² **Figure 2.8** shows how the local concentrations of the cations and anions differ in the Gouy-Chapman model from their bulk concentrations. Ions of opposite charge to the electrode cluster close to the electrode surface and ions of the same charge

are repelled into the bulk solution. The concentration of the ionic species at a given distance from the surface decays exponentially. However, this model ignores the ions' own size and allows the centres of the ions to approach close to the physical surface, which leads to the capacitance values calculated being much higher than the experimental values for concentrations greater than 10^{-2} M.

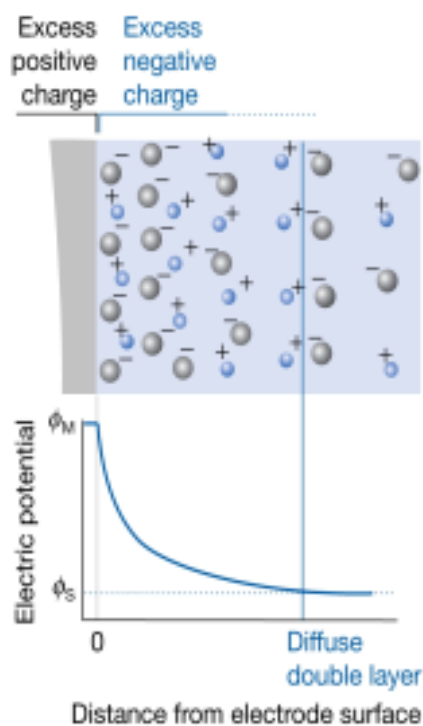


Figure 2.8 The Gouy-Chapman model of the double layer.¹⁰

From this, it is seen that the Gouy-Chapman model underemphasizes the rigidity of the double layer whilst the Helmholtz model overemphasises it, neither of which is sufficient to represent the true structure of the EDL. Based on this fact, the Stern-Grahame model of the EDL (**Figure 2.9**) was proposed by combining both the Helmholtz and Gouy-Chapman models.^{11, 12} In this model, it was suggested that ions closest to the electrode surface are constrained into a rigid Helmholtz plane, whilst the ions outside this plane are diffuse as in the Gouy-Chapman model. The EDL model was made more sophisticated by Stern and Grahame as they added the Inner Helmholtz Plane (IHP) to the structure of the double layer. The IHP is the most inner layer and contains solvent molecules and ions. Their size and possibility of specific (non-electrostatic) adsorption onto the electrode surface were taken into account. Hence, the IHP is defined by the

loci of the centres of the specifically adsorbed ions directly attached to the electrode surface without hindrance from water molecules in the solvation shell.

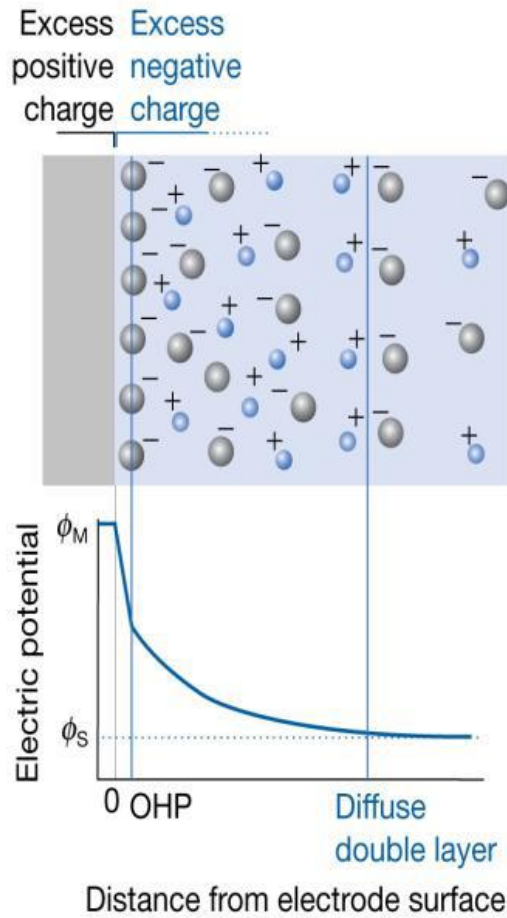


Figure 2.9 Stern-Grahame model of the double layer.¹⁰

The electrical double layer resembles an ordinary (parallel plate) capacitor. For an ideal capacitor, the charge Q is proportional to the potential difference:

$$Q = CE \quad (\text{Eq 2.5})$$

where C is capacitance (in farads, F), the ratio of charge stored with respect to the applied potential E (V). The charge-potential relationship for the electrical double layer is given by equation 2.6:

$$Q = C_{DL}A(E - E_{PZC}) \quad (\text{Eq 2.6})$$

where C_{DL} is the capacitance of the double layer (F), A is the electrode area (cm^2) and E_{PZC} is the potential of zero charge (PZC), where no net charge exists on the electrode. The capacitance of the double layer consists of a combination of the Helmholtz and the Gouy-Chapman layers. For two capacitors in series, the total capacitance is given by:

$$\frac{1}{C} = \frac{1}{C_H} + \frac{1}{C_{GC}} \quad (\text{Eq 2.7})$$

where C_H and C_{GC} represent the capacitance of the Helmholtz and Gouy-Chapman layers. The smaller of these capacitances determines the observed behaviour. By analogy, with a parallel plate capacitor, C_H is given by:

$$C_H = -\frac{\varepsilon}{4\pi d} \quad (\text{Eq 2.8})$$

where d is the distance between the surface and the counter ionic layer, and ε is the dielectric constant. C_H increases with the separation of the surface and counter ionic layer as well as the dielectric constant. The value of C_{GC} is affected by the concentration of electrolyte whereas C_H is largely independent. For dilute electrolytes ($< 10^{-2}$ M), C_{GC} dominates close to the PZC whereas for more concentrated electrolytes, the behaviour of the capacitance as a function of potential resembles more the Helmholtz behaviour of equation 2.8. Hence, according to equation 2.7, if $C_H \gg C_{GC}$, $C \approx C_{GC}$, whereas if $C_{GC} \gg C_H$, $C \approx C_H$.

In **Figure 2.10**, it illustrates how the double layer capacitance varies depending on the change in applied potential and electrolyte concentration. It can be seen that if the concentrations of an electrolyte is high, the capacitance of the double layer resembles that of a parallel plate capacitor, which means, the capacitance is independent of the applied potential and concentration. However, at much lower concentrations of electrolyte, a sharp drop in the capacitance curve is observed at

the PZC of the surface, suggesting the contribution of the Gouy-Chapman layer. Therefore, it is more appropriate to make comparison of the double layer with a parallel plate capacitor when using strong concentrations of electrolyte.

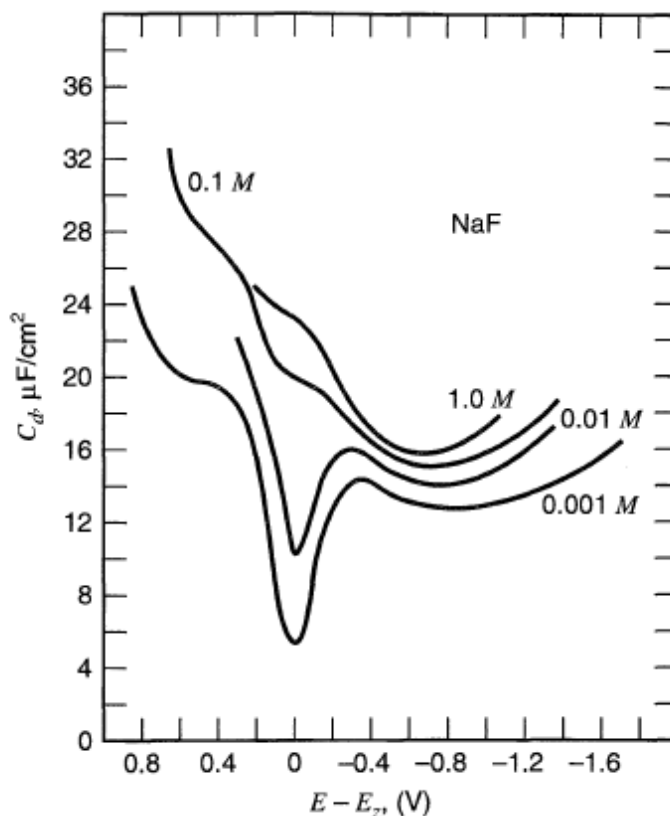


Figure 2.10 Effect of concentration and potential on double layer capacitance, reprinted from reference 13.

2.3 Cyclic Voltammetry

Cyclic voltammetry (CV) is the most versatile electroanalytical technique for the study of electroactive species. It is an important method for characterising electrode surfaces and testing the cleanliness and reproducibility of an electrochemical system.⁷ A typical CV experiment corresponds to a simultaneous measurement of current density and applied voltage. This voltage is applied to the working electrode and a reference electrode. With a fixed rate, ν ($\text{V}\cdot\text{s}^{-1}$), the potential is swept between two set potentials (E_1 and E_2). The current generated, i , is recorded for both the forward scan (anodic current) and the reverse scan (cathodic current). The current is

usually divided by the surface area of the working electrode and therefore referred to as current density. The peaks and troughs of the resulting i - V cycle, are known as a cyclic voltammogram or CV. The general features of the CV may be used to interpret redox processes at the interface.⁴
¹³ **Figure 2.11a** shows the saw-tooth waveform applied in cyclic voltammetry. In this example, the potential is scanned from 0 – 0.8 V with v at $0.05 \text{ V}\cdot\text{s}^{-1}$, defined by equation 2.9, and is cycled three times.

$$v = \frac{dV}{dt} \quad (\text{Eq 2.9})$$

Figure 2.11b shows a cyclic voltammogram for a simple reversible redox process of the form:



where O is the oxidised species, R is the reduced species, and n is the number of electrons involved in the reaction. The process in equation 2.10 is chemically reversible with the product of the forward reaction being the reactant for the reverse reaction and *vice versa*. Within certain time, one system can reach equilibrium after completing n electrons transfer. Then the thermodynamic equilibrium will be broken and cause a reversal when an infinitesimal change in the direction of the applied potential occurs in the process.¹⁴

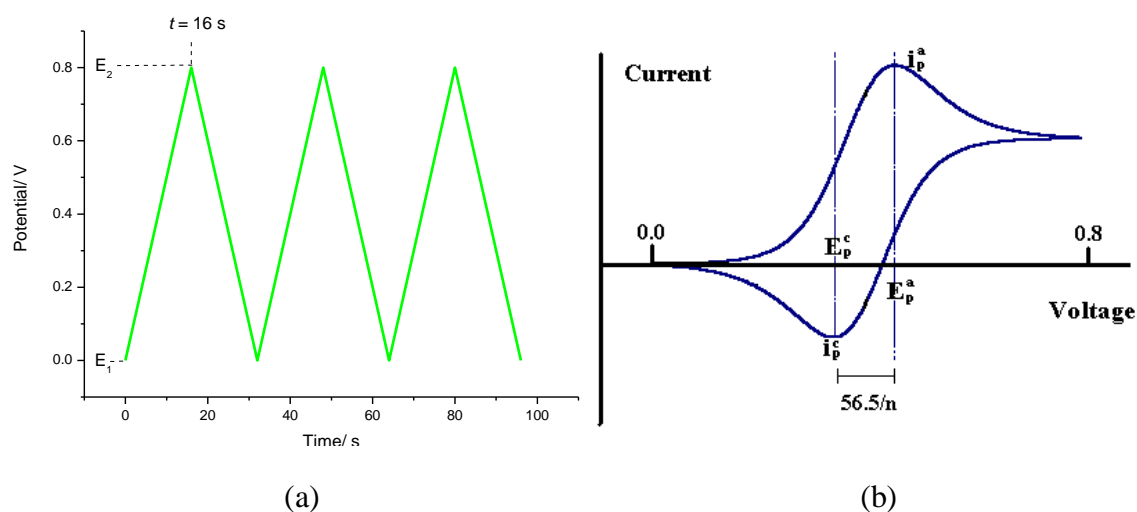


Figure 2.11 (a) ‘Saw Tooth’ potential waveform applied to a working electrode in cyclic voltammetry. E_1 : 0 V, E_2 : 0.8 V, ν : 0.05 V s⁻¹. (b) The expected CV in a simple reversible redox process. Reprinted from reference 7.

For a reversible reaction in solution, the position of the voltammetric peaks is independent of ν , and the separation of the peaks can be calculated with the equation¹⁴:

$$\left| E_p^{Ox} - E_p^{Red} \right| = 2.2 \frac{RT}{nF} \quad (\text{Eq 2.11})$$

where R is the gas constant, T is temperature (K), n is the number of electrons involved in the reaction and F is the Faraday constant. At 298 K the separation is 56.5/ n mV. Hence the number of electrons involved in the reaction can be calculated from the measured peak separation. The peak current, i_p , for both forward and reverse reactions should be the same under reversible conditions and is calculated with the following equation¹⁴:

$$i_p = (2.69 \times 10^5) n^{3/2} \cdot A \cdot D_o^{1/2} \cdot \nu^{1/2} \cdot C_o \quad (\text{Eq 2.12})$$

where A is the area in cm², D_o is the diffusion coefficient in cm²·s⁻¹ and C_o is the concentration of the electroactive species in the bulk solution in mol·cm⁻³. Hence, solution peak intensity redox processes will exhibit a $\nu^{1/2}$ dependence on sweep rate. On the contrary, surface adsorption may be distinguished from solution processes since $i_p \propto \nu$, which shows a linear dependence of i_p on

sweep rate.¹⁴ The peak separation for surface processes at equilibrium is also close to zero mV because bulk diffusion no longer occurs.¹⁵ The electrical current generated is from charge transferring across the electrode/electrolyte interface and causes oxidation or reduction to occur. Hence it is referred to as a Faradaic process. However, adsorption and desorption processes at surfaces can also occur without the transfer of Faradaic charge and these are known as non-Faradaic processes. The structure of the electrode/electrolyte interface may change with potential or electrolyte composition. This kind of process is responsible for electrostatic external currents even though charge does not cross the interface. For example, migration of ions from the electrode surface into the double layer and capacitive charges are due to formation of chemisorption bonds.¹⁴

2.3.1 CV of polycrystalline platinum surfaces

The magnitudes of the peaks in a voltammogram depend on the electroactive species, the bulk solution concentration, the sweep rate (assuming no mass transport limitations) and surface area of the electrode material. The example of a platinum electrode in sulphuric acid is used in studies of adsorption, as it is a well understood system.

Figure 2.12 shows a typical CV generated on a polycrystalline platinum electrode versus a Pd/H reference electrode sweeping at $0.05 \text{ V}\cdot\text{s}^{-1}$ at room temperature. The CV was taken in a spectro-electrochemical flowcell, which was designed and built in-house. The baseline should be parallel to the potential axis and centred at 0 A on the current axis. Sometimes a slope to the baseline may be encountered, which indicates an Ohmic drop and is due to distance to the counter electrode through a thin layer configuration.

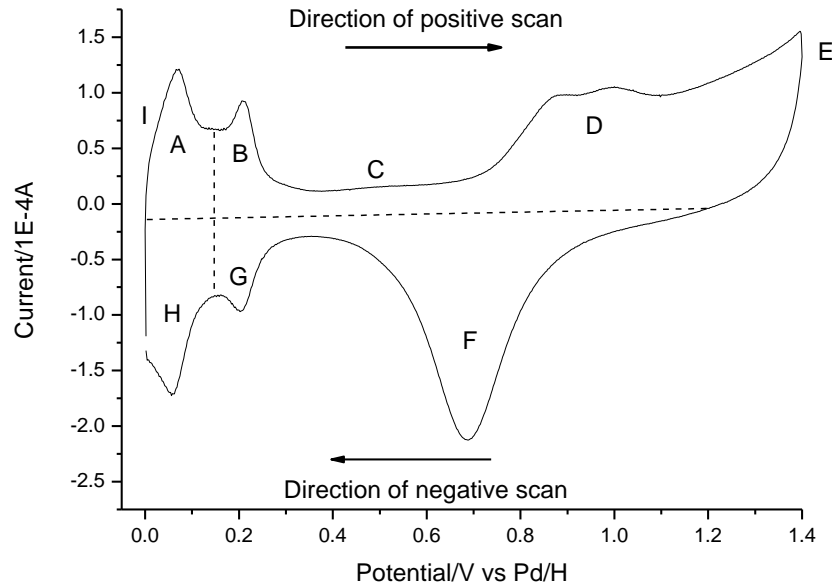


Figure 2.12 Cyclic voltammogram of polycrystalline platinum in 0.1 M H₂SO₄. (A) H desorption from {110} sites; (B) H desorption from {100} sites; (C) double layer; (D) oxide formation; (E) potential sweeping direction switching to negative; (F) oxide desorption; (G) H adsorption on {100} sites; (H) H adsorption on {110} sites; and (I) potential sweeping direction switching to positive. Sweep rate = 0.05 V·s⁻¹.

In the voltammogram of **Figure 2.12**, the result of an electrochemical process occurring on the working electrode surface is labelled and classified into a number of distinct regions. In regions A and B, due to the electron transfer from adsorbed hydrogen on the electrode surface into the bulk of the electrode, a positive electrical current (anodic) is produced. This process involves the oxidation of under potentially deposited H_(ads),¹⁶ resulting in the desorption of the cationic hydrogen ions generated into the bulk of the electrolyte:

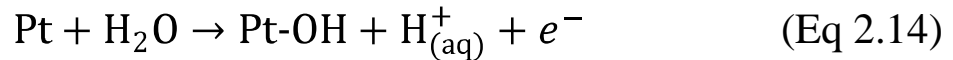


There are two peaks in regions A and B, which are due to the hydrogen desorption from different sites of the platinum surface. Hydrogen desorbs firstly from so-called ‘{110} defect sites’ in

region A as these are the most weakly bound with the surface. Then the hydrogen desorption occurs at the corresponding ‘{100} defect sites’ that compose region B.¹⁶

Region C is called the double layer region. There is only the capacitive charge of the electrochemical double layer causing the current flowing.¹⁴ In this region, non-Faradaic processes are occurring. Ions of the opposite charge migrate towards the electrode surface as it becomes more positively charged. The ‘thickness’ of the double layer region of the CV is a significant measurement, as its size is proportional to the capacitance of the electrode. Not only the material, but also the surface area of the electrode needs to be taken into account. Therefore, electrodes with large surface areas have wider double layer regions than low surface area electrodes. Numerous models have been proposed for the distribution of ions at the electrode/electrolyte interface leading to capacitive processes.

The formation of oxide occurs in region D, where water from the electrolyte adsorbs on the platinum surface and dissociates into adsorbed OH and solution phase hydrogen cations. Hence, a surface hydroxide is produced.



Then the free electron from the broken O-H bond is transferred into the bulk of the electrode and generates anodic current. If the potential extends further positive, the second O-H bond will be broken and one more electrons will be released into the bulk of the electrode, resulting in leaving the surface metal atoms in an oxidized state. These may then decompose to a free platinum site together with oxygen gas (electrolysis occurs).

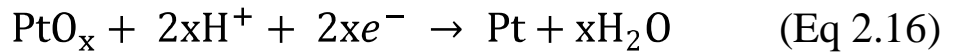


It is worth noticing that the reformation of the platinum site will not be geometrically the same as before the oxidation process, but will tend to form clusters instead. This process is known as place-exchange and can lead to etching, leaving the surface with a rough topography.¹³

At Point E, the upper potential limit is reached and the direction of the scan is switched to a negative going sweep. While this repeated oxidation and reduction of the electrode surface can

electrochemically clean a thin platinum metal film (as will be performed in the present study), it might also eventually lead to defects accumulating in the surface. The integrity of the surface will be lost and if the surface consists of a thin film surrounding a core of different composition undesirable interactions between target molecules and the underlying base material can occur (see latter for Au@M type nanoparticles – section 3.3.1). To avoid this situation, the upper potential limit is always carefully controlled in each experiment.

In region F, the oxide stripping, which is the reverse reaction to that of region D, occurs. During this process, electrons are transferred from the bulk of the electrode to form O-H bonds followed by desorption of water molecules in a cathodic current.

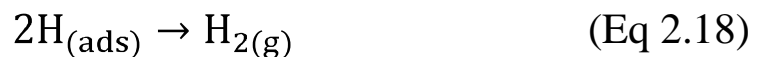


The cathodic current is generated again at regions G and H because of the adsorption of $\text{H}^+_{(\text{aq})}$, which is the reverse reaction of that in regions A and B. Therefore, regions A, B, G and H are together known as the hydrogen under-potential deposition region (H UPD) of a platinum CV.

H UPD region is very important in understanding a CV as the charge in the H UPD region can be used to estimate the real surface area of the working electrode. Based on the assumption of one electron transfer per surface platinum atom, the charge density σ_d ($210 \mu\text{C}\cdot\text{cm}^{-2}$ for the polycrystalline Pt electrode). The charge Q ($\text{C}\cdot\text{cm}^{-2}$) generated is calculated by integrating the area of the H UPD region in the CV. The values are then entered into equation 2.17 and the area A is found.

$$A = \frac{Q}{\sigma} \text{cm}^2 \quad (\text{Eq 2.17})$$

Point I is the lower potential limit set in the waveform. It is the point where the negative potential scan is switched in direction to a positive potential scan. At potentials more negative than -0.05 V vs Pd/H , hydrogen gas will be evolved. From equation 2.13:



2.3.2 CV of platinum single crystal electrodes

Single crystal electrodes are electrodes that contain one repeating pattern of atoms extended throughout the material. As described earlier, their surfaces contain a high ratio of terrace to defects and consist of just one type of atom. By using cyclic voltammetry as a probe, different surface structures could be detected and distinguished.

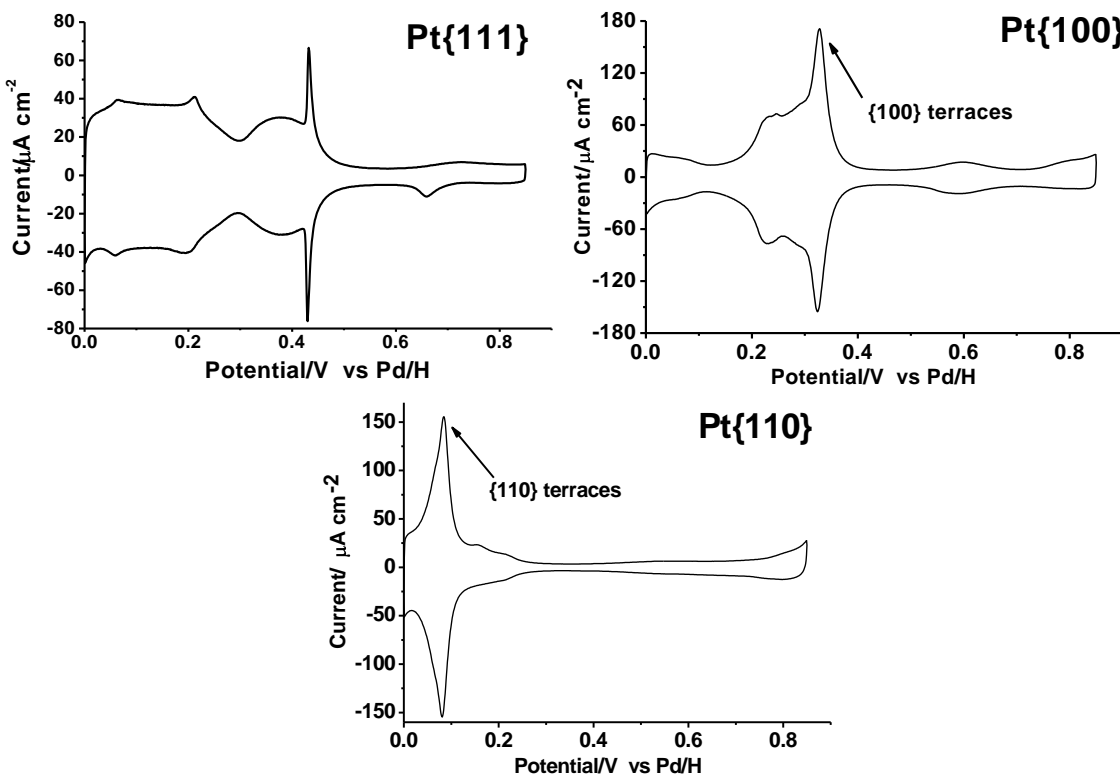


Figure 2.13 CVs of Pt{*hkl*} single crystal electrodes in 0.1 M H₂SO₄. Sweep rate = 0.05 V·s⁻¹.

Figure 2.13 shows the typical CVs of the low Miller index plane Pt{*hkl*} single crystal electrodes in 0.1 M H₂SO₄ at a sweep rate of 0.05 V·s⁻¹. It is apparent that different surfaces generate different CV profiles. The CV of Pt{111} shows the main features which include a sharp peak at 0.44 V reflecting the extent of long range order, a broad shape from 0.35 V to 0.55 V for bisulphate adsorption/desorption, and a rather flat, box like region between 0 V and 0.3 V for hydrogen adsorption/desorption.¹⁷ The CV of Pt{100} gives a pair of sharp peaks at 0.325 V, which reflects the presence of (1 x 1) long range order of {100} terrace sites.¹⁸ The shoulder at

0.225 V is caused by {100} x {111} step sites. Finally for Pt{110}, the characteristic peaks at 0.086 V are due to the adsorption/desorption of hydrogen and anions on {110} terrace sites.¹⁹

Therefore, cyclic voltammetry is a powerful tool to characterise different single crystal electrode surfaces. Not only surfaces exhibiting low Miller indices listed above, but also other more complicated surfaces containing steps and kinks and even chiral sites may be distinguished using CV.²⁰

2.4 Spectroscopy

Molecular spectroscopic techniques work on the principle that energy is quantised and this can be measured through interaction with electromagnetic (EM) radiation. In classical theory, EM radiation propagates in waves of alternating electric (\vec{E}) and magnetic (\vec{B}) field vectors, which stand in a fixed ratio of intensity to each other and oscillate perpendicular to each other and perpendicular to the direction of energy and wave (\vec{k}) propagation (**Figure 2.14**). In reality, they also contain particle like character in terms of discrete bundles of energy called quanta. Einstein regarded quanta of light as real particles and named them as photons. A photon has an energy, E (eV), which is proportional to its frequency, ν (s^{-1}), as shown in the following equation:²¹

$$E = \frac{hc}{\lambda} = h\nu \quad (\text{Eq 2.19})$$

where h is Planck's constant (J·s), λ is wavelength (m) and c is the speed of light ($m \cdot s^{-1}$) through vacuum.

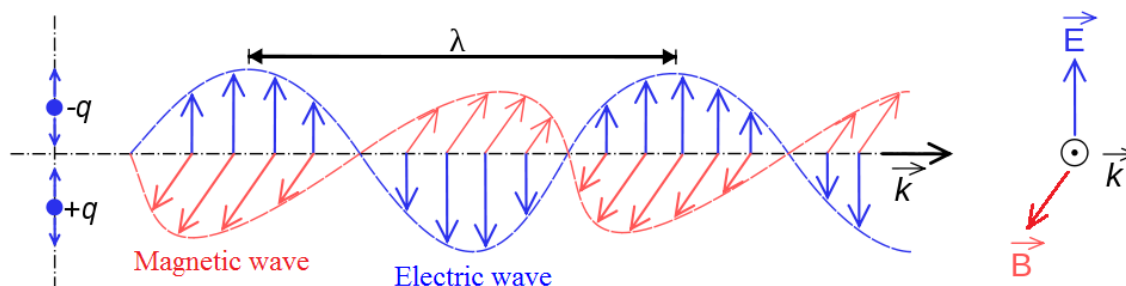


Figure 2.14 An electromagnetic wave propagating in free space, the amplitude of the wave is the magnitude of the field and the distance between the wave peaks is the wavelength (λ).

The electric field strength, \bar{E} ($\text{V}\cdot\text{m}^{-1}$) at a given time (t) may be expressed by:

$$\bar{E} = E_0 \cos 2\pi\nu t \quad (\text{Eq 2.20})$$

where E_0 is the amplitude of the wave and ν is the frequency of radiation. All EM radiation travels at the speed of light through a vacuum and so ν (s^{-1}) is found:

$$\nu = \frac{c}{\lambda} = \tilde{\nu}c \quad (\text{Eq 2.21})$$

often expressed as wavenumbers $\tilde{\nu}$ (cm^{-1}), which is most common parameter to vibrational spectroscopy.

Table 2.1 Spectroscopic techniques, the general frequency ranges used and their origins.²²

Spectroscopy	Range (cm^{-1})	Origin
Gamma-ray	$10^{10} - 10^8$	Rearrangement of elementary particles in the nucleus.
X-ray	$10^8 - 10^6$	Transitions between energy levels of core electrons of atoms and molecules.
UV-visible	$10^6 - 10^4$	Transitions between energy levels of valence electrons of atoms and molecules.
Raman and Infra-Red	$10^4 - 10^2$	Transitions between vibrational levels.
Microwave	$10^2 - 1$	Transitions between rotational levels.
Electron spin resonance	$1 - 10^{-2}$	Transitions between electron spin levels in magnetic field.
Nuclear magnetic resonance	$10^{-2} - 10^{-4}$	Transitions between nuclear spin levels in magnetic field.

Table 2.1 shows the full frequency range of the EM spectrum used in analytical chemistry with the energy transitions and the associated techniques normally used to measure them. In this

study, it is mainly concerned with molecular vibrations whose frequencies are observed in the Infra-Red (IR) region of the EM spectrum corresponding to wavelengths between 2.5×10^{-6} and 2.5×10^{-5} m.

2.4.1 Molecular vibrations

2.4.1.1 Vibrations of diatomic molecules

The potential energy curve for a diatomic molecule is shown in **Figure 2.15**. According to the harmonic oscillator model, the variation of potential energy versus the inter-atomic distances in a diatomic molecule is displayed as the parabolic curve (dash line). It represents the extremes of the atomic displacements (inter-nuclear distance) during a vibration at different vibrational energy states (v). For example, when $v = 0$, it is the ground state energy and when $v > 1$, it represents the corresponding first excited energy state. From equation 2.22, it can be seen that the energy of the vibrational state is related to the frequency of the vibration in wavenumbers ($\bar{\omega}$). The difference between $v = 0$ and $v = 1$ is the fundamental frequency of the vibration (ν). Also, the harmonic oscillator model predicts that the difference between successive states is constant. Hence, the energy for each vibrational state may be calculated by a simple harmonic approximation:²³

$$E_v = (v + 1/2)hc\bar{\omega} \quad (\text{Eq 2. 22})$$

As described in Hooke's law of elasticity, the maximum inter-nuclear distance can infinitely increase with each successive vibrational state. However, chemical bonds in real molecules are not infinitely elastic. So at higher energy states, the displacement of the atoms is greater than that predicted by the harmonic oscillator model. Meanwhile, the energy gap between states becomes progressively smaller. Hence a more accurate approximation, which is closer to the situation in real molecules, would be the anharmonic oscillator represented by the Morse curve, as shown with solid line in **Figure 2.15**. It predicts that the displacement of the atoms will eventually overcome the recoiling force of the bond and result in the dissociation of the molecule.

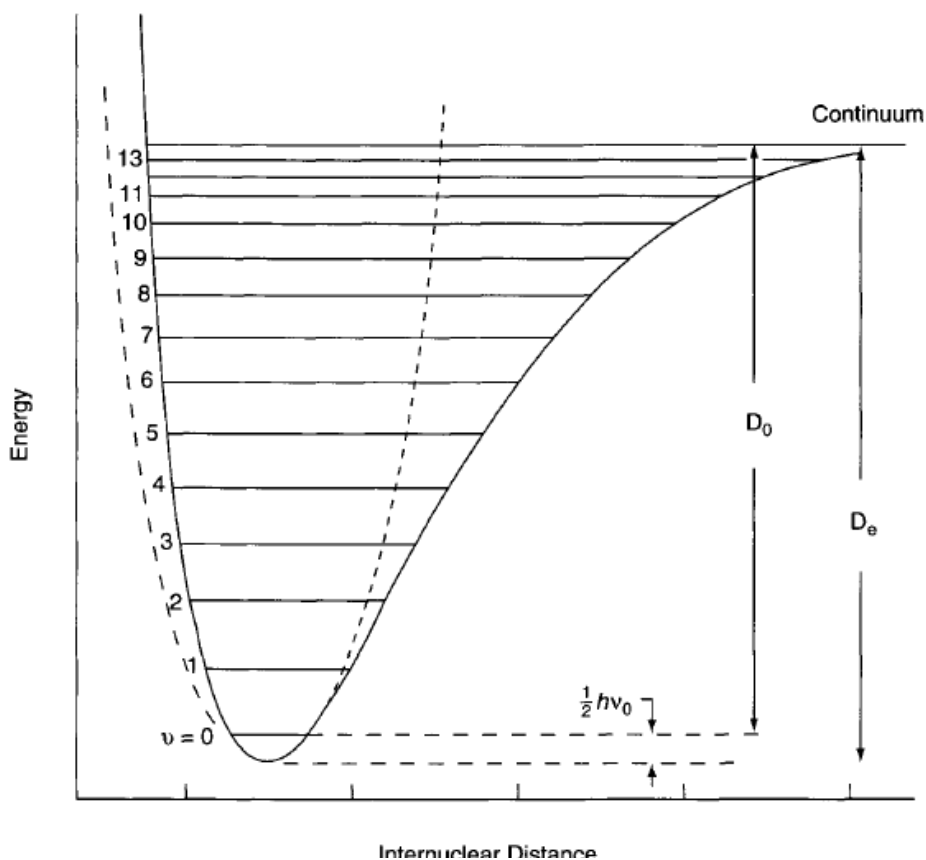


Figure 2.15 Harmonic oscillator model (dash line) of vibrational energy levels (v) and the Morse curve of the anharmonic oscillator model (solid line), reprinted from reference 23.

Therefore, anharmonicity constants x_e is included in equation 2.22 to give:

$$E_v = \left(v + \frac{1}{2}\right) hc\omega_e - \left(v + \frac{1}{2}\right)^2 hc x_e \omega_e + \dots \quad (\text{Eq 2.23})$$

where ω_e is the wavenumber corrected for anharmonicity.²² So together, $x_e \omega_e$ indicates the magnitude of anharmonicity. The strength of the bond is determined by the energy when the atoms dissociate (D_e , **Figure 2.14**). To calculate the energy at higher vibrational energies, one should include further terms for $(v + 1/2)$, but these are less significant at lower energy levels.²⁴

For a harmonic oscillator, the masses of each atom (m_1 and m_2) are known then the reduced mass (μ) of the diatomic molecule system is given by:

$$\mu = \frac{m_1 m_2}{(m_1 + m_2)} \quad (\text{Eq 2.24})$$

The equilibrium distance between the atoms is the bond length. So the force constant (k), or the ‘stiffness’ of the bond is calculated:

$$k = 4\pi^2 \nu^2 c^2 \mu \quad (\text{Eq 2.25})$$

The magnitude of k is represented by the ‘steepness’ of the potential energy curve; the higher the value of k , the steeper the curve will be. The natural frequency of vibration (ν) of a bond may then be calculated in the following equation:

$$\nu = \frac{1}{2\pi} \sqrt{\frac{k}{\mu}} \quad (\text{Eq 2.26})$$

2.4.1.2 Vibrations of polyatomic molecules

For any given chemical compound, there are a total of $3N$ *degrees of freedom*, where N is the number of atoms. This number arises from the ability of each atom to move in three different directions (x , y and z axes). Usually, the movement of molecules is considered as a whole, resulting in partitioning the $3N$ degrees of freedom into molecular translational, rotational and vibrational motion. Hence, by subtracting three of the degrees of freedom corresponding to translational motions and rotations each, the number of vibrations of a molecule is $3N-6$. However, as linear molecules only have two non-equivalent axes to rotate around, the equation for the number of vibrational modes becomes $3N-5$.²⁵ The two most common molecules used to demonstrate such relationships are H_2O and CO_2 .

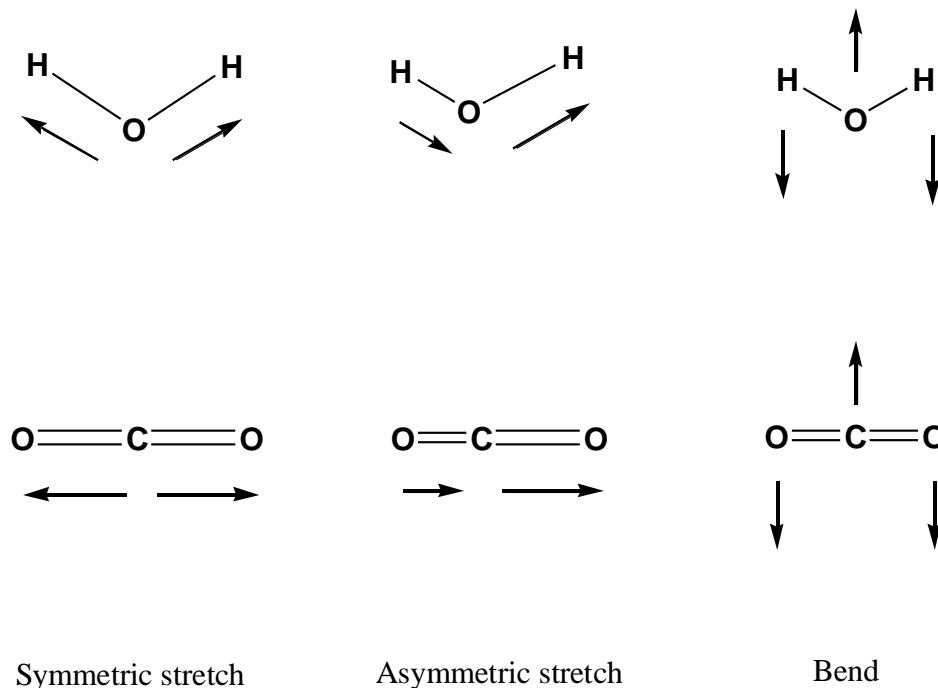


Figure 2.16 Vibrational modes of water and carbon dioxide.

As the water molecule is non-linear, it has $3N-6 = 3$ modes of vibration as illustrated in **Figure 2.16**. Carbon dioxide is a linear molecule, so it has $3N-5 = 4$ modes of vibration, three of which are shown in the above figure. The fourth one is another bending mode and is perpendicular to the plane of the paper. However, it has the same energy as the bending mode in the plane of the paper. Hence, such a pair is termed degenerate.²⁶

In more complex molecules, various types of vibrational modes will exist and are usually difficult to assign to a peak in a spectrum. When the vibrational spectra of similar molecules are compared, such as a homologous series of organic compounds, it is found that similar functional groups often come up with similar bands among all the compounds in the series. Therefore, the frequencies of these bands are referred to as *group frequencies*, which can be used to help identify an unknown sample. The vibrational modes of two ubiquitous groups in organic chemistry are graphically illustrated in **Figure 2.17**.

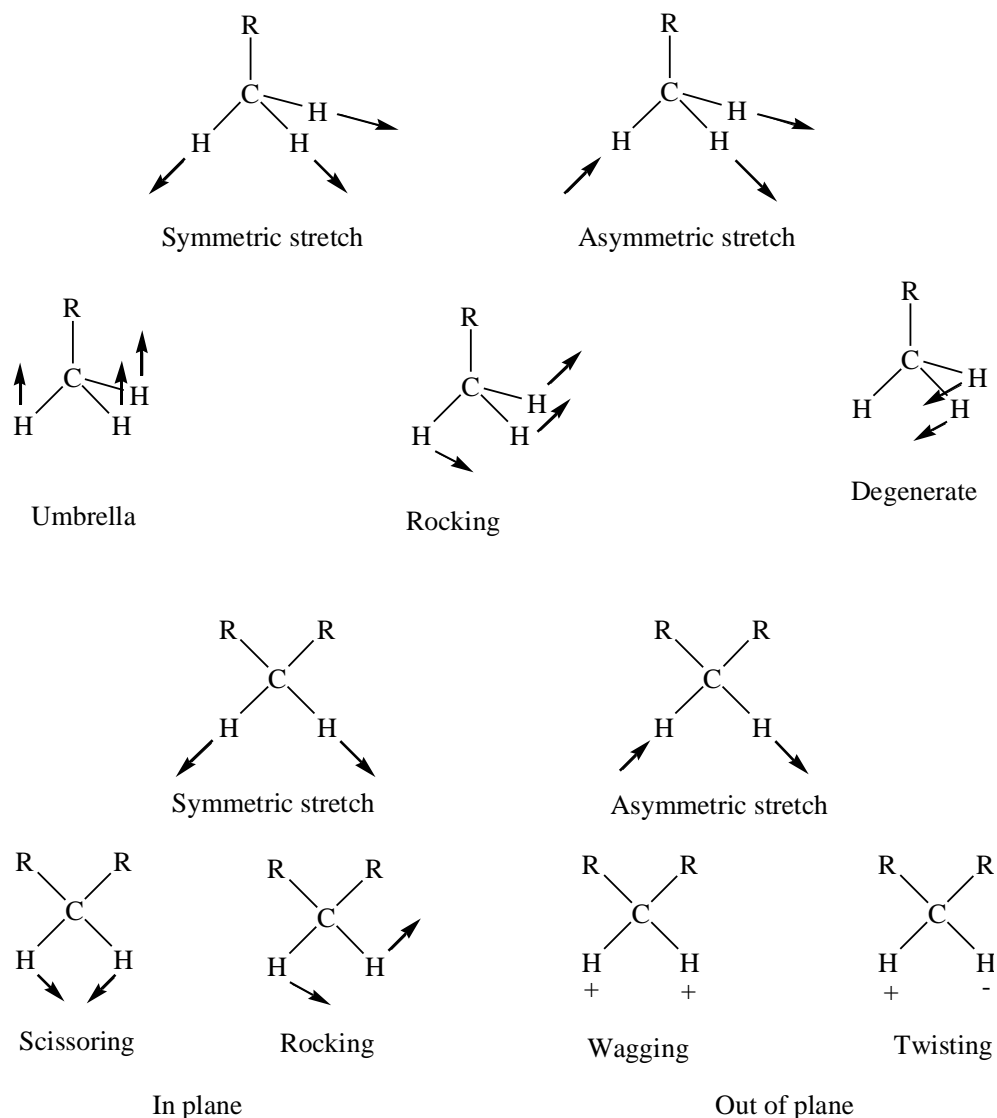


Figure 2.17 Vibrational modes of CH_3 and CH_2 groups (+ and – denote vibrations going upward and downward in direction perpendicular to the paper plane).

In this thesis, symmetric stretching modes will be given the symbol ν_s , anti-symmetric stretching modes ν_a , rocking modes δ_r , umbrella modes δ_u , degenerate bending modes δ_d , scissoring modes δ_s , wagging modes δ_w and twisting modes δ_t .

Usually in frequency correlation tables, a frequency range will be quoted for the frequency of group vibrations. The exact position of the observed peak will be determined by the molecule that the group belongs to and the position of the group in the molecule according to:

1. Vibrational coupling; a fundamental vibrational mode may be described as a mixture of group vibrations coupled together to vibrate at the same frequency.²⁷ This will happen when the respective groups are reasonably close to each other in a molecule and have similar bond force constants. The peak in the spectrum is usually assigned to the most dominant group vibration. Take the $\delta(\text{C-H})$ vibrations of methylene groups in the n-paraffin series as an example of coupling.²⁸ The $\delta(\text{C-H})$ vibration is coupled to the skeletal vibration, whose frequency varies when the carbon chain increases. Therefore, the peak in the spectrum shifts according to the frequency of the fundamental mode.
2. Orbital hybridisation; a process in which the atomic orbitals mix when atoms interact to form a chemical bond. The angle between the bonds are determined by the repulsive forces between orbitals hybridised around a central atom.²⁹ For example, the H-O-H bond angle on water is 104.45° . The bond angles may also change according to the relative repulsive forces of the adjacent atom or group. The stronger repulsion the atoms/groups have, the smaller the bond angle will become, and *vice versa*. The larger the bond angle between sp^3 hybridised orbitals, the higher the percentage of *s* character, which therefore results in a larger force constant and a higher vibrational frequency.³⁰
3. The electronegativity, which describes the tendency of an atom or a functional group to attract electrons toward itself, of the adjacent substituent can also have an effect on the vibrational frequency by withdrawing/donating electrons from/into a specific bond. Generally, electron withdrawal may cause a down-shift (red frequency shift) and electron donation may cause an up-shift (blue frequency shift) to the vibrational frequency of the adjacent bond. The Hammett parameters (σ) are used to specify the degree to which the substituent does this. A substituent with a positive Hammett value will withdraw electrons and *vice versa*. In particular, the electronegativity can have noticeable effects on chemical bonds of functional groups in the α -position to the electronegative/positive group. For example, the $\nu(\text{C=O})$ of a carbonyl in an ester will withdraw electrons from the carbon of the carbonyl group since oxygen is more electronegative than carbon. In this case, a higher vibrational frequency

absorption results as a shortening of the π -bond in the carbonyl group leading to an increase in the force constant.²¹

For further analysis of the vibrational frequency, substituting an atom for its heavier isotope can help. From **equation 2.26**, it can be seen that the fundamental vibrational frequency is inversely proportional to the reduced mass across the bond. Therefore an increase in the reduced mass will lower the frequency of vibration. For polyatomic molecules, two or more fundamental vibrations of different symmetry may vibrate at a similar frequency. From the spectroscopic point of view, these vibrational modes only result in one peak. So they are degenerate, due to their ‘accidental’ differing symmetry.³¹ However, the vibrational coupling for accidental degenerate modes may be disrupted by isotopic substitution which leads to frequency shifts to multiple bands.³² Furthermore, in the case of H/D exchange in heavy water, intra-/inter-molecular hydrogen bonds can also be affected as previously reported.³³ In general, OD \cdots X type bonds are considered to be stronger than OH \cdots X.³⁴ This will further perturb the vibrational frequency of groups both directly bonded to the H/D and those coupled to the H/D bonded group.

2.4.2 The Absorption Process

In order to facilitate a molecule to absorb EM radiation, the energy of the radiation $h\nu$ should be equal to the energy difference ΔE between the ground and excited state. This is known as Bohr’s frequency condition based on Einstein’s equation (equation 2.21). Only under this condition, a photon is released or absorbed in the process. In vibrational spectroscopy, a peak in the spectrum indicates a fundamental vibrational mode whose energy equals the energy transition between the ground state ($v = 0$) and the first excited state ($v = 1$). The Boltzmann distribution predicts that most molecules exist in the ground vibration state $v = 0$ at room temperature:

$$\frac{N_n}{N_m} = \frac{g_n}{g_m} \exp \left[\frac{-(E_n - E_m)}{kT} \right] \quad (\text{Eq 2.27})$$

where N_n is the number of molecules at the excited vibrational state, N_m is the number of molecules at ground state, g is the degeneracies of both states, E is the energy of both states, k is the Boltzmann constant and T is the absolute temperature in Kelvin. Therefore the majority of transitions will be from ground state, $v = 0$. With the harmonic approximation, an energy

transition can only occur between adjacent states ($\Delta v = \pm 1$), so the fundamental transition will be dominant. In the anharmonic approximation, Δv can be $\pm 1, 2, 3, \dots$, which gives rise to the first, second, third... overtone peaks. But these transitions are much less probable, hence giving us peaks with weak intensities. At elevated temperatures, more molecules will exist at the first excited state so the transition from state 1 to state 2 will occur more frequently. Again, according to the anharmonic approximation, it results in a peak at a frequency lower than the fundamental peak since $\Delta E_{v=0}^{v=1}$ is greater than $\Delta E_{v=1}^{v=2}$.²²

In order to absorb IR radiation and cause vibrations in a covalently bonded, the molecule also has to possess a changing dipole moment, μ during the vibration. A dipole moment is a vector because it has X, Y and Z components. It is defined as the magnitude of the charge (δ) multiplied by the distance between them (l). It is measured in coulomb-metres often quoted in Debyes ($1 \text{ D} = 3.34 \times 10^{-30} \text{ Cm}$).

$$\mu = \delta l \quad (\text{Eq 2.28})$$

In order to allow a transition between states, the transition dipole moment M_{01} should be non-zero:

$$M_{01} = \int_{-\infty}^{\infty} \psi_1 \mu_x \psi_0 dx \quad (\text{Eq 2.29})$$

where ψ_1 and ψ_0 are the wave functions of the excited and ground energy states respectively, μ_x is the dipole moment (a vector) in the x direction (y and z are also evaluated) at any point during the vibration and dx is the change in the vector length. The integral for M_{01} is taken from $-\infty$ to $+\infty$ over all space. During a vibration, dx is non-zero. So for M_{01} to be non-zero and absorption to take place, μ_x must also be non-zero.³⁵

$$\mu_x = \mu_0 + \left(\frac{d\mu_x}{dx} \right) x \quad (\text{Eq 2.30})$$

μ_0 is the dipole moment of the molecule at equilibrium vector length, which is not dependent on x . So by combining equation 2.29 with 2.30, the following equation is obtained after arrangement:

$$M_{01} = \mu_0 \int_{-\infty}^{\infty} \psi_1 \psi_0 dx + \left(\frac{d\mu_x}{dx} \right) \int_{-\infty}^{\infty} \psi_1 x \psi_0 dx \quad (\text{Eq 2.31})$$

ψ_1 and ψ_0 are orthogonal to each other, therefore the integration of their product is zero and the first term vanishes. The integrand of the second term is non-zero and $\Delta v = \pm 1$ for a harmonic vibration (forbidding overtone transitions). Hence, M_{01} is non-zero when $\left(\frac{d\mu_x}{dx} \right)$ is non-zero. In summary, a vibration is IR-active if the dipole moment is changed in either x , y or z direction during the vibration.²²

The intensity of a peak in an absorption spectrum is defined by the absorbance (A), which is inversely proportional to the percentage of light transmitted through the sample and is related to the concentration of the absorbing species (\bar{c}) in molarity using the Beer-Lambert law:

$$A = \epsilon b \bar{c} \quad (\text{Eq 2.32})$$

where b is the path length in centimetres through which the radiation travels and ϵ is the molecular absorption coefficient. ϵ measures how strongly a chemical species absorbs light. Its value indicates the probability of a vibrational transition to occur. When both Bohr's frequency condition and the selections rules for IR absorption are satisfied,²⁴ a high probability occurs, hence the value of A is large.

2.4.3 Light Scattering

As previously discussed, in order to make absorption occur, the frequency of the oscillating dipole moment of the molecule must be in resonance with the frequency of the incident light. Even if the frequency is not the same, the EM field of the incident light can still interact with the electron cloud surrounding the molecule to cause polarisation. The electron cloud will distort in shape and an electric dipole moment P is induced:²²

$$P = E\alpha = E_0 \alpha \cos 2\pi\nu_0 t. \quad (\text{Eq 2.33})$$

Here, α is a proportionality constant called *polarisability*. The magnitude of the induced dipole moment is dependent on the electric field E and the polarisability α . By utilising equation 2.20,

the electric field strength can be modified and the right hand side of equation 2.33 is given. The induced dipole will oscillate at the same frequency as the incident light and form a short-lived complex known as a *virtual state*. The excited virtual state will relax and eventually return back to the original electronic state by emitting photons of light in random directions, known as *scattering* (**Figure 2. 18**). Similar to fluorescence, scattering is a process involving two photons, one of which interacts before the other is emitted. However, unlike the process of fluorescence, scattering does not meet Bohr's frequency condition, so no absorption will take place. The scattering process is faster at 10^{-12} seconds compared to 10^{-8} seconds for fluorescence.³⁶

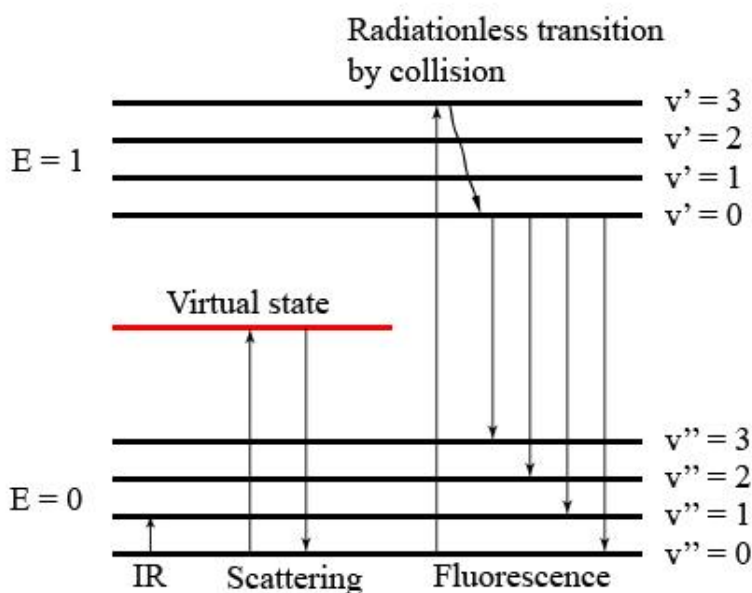


Figure 2.18 Absorption and emission processes for Infra-Red, scattering and fluorescence mechanisms. E=0: electronic ground state, E=1: first electronic excited state, v'': vibrational states at electronic ground state, v': vibrational states at first electronic excited state.

The energy changes detected in vibrational spectroscopy are those that cause nuclear motion. The majority of scattering usually occurs in a time too short for the nuclei in the bond to adjust to the energy of the virtual state. So there is no effect on the scattered photons, and their energy is close to the frequency of the incident light. Hence, this type of scattering is termed elastic or *Rayleigh scattering*. If only the electron cloud is distorted in scattering, the scattered photons will exhibit very small frequency changes. The energy of the virtual state can be described as the degree of distortion imposed on the electron cloud. In a scattering event, the greater the

distortion, the higher the energy of the virtual state and the more likely the excess energy will be used.²⁵ The Rayleigh scattering intensity is inversely proportional to the fourth power of the wavelength of the incident light.³⁷ This means that the shorter the wavelength of light, the stronger it will be scattered.

2.4.4 Raman Spectroscopy

As previously discussed, by classifying different energies arising from the scattered light, various types of spectroscopic techniques are invented, which make it very common in spectroscopy (with examples even in the X-ray region³⁸). For vibrational transitions, Raman spectroscopy is the dominant scattering mechanism and was first discovered by Sir Chandrasekhara Venkata Raman in 1928 who won the Nobel Prize later in 1930 because of this.

Different from the elastic Rayleigh process in which the scattered photons from an atom or molecule have the same kinetic energy as the incident photons, Raman spectroscopy involves a type of inelastic scattering by an excitation. In Raman scattering the nuclei in the molecule interact with the complex of the distorted electron cloud and EM wave in the virtual state. Hence, a quantity of the energy is transferred between the virtual electronic state and the vibrational state. The scattered photon is either augmented (anti-Stokes shift) or diminished (Stokes shift) in energy by the quantum of the vibrational state (**Figure 2.19**). At room temperature, most of molecules are usually in the lowest energy state (ground state), while in some circumstances, only a few molecules will be in higher energy states (excited states). Using the Boltzmann distribution, the fraction of molecules occupying a certain vibrational state can be calculated at different temperatures. Therefore, for relatively low temperatures used for spectroscopy in this thesis, most energy transfer will be from the incident radiation to the molecule giving rise to Stokes shifted Raman scattering.

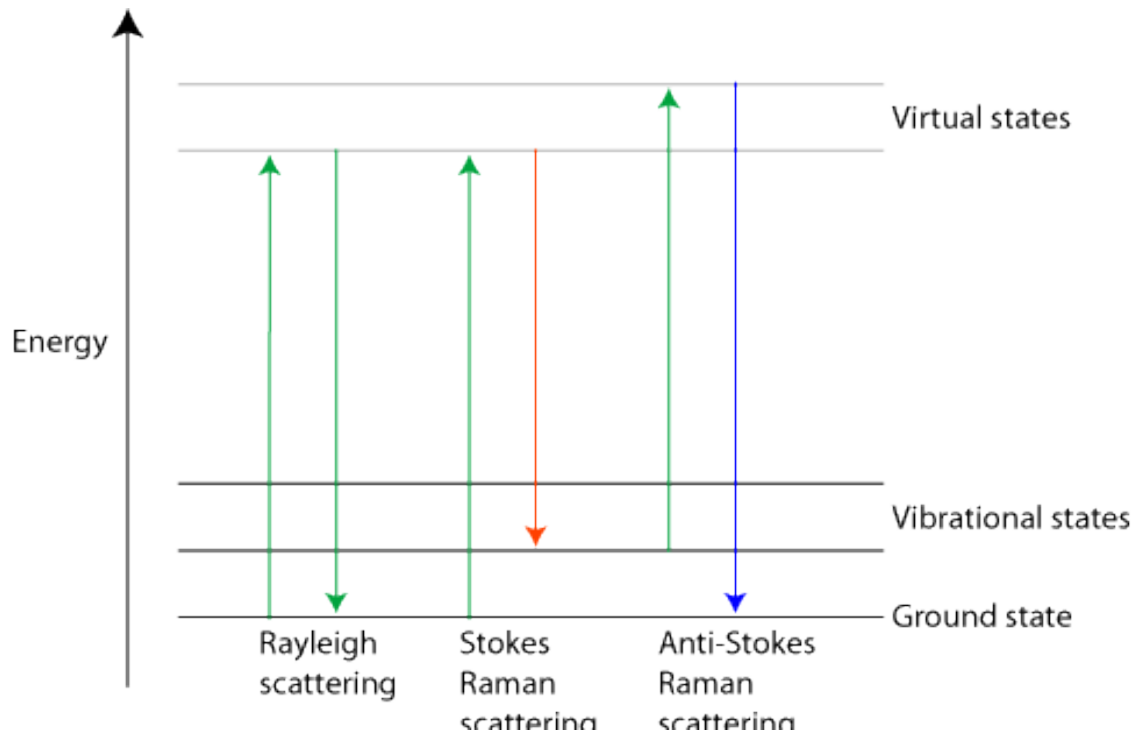


Figure 2.19 Energy states in the scattering process.

As described in section 2.4.3, a dipole P is induced on the molecule by interaction with EM radiation and is proportional to the magnitude of the electric field E and the polarisability of the molecule, α . For small amplitude vibrations, α is a linear function of the nuclear displacement q :

$$\alpha = \alpha_0 + \left(\frac{\delta\alpha}{\delta q}\right)_0 q \quad (\text{Eq 2.34})$$

where α_0 is the polarisability at the equilibrium position, $\left(\frac{\delta\alpha}{\delta q}\right)_0$ is the change of polarisability with respect to the nuclei move and q_0 is the vibrational amplitude at the equilibrium position. If the molecule is vibrating with a frequency ν_m , the nuclear displacement is found:

$$q = q_0 \cos 2\pi\nu_m t \quad (\text{Eq 2.35})$$

By combining equations 2.33 to 2.34 and 2.35 a complete derivation of the induced dipole moment is obtained:

$$P = E_0 \alpha_0 \cos 2\pi \nu_0 t + \frac{1}{2} \left(\frac{\delta \alpha}{\delta q} \right)_0 q_0 E_0 [\cos \{2\pi(\nu_0 + \nu_m)t\} + \cos \{2\pi(\nu_0 - \nu_m)t\}] \quad (\text{Eq 2.36})$$

The first term of this equation corresponds to an oscillating dipole and causes Rayleigh scattering of frequency ν_0 according to classical theory. While the second term represents Raman scattering of frequency $\nu_0 + \nu_m$ as anti-Stokes and $\nu_0 - \nu_m$ as Stokes scattering from incident light.²² Namely, if the vibrational mode is Raman active, the term $\left(\frac{\delta \alpha}{\delta q} \right)_0$ should not be zero. Hence, the selection rule for Raman spectroscopy is that the rate of molecular polarisability during the vibration must change for absorption to occur.

To further discuss Raman activity, the nature of the polarisability needs to be considered. If a molecule is placed in an electric field where it suffers distortion, the nuclei are attracted to the negative pole and electrons towards the positive pole. As the electron cloud around the molecule is distorted in all directions by light polarised in any plane, the induced dipole needs to be described for all three Cartesian coordinates. The induced dipoles of the x , y and z axes are described by the polarisability of the electron cloud in the specific axis induced by light polarised in each plane:

$$P_x = \alpha_{xx} E_x + \alpha_{xy} E_y + \alpha_{xz} E_z$$

$$P_y = \alpha_{yx} E_x + \alpha_{yy} E_y + \alpha_{yz} E_z \quad (\text{Eq 2.37})$$

$$P_z = \alpha_{zx} E_x + \alpha_{zy} E_y + \alpha_{zz} E_z$$

This can be written in matrix form as such:

$$\begin{bmatrix} P_x \\ P_y \\ P_z \end{bmatrix} = \begin{bmatrix} \alpha_{xx} & \alpha_{xy} & \alpha_{xz} \\ \alpha_{yx} & \alpha_{yy} & \alpha_{yz} \\ \alpha_{zx} & \alpha_{zy} & \alpha_{zz} \end{bmatrix} \begin{bmatrix} E_x \\ E_y \\ E_z \end{bmatrix} \quad (\text{Eq 2.38})$$

The 3×3 matrix of polarisability values on the right-hand side is known as the *polarisability tensor*. It represents the polarisability of the molecule in all three coordinates during a vibrational

mode. Therefore, the term $\left(\frac{\delta\alpha}{\delta q}\right)_0$ will be non-zero if one of the values in the tensor changes during the vibration.³⁷ Each value can be assessed in the same integration procedure seen with equations 2.29-2.30.

A change in polarisability can be depicted by a *polarisability ellipsoid* which is a three dimensional surface that represents the electron cloud surrounding the molecule. The size, shape and orientation of the ellipsoid are determined by plotting $1/\sqrt{a_i}$ (in the i -direction) rather than a_i itself. For a mode to be Raman active the shape, size or orientation should change during the normal vibration at the extremes (+q, -q).²² **Figure 2.20** shows the polarisability ellipsoids to describe three vibrational modes of CO₂. The symmetric stretch (ν_1) shows the size of the ellipsoid is changing and it is different at +q from that at -q. Thus, the mode is Raman active. Note that $\left(\frac{\delta\alpha}{\delta q}\right)_0$ (slope near the equilibrium position) determines the Raman activity. For both the anti-symmetric stretch (ν_3) and bending mode (ν_2) the ellipsoids at the extremes are exactly the same regarding their size and shape, so they are Raman inactive.

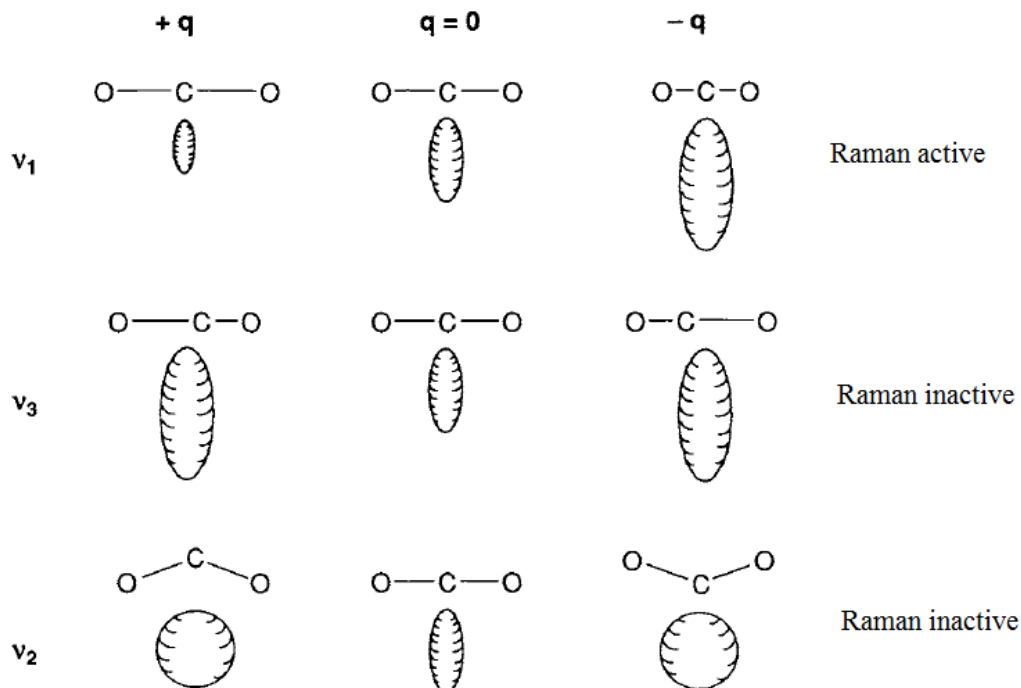


Figure 2.20 Polarisability ellipsoids showing the change in polarisability during a vibration. Reprinted from reference 23.

For larger molecules, the number and symmetry of vibrational modes may be determined using group theory. Which of them are Raman or IR active may also be determined in this way. Briefly, the molecule is classified by the symmetry elements that it possesses (such as identity (E), rotation axes (C_n), planes of symmetry (σ), centre of symmetry (i), and rotation reflection axes (S_n)) and the number of operations that can be performed on each element (i.e. $2\sigma_h$ which means two horizontal reflection planes). If some molecules can undergo the same type and number of symmetry operations, then all of them can be assigned to a class, known as a *point group*. Then by using a basis set, the atomic displacements in a fundamental vibration can be illustrated. In an example of a C-H bond stretch represented by a vector pointing along the bond in the direction of the atomic displacement, the vectors for all C-H stretches are known as the basis set. The character of how the basis set transforms under each of the symmetry operations in the point group has the function of evaluating the fundamental vibration. The symmetry of the vibration will finally be decided corresponding to one of the irreducible representations in the character table of the point group.²²

The character table, which contains the character matrix in equation 2.37, provides information about IR and Raman activities of normal vibrations. The linear functions column (next to the character matrix) in the character table lists the species of translational (or rotational) motions along (or around) the Cartesian axis. The x, y or z indicates that a change in the dipole moment with the fundamental vibration, which suggests the mode is IR-active. Likewise, the quadratic function (x^2 , y^2 , z^2 , xy , xz , yz , $x^2 - y^2$ or $x^2 + y^2$) in the column to the right of the linear functions indicates a change in polarisability. Therefore, the vibration is Raman-active. In this thesis, all the molecules under study possess very low symmetry with the highest symmetry molecules belonging to the C_s point group. Hence, the fundamental vibrations can only be described as being in the molecular plane (A') or out-of-plane (A'') by group theory, both of which are IR- and Raman-active. For molecules with no symmetry, group theory is not suitable for describing the symmetry of the vibrations. Readers are recommended to consult reference 37 for further elaboration.

Cross section (σ) is a hypothetical area which is used to describe the probability of a molecule to undergo Raman scattering. In order to measure the cross section, or the intensity of Raman scattering, from a certain number of molecules illuminated by an incident monochromatic beam,

the wavelength, volume and power of the beam must be known. Since scattering is assumed to occur homogeneously in all directions, it would form a spheroid if the photons travel a certain distance from the source. To quantify this, first the scattered photons are generally collected only through a specified area of the sphere. Then the size of the collecting area and its distance from the source is used to determine the solid angle (Ω) in steradians (sr). It is used to quantify two-dimensional angular spans in three-dimensional space, so is proportional to the total area of the sphere (**Figure 2.21**). Therefore, the integrated cross section $\int \frac{d\sigma_c}{d\Omega}$ of a molecular vibration is generally used for making comparisons in units of $\text{cm}^2 \text{ molecule}^{-1} \text{ sr}^{-1}$.³⁹

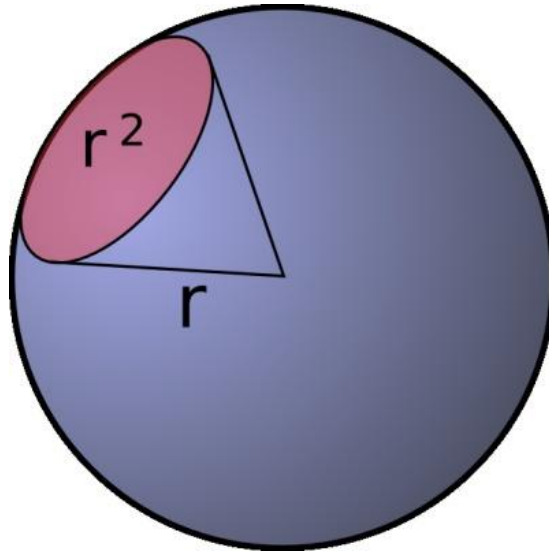


Figure 2.21 Graphic representation of 1steradian subtended at distance r from the centre of the sphere.

Knowing the differential crosssection of the vibrational mode, the intensity of the Raman scattering (I_R) in photons s^{-1} may be calculated with the following equation:

$$I_R = \left(\frac{d\sigma}{d\Omega} \right) \Omega \left(\frac{I_L}{A} \right) \rho ALK_e = \left(\frac{d\sigma}{d\Omega} \right) \Omega I_L \rho LK_e \quad (\text{Eq 2.39})$$

where I_L is the intensity of the incident laser beam (photons s^{-1}), A is the cross sectional area of the laser beam (cm^2), ρ is the molecular density (molecules cm^{-3}), L is the path length of the laser (cm) and K_e is a constant which depends on instrumental factors such as the transmission of the optics and the quantum efficiency of the detector. The Boltzmann distribution can then be

adapted for the relative intensity of anti-Stokes (I_{aS}) and Stokes (I_S) shifted scattering of the Raman shifted frequency (ν_R) of the vibrational mode.⁴⁰

$$\frac{I_{aS}}{I_S} = \frac{g_{aS}}{g_S} \exp \left[\frac{-\nu_R}{kT/hc} \right] \quad (\text{Eq 2.40})$$

where g_{aS} and g_S are the degeneracy for anti-Stokes and Stokes, respectively.

2.4.5 Surface Enhanced Raman Spectroscopy

In 1974, Fleischmann and co-workers produced unusually high Raman scattering from pyridine adsorbed on a electrochemically roughened silver electrode.⁴¹ This was first assigned to the high surface area of the electrode enabling a large number of pyridine molecules to adsorb, but did not recognize the major enhancement effect. Only later in 1977, it was found independently by Jeanmarie and Van Duyne⁴² and Albrecht and Creighton⁴³ to be more than just the factors of surface area and the concentration of scattering species. The observed increase in intensity was about 10^6 times, which was far beyond the expectation in Fleischmann's work where the increase in surface area was accounted. Since then, the effect of increased intensity from molecules on other metal surfaces has been found on lithium, sodium and potassium.^{44, 45} Especially, the coinage metals namely silver, copper and gold gave rise to the strongest and most reliable activity.⁴⁶ This type of spectroscopy is known as Surface Enhanced Raman Spectroscopy (SERS) and is capable of detecting femtomole levels of adsorbate.²² Because of its high sensitivity, this technique is a useful probe for the studies of *in situ* gas-solid, liquid-solid and solid-solid interfaces. Hence, it is a helpful tool for the surface science and heterogeneous catalysis.

The exact mechanism of the SERS effect is still under debate with two theories proposed to explain it. Whilst both have their merits, neither can explain the full range of reported phenomena. Also, they are different substantially but cannot be distinguished experimentally. Empirically, SERS activity is achieved from rough metal surfaces and this physical nature is satisfied in the electromagnetic theory (EM). However, it does not fully explain the magnitude of the enhancement observed in many systems. The chemical theory proposes the formation of charge-transfer complexes, which only applies for species which have formed a chemical bond with the surface. Hence, it cannot explain the enhancement of the observed signal in all cases.

2.4.5.1 The electromagnetic enhancement theory for SERS

The conduction band electrons in a metal are able to move laterally across the surface of the metal. When they are irradiated with an EM field, the electrons will oscillate as a group known as a *plasmon*, which is the collective excitation of the electron gas. If the excitation is confined to near surface, it is called a surface plasmon, which interacts strongly with light. Surface roughness of a metal is required, so that the plasmon can be excited by light and resonates with the incident field, which causes an enhancement of the electric field on the metal surface. As is shown in **Figure 2.22**, the nanostructures on the surface can also put the oscillation in a direction normal to the surface plane, resulting in strengthening the EM field in localised areas of the surface. The interaction between the electrons in a molecule and the plasmon electrons will then increase the Raman cross-section of the adsorbate.²⁵

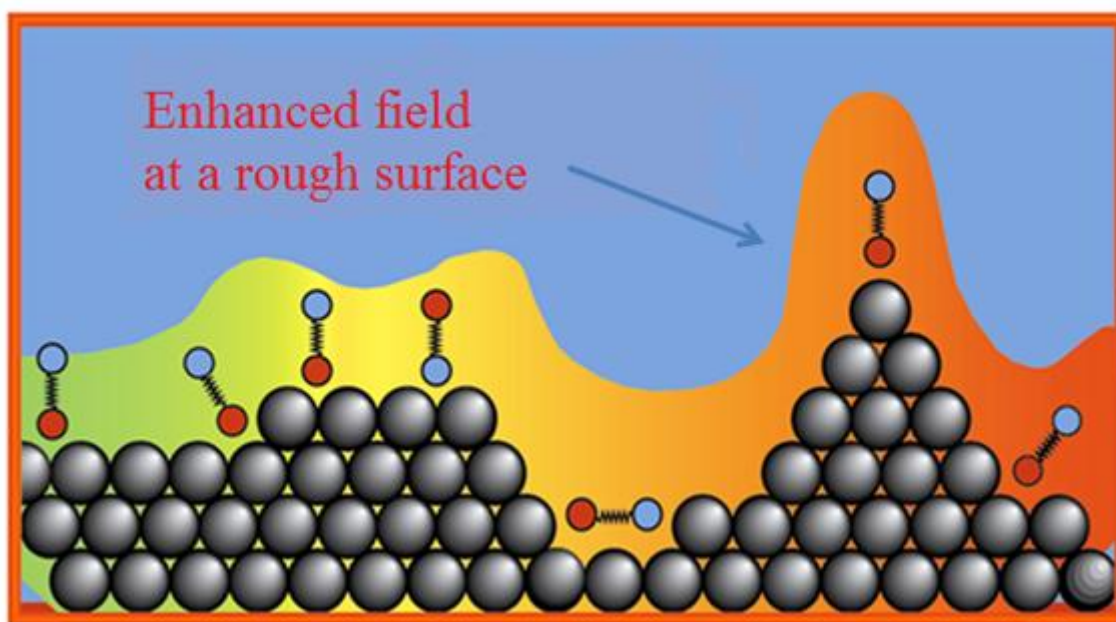


Figure 2.22 EM theory for SERS enhancement. The height of the shaded area above the surface metal atoms indicates a greater EM enhancement.

On a flat surface, the plasmon will propagate along the surface. However, for the electric field on a roughened surface, the nanostructure is simply considered to be a sphere. Different from the former situation, because the size of the sphere is much smaller than the wavelength of the incident light, the plasmon will not propagate along the surface, but will polarise around the

sphere as described by the Rayleigh approximation.⁴⁰ The field of the plasmon will be localised near the sphere, as the induced electric dipole oscillates at the same frequency as the incident light. Contrarily, the field of the plasmon will propagate along a plane parallel to the flat surface in a delocalised fashion, causing the energy to be dissipated as heat.⁴⁷

To describe the electric field E_r at a distance r from the spheroid surface of radius a , the following equation is used:⁴⁰

$$E_r = E_0 \cos\theta + g \left(\frac{a^3}{r^3} \right) E_0 \cos\theta \quad (\text{Eq 2.41})$$

where E_0 is the incident field, θ is the angle relative to the direction of the incident field and g is a constant related to the dielectric constants of the metal and surrounding medium at a frequency of the incident radiation:

$$g = [\varepsilon_1(\omega_L) - \varepsilon_0] / [\varepsilon_1(\omega_L) + 2\varepsilon_0] \quad (\text{Eq 2.42})$$

The dielectric constant of the surrounding medium, ε_0 , is assumed to be close to unity in the range of frequencies used in Raman spectroscopy. The magnitude of the electric field is proportional to g and at some point it will be at a maximum. When the dielectric constant of the metal, $\varepsilon_1 = -2\varepsilon_0$, the denominator will be 0 for equation 2.42, and an infinite value of g is obtained. At this frequency, the excitation of the surface plasmon will massively increase the local field around the molecule absorbed on the metal surface. The electron can move freely in the cloud and intensify the polarisation around the molecule. ε_1 is dependent on the incident frequency of light (ω_L), therefore a maximum value of g can be achieved by tuning ω_L to meet the resonance condition.

As previously mentioned the SERS phenomenon is limited to the coinage metals (copper, silver and gold) and alkali metals, among which the former provide the best activity. This is simply because a large value for g can be attained with these metals and the resonance condition is satisfied in the frequency range normally used for Raman spectroscopy.⁴⁸ Theoretically, as long as the metal plasmon resonance condition is met, it is possible to generate surface scattering at

different frequencies in the EM spectrum. However, with the probability of scattering decreasing with the fourth power of frequency, the sensitivity will also decline at lower incident frequencies.

This simple sphere model requires some adjustment as the nanostructures on a roughened surface are not exactly spherical. Also, it is found that the junction between two or more nanoparticles may generate extremely active SERS signal. The essence of the EM theory is that in the enhanced electric field the analyte does not need to be directly attached to the metal surface. As long as it is within the field, the molecule can sense the resonance, making the SERS effect active. This allows molecules adsorbed in multilayers to be SERS enhanced, with the greatest enhancement observed for them adsorbed directly on the surface. However, the enhancement drops off rapidly with distance from the surface as the field is proportional to $1/r^3$.

2.4.5.2 Surface selection rules

It is not straightforward to interpret SERS spectra, as some peaks which cannot be found in normal Raman scattering may appear in SERS, and other peaks which are originally strong in Raman scattering may become weaker or even disappear. In the first case, a molecule usually has a centre of symmetry. When the molecule is adsorbed onto a metal surface, particularly for chemisorbed complexes,⁴⁹ its symmetry may be broken by the adjacent surface metal atoms. This results in changing the symmetry of a molecular vibration and its Raman-active status. Therefore, new peaks can emerge.

Actually, the situation is more complex as some types of bands are more intense in SERS than in normal Raman scattering. When the molecule interacts with the metal surface, it creates an image charge of the molecular dipole in the sub-surface of the metal.⁴⁰ Then when light interacts with the molecule, two electric dipole components parallel and perpendicular to the surface will be generated. If the dipole moment of a molecule and its image are parallel, then the molecular dipole moment is screened by the image. This results in no net polarisability change in the dipole moment. Consequently, there is no contribution to the scattering of the incident light. On the contrary, when the molecular dipole moment is perpendicular to its image, it is augmented by the image and contributes to intense absorption. Therefore, not only can the number and position of active modes change, but the relative intensities may also change according to the degree of image screening.⁵⁰ For surface Infra-Red spectroscopies, most transition metals are highly

reflective for the frequency range studied, so the image screening effect is prevalent. For surface Raman techniques, the induced dipole moments may also be augmented by the sub-surface image charges. However, the frequency range used is generally less efficiently reflected by the transition metals, so the image charge can hardly screen parallel modes. Due to the difference in surface morphology of SERS active species, the result is more relaxed by following the surface selection rules but not necessarily adhering to it.⁵⁰

2.4.5.3 The charge transfer theory for SERS

Charge transfer theory is another theory for SERS, which is more focused on the interaction between the metal and the analyte/adsorbate. It involves a chemical bond forming between the analyte and the metal surface atoms. This makes it possible to enable charge to transfer between discrete energy states in the molecule and occupied or unoccupied states in the metal (**Figure 2.23**). The formation of this surface species causes the change of the molecular polarisability. Due to interaction with the metal electrons, the enhancement is believed to occur via new electronic states which are from the formation of the bond. Therefore, as resonant intermediates, they affect the Raman scattering.²⁵

The charge transfer process can be stimulated by the incident light if it is in resonance with the energy gap of the transition. For the metal to molecule transition process shown in dotted arrow in **Figure 2.23**, it is briefly described by the following steps. First, an electron from the conduction band of the metal is excited by absorption of an incident light to an unoccupied state above the Fermi level, leaving a hole behind. Then via the adsorbate-substrate complex, this electron jumps to an excited electronic state of the molecule. It immediately returns to fill the hole in the metal conduction band, leaving the molecule in an excited vibrational state trying to return to the electronic ground state. This is the process where the radiation of a Raman shifted photon occurs.

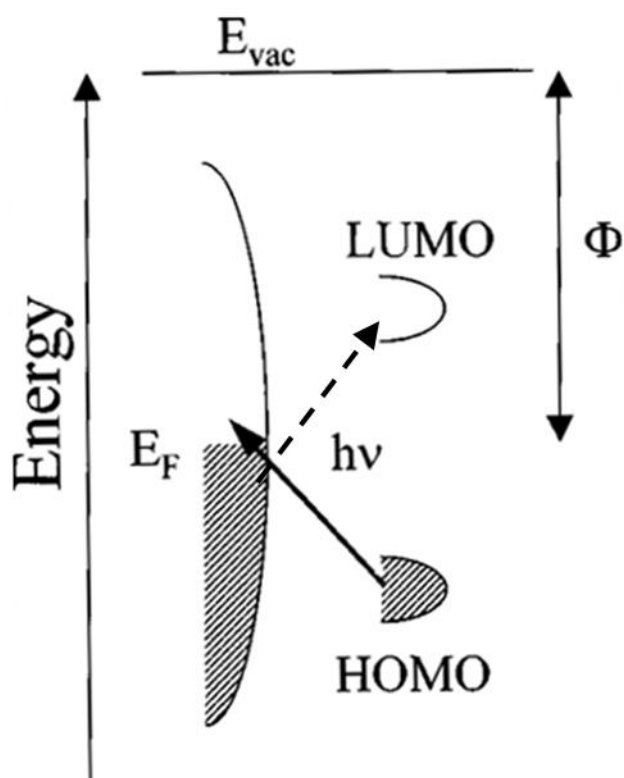


Figure 2.23 Energy levels of the metal states (left) and HOMO and LUMO of the molecule (right), E_F , E_{vac} and Φ are the Fermi energy, vacuum energy and work function of the metal. The solid arrow represents a molecule to metal charge transfer and the dotted arrow represents a metal to molecule transfer.⁵¹

For molecule to metal transfer process (**Figure 2.23**, solid arrow), it is similar to the above, except the electron excited by absorption of a photon is from the ground electronic state of the molecule. It then crosses to the unoccupied conduction band of the metal before returning to the original state. However, the molecule now is in a vibrationally excited state because of this excited electron. Once the molecule relaxes back to the ground state, a Raman shifted photon is scattered.

2.4.5.4 Applications

SERS is easy but not the simplest technique to master in many applications. One can easily attain SERS activity on the coinage metals by mechanical or chemical abrasion of the surface. However, the difficulties may appear when one tries to establish uniform activity across the

whole surface. Also, for surfaces that are non-uniform, it is unavoidable to come across some sites of extremely high intensity known as ‘hotspots’, which may misrepresent the enhancement factor of the surface.

Due to some metals of interest lacking any SERS activity (but still possessing exceptional catalytic abilities, e.g. Pt), the surface vibration information of these metals in contact with adsorbates is still important. In this kind of situation, a thin film of the non-active metal (like Pt) can be deposited on the surface of a SERS active substrate (like gold). Since the activity extends through the metal film, SERS may be obtained from the adsorbate so long as the film is thin enough (< 2 nm).⁵² One thing needs to be noted, which is in order to avoid the contributions from the target analyte adsorbed on the active substrate, the nanofilm should cover the metal completely. Pinholes may be generated for sites exposing the substrate if it is not fully covered. Islands may also form due to the variation of the geometrical growth of the film, which depends on the film material and the substrate. Special techniques for achieving pinhole-free surfaces are necessary and will be introduced in Chapter Three.

Recent developments utilise a gold STM tip in conjunction with a Raman spectrometer in a so-called Tip Enhanced Raman Scattering (TERS) configuration.⁵³ By combining the sharp gold tip and the laser light, the electric field around a single molecule adsorbed on a well-defined surface of any material can be enhanced.^{54,55} The sensitivity and information it can provide makes TERS potentially a very powerful surface analytical technique.

2.5 References

1. K. K. Kolasinski, *Surface Science: Foundations of Catalysis and Nanoscience*, Wiley, 2012.
2. G. A. Somorjai, *Principles of surface chemistry*, Prentice-Hall, 1972.
3. D. M. Kolb, *Surface Science*, 2002, **500**, 722-740.
4. D. J. Watson, PhD Thesis, Cardiff University, 2002.
5. O. A. Hazzazi, PhD Thesis, Cardiff University, 2002.
6. R. J. Taylor, PhD Thesis, Cardiff University, 2010.
7. S. P. Smale, PhD Thesis, Cardiff University, 2008.
8. J. A. Bennett, G. A. Attard, K. Deplanche, M. Casadesus, S. E. Huxter, L. E. Macaskie and J. Wood, *ACS Catalysis*, 2012, **2**, 504-511.
9. G. Attard and C. Barnes, *Surfaces*, Oxford University Press, 1998.
10. M. Ahmed, Cardiff University, 2012.
11. J. Koryta, J. Dvořák and L. Kavan, *Principles of electrochemistry*, Wiley, 1993.
12. A. C. Fisher, *Electrode Dynamics*, Oxford University Press, 1996.

13. A. Więckowski, *Interfacial Electrochemistry: Theory, Experiment, and Applications*, Marcel Dekker, 1999.
14. A. J. Bard and L. R. Faulkner, *Electrochemical Methods: Fundamentals and Applications*, Wiley, 2000.
15. J. Zhang and F. C. Anson, *Journal of Electroanalytical Chemistry*, 1992, **331**, 945-957.
16. F. G. Will and C. A. Knorr, *Zeitschrift für Elektrochemie, Berichte der Bunsengesellschaft für physikalische Chemie*, 1960, **64**, 258-269.
17. J. Clavilier, *Journal of Electroanalytical Chemistry and Interfacial Electrochemistry*, 1979, **107**, 211-216.
18. J. Clavilier, R. Durand, G. Guinet and R. Faure, *Journal of Electroanalytical Chemistry and Interfacial Electrochemistry*, 1981, **127**, 281-287.
19. J. Clavilier, R. Faure, G. Guinet and R. Durand, *Journal of Electroanalytical Chemistry and Interfacial Electrochemistry*, 1979, **107**, 205-209.
20. J. Clavilier, D. Armand, S. G. Sun and M. Petit, *Journal of Electroanalytical Chemistry and Interfacial Electrochemistry*, 1986, **205**, 267-277.
21. D. L. Pavia, *Introduction to Spectroscopy*, Brooks/Cole, 2009.
22. J. R. Ferraro, *Introductory Raman Spectroscopy*, Elsevier Science, 2003.
23. S. Walker and H. Straw, *Spectroscopy volume two ultra-violet, visible, infra-red and roman spectroscopy*, Chapman & Hall, 1962.
24. C. N. Banwell and E. M. McCash, *Fundamentals of molecular spectroscopy*, McGraw-Hill, 1995.
25. E. Smith and G. Dent, *Modern Raman Spectroscopy: A Practical Approach*, Wiley, 2005.
26. D. C. Harris, *Quantitative Chemical Analysis*, W. H. Freeman, 2010.
27. G. Socrates, *Infrared and Raman Characteristic Group Frequencies: Tables and Charts*, Wiley, 2004.
28. J. H. Schachtschneider and R. G. Snyder, *Spectrochimica Acta*, 1963, **19**, 117-168.
29. S. N. Ege, *Organic Chemistry: Structure and Reactivity*, Houghton Mifflin Company, 2004.
30. L. J. Bellamy, *The infrared spectra of complex molecules: advances in infrared group frequencies. vol. two*, Chapman and Hall, 1980.
31. P. S. Sindhu, *Fundamentals Of Molecular Spectroscopy*, New Age International, 2006.
32. J. O. Jensen, *Spectrochimica Acta Part A: Molecular and Biomolecular Spectroscopy*, 2004, **60**, 1895-1905.
33. A. K. Soper and C. J. Benmore, *Physical Review Letters*, 2008, **101**, 065502.
34. H. D. Lutz, K. Beckenkamp and H. Möller, *Journal of Molecular Structure*, 1994, **322**, 263-266.
35. D. Willock, *Molecular Symmetry*, John Wiley & Sons, 2009.
36. M. C. Tobin, *Laser Raman Spectroscopy*, R.E. Krieger Publishing Company, 1982.
37. D. A. Long, *The Raman Effect: A Unified Treatment of the Theory of Raman Scattering by Molecules*, Wiley, 2002.
38. W. Schülke, *Electron Dynamics by Inelastic X-Ray Scattering*, OUP Oxford, 2007.
39. R. L. McCreery, *Raman Spectroscopy for Chemical Analysis*, Wiley, 2005.
40. R. J. Gale, *Spectroelectrochemistry: Theory and Practice*, Plenum Press, 1988.
41. M. Fleischmann, P. J. Hendra and A. J. McQuillan, *Chemical Physics Letters*, 1974, **26**, 163-166.
42. D. L. Jeanmaire and R. P. Van Duyne, *Journal of Electroanalytical Chemistry and Interfacial Electrochemistry*, 1977, **84**, 1-20.
43. M. G. Albrecht and J. A. Creighton, *Journal of the American Chemical Society*, 1977, **99**, 5215-5217.
44. P. A. Lund, D. E. Tevault and R. R. Smardzewski, *The Journal of Physical Chemistry*, 1984, **88**, 1731-1735.

45. W. Schulze, B. Breithaupt, K. P. Charlé and U. Kloss, *Berichte der Bunsengesellschaft für physikalische Chemie*, 1984, **88**, 308-310.
46. A. Kudelski and J. Bukowska, *Vibrational Spectroscopy*, 1996, **10**, 335-339.
47. M. Moskovits, *Reviews of Modern Physics*, 1985, **57**, 783-826.
48. A. Campion and P. Kambhampati, *Chemical Society Reviews*, 1998, **27**, 241-250.
49. H. Nichols and R. M. Hexter, *The Journal of Chemical Physics*, 1981, **75**, 3126-3136.
50. M. Moskovits, *The Journal of Chemical Physics*, 1982, **77**, 4408-4416.
51. P. Kambhampati, M. C. Foster and A. Campion, *The Journal of Chemical Physics*, 1999, **110**, 551-558.
52. J.-F. Li, Z.-L. Yang, B. Ren, G.-K. Liu, P.-P. Fang, Y.-X. Jiang, D.-Y. Wu and Z.-Q. Tian, *Langmuir*, 2006, **22**, 10372-10379.
53. E. Bailo and V. Deckert, *Chemical Society Reviews*, 2008, **37**, 921-930.
54. R. M. Stöckle, Y. D. Suh, V. Deckert and R. Zenobi, *Chemical Physics Letters*, 2000, **318**, 131-136.
55. M. S. Anderson, *Applied Physics Letters*, 2000, **76**, 3130-3132.

CHAPTER THREE

Experimental

3.1 Introduction

The combination of cyclic voltammetry (CV) with *in situ* SERS presents a novel and unrivalled method of investigating surface reactions under relevant catalytic conditions. Shape-controlled nanoparticles can be examined by CV to confirm the surface population of various types of adsorption site (step, terrace, kink). The magnitude of the effect on different sites arising from these substrates can be examined by SERS.

However, there are two major drawbacks to the application of SERS. First, a lack of generality of substrate/molecule limits the study of the atomically flat single crystals that are of interest to surface science. The second limitation stems from an inability to manage hot spots, where most of the signal is generated. Tian's Au@silica shell-isolated nanoparticle-enhanced Raman spectroscopy (SHINERS) NPs overcome the limitations and expand on the SERS strategy.¹ In SHINERS, the probe/analyte molecule is located on a bulk sample of the weakly enhancing or nonenhancing material, and shell-isolated nanoparticles (SHINs) are spread on top to generate the SERS signal. The isolating shell, which is made of an inert dielectric material, keeps the core from interacting chemically or electrically with any components of the system under study. Then the weakly enhancing or nonenhancing materials can be examined by SERS without limitations.

3.2 The Spectro-electrochemical Flowcell

The spectro-electrochemical flowcell was designed to carry out *in situ* SERS spectroscopic measurements with electrochemical control of the potential. The main body of the cell was made from PTFE and can shelter three electrodes in a 12 × 30 × 1 mm channel. A 24 × 50 mm borosilicate glass spectral window (Sigma-Aldrich, cover glass) was sealed on to the channel using Viton® gaskets. In order to avoid contamination, Klingerflon® PTFE thread seal tape was used to wrap over the gaskets to prevent contact with electrolytes. Then the glass window was secured in place by hand with an aluminium top-plate and tube clamps. Finally, PTFE inlet and

outlet tubes (1.58 mm O.D. \times 0.8 mm I.D) were screwed in to the PTFE block with Supelco® HPLC fittings and then sealed with ferrules, as shown in **Figure 3.1**.

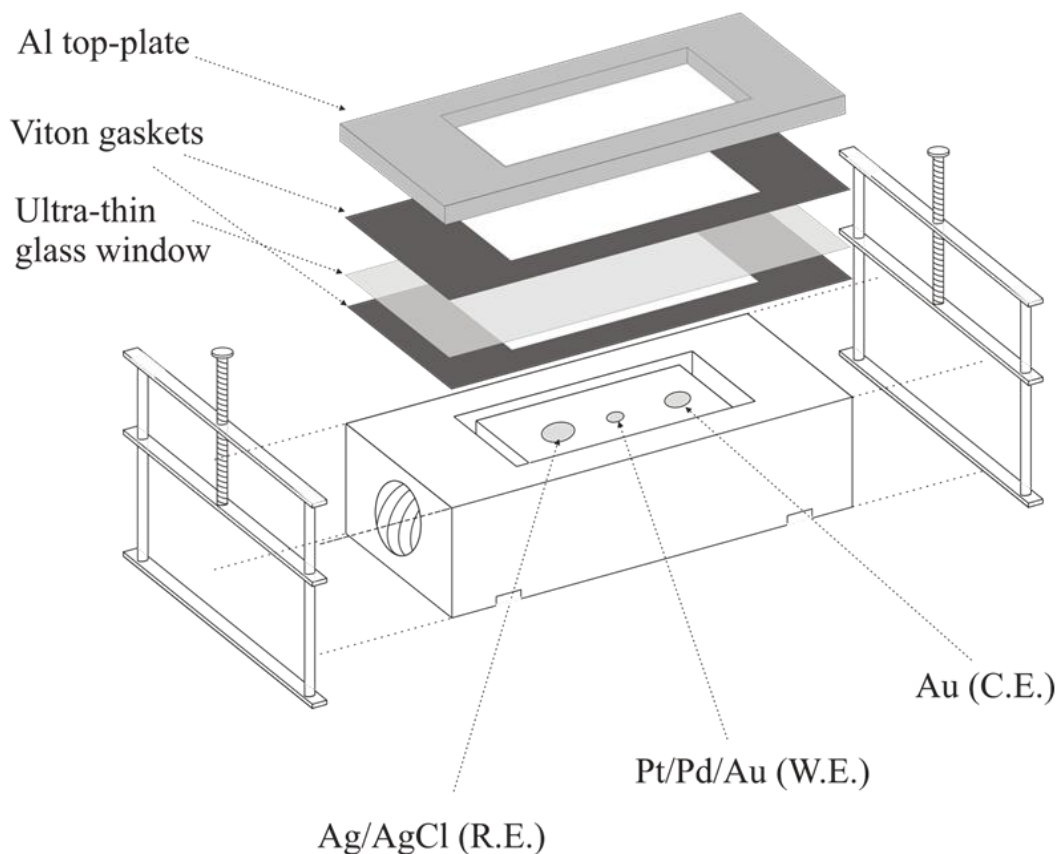


Figure 3.1 Schematic diagram of the spectro-electrochemical flowcell. Reprinted from ref. 7.

Before each experiment, all the components of the cell that would have contact with the electrolyte were cleaned thoroughly. The PTFE cell, the Viton® gaskets and the spectral window were all immersed in a solution of green acid (a dilute solution of permanganic acid, formed from mixture comprising of 98% sulphuric acid and a few grains of potassium permanganate) for up to one hour. The green acid solution could be re-used or disposed of in an appropriate waste container after dilution with 50% water by volume. All components were thoroughly rinsed, then boiled for 10 minutes and rinsed twice with ultra-pure water. With regard to the PTFE inlet and outlet tubes, one could clean them by flowing ethanol for 30 minutes followed by ultra-pure water.

The platinum polycrystalline working electrodes were flame annealed in a Bunsen burner until the colour of cherry red appeared. All contaminants could be removed as judged by the colour of the flame remaining blue. The gold counter electrode was cleaned in the same way but with a smaller flame as the temperature of a standard Bunsen flame was higher than the melting point of gold (1064 °C). When the electrode was clean, it was cooled in ultra-pure water leaving a droplet on top of the surface to help it remain clean before inserting into the cell. Layers of PTFE tape were wrapped around the electrode to ensure it was well sealed into the cell. By dripping liquid paraffin wax onto the junction between the electrode and the back of the cell also helped improve sealing. The height of the electrode could be carefully adjusted so that the electrode surface was at the same level as the channel bed. In this configuration, there was no turbulence in the stream when electrolytes flowed through the channel. A palladium electrode charged with hydrogen until a Pt-H β -hydride phase was formed was used as a potential reference electrode and was upstream of the working electrode to minimise Ohmic drop. The gold counter electrode was downstream of the working electrode in case the electrochemical products from the gold impinge on the working electrode. Electrical contact was then made to the potentiostat with the supplied crocodile clips making sure that the cables were connected correctly (red for the counter, white for the reference and green for the working electrode).

According to Etchegoin,^{2,3} due to dioxygen interactions with the metal surface, ‘rogue signals’ can often be observed in SERS, hence solutions were degassed by Argon (BOC) at the reservoir in order to minimise the ‘rogue signals’. Then, the solutions were drawn through the cell and into an appropriate waste container using a single channel peristaltic pump (Cole Parmer, Masterflex C/L) which can deliver a range of volume flow rates from 1.3 to 7.2 mL·min⁻¹. The vacuum created by drawing in the solutions helped check the sealing of the cell. If any leak existed, it would result in air bubbles in the flow, which then could be fixed manually. Instead of creating a vacuum, if the solution was pushed into the cell through a higher pressure, a leak was more likely to occur as the gaskets might be lifted away from the block by positive pressure. This would then result in potentially harmful solution spilling onto the microscope stage and corroding it.

In order to ensure the suitable effectiveness of analyte delivery and removal, the hydrodynamics of the flow-cell was tested beforehand. Briefly, whilst holding the working electrode at a

potential at which the ferricyanide anion could be reduced, the flowing electrolyte was switched between 0.1 M KCl and 10 mM $K_3Fe(CN)_6$. The resulting ‘concentration transient’ when ferricyanide was injected into the flow for moderate solution flow rates is shown in **Figure 3.2**. One can tell that there was some mixing of the solutions, which could be affected by the depth of the channel and especially the depth of the trench in the entry to the flow-cell. However, this result was not critical for the present study. If necessary, the cell could be redesigned for future studies to minimise the mixing.

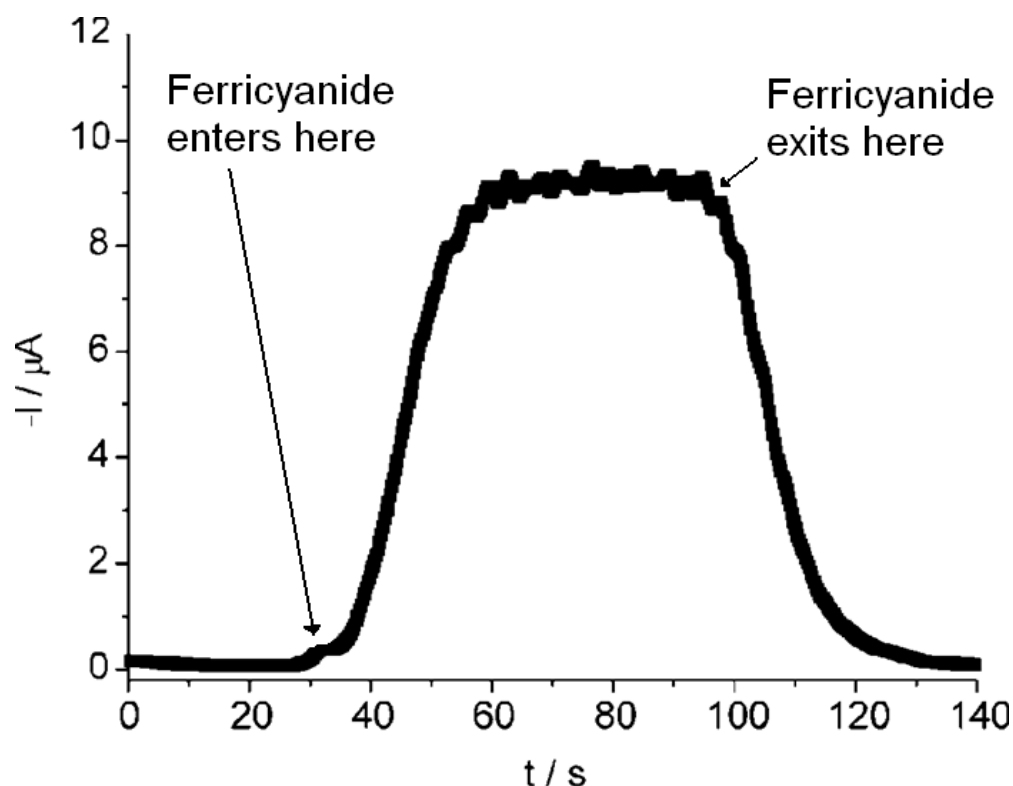


Figure 3.2A current vs. time plot as ferricyanide entered ($t = 30$ s) and left ($t = 100$ s) the cell to ascertain the fluid dynamics of the spectro-electrochemical flowcell at a moderate flow rate. Reprint from reference 4.

3.3 Preparation of Surfaces for SERS Analysis

The electromagnetic theory for Surface Enhanced Raman Scattering (SERS) dictated that the surface should be rough so that the resonating plasmons from the metal, oscillate in a vector perpendicular to the surface.⁴ Due to certain properties of the metal such as plasmon resonance

frequency and the dielectric constant of the metal, SERS was limited to a select few metals with the most reliable and strong scatterers being the coinage metals such as copper, silver and gold. Platinum was the key metal required for the present study. Unfortunately, it did not possess the ideal physical properties to generate SERS.

The method to achieve SERS activity on ‘non-active’ metals was to deposit a thin layer of the ‘non-active’ metal over an active substrate. In this way, the SERS activity was ‘donated’ to the non-active metal surface. The chosen SERS active metal in this study was gold and two methods to activate it were attempted. The first involved electrochemical oxidation-reduction cycles (ORC) to roughen a gold surface and the second involved chemical reduction of a gold solution to form colloidal nanoparticles. Platinum was subsequently deposited on the roughened gold surface or nanoparticle. For the first method discovered by Weaver *et al.*,⁵ the electrochemical waveform was used to roughen the surface of gold. Then platinum was plated on the SERS active surface by flowing hexachloroplatinic-sulphuric acid solution with potential cycling of gold working electrode in and out of the platinum H UPD region so that the platinum was reduced onto the surface. However, the preparation and rigorous cleaning procedures for the electrochemical treatment were time consuming and resulted in one SERS active substrate. In addition, the roughened surface might not exhibit consistently high SERS active uniformly across the surface. More often, this usually resulted in areas of abnormally high activity known as ‘hot-spots’. Hence, the second method was applied in the present study.

3.3.1 Au@Pt Core-shell Nanoparticles

In order to overcome the problems that the first method has, another approach was introduced to develop clean and reproducible SERS active electrodes. This method involved preparing colloidal gold nanoparticles coated with platinum. The Au@Pt core-shell nanoparticles (CS-NP, **Figure 3.3**) were then allowed to ‘settle’ on a generic working electrode as described by the Zhang method.⁶

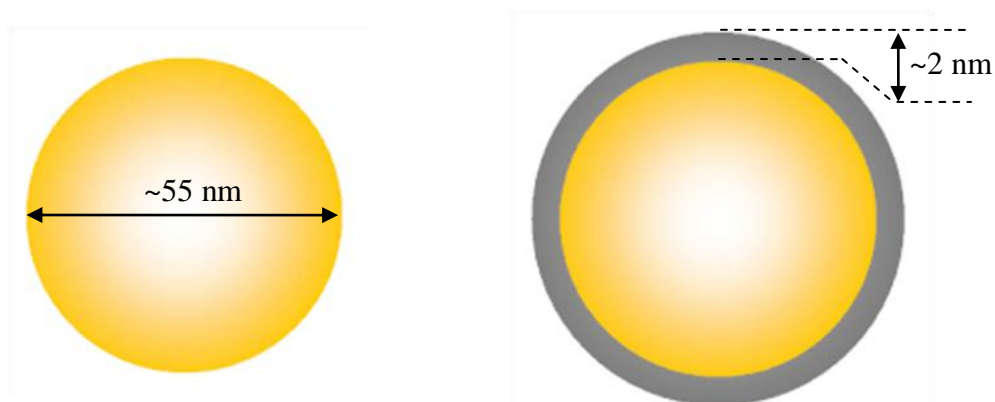


Figure 3.3 Schematic diagram of the gold seed (left) and Pt coated CS-NP (right) used to produce highly SERS active electrodes.

The detailed preparation for this method could be found in Taylor's PhD thesis.⁷ Briefly, this included refluxing 100 mL 0.01% HAuCl_4 solution in a silicon oil bath at 112 °C for 30 min before adding 600 μL 1% sodium citrate aqueous solution straight into it. Then after another 30 min reflux, the 55 nm gold seeds were prepared. The principle behind using nanoparticles for SERS was that instead of electrochemically roughening the substrate to create the nanostructures, the nanostructures were created in suspension and dropped onto the surface. The platinum shell became SERS active as it 'borrowed' the enhancement from the gold core. Therefore, the platinum shell became the target that was studied, not the working electrode that the nanoparticles were plated on.

3.3.2 Au@SiO₂ Core-shell Nanoparticles

As a polycrystalline surface, the platinum shell covering the gold core (**Figure 3.3**) must contain all kinds of facets including terraces, steps and kinks. Therefore, the contribution of each site to surface reactions remains obscure. Tian and co-workers¹ demonstrated that Au@SiO₂ nanoparticles (55 nm diameter gold core, 2 nm thick silica shell) deposited on a single crystal electrode could be used to observe SERS even from a well-defined single crystal surface. So instead of having a 2 nm platinum shell, the gold core was coated by 2 nm silica shell which was electrochemically inert. In theory, the property of the platinum single crystal electrode would not be affected after depositing the Au@SiO₂ nanoparticles on the surface. Therefore, with the

control of the potential on the platinum single crystal working electrode and the molecular vibrations of adsorbed intermediates formed on various kinds of single crystal surfaces during the reaction process could be monitored by this *in situ* SERS technique.

Before any preparation, all glass vessels to be used were cleaned by immersion in *aqua regia* (3 parts 40% hydrochloric acid to 1 part 70% nitric acid by volume) for 30 minutes and rinsed thoroughly with ultra-pure water. Aqua regia is a very toxic and corrosive substance and should only be handled with the appropriate personal protective equipment in a fume cupboard. All solutions were prepared with high purity chemicals and ultra-pure water.

The method for preparation of the core-shell nanoparticles was as follows:

1. 100 mL of 0.01% by mass chloroauric acid in a 250 mL round bottom flask was refluxed at 110°C until boiling. A silicone oil bath on a hot-plate/stirrer with a temperature probe feedback was used for this step.
2. 0.039 M of sodium citrate was prepared and 600 μ L was pipetted directly into the chloroauric acid taking care not to touch the sides (the condenser was briefly removed for this step).
3. Refluxing was continued for 30 minutes. The solution should have changed in colour from light yellow to black and then to red during this period.
4. After 30 minutes, the hot-plate was turned off and the round bottom flask was raised out of the silicone oil bath allowing it to cool. After approximately 15 minutes, the temperature was low enough to allow the flask to cool more rapidly to room temperature under flowing water without the risk of cracking the glass.

The particle size was dictated by the relative quantity of the reductant added to the amount of metal. The nanoparticle size generated was between 50-60 nm diameter as verified by TEM (**Figure 3.4**).

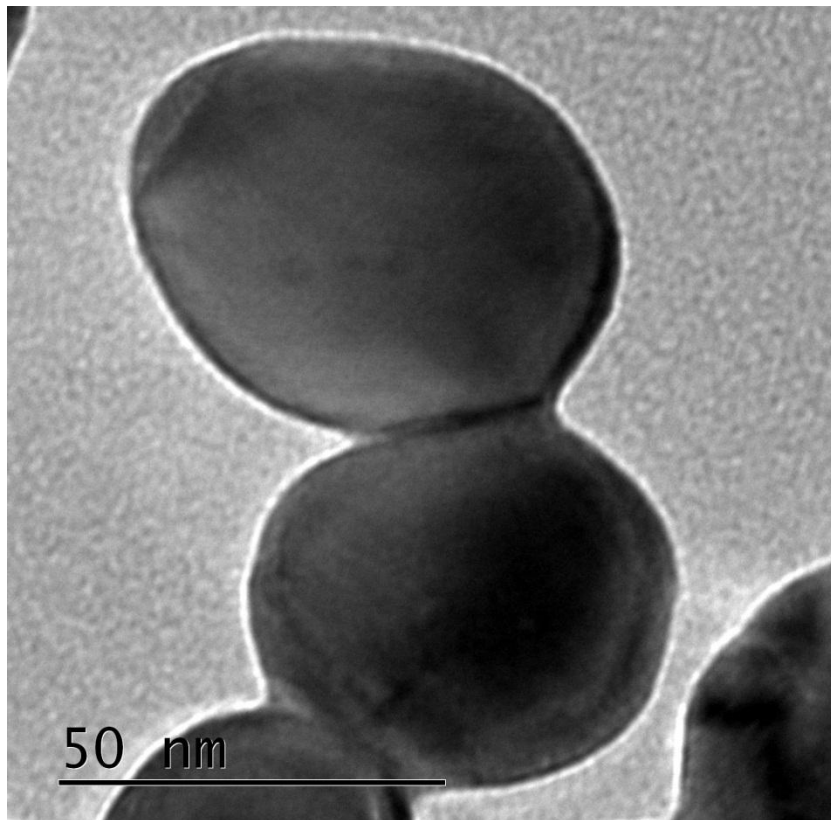


Figure 3.4A TEM image of SERS active gold nanoparticles.

After preparing the gold seed nanoparticles, the next step was to deposit a thin shell of the desired silica on to the nanoparticles. The requirement for the thickness of the silica shell was very crucial. If it was too thick, the SERS enhancement was not as good as expected and the vibrations would not be measured. If it was not fully coated and had some pin-holes, the gold core would affect the property of the substrate and generate false SERS signals as molecules went through the holes and adsorbed on the gold.

Gold metal itself has very little affinity for silica, as it does not form a passivating oxide film in solution. Here, the citrate stabilized gold seed nanoparticles could not be coated by silica straight away. Hence, the replacement of citrate was required and a proper coupling agent was needed so that a hydrated silica monolayer could be bonded to the metal substrate. The approach presented here was to use a silane coupling agent as the surface primer to make the Au surface vitreophilic. The preparation in detail was as follows:

5. 30 mL of the gold seed solution was decanted into a 100 mL round bottom flask.
6. 1.0 mM aqueous solution of (3-aminopropyl)trimethoxysilane was freshly prepared and 0.4 mL was pipetted into the flask under vigorous stirring. The solution was kept stirring at room temperature for 20 minutes.
7. 0.54 wt% sodium silicate solution was freshly prepared and the pH was adjusted to 10.28 using 0.1 M HCl. Then 3.2 mL of this silicate solution was added straight into the flask and the mixture was stirred at room temperature for 20 minutes.
8. The reaction mixture was kept at 70 °C for 13 min to form Au@SiO₂ NPs with an ultrathin shell (2 nm) and then allowed to cool down to room temperature.

In order to be separated from the excess reagents and cleaned, the CS-NP colloid was now centrifuged and ready to be dropped onto the electrode surface using the following procedure:

9. Two aliquots (~9 mL) of the CS-NP colloid were decanted into centrifuge tubes (Fisher, 15 mL).
10. The two tubes were placed on opposite sides of the appropriate rotor (balanced) in a centrifuge (Beckman Coulter, Allegra™ 21R Centrifuge).
11. The tubes were then centrifuged at 5000 rpm for 15 minutes.
12. The aqueous layer was removed with a pipette from both tubes, leaving as little as possible of the supernatant at the bottom of each tube.
13. The volume of both tubes was made up to ~8 mL with ultra-pure water. After sonicating the tubes to ensure that all nanoparticles were in solution (not adhered to the wall of the tube), they were centrifuged again.
14. Step 12 was repeated before adding 2 mL water to the nanoparticles which settled at the bottom.
15. The concentrated nanoparticle colloid was then sonicated and then transferred into a small sample vial. The SHINERS particles should now be ready to use.

The nanoparticles (**Figure 3.5**) could remain concentrated in the sample vial for up to four days, after which they may begin to aggregate and would no longer adhere to the electrode in a uniform layer. Also, the leftover unreacted agents might cause contamination during any experimental measurement. When deposited on the electrode surface, it is suggested that fresh

drops are introduced before experiments every day. Cyclic voltammograms and surface spectra were used to clarify that the surface was clean before analyte introduction.

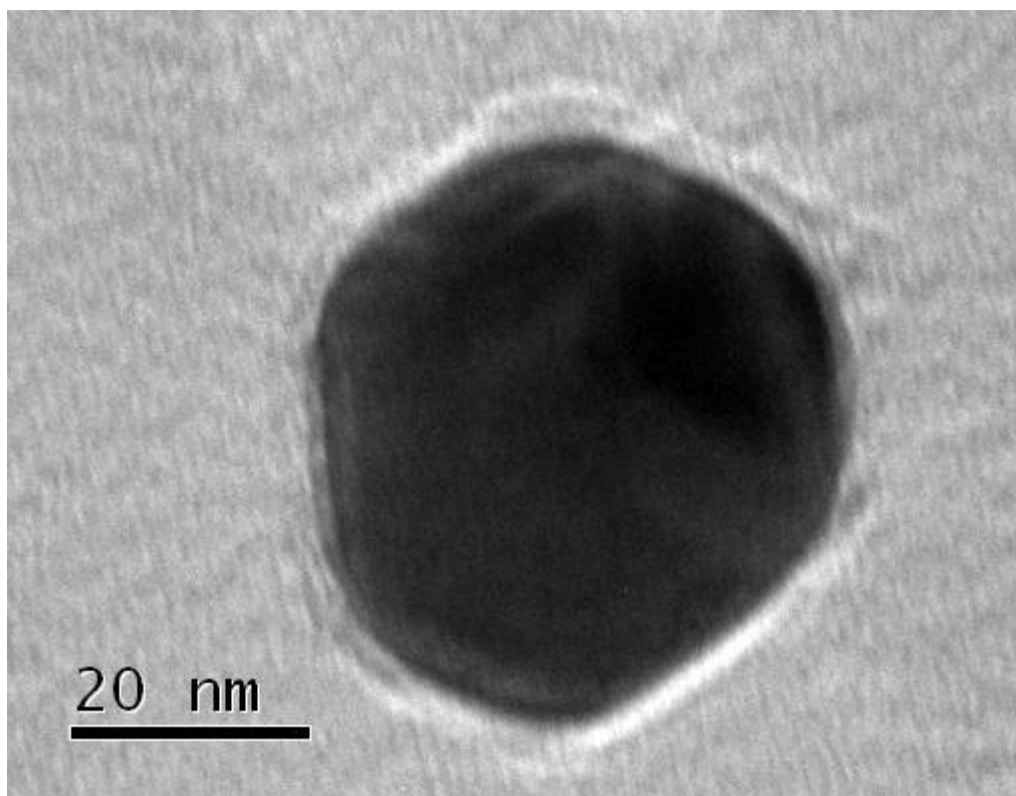


Figure 3.5 A TEM image of Au@SiO₂ nanoparticles.

3.4 Cyclic Voltammetry

3.4.1 Single Crystal Measurements

CV measurements on single crystals, which were all manufactured according to the method reported by Clavilier⁹ and Hazzazi¹⁰, were carried out in a standard two-compartment, three-electrode cell (**Figure 3.6**). The cell was composed of a high surface area platinum mesh counter electrode and a palladium hydride reference (Pd/H) with a high surface area as well. A CHI812 electrochemical analyser (from CHI instruments) was used for potentiostatic control.

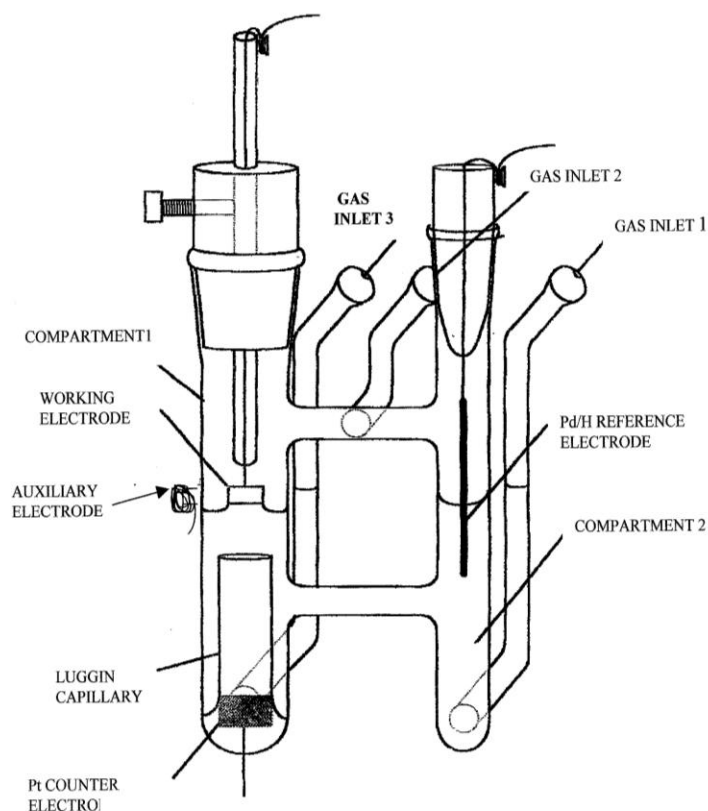


Figure 3.6 Electrochemical cell used for cyclic voltammetry, reprinted from reference 4.

All glassware, including the electrochemical cell and its components, must be kept clean without any contaminants. Before the usage of the glassware and Teflon® materials or components, all of them should be cleaned by immersing in ‘green acid’ for at least one hour (usually overnight) with the guarantee of full contact with all the internal surfaces. Green acid was then discarded into the appropriate waste container and all equipment (the cell and all components) was thoroughly rinsed with ultra-pure (Milli-Q) water (10-15 minutes) to ensure that all traces of green acid were removed. To make sure all the components are pristine clean, they were then steam cleaned with ultra-pure water (UPW). In order to keep them free of contamination, once steamed, the cell was then thoroughly rinsed with Milli-Q water and filled to the bridge that separates the two compartments. The unused components were kept in a clean beaker filled with ultra-pure water for later use.

The palladium hydride reference electrode was made of a Pd wire (1 mm diameter) spot-welded onto a thin Pt wire which was fixed in a glass jacket. The Pd part of the reference electrode was

first gently heated in a Bunsen flame to clean off the contaminants. Then it was placed into compartment 2 (shown in **Figure 3.6**) of the cell and partially immersed into the water, allowing hydrogen gas bubbling. For about 30 minutes, the reference was charged by absorbing hydrogen; the palladium formed a stable, non-polarisable β -hydride phase and may keep its potential for up to 10 hours in aqueous acidic electrolyte. The resulting potential of the Pd/H reference electrode was approximately +50 mV compared to the reversible hydrogen electrode, and was independent of the amount of hydrogen absorbed.¹¹

Once the reference electrode had finished charging, the cell was thoroughly rinsed with fresh water and was then filled with the desired electrolyte. Typically, electrolytes used for single crystal measurements were 0.1 M HClO₄ and 0.1 M H₂SO₄. Dissolved oxygen in the electrolyte was removed by bubbling nitrogen gas through inlet 3 for 30 minutes. In order to prevent oxygen leaking into the cell, an overpressure of the inert gas nitrogen was maintained through inlet 2 of the electrochemical cell. After 20-30 minutes of continuously bubbling gas through inlet 2, voltammograms of the working electrode were ready to be collected in the non-oxygen environment. The stem of the single crystal bead was wrapped around an electrical conducting wire, usually platinum or copper, and threaded through a glass capillary. One needed to make sure that the conducting wire was not overheated by the Bunsen flame as it might attract contaminants from it. The connecting wire then passed through the capillary tube and was secured by wrapping around the nub at the top.

The capillary tube was situated in the Teflon® stopper, which allowed the tube to be raised or lowered such that a meniscus contact was formed between the electrode face and the electrolyte. Without a meniscus, the solution would climb up the side of the electrode and the un-defined surface sites on the outside of the bead would become accessible to electrochemical processing and affect the accuracy of the results. The platinum single crystal, which was secured in the tube and stopper, was then flame annealed in the hottest point of the blue flame of the Bunsen burner (the crystal would glow a bright yellow colour). After 30 seconds, it was then cooled in a bubbler containing degassed Milli-Q water and a steady flow (1-2 bubbles per second) of hydrogen gas. Care must be taken here as too hot a crystal bead may cause an explosion (ignition) of the hydrogen gas. Hence, the single crystal bead was transferred into the hydrogen atmosphere after

the glow had just faded and the volume of hydrogen gas above the water surface was kept to a minimum.

The crystal face was then dipped into the pure water of the hydrogen bubbler and removed from the bubbler before transferring to the electrochemical cell. A droplet of pure water was attached to the crystal face to prevent any contamination from the air during the transfer from the hydrogen bubbler to the electrochemical cell. It was advisable to make the connections to the potentiostat with the supplied crocodile clips before attempting the meniscus formation step as any vibration would disrupt the surface tension of the solution and the meniscus would break. At this point, electrochemical processes could be measured. The starting potential for the sweep was set at 0.85 V (vs. Pd/H) and swept negatively to 0 V with a scan rate of 0.05 Vs⁻¹. The reason to set the starting potential as 0.85 V is to observe the desorption of the thermal oxide that is formed whilst transferring the platinum surface from the hydrogen bubbler to the electrochemical cell.¹² Deterioration in the CV indicated the presence of a contaminant. The contamination source needed to be located and remedied – a potentially lengthy process that could require complete overhaul of the system (cleaning followed by reassembly).

3.4.2 CV Measurements of Pt Single Crystals decorated with Au@SiO₂ NPs

In order to obtain a SERS signal on the flat surface of Pt single crystals, SHINERS NPs Au@SiO₂ were coated on it and cleaned. This technique allowed one to acquire a clean Pt single crystal electrode which exhibited its own singular electrochemical properties and enhanced its SERS effect thanks to the Au@SiO₂ NPs coated on it. The procedure in detail is described as follows:

1. After flame-annealing the Pt single crystal with the Bunsen flame, it was cooled in the hydrogen bubbler.
2. The crystal bead was then dipped into a potassium bromide aqueous solution, which was prepared with a few grains of KBr and 3 mL UPW. It was then rinsed by fresh water in order to form a monolayer of bromide on the Pt single crystal surface and remove excess KBr. This was the step to protect the metal surface from contamination in the air.

3. One droplet of the washed and centrifuged Au@SiO₂ NPs solution was transferred from the sample vial by a pipette and gently placed onto the Pt single crystal surface protected by the bromide layer.
4. The droplet of the Au@SiO₂ NPs colloid was dried under gentle nitrogen flow and then ready to be cleaned electrochemically.

3.4.3 *In situ* Measurements of CV and SERS

The spectro-electrochemical flowcell was designed to take electrochemical measurements for composition and surface structure determination, also with the functions to clean the electrode surface *in situ* and control the surface environment. A CHI750 model potentiostat was used to run cyclic voltammograms (CV) with the proprietary program on an RM PC.

Before performing any electrochemical measurements, charging the Pd/H reference electrode was required as usual. Different from the glass cell described previous, this Pd/H reference electrode was charged by evolving hydrogen on the palladium by electrolysis in the flowcell. Using the gold as the counter electrode as normal, the connections to the potentiostat between working electrode and reference electrode were swapped. Instead of platinum, the palladium was now treated as the working electrode. Hence, whilst controlling the potential at -0.85 mV (*vs.* Pt reference) for 30 minutes, hydrogen was generated and absorbed into the palladium forming the Pd/H reference electrode which would maintain its potential for as long as 8 hours. Of course, the electrolyte which flowed through the cell at the rate of 2.5 mL/min was either sulphuric acid or perchloric acid aqueous solution (0.1 M).

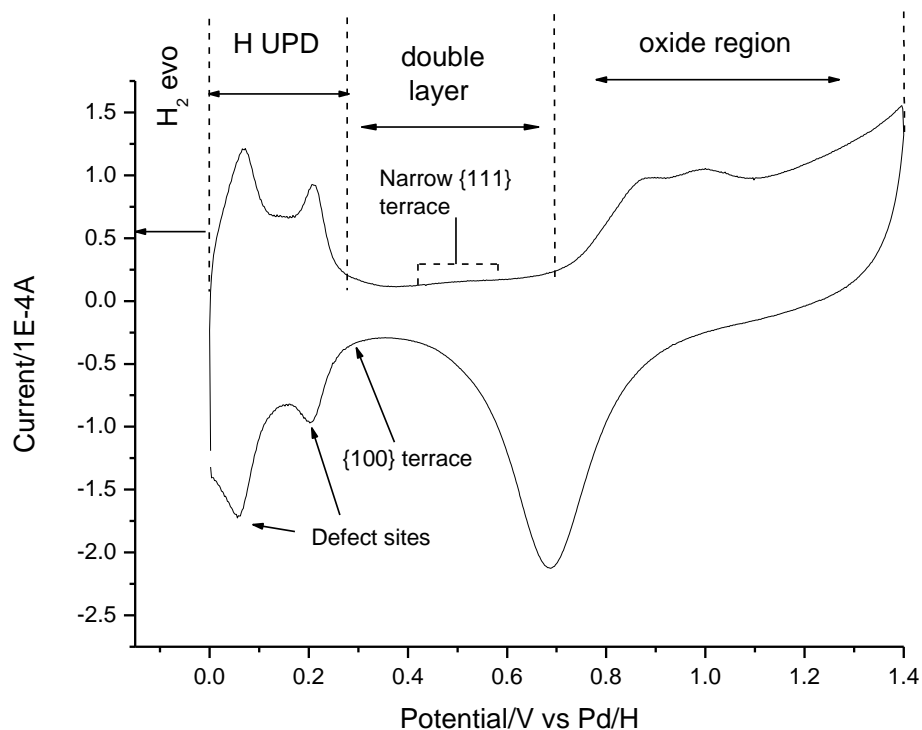


Figure 3.7 Cyclic voltammogram of Au@Pt core-shell NPs on a polycrystalline platinum electrode in 0.1 M H₂SO₄. Sweep rate = 50 mV·s⁻¹.

The cleaning procedure (for Au@Pt NPs coated on polycrystalline Pt working electrode) also involved a flowing solution (flow rate: 2.5 mL/min) of Aristar grade sulphuric acid at a concentration of 0.1 M in ultra-pure water. The platinum working electrode was cycled between -0.1 and 1.3 V vs. Pd/H at a scan rate of 0.1 V/s for 50 cycles or until the CV was stable (**Figure 3.7**). If not, the electrolyte was changed to 0.1 M sodium hydroxide solution and the Pt working electrode was cycled between -0.3 and 1.1 V vs. Pd/H at the same scan rate. Finally, the sulphuric acid was swapped back to carry out the last clean of the NPs and the electrode. All the organic remnants from the reagents and other contaminants could be removed by this so called oxidation-reduction cycles (ORC) cleaning procedure.

However, a different cleaning procedure for Au@SiO₂ NPs coated on platinum single crystal electrodes had to be used because a potential in excess of 0.8 V would roughen a single crystal surface. After drying the droplet of the Au@SiO₂ NPs onto the single crystal surface, the electrode was transferred to the degassed electrochemical cell which contained 0.1 M HClO₄ as

the electrolyte. A meniscus contact was formed between the crystal bead and the electrolyte before the cycling voltammetry cleaning was carried out.

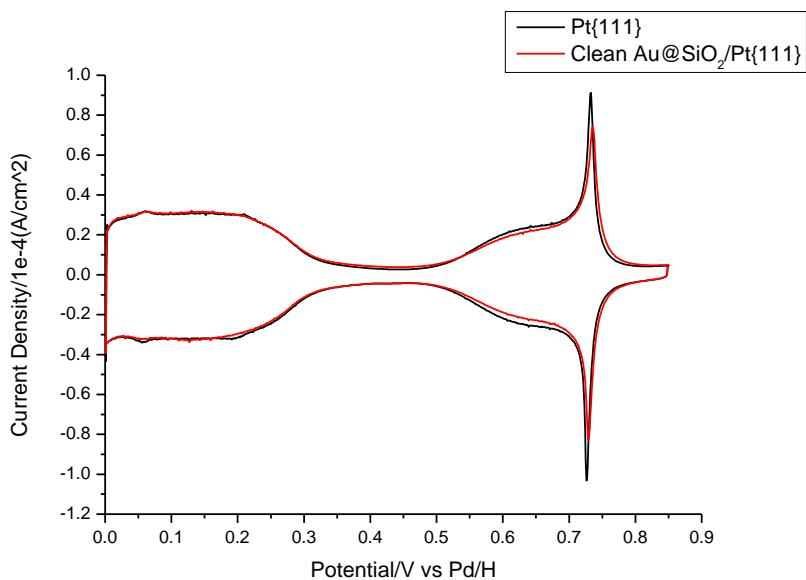


Figure 3.8 Cyclic voltammograms of clean Pt{111} (black) and Au@SiO₂ core-shell NPs on Pt{111} electrode (red) in 0.1 M HClO₄. Sweep rate = 50 mV·s⁻¹.

Therefore, instead of oxidizing the surface, hydrogen evolution on the surface was performed to strip of the bromide layer and clean the surface of the platinum single crystal electrode. It involved fast cycling the potential between -0.1 V and 0.85 V at the scan rate of 200 mV·s⁻¹ for at least 100 cycles until the voltammogram was stable. This method was devised at Cardiff and the cleaning effect was profound. For the first time, the cyclic voltammograms of clean Au@SiO₂ NPs coated on platinum single crystal electrodes were established. **Figure 3.8** shows an example of CV of clean and pin-hole free Au@SiO₂ NPs coated on Pt{111}. If the NPs were not clean, the features of the voltammogram would change, e.g. the disappearance of the sharp peaks at 0.72 V. If there were pin-holes on the NPs, features due to oxide adsorption/desorption on the Au surface would be observed above 0.8 V in CV. Once the surface was proved to be clean, it was ready for *in situ* SERS tests.

Also, both Au@Pt and Au@SiO₂ NPs can be proved to be clean and pin-hole free by running SERS tests in the flowcell system. Since the NPs were prepared using various capping/stabilising agents, such as sodium citrate, ascorbic acid and trimethoxysilane *etc.*, these chemicals may contribute to the Raman spectra obtained due to the interaction between them and the gold substrate. The vibrational bands caused by the agents usually interfere the interpretation of the spectra. Therefore, it is crucial to rule out the possible contribution by them.

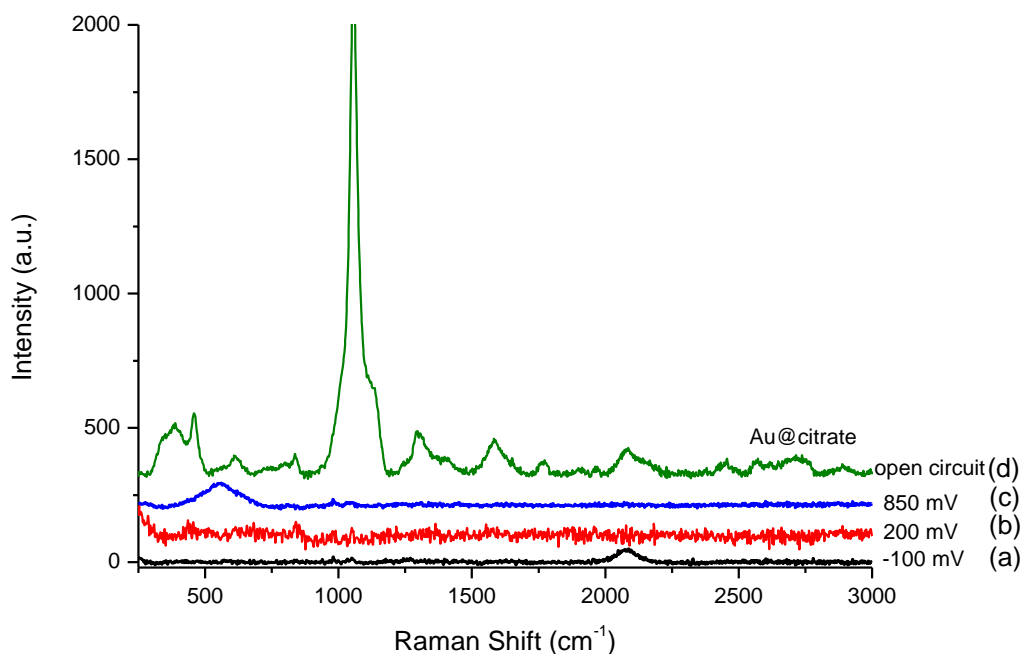


Figure 3.9 SER spectra of Au@citrate NPs (d, open circuit) and clean Au@Pt NPs on polycrystalline Pt electrode in 0.1 M H₂SO₄ at (a) -100 mV, (b) 400 mV and (c) 800 mV vs. Pd/H.

Figure 3.9 shows the comparison of SER spectra of citrate stabilised gold NPs and clean Au@Pt NPs deposited on the polycrystalline Pt electrode at three typical potentials. From the figure, it can be seen that the Au@citrate NPs have huge SERS enhancement effect because gold is exposed and can enhance all the vibrations of the bonds from citrate capped on it (**Figure 3.9d**). Readers may refer Kerker *et al.* and Munro *et al.*'s papers for detailed interpretation of the Raman peaks related to citrate.^{16,17} However, no further contributions of citrate to the spectra of

the clean NPs. Typically, only the Pt-H stretching band at 2090 cm^{-1} (**Figure 3.9a**) and Pt-O vibrational band at 553 cm^{-1} (**Figure 3.9c**) were observed at hydrogenative and oxidative conditions, respectively. Especially, no bands were observed at any potential around 1500 cm^{-1} (very crucial range of wavelength) which might be due to the vibrational signals of citrate and its decomposition products. Hence, the NPs were proved to be pin-hole free as well. Similar spectra (not shown) were also obtained from clean Au@SiO₂ NPs deposited on Pt single crystal electrodes. Once the possibility of the vibrational bands due to citrate has been ruled out, all the bands newly appeared would be attributed to the selected molecules in the present study.

Although the SER spectra were the main focus of the *in situ* SERS tests of different target molecules (alkynes and activated ketones), the CV data were not negligible. Hence, the cyclic voltammograms for all the target chemicals dissolved in the electrolyte were collected in the flowcell system before the SERS tests were carried out.

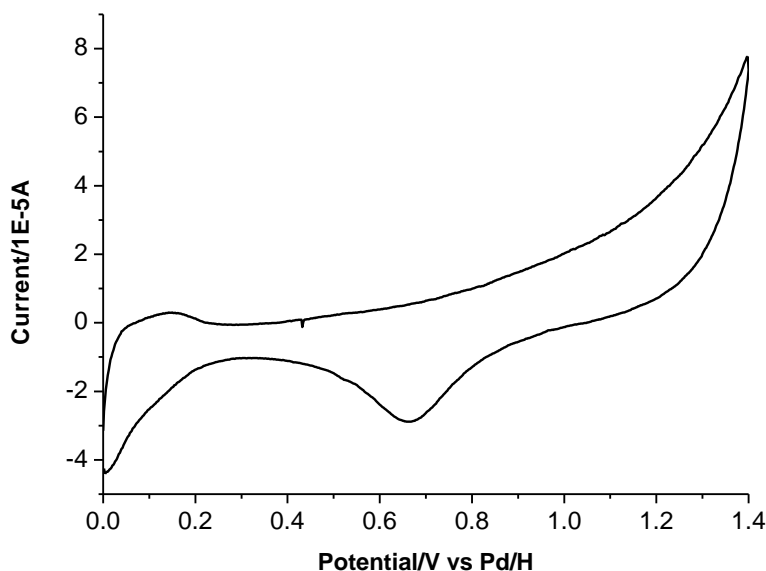


Figure 3.10 CV of 0.1 M butynediol adsorbed on Au@Pt NPs coated on Pt polycrystalline electrode in 0.1 M sulphuric acid. Sweep rate: $50\text{ mV}\cdot\text{s}^{-1}$.

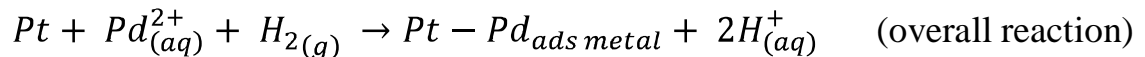
Figure 3.10 shows the example of CV of 2-butyne-1,4-diol adsorption (butynediol) on Au@Pt NPs deposited on Pt polycrystalline electrode. In the positive scan, the H UPD region below 0.24

V lost most of the features (compared with **Figure 3.7**) due to the adsorption of butynediol that blocked Pt surface sites. The adsorption also increased the double layer region. The high potential (up to 1.4 V) applied on the electrode could oxidise the molecules adsorbed on the surface. However, after the potential decreased and the oxide was removed from the Pt surface, the butynediol molecules re-adsorbed on the surface and caused a current drop in the H UPD region. When Au@SiO₂ coated Pt single crystal electrodes were used, the upper limit of the potential was set as 0.85 V. It was because higher potentials would roughen the surface of the single crystal electrodes.

3.5 Metal Deposition on Single Crystal Electrodes

Pd²⁺_(aq) and Bi³⁺_(aq) aqueous solutions were prepared using a palladium nitrate (Pd(NO₃)₂, Sigma Aldrich) and bismuth nitrate pentahydrate (Bi(NO₃)₂·5H₂O, Sigma Aldrich) solutions respectively in the concentration ranges between 10⁻⁵-10⁻⁶ M using Milli-Q water. These electrolytes were used as the source of metal adatoms in subsequent measurements of Pt bimetallic surfaces.

The forced deposition method was used to produce ordered palladium adlayers onto single crystal electrodes.¹³ The coverage could range from sub-monolayer to multilayer amount. First, the technique required a clean CV of the well-ordered single crystal electrode to verify surface order. Once a good CV of the electrode was obtained, the electrode was rinsed with Milli-Q water and then dipped into the aqueous Pd(NO₃)₂ solution, before it was transferred to the hydrogen bubbler with a droplet of palladium solution attached. By holding the crystal bead above the water level for 1-2 seconds, it allowed a stream of hydrogen to pass over the electrode surface. This resulted in palladium being reduced to form palladium metal adsorbed on the surface of the electrode. The deposition of Pd at Pt single crystals therefore occurred as follows:



The electrode was then removed from the hydrogen bubbler and rinsed with Milli-Q water, in order to remove the excess palladium nitrate. It was then re-introduced to the electrochemical cell via a meniscus contact. By fast cycling of voltammetry between the usual range of potential (0 V to 0.85 V), the palladium metal atoms would rearrange on the platinum surface and finally form a monolayer. The coverage of palladium was subsequently characterised by CV. Further layers of palladium could be deposited by repeating the steps described above if necessary. The recovery of the platinum crystal electrode features could be obtained by flame annealing the electrode to remove the palladium film as a volatile palladium oxide, followed by cooling in hydrogen.¹³

It has been shown previously that the immersion of single crystal electrodes into certain metal ion solutions at open circuit can result in the spontaneous deposition of the metal onto the single crystal electrodes.¹⁴ The amount of metal that is deposited depends on the concentration of the metal solution and the time that the electrode is held in the metal solution. Coating bismuth on the surface of platinum single crystal electrodes could be easier. Simply by dipping the flame annealed electrode into the bismuth nitrate solution and rinsing, an adlayer of bismuth adatoms could irreversibly adsorb. However, in order to form a uniform bismuth coverage, the Pt single crystal electrode with bismuth nitrate droplet attached needed to be treated electrochemically like the deposition of palladium. After it was flame annealed and characterised by CV, the electrode was immersed in a bismuth nitrate solution (10^{-5} M). Then, it was rinsed with Milli-Q water to remove excess nitrate ions. Finally, it was re-introduced to the electrochemical cell for further characterisation. Repeated immersions in the bismuth nitrate solution followed by rinsing would increase the coverage of the bismuth adlayer. The platinum electrode may recover its original features by following the procedure used to remove palladium.

3.6 Raman Spectrophotometer and Microscope

The apparatus used to run the Raman experiments was a LabRam HR confocal microscope from HORIBA JobinYvon Ltd. with the following specifications:⁷

- A 10 mW He-Ne 633 nm laser.

- A $\times 50$ long working distance objective lens with a numerical aperture of 0.55 and a working distance of 8.1 mm producing a spot size of 1.4 μm .
- A $\times 10$ condenser lens with a focal length of 300 mm that focussed the laser into the objective lens.
- A confocal hole with adjustable aperture set to 200 μm .
- 5 density filters that reduce the power to 50%, 25%, 10%, 1% and 0.1% and a sixth position with no filter i.e. 100% of the power is transmitted in this configuration.
- A notch filter for a 633 nm laser set at an angle to reject this light frequency.
- 1800 grooves/mm diffraction grating.
- 1024 pixel CCD Peltier cooled detector.
- Manually operated X-Y stage.
- Motorised Z-slider.
- Video camera.

The above configuration generated a resolution of 1.539 cm^{-1} , but other components and configurations were available including:

- 30 mW YAG 532 nm laser.
- $\times 10$ and $\times 100$ objective lenses.
- A notch filter for a 532 nm laser.
- 600 gr/mm diffraction grating.

Collection and analysis of the data was performed on the proprietary LabSpec program run on a Dell Precision T1650 PC. The Raman detector was kept at $-75 \text{ }^\circ\text{C}$ constantly by a Peltier device. Room temperature was also maintained at $20 \text{ }^\circ\text{C}$ by air conditioning. Any minor temperature changes might affect the 'zero' coefficient of the detector and eventually cause an error in the position of spectral peaks. Before running an experiment, the He-Ne laser was switched on to warm up to the maximum output power for at least 30 minutes. A shutter was used to prevent the laser beam from emerging from the unit and was always closed unless recording a spectrum. Every time the detector was switched on, it needed to be calibrated. When in constant use, it was necessary to re-calibrate the detector every two to three days. In order to record a well-defined Raman shift, the LabSpec program also needed to be calibrated frequently by using a silicon

single crystal whose lattice vibration (phonon) occurred reliably at 520.7 cm^{-1} . This would only vary with the zero coefficient so did not need to be checked as often. Once the calibration was performed each time, all the parameters used were saved so profiles of intensity vs. time were kept on record. This allowed the operator to check if the performance of the Raman spectrometer was falling. A fall in performance could be due to several reasons, such as the optics changing position or efficiency, the laser becoming misaligned or loss of power or the detector losing sensitivity. Then re-calibration must be done before carrying out further experiments.

3.6.1 The Raman Experiment

To run an experiment, the following steps were taken:

1. The sample was placed on the X-Y stage and moved under the objective lens before securing it.
2. An emission guard was put around the objective lens turret to enclose the laser emission and prevent contamination from other light resource when running a spectrum.
3. A white light source was turned on, and set a beam splitter to direct the image from the objective lens to a video camera.
4. The camera icon in the LabSpec program was engaged to open the camera image displaying on the computer screen in real time.
5. In order to focus the image, the joystick connected to the Z-slider was used to move the objective lens up or down until the sample could be seen clearly.
6. Once focussed, the white light source was switched off and the beam splitter raised to allow the laser light to impinge on the surface and direct the scattering to the detector.
7. Parameters of the spectrum based on the specific requirements for each test were set up. These would include the accumulation time, the number of accumulations, the density filter, the frequency range set by the position of the grating and the acquisition function (simple, multi-window, depth profile, time profile etc). The correct hardware was then selected, such as emission source, confocal hole aperture, grating *etc.*
8. All personnel present should wear the appropriate filter goggles. If the 633 nm (red) laser was used, green or blue coloured goggles would be worn.

9. The laser shutter was open and the spectrum accumulation icon was clicked to start the tests.
10. Each spectrum was accumulated with the exposure time of 10 seconds for 20 times.
11. The laser focusing spot was not moved before the experiment was finished.
12. After the run, the laser shutter was closed and the spectrum saved as a .ngs file in the appropriate folder. (The .ngs file would save the data as well as the parameter settings unlike .txt file which only saved data).
13. All the spectra shown in this thesis are reproducible.

3.6.2 Data Processing and Analysis

In order to cover the full frequency range ($200\text{-}3200\text{ cm}^{-1}$), the original data were usually collected at different frequency ranges of the diffraction grating. Also, due to fluorescence, the spectra showed a curving background. For display purposes, the data collected could be processed using the LabSpec facilities.

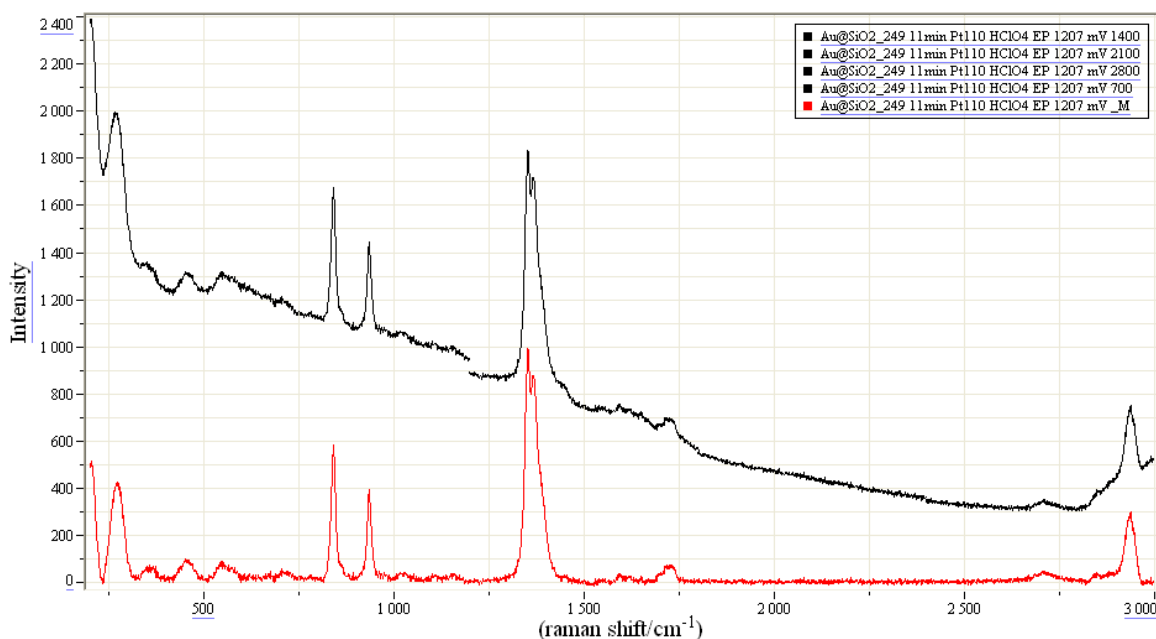


Figure 3.11 An example of typical SERS data before (black line) and after (red line) processing. In this case, the oxidized ethyl pyruvate adsorbed on platinum is being measured.

Figure 3.11 shows overlapping spectra in black. To present the data more clearly, one can improve them by subtracting the baseline of each spectrum and combining all four sections to form one full range spectrum, as shown in red. Care must be taken when performing these tasks as during the process, the data could be altered and the shape or intensity of a peak might be changed. False processing would eventually lead to an incorrect interpretation of a spectrum.

The processed data was then saved as a .txt file as it could be transferred to other graphical programs such as Microsoft Excel or OriginLab for more advanced presentation processing. Further analysis on the data could be performed with the LabSpec program, such as peak area integration. Here two methods were introduced briefly. The first was simply highlighting a peak using peak integration cursors. It would require manual set of a baseline, as shown in **Figure 3.12a**. However, if there was a shoulder contributing to a peak, this method wouldn't be suitable anymore as it automatically integrated the whole area under a selected peak indiscriminately. Then a second method could solve this issue. It involved searching and labelling for all the peaks. Then by using a Gaussian and/or Lorentzian peak fitting routine, it estimated the peak shape and its contribution, as shown in **Figure 3.12b**.

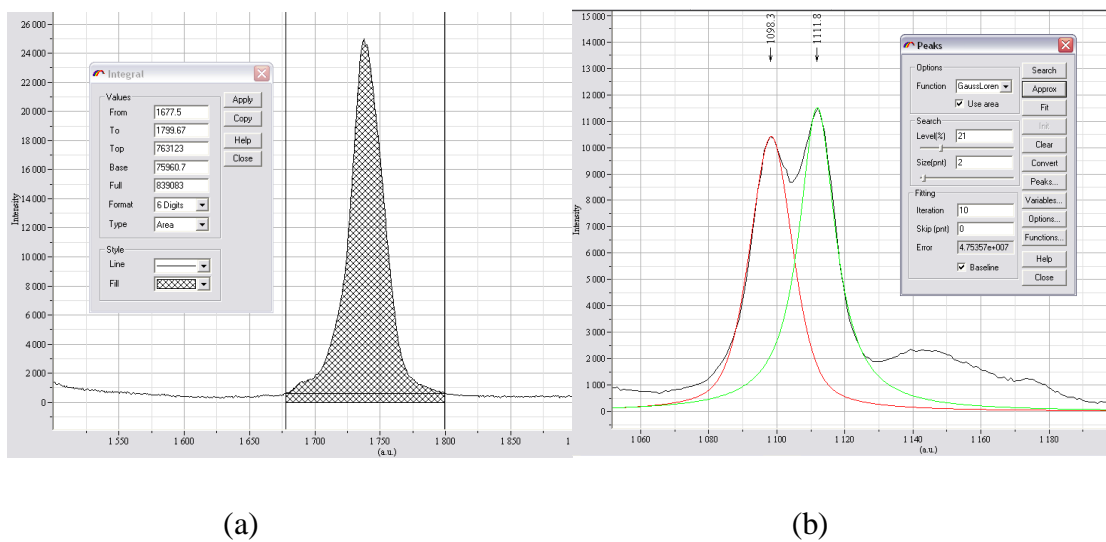


Figure 3.12 Peak area integration methods (a) integration cursors, (b) a peak fitting routine.

3.7 Running a SERS Experiment

Usually, before running any experiments, the system was cleaned and prepared as described previously. For studies in aqueous liquid media, the analyte could be introduced immediately after the rinse with ultra-pure water for SERS measurements. A typical experiment involved the following procedure:

1. Sulphuric acid was re-introduced into the flowcell with a constant flow rate of 2.5 mL/min and the potential of the working electrode was held in the double layer region. SER spectra were recorded.
2. The analyte was introduced into the flowcell with a constant flow rate of 2.5 mL/min and SER spectra were recorded.
3. The potential was set to the desired value and SER spectra were recorded. The potential was swept to different values between each test.

Typically, the potential was held in either the oxide region or H UPD region to investigate the effect of co-adsorbed oxygen or hydrogen respectively. Sometimes, the potential was held at double layer potentials, in order to compare the difference when neither oxygen nor hydrogen was present. Between each SERS test, there was at least five minutes break for the electrode condition to be settled at desired potential value. The potential at which the hydrogen evolution reaction (HER) occurred (-0.05 V vs. Pd/H) could also be set to simulate conditions at high hydrogen gas pressure. At potentials more negative than -0.15 V , the volume of hydrogen gas at the surface evolved with a speed such that the hydrogen bubbles would affect the focus of the laser spot on the electrode surface, which resulted in losing SERS sensitivity and intensity. To minimise this interference, the cell could be placed vertically in an aluminium bracket fixed to the X-Y stage, which was designed and manufactured in-house. Then, a 90° angle-piece was needed to mount the objective lens 90° from the z-axis. The vertical arrangement of the cell and the ascending flow of the electrolyte help remove gas bubbles generated at the electrode surface. Focusing was then controlled by movement along the x-axis. However, it still required careful control with the potential.

Due to the usage of aqueous electrolytes, there was an aqueous layer on the electrode, leaving the surface hydrophilic. Naturally, it prevented organic solvents with low water solubility from accessing to the surface if they were to be used. However, constant flow of the organic solvent would eventually remove the hydrophilic layer. Another way to achieve this purpose was to flow intermediary solvent, such as ethanol, through the cell.

3.8 Water Purification System

The Millipore Milli-Q Plus water system (Millipore, Watford, Hertfordshire) supplied research grade ultra-pure water at a rate of 1.5 litres per minute.¹⁵ First, laboratory tap water passed through 5 µm filter (Water Filtration Ltd., Cardiff) before flowing into the Milli-RO 10 Plus purification system. This contained an activated charcoal pre-filtration unit to remove chloride and organic compounds. The water then passed through a semi-permeable reverse osmosis membrane before being stored in a sixty litre reservoir. In order to prevent growth of photosynthetic bacteria, the tank was kept in dark conditions. The reservoir was automatically refilled by the water when the volume in it dropped below a certain level. As for the production of ultra-pure water, the Milli-Q system was switched on and set to ‘cycle’. Water from the reservoir was pumped into the Milli-Q system where it passed through a mixed bed of purification media and achieved a resistivity of 18.2 MΩ·cm. The ultra-pure water was ready to use if the Milli-Q system was then switched to ‘production’. Passing through a 0.22 µm final filter and out of the delivery nozzle, the water could be collected manually.

3.9 Chemical Reagents

Chemical	Formula	Grade	Supplier
Sulphuric acid	H ₂ SO ₄	Aristar	BDH, Poole
Sulphuric acid	H ₂ SO ₄	GPR	Fisher
Hydrochloric acid	HCl	GPR	Fisher
Argon	Ar	Pureshield	BOC
Hydrogen	H ₂	High Purity 99.995%	BOC
Potassium permanganate	KMnO ₄	GPR	BDH, Poole
Platinum wire, 2 mm diameter	Pt	99.95%	Advent Research Materials Ltd, Eynsham, Oxon. UK

Platinum wire (for single crystal manufacture)	Pt	99.999%	Goodfellows
Platinum/graphite catalyst	Pt/G	5%	Johnson Matthey
Palladium wire, 2 mm diameter	Pd	99.9%	Advent Research Materials Ltd, Eynsham, Oxon.UK
Gold wire, 3 mm diameter.	Au	99.95%	Advent Research Materials Ltd, Eynsham, Oxon. UK
Perchloric acid	HClO ₄	Aristar	BDH, Poole
(3-Aminopropyl)-trimethoxysilane	C ₆ H ₁₇ NO ₃ Si	97%	Alfa Aesar
Sodium hydroxide	NaOH	>97%	Fisher Scientific
Chloroauric acid	HAuCl ₄	41.29%	Johnson Matthey
Hexachloroplatinic acid	H ₂ PtCl ₆	24.95% assay	Johnson Matthey
Tetrachloropalladic acid	H ₂ PdCl ₄	32.19%	Johnson Matthey
Palladium nitrate	Pd(NO ₃) ₂ ·H ₂ O	41.54%	Johnson Matthey
Bismuth(III)nitratepentahydrate	Bi(NO ₃) ₃ ·5H ₂ O	>98%	Sigma-Aldrich
Sodium citrate	Na ₃ C ₆ H ₅ O ₇	99+%	Aldrich
L-Ascorbic acid	C ₆ H ₈ O ₆	99+%	Aldrich
Ethyl pyruvate	C ₅ H ₈ O ₃	>97%	Fluka
Sodium silicate solution	Na ₂ O(SiO ₂) _x ·xH ₂ O	Reagent Grade	Sigma-Aldrich
Cinchonidine	C ₁₉ H ₂₂ N ₂ O	>98%	Fluka
Cetyltrimethylammoniumbromide	C ₁₉ H ₄₂ BrN	>98%	Sigma-Aldrich
2-Butyne-1,4-diol	C ₄ H ₆ O ₂	99%	Sigma-Aldrich
cis-2-Butene-1,4-diol	C ₄ H ₈ O ₂	97%	Sigma-Aldrich
2-Pentyne	C ₅ H ₈	98%	Sigma-Aldrich
4-Octyne	C ₈ H ₁₄	99%	Sigma-Aldrich
2-Methyl-3-butyn-2-ol	C ₅ H ₈ O	98%	Sigma-Aldrich
Propargyl alcohol	C ₃ H ₄ O	99%	Sigma-Aldrich

3.10 References

1. J. F. Li, Y. F. Huang, Y. Ding, Z. L. Yang, S. B. Li, X. S. Zhou, F. R. Fan, W. Zhang, Z. Y. Zhou, Y. Wu de, B. Ren, Z. L. Wang and Z. Q. Tian, *Nature*, 2010, **464**, 392-395.
2. P. Etchegoin, H. Liem, R. C. Maher, L. F. Cohen, R. J. C. Brown, H. Hartigan, M. J. T. Milton and J. C. Gallop, *Chemical Physics Letters*, 2002, **366**, 115-121.
3. P. Etchegoin, H. Liem, R. C. Maher, L. F. Cohen, R. J. C. Brown, M. J. T. Milton and J. C. Gallop, *Chemical Physics Letters*, 2003, **367**, 223-229.
4. E. Smith and G. Dent, *Modern Raman Spectroscopy: A Practical Approach*, Wiley, 2005.
5. P. Gao, D. Gosztola, L.-W. H. Leung and M. J. Weaver, *Journal of Electroanalytical Chemistry and Interfacial Electrochemistry*, 1987, **233**, 211-222.

6. L. Lu, H. Wang, S. Xi and H. Zhang, *Journal of Materials Chemistry*, 2002, **12**, 156-158.
7. R. J. Taylor, Cardiff University, 2010.
8. T. K. Sau and C. J. Murphy, *Journal of the American Chemical Society*, 2004, **126**, 8648-8649.
9. J. Clavilier, D. Armand, S. G. Sun and M. Petit, *Journal of Electroanalytical Chemistry and Interfacial Electrochemistry*, 1986, **205**, 267-277.
10. O. A. Hazzazi, Cardiff University, 2002.
11. M. Fleischmann and J. N. Hiddleston, *Journal of Physics E: Scientific Instruments*, 1968, **1**, 667.
12. J. Clavilier, R. Durand, G. Guinet and R. Faure, *Journal of Electroanalytical Chemistry and Interfacial Electrochemistry*, 1981, **127**, 281-287.
13. F. Vidaliglesias, A. Alakl, D. Watson and G. Attard, *Electrochemistry Communications*, 2006, **8**, 1147-1150.
14. T. J. Schmidt, V. Stamenkovic, G. A. Attard, N. M. Markovic and P. N. Ross, *Langmuir*, 2001, **17**, 7613-7619.
15. M. G. Catalogue, Millipore U.K. Ltd., Watford, Hertfordshire, Editon edn.
16. M. Kerker, O. Silman, L. A. Bumm and D.-S. Wang, *Applied Optics*, 1980, **19**, 3253-3255.
17. C. H. Munro, W. E. Smith, M. Garner, J. Clarkson and P. C. White, *Langmuir*, 1995, **11**, 3712-3720.

CHAPTER FOUR

Hydrogenation of Alkynes at Nanoparticle and Single Crystal Platinum Surfaces

4.1 Introduction

The catalytic selective hydrogenation of alkynes has attracted significant research interest worldwide and is reported to be a structure sensitive reaction.¹⁻⁴ By comparing the selectivity of cubic, octahedral and cuboctahedral particles of platinum during the hydrogenation of 2-methyl-3-butyn-2-ol, Crespo-Quesada *et al.*⁴ confirmed structure sensitive behaviour. Lee and co-workers also studied structure sensitivity for alkyne partial hydrogenation products in the *cis-trans* isomerisation of 2-butene, whereby Pt{111} single crystals were found to favour *trans*-over *cis*- isomerisation.⁵ Both investigations mentioned above required the synthesis of metal particles with specific shapes. Previous work by Attard *et al.* used an alternative route for exploring the reactivity of different surface structures by selectively blocking surface sites using controlled dosing of surface poisons and measuring subsequent changes in catalytic properties.^{6,7}

By modifying the surface of an active metal, one can fully understand the changes in catalytic properties. In order to do this, a range of complementary techniques to characterise the surface are required. By combining cyclic voltammetry (CV) and *in situ* surface enhanced Raman spectroscopy (SERS), not only could the proportions of different surface sites available for adsorption at the catalyst surface after various surface modifications be determined, but also insight concerning the nature of adsorbed reaction intermediate and their bonding with the surface could be observed.

In the present study, two variants of surface Raman spectroscopy are brought to bear in order to obtain information concerning the nature of the surface intermediates forming when alkynes are undergoing hydrogenation at platinum electrode surfaces. In the first of these, Au@Pt core-shell nanoparticles are deposited on polycrystalline platinum electrodes.⁸ By limiting the gold core to a diameter of approximately 55 nm and the platinum shell to 2 nm in thickness, the nanoparticle reproduces surface-enhanced Raman properties similar to roughened gold electrode yet

exhibiting the surface chemistry of a normal platinum catalyst. Hence, SERS from a weakly SERS-active (but catalytically far more interesting) metal surface may readily be collected. In a more recent development, Tian and co-workers⁹ demonstrated that Au@SiO₂ nanoparticles (55 nm diameter gold core, 2 nm thick silica shell) deposited on a single crystal electrode could be used to observe SERS even from a well-defined single crystal surface. This breakthrough in the application of SERS was designated by these workers as shell-isolated nanoparticle enhanced Raman spectroscopy (SHINERS) and the method holds great potential for future *in situ* catalytic studies. Here, we exploit the technique to study, for the first time, molecular vibrations of adsorbed intermediates formed during the hydrogenation of a series of alkynes (**Figure 4.1**).

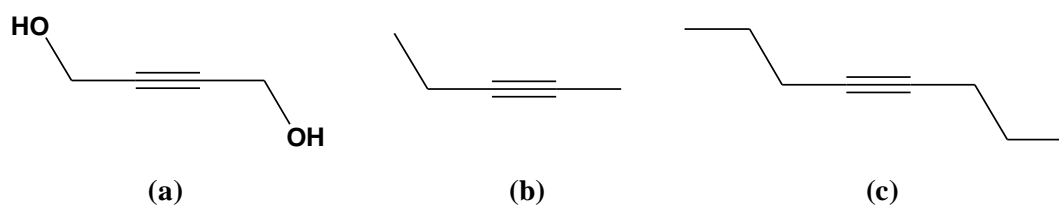


Figure 4.1 A scheme of targeted alkynes used in the present study. (a) 2-butyne-1,4-diol, (b) 2-pentyne, and (c) 4-octyne.

4.2 Results and Discussions

4.2.1 Studies of butynediol adsorption at Pt surfaces

4.2.1.1 CV of butynediol adsorption on Pt{*hkl*}single crystal electrodes

Firstly, butynediol adsorption on different Pt single crystal electrodes was explored using cyclic voltammetry. After dipping the flame-annealed single crystal electrodes into the 0.1 M butynediol aqueous solution and washing with water, cyclic voltammetry was carried out using a selected range of potential limits. In **Figure 4.2**, it is shown that only 25% of the Pt{111} surface area (as measured by H UPD charge) was blocked by butynediol after fast cycling between 0 ~ 0.4 V to obtain a stable voltammetric response (pink CV). The reason that the potential limit was initially maintained below 0.4 V was to avoid electrooxidation of butynediol adsorbed fragments in the first instance. In order to investigate how readily butynediol adsorbed species could be removed from the Pt surface, potential cycling between 0 and 0.8 V was carried out until a stable

voltammogram remained. A peak appearing between 0.6 and 0.7 V on the first cycle was strongly suggestive of adsorbed CO being removed from the surface during this procedure. It was estimated that approximately 90% of the irreversibly adsorbed butynediol was oxidized after potential cycling to 0.8 V resulting in an essentially unmodified Pt{111} CV (green) response save for the absence of the sharp sulphate phase transition peaks at 0.44 V.

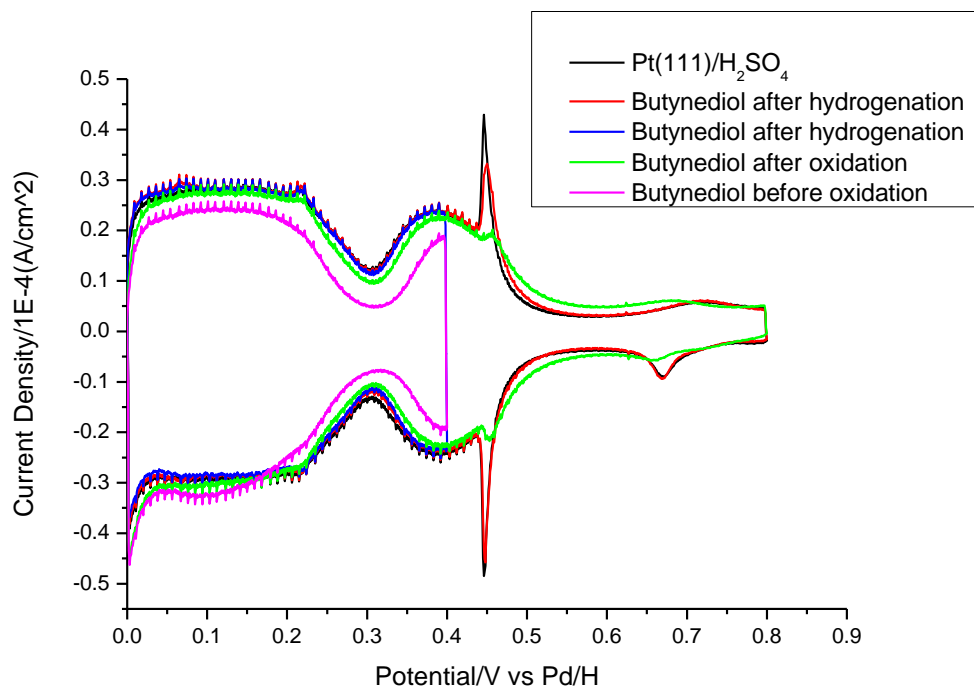


Figure 4.2 Cyclic voltammograms of butynediol irreversible adsorption on a Pt{111} single crystal electrode in 0.1 M sulphuric acid: before (pink) and after (green) electrooxidation (0.8V); after hydrogenation (blue and red, different positive potential limits), and the clean Pt{111} (black) CV response. Scan rate: $50 \text{ mV} \cdot \text{s}^{-1}$.

To further clean the Pt surface, hydrogen evolution on the Pt electrode surface was attempted in order to hydrogenate the residual adsorbed butynediol molecular fragments. The final voltammogram (red) was obtained after cycling voltammetry scans between -0.1 V and 0.8 V corresponding to both electrooxidation and hydrogenation steps. It is evident after excursions into the hydrogen evolution potential range that the resulting CV almost overlaps exactly with the CV of the clean Pt{111} surface signifying complete recovery of all Pt{111} adsorption behaviour. Hence, it is concluded that all irreversibly adsorbed butynediol has been removed

after this treatment. The presence of adsorbed CO would also indicate that some C–C bond cleavage may occur when butynediol adsorbs on platinum although electrochemical removal of all molecular intermediates formed on Pt{111} is straightforward.

In order to make a comparison of the butynediol adsorption behaviour between structurally different Pt surfaces, Pt{110} and Pt{100} single crystal electrodes were also used to carry out the same tests shown above. It can be seen that in **Figure 4.3**, more than 40% of the Pt{110} surface (pink) was blocked by butynediol irreversible adsorption before any electrooxidation treatment. Then, after potential cycling between 0 and 0.8 V, some of the adsorbed butynediol species were electrooxidised but residual amounts remained amounting to approximately 25% of H UPD sites blocked (green). Only after hydrogen evolution on the electrode surface at -0.1 V was carried out were the rest of the butynediol molecular fragments removed, leaving behind a voltammetric response almost indistinguishable from that of the pristine Pt{110} surface.

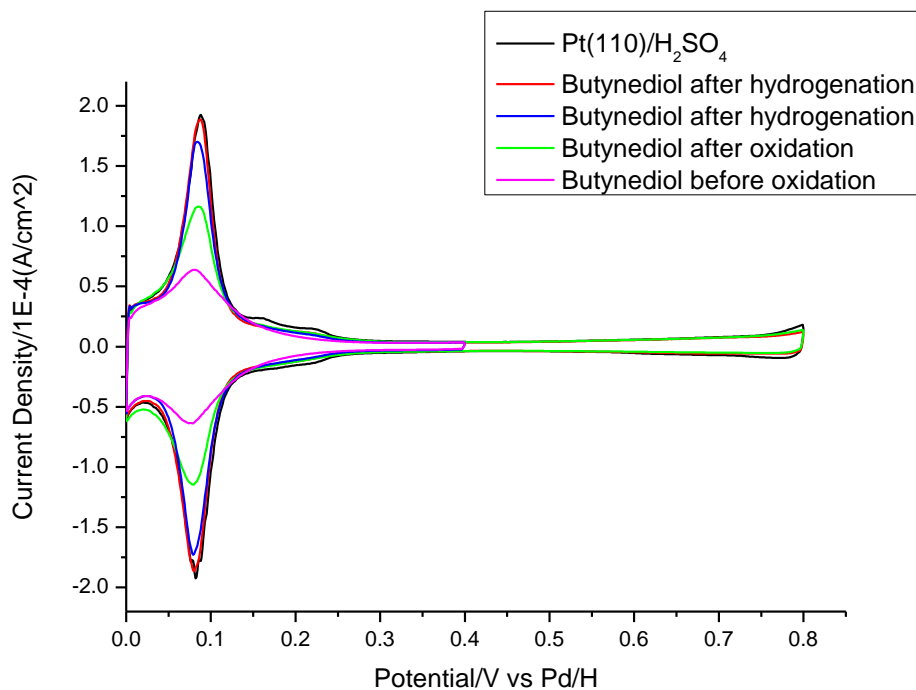


Figure 4.3 CVs of butynediol adsorption on a Pt{110} single crystal electrode in 0.1 M sulphuric acid: before (pink) and after (green) electrooxidation (0.8V); after hydrogenation (blue and red, different positive potential limits), and the clean Pt{110} voltammetric response (black). Scan rate: 50 mV·s⁻¹.

For the Pt{100} electrode, irreversible adsorption of butynediol was also observed with approximate 50% of H UPD sites being blocked (pink) as shown in **Figure 4.4**. However, most of the adsorbed butynediol could be removed easily by electrooxidation (green). The CV (red) showed limited change after evolving hydrogen at the electrode surface at -0.1 V. Hence, the clean Pt{100} surface couldn't be recovered completely suggesting a strongly adsorbed intermediate being formed resistant to electrooxidative or hydrogenative removal. The partially recovered CV (red) showed a 9% loss of H UPD charge relative to the clean surface CV.

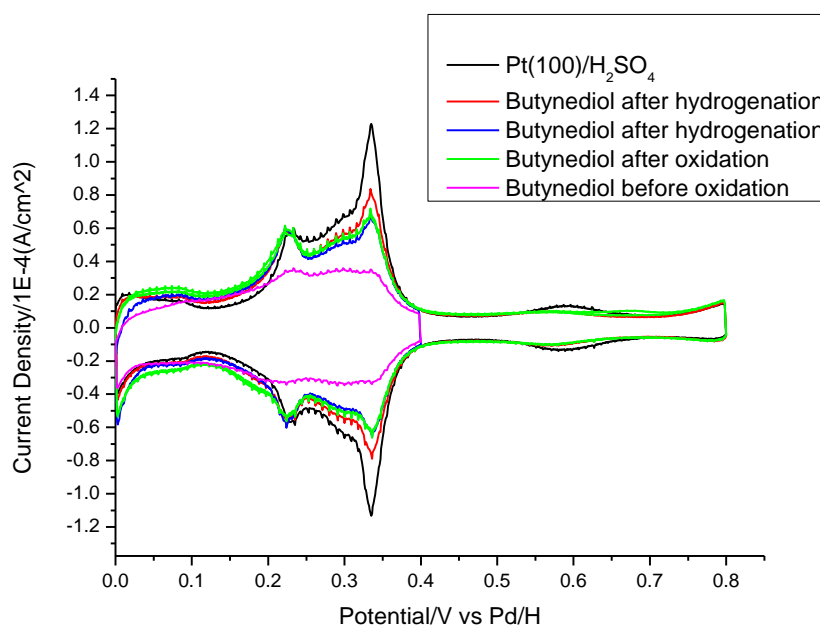


Figure 4.4 CVs of butynediol adsorption on a Pt{100} single crystal electrode in 0.1 M sulphuric acid: before (pink) and after (green) oxidation (0.8V); after hydrogenation (blue and red, different positive potential limits), and the clean Pt{100} CV response (black). Scan rate: 50 $\text{mV}\cdot\text{s}^{-1}$.

In order to gain further insight into the electrochemical stability of the various adsorbed intermediates together with some indication of when they form, one may perform so-called potential window opening experiments. For example instead of engaging a single potential sweep from 0 V to 0.8 V as described above, the start potential is set at 0.85 V followed by a series of potential sweeps to increasingly negative potential limits. In this way, the generation of surface intermediates as a consequence of surface redox reactions may be interrogated. Hence,

for Pt{111} modified with a layer of irreversibly adsorbed butynediol, **Figure 4.5** shows that Pt{111} surface sites were completely blocked as the {111} terrace sulphate electroadsorption feature at 0.44 V, the so-called butterfly peak, was not observed on the 0.85 V to 0.5 V sweep. This contrasts with the results depicted in **Figure 4.2**. This suggests that at an initial potential in the H UPD region enables some stripping of molecular fragments, freeing up H UPD sites.

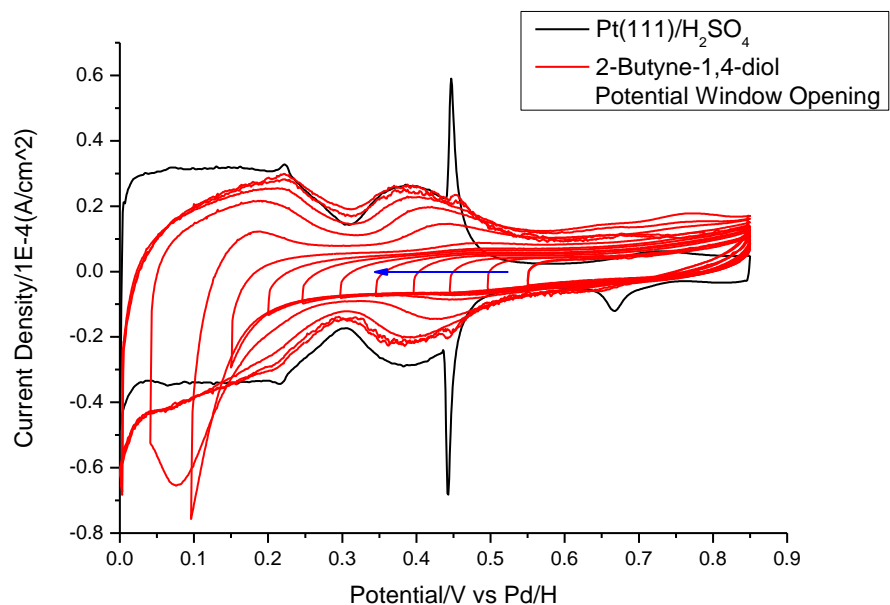


Figure 4.5 CVs of Pt{111} before (black) and after adsorption of butynediol in 0.1 M sulphuric acid. The red cycles indicate a window opening experiment in the direction of the horizontal arrow (blue). Scan rate: $50\text{mV}\cdot\text{s}^{-1}$.

In addition, no CO stripping peak between 0.6 and 0.7 V was observed on the initial potential sweep in **Figure 4.5** although CO was a known decomposition product of butynediol at platinum surfaces.¹⁰ This also suggested that activation of the surface to generate adsorbed CO requires a potential excursion to more negative potentials. Inspection of subsequent potential sweeps in the window-opening experiment depicted in **Figure 4.5** confirms this hypothesis. As long as the negative-going potential sweep reached into the H UPD region, CO electrooxidation was observed on the subsequent positive sweep, as a broad feature above 0.7 V which grew bigger in size the more negative the sweep.¹¹ As the potential was swept more negative, more surface H UPD sites were exposed. When the potential reached below 0.2 V, where H UPD on the

platinum occurred, a significant reduction current was observed. It is proposed that molecular fragments from butynediol adsorption are being hydrogenated at this point (with simultaneous formation of adsorbed CO) and subsequent removal of these fragments is manifested as an increase in the number of free Pt surface sites. It may be that CO formation requires an ensemble of at least two free Pt sites and therefore its appearance in CV is not seen until such sites are generated following electrochemical reduction/hydrogenation of adsorbed molecular fragments. It is evident that although CV can indicate the relative stability of molecular fragments, their amounts (in relation to blocked H UPD sites) and their nature (at least for adsorbed CO) cannot be exactly determined. Hence, *in situ* SERS tests are still required in order to discover the actual nature of the adsorption fragments themselves.

4.2.1.2 SERS of butynediol adsorption at a polycrystalline Pt surface

Figure 4.6 shows the Raman spectrum recorded using solid butynediol. The Raman bands were assigned using standard references^{12, 13} and these are listed in **Table 4.1**.

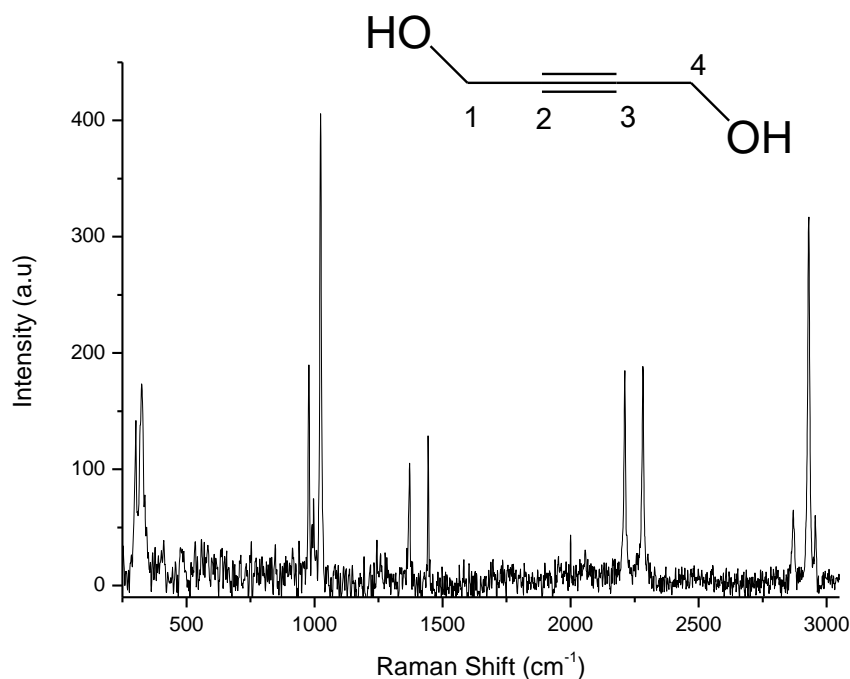


Figure 4.6 Raman spectrum of solid butynediol.

Table 4.1 Raman spectrum band assignments for solid butynediol

Band Positions (cm ⁻¹)	Assignment
2955	va(C ¹ -H ₂)(C ⁴ -H ₂)
2930	
2870	vs(C ¹ -H ₂)(C ⁴ -H ₂)
2283	va(C ² ≡C ³)
2212	vs(C ² ≡C ³)
1444	δd(C ¹ -H ₂)(C ⁴ -H ₂)
1371	δw(C ¹ -H ₂)(C ⁴ -H ₂)
1024	va(C ¹ -C ²)(C ³ -C ⁴)/v(C ¹ -O)(C ⁴ -O)
978	vs(C ¹ -C ²)(C ³ -C ⁴)
325	skeletal (C ² ≡C ³)
302	
172	

Figure 4.7 shows the SER spectra from a variety of platinum electrode surfaces undergoing the hydrogen evolution reaction (HER) in the presence of 0.1 M butynediol electrolyte flowing through the cell. Some of the Raman peaks were readily identified, such as C-H stretches at 2955, 2930 and 2870 cm⁻¹, C≡C triple bond stretches at 2283 and 2212 cm⁻¹, and C-C stretches at 1024 cm⁻¹. As shown in **Figure 4.7a** and **4.7b**, rather weak SER spectra were obtained from spherical platinum nanoparticles supported on a platinum electrode. This was consistent with the known Raman behaviour of roughened platinum relative to the coinage metals, such as silver and gold.¹⁴ However, two new features in the spectra were observed from Pt nanoparticles under electrochemical conditions associated with the presence of the peaks at 1580 and 490 cm⁻¹. The first of these was ascribed to an alkenic stretch associated with a di-sigma/pi-bonded surface intermediate reported previously (**Figure 4.8**).^{15, 16} Compared to a normal non-conjugated alkene stretch (~ 1640 cm⁻¹), there was a red shift in frequency of the 1580 cm⁻¹ band. This was rationalised previously as being due to a strong interaction of the double bond with the platinum surface.¹⁰ There were other differences between these two spectra. When the electrode potential was held at potentials in the double layer region (0.4 V, **Figure 4.7a**) where adsorbed hydrogen

was absent, the 1580 cm^{-1} peak was more intense compared to when the electrode was evolving hydrogen (**Figure 4.7b**). This behaviour is consistent with a steady state scenario whereby the rates of adsorption and hydrogenative desorption determine the overall surface coverage. Hence, a larger amount of the di-sigma/pi-bonded complex could remain in steady state on the surface in the absence of electroadsorbed hydrogen. Conversely, in the presence of hydrogen, a relative decrease in the surface population of the di-sigma/pi-bonded surface complex occurred, which would be caused by hydrogenative desorption of the alkenic surface intermediate to the corresponding alkane. Hence, a corresponding decrease in band intensity would be observed. The peak at around 490 cm^{-1} would be consistent with a metal-carbon stretch vibration.

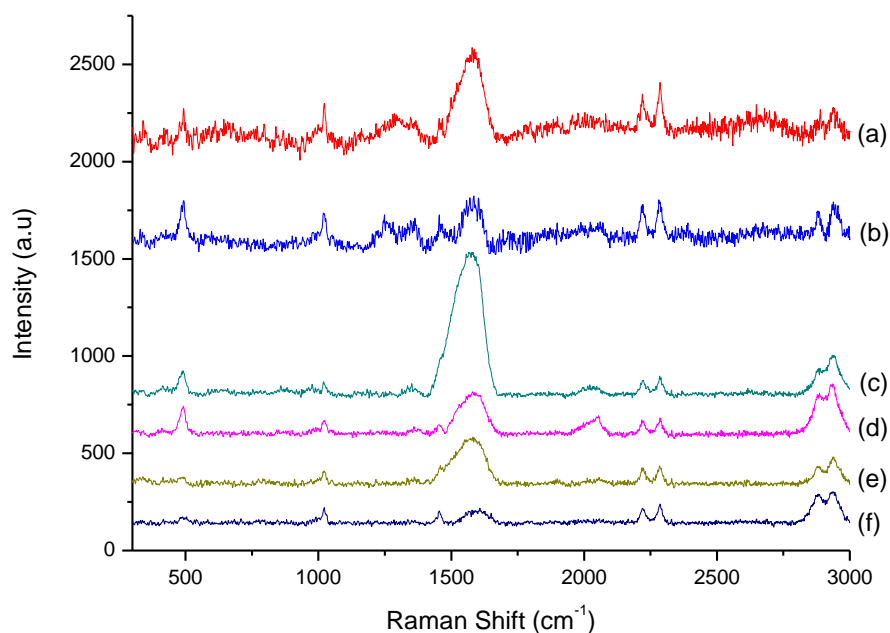


Figure 4.7 SER spectra (a-f) of butynediol. (a) and (b) spherical Pt NPs at double layer and HER potentials respectively. (c) and (d) Au@PtNPs at double layer (0.4 V) and HER (-0.1 V) potentials respectively. (e) and (f) as for (c) and (d) except Pt defect sites were blocked by bismuth. Electrolyte consists of aqueous 0.1 M sulphuric acid together with 0.1 M butynediol.

In order to increase the magnitude of the SERS signal from standard platinum substrates, experiments were next performed on Au@Pt core-shell nanoparticles, as described previously in the experimental section.⁸ By the long range effect of the electromagnetic field enhancement

created by the gold core, more intense SER spectra of species adsorbed on the platinum shell were observed. In **Figure 4.7c** and **4.7d**, typical data of butynediol adsorption were observed by using this approach. The peaks associated with both solution phase and chemisorbed butynediol were clearly seen in the spectra. A much better signal-noise ratio than found using spherical Pt nanoparticles was observed with adsorbed butynediol peak intensities being greater than those originating from the bulk electrolyte peaks. Under HER conditions, a broad series of peaks ranging from 1280 to 1575 cm^{-1} appeared immediately. In addition, the peak centred at 2025 cm^{-1} provided evidence for the presence of atop adsorbed CO on the platinum surface. Hence, the peak at around 490 cm^{-1} may be ascribed to the metal-carbon stretch of adsorbed CO.¹⁷ However, weak metal-carbon vibrations from the sigma-bonded surface intermediate are also expected to appear in this spectral region and therefore cannot be ruled out entirely. At the potential of 0.4 V (**Figure 4.7c**), the magnitude of the 1574 cm^{-1} peak was three times larger than when the surface was evolving hydrogen. This was because even under hydrogenation conditions, the di-sigma/pi- complex was still stable to a certain extent due to the steady state between adsorption rate and hydrogenation rate. In addition, the surface coverage of CO decreased in the absence of hydrogen gas, which was proved by the fall in intensity of both the 2000-2040 cm^{-1} and 490 cm^{-1} peaks. There were also some interesting changes in the intensity of the C-H stretch region. When the electrode surface was undergoing hydrogen evolution, more intense peaks appeared compared to their intensity at potentials removed from the HER. This phenomenon was tentatively ascribed to a change in the interaction of the (CH₂) groups with the surface. Under hydrogenation conditions, a tilting towards the surface of the alkenic bond of the di-sigma/pi- complex possibly occurred as previously reported by Foucault and co-workers for the case of long chain surfactant molecules (see **Figure 4.8**).¹⁸

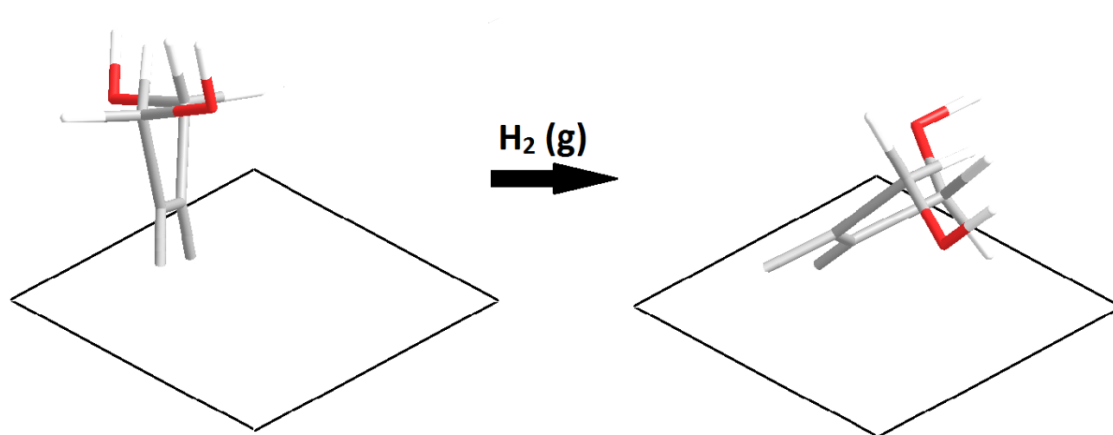


Figure 4.8 Schematic diagram showing tilting of surface di-sigma/pi-bonded intermediate upon evolving hydrogen leading to greater interaction of methylene groups with surface.

The defect sites of a catalyst played a really important role in promoting the hydrogenation of alkynes to alkanes. If defect sites were deliberately blocked by either bismuth or organic residues (Pt nanoparticles prepared via biological/bacteria means), a significant increase in selectivity towards semi-hydrogenation products was observed, as reported in reference 15. Therefore, *in situ* and spectroscopic re-evaluation of such surface-modified particles was thought crucial to discover changes in the nature of the adsorbed intermediates derived from butynediol when such defect sites were blocked. For a surface in which 80% of defect sites on the Au@Pt NPs were blocked by bismuth, **Figure 4.7e** and **4.7f** revealed that substantial perturbations had indeed been promulgated relative to the SERS data obtained in the absence of bismuth. In particular, the intensity of the di-sigma/pi-bonded surface complex peak at 1574 cm^{-1} became very weak when the surface was undergoing HER (**Figure 4.7f**). It only recovered to about 25% of its original value in the absence of adsorbed bismuth (**Figure 4.7c**) when data were collected at potentials positive of the HER. This suggested that the di-sigma/pi-bonded surface complex was strongly associated with defect sites. If prevented from forming at defect sites, it would result in large increases in semi-hydrogenation selectivity.¹⁹ In addition, the intensity of peaks associated with adsorbed CO was also weakened when bismuth was adsorbed at defect sites. This was consistent with previous electrochemical studies in which the CO formation, derived from organic molecules decomposing primarily at defect sites on platinum electrodes, was suppressed when bismuth was adsorbed in these defect sites.²⁰

4.2.1.3 SHINERS of butynediol adsorption at Pt{111} single crystal electrode

In order to confirm that alkyne adsorption on Pt defect sites are intimately connected with di-sigma/pi- surface complex formation, SHINERS was used to investigate the electrochemical hydrogenation of butynediol using both pristine and defective single crystal Pt{111} electrodes. **Figure 4.9** shows SHINERS data for butynediol adsorption at a Pt{111} electrode surface as a function of potential. Because 0.1 M perchloric acid was used as the electrolyte, a sharp peak at 934 cm^{-1} was observed in both spectra due to the symmetric Cl–O stretch of the perchlorate anion of the electrochemical double layer. As seen with the Pt and Au@Pt core-shell nanoparticles, peaks ascribable to both adsorbed and electrolyte phase butynediol were observed in the spectra. However, unlike previous results, no matter whether the electrode was evolving hydrogen or not, the 1574 cm^{-1} peak hardly changed in size. This behaviour was attributed to the absence of surface defect sites at the Pt{111} electrode surface. In order to further confirm this assertion, the electrode potential was cycled to more positive potentials to form/desorb an electrochemical oxide layer in the electrolyte containing 0.1 M sulphuric acid. During this procedure, surface defects would be formed at the Pt{111} electrode surface, which may be monitored by CV as the appearance of {110} step sites at 0.1 V whilst {111} terrace anion adsorption sites at 0.4 V were attenuated.²¹ **Figure 4.10** shows the subsequent butynediol hydrogenation SHINERS data using the electrochemically roughened Pt{111} electrode in aqueous sulphuric acid. As can be seen, the data revealed features more similar to spectra collected previously using the Au@Pt nanoparticles. First of all, the intensity of the 1580 cm^{-1} peak increased substantially when the electrode was swept to potentials in the double layer (by a factor of three compared to the HER region). In addition, the presence of adsorbed CO was indicated by enhanced peak intensity around 489 and 2032 cm^{-1} . Furthermore, a slight increase in the C–H stretch peak intensities at HER potentials, particularly the symmetric (CH_2) stretch at 2879 cm^{-1} relative to the asymmetric stretch at 2938 cm^{-1} , was observed.

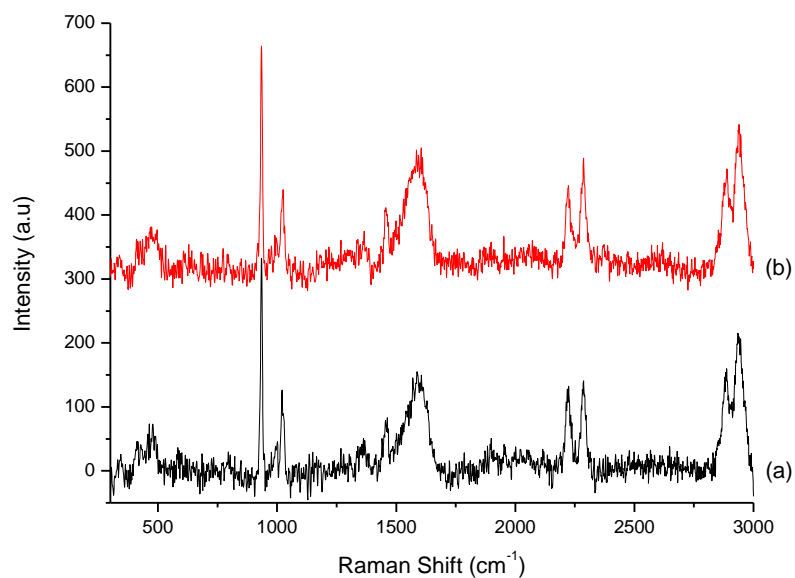


Figure 4.9 SHINERS of 0.1 M butynediol in 0.1 M perchloric acid adsorbed at Pt{111} at (a) HER potential (-0.1V) and (b) double layer potential (0.4V).

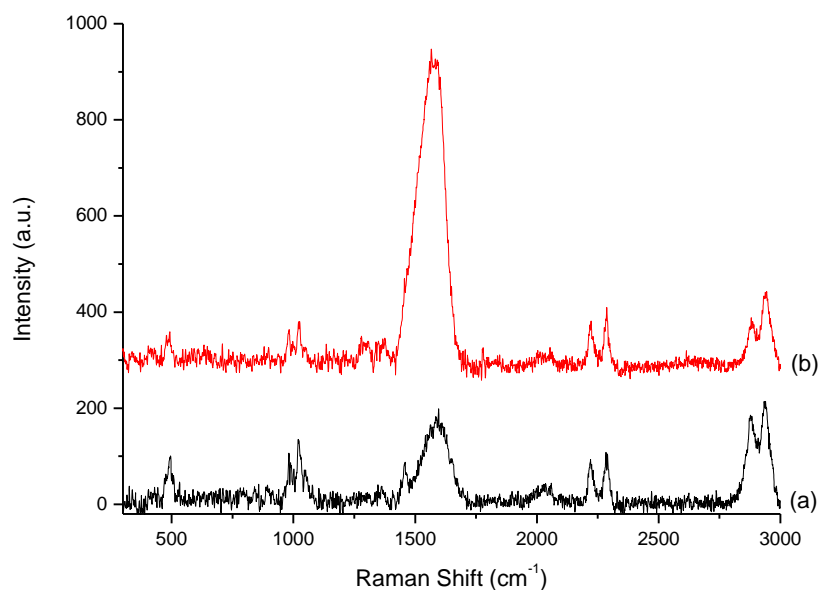


Figure 4.10 Same as Figure 4.9 except that the Pt{111} surface has been electrochemically roughened and the perchloric acid electrolyte replaced with aqueous sulphuric acid.

4.2.1.4 SERS of butenediol adsorption on Au@Pt NPs surface

In order to compare with butynediol adsorption behaviour, the final experiment performed was to investigate the SERS of 2-butene-1,4-diol (butenediol) under HER conditions. Butenediol is the semi-hydrogenated product of butynediol. **Figure 4.11a** shows the Raman spectrum of bulk butenediol. Intense bands at 3082, 2935 and 2876 cm^{-1} were ascribed to C–H stretch vibrations of the C=C–H, CH_2 asymmetric and CH_2 symmetric stretches respectively. The sharp peak at 1660 cm^{-1} was assigned as the C=C stretch. The CH_2 distortion mode was ascribed to the 1464 cm^{-1} peak, while the CH in plane bend of the alkene was assigned to the 1259 cm^{-1} feature. Finally, the three bands around 1000 cm^{-1} were assigned to skeletal C–C stretches.

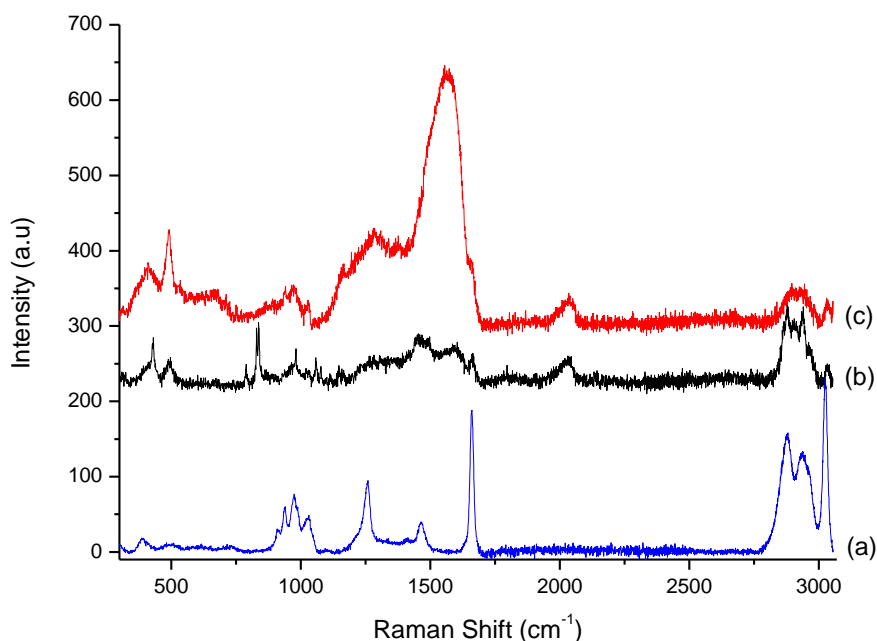


Figure 4.11 Raman spectra of (a) bulk butenediol and (b) SER spectra of 0.5 M butenediol in 0.1 M sulphuric acid adsorbed on Au@Pt NPs at HER potential (-0.1V) and (c) double layer potential (0.4V).

In **Figures 4.11b** and **4.11c**, the SER spectra for butenediol adsorbed on Au@Pt nanoparticles at HER and double layer potentials are shown. The adsorbed intermediate band appearing at 1567 cm^{-1} was remarkably similar to that observed for butynediol adsorption. Other similarities, such

as CO formation (peaks at 2030 and 494 cm^{-1}) and a relative increase in intensity of all C–H stretches with the presence of hydrogen gas, were also noted. These aspects strongly suggested a common surface di-sigma/pi-bonded surface intermediate being formed in both the alkyne and alkene surface reactions. Avery and Sheppard¹⁶ who studied *cis*- and *trans*- but-2-ene and but-2-yne on Pt{111} under ultra-high vacuum conditions reached exactly the same conclusion for room temperature alkyne adsorption utilising thermal desorption spectroscopy and high resolution electron energy loss spectroscopy. They proposed the same common surface intermediate being formed at room temperature consisting of a di-sigma/pi-bonded alkene. It should be noted also that the solution phase (bulk) butenediol peaks were very weak compared to the situation involving butynediol. This was even more remarkable when the fact that the bulk concentration of butenediol was five times greater than the butynediol concentration (**Figure 4.7**) was taken into consideration. This suggested that the much stronger interaction of alkynes compared to alkenes with the metal surface caused a physisorbed layer of alkyne to form in which negligible perturbation of the molecular integrity of the alkyne was observed. Also, the chemisorbed layer gave rise to stronger SERS signal for the ‘bulk’ alkyne, especially when the decay in SERS from the surface is reported to fall rapidly with distance.²²⁻²⁴ That is, the localised surface plasmon resonance extinction wavelength maximum, λ_{max} , is sensitive to the dielectric constant ε (or refractive index, n ; both are related by $\varepsilon = n^2$. Eq. 4.1),^{25, 26} the EM-field decay length is approximated as a single exponential decay with characteristic decay length l_d .

$$\Delta\lambda = m\Delta n \left[1 - \exp\left(-2d/l_d\right) \right] \quad (\text{Eq. 4.1})$$

Where m is the bulk refractive-index response of the NPs; Δn is the change in refractive index induced by the adsorbate; d is the effective adsorbate layer thickness; and l_d is the characteristic EM-field-decay length.

4.2.2 Studies of 2-pentyne and 4-octyne adsorption at Pt surfaces

4.2.2.1 CV of 2-pentyne and 4-octyne adsorption on Pt{*hkl*} single crystal electrodes

Other alkyne adsorption behaviour on platinum surfaces was studied to compare with the butynediol results. 2-Pentyne (pentyne) and 4-octyne (octyne) were chosen to be tested as they lack OH groups which could affect their adsorption ability. In addition, comparison of octyne

and pentyne might afford interesting results as well. Due to differences in chain length and solubility in aqueous media.

Firstly, pentyne and octyne adsorption on Pt{111} single crystal electrodes was explored with CV. After adsorbing the alkynes (the procedure was similar to the one used for butynediol adsorption except dosing was from the pure liquid alkyne), the Pt{111} electrode was transferred into the cell containing 0.1 M degassed sulphuric acid. **Figure 4.12** shows the CVs of Pt{111} single crystal electrodes before and after adsorption of the alkynes. In **Figure 4.12a**, the CV (pink) showed that more than half of the H UPD sites of Pt{111} were blocked by pentyne, whilst only 25% of these sites were blocked by octyne (pink CV in **Figure 4.12b**). The electrode potential was then cycled between 0-0.85 V as usual to oxidise the molecular fragments adsorbed on the platinum surface. Both pentyne and octyne were mostly electrooxidised and removed from the surface, leaving the electrode with 90% of its H UPD sites available compared to the clean electrode surface (green CVs in **Figure 4.12**). Only by evolving hydrogen gas on the electrode surface, could the Pt{111} electrode recover 98% of its original features, with the appearance of the sharp sulphate phase transition peak at 0.44 V (red CVs in **Figure 4.12**). However, the surface containing adsorbed octyne was slightly cleaner than the one with pentyne, presumably because it had fewer H UPD sites blocked to begin with.

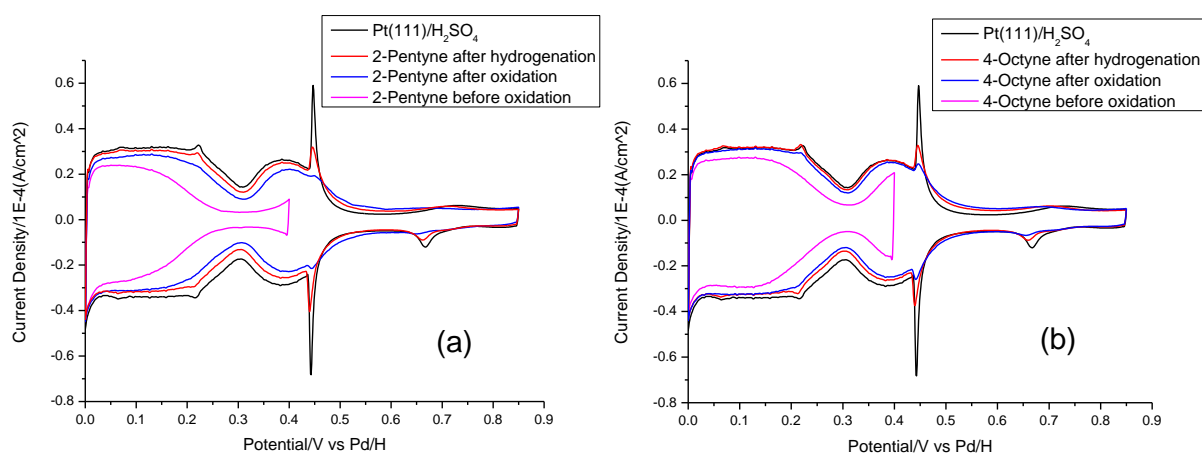


Figure 4.12 CVs of (a) 2-pentyne and (b) 4-octyne adsorption on a Pt{111} single crystal electrode in 0.1 M sulphuric acid: before (pink) and after (blue) electrooxidation (0.85 V); after hydrogenation (red, -0.1 V), and the clean Pt{111} CV response (black). Scan rate: 50 mV·s⁻¹.

Pentyne and octyne adsorption on Pt{110} and Pt{100} surfaces was also studied to make a comparison with the behaviour exhibited by Pt{111}. Unlike their adsorption on Pt{111}, both alkynes displayed hardly any variations in their adsorption behaviour irrespective of the Pt{*hkl*} plane employed, *ie.* both octyne and pentyne adsorbed to the same extent. This is different to the case of Pt{111}. As shown in **Figure 4.13**, the pink CVs suggest that both pentyne and octyne exhibited a coverage of about 50% of H UPD sites on both Pt{110} and Pt{100} prior to any electrochemical treatment. After both electrooxidation and hydrogenation procedures, the platinum surfaces were cleaned more and more until reaching a limit where by 95% of H UPD sites were recovered for Pt{110} and 80% for Pt{100} (red CVs). This indicated once again that the alkynes interacted most strongly with Pt{100}. In addition, the surfaces with adsorbed octyne were always cleaner than with pentyne, also suggesting pentyne had a stronger bonding with the platinum surfaces.

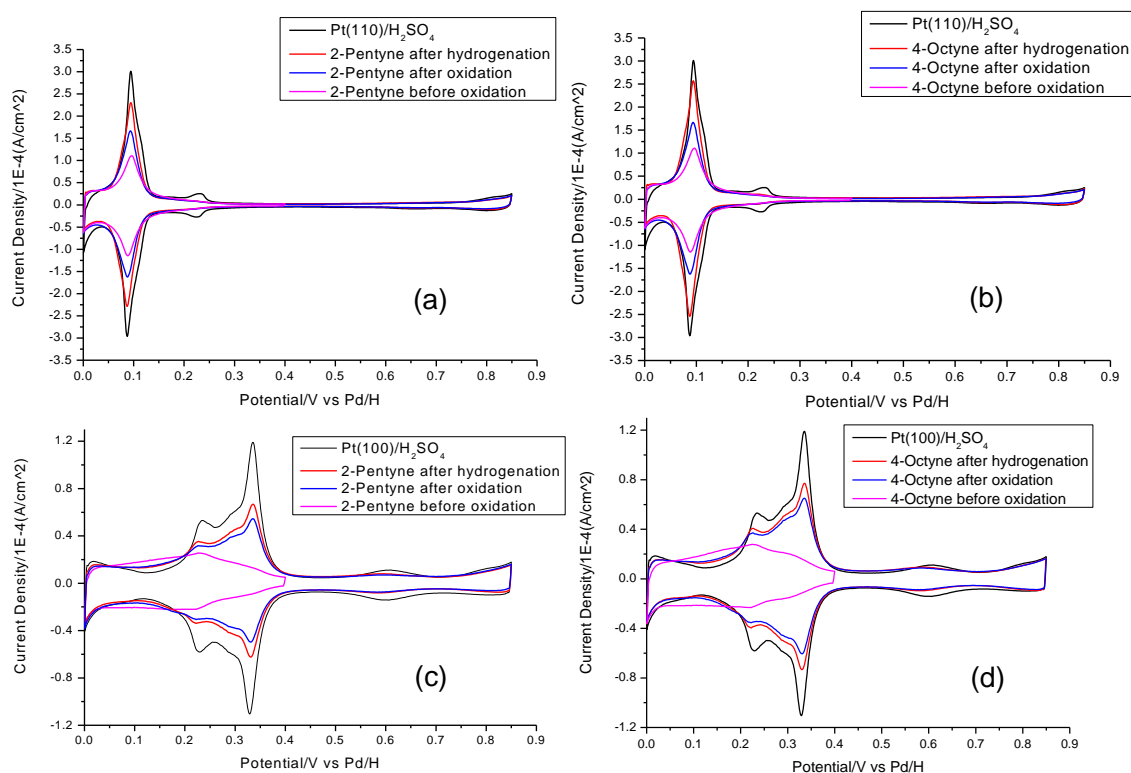


Figure 4.13 CVs of (a, c) 2-pentyne and (b, d) 4-octyne on Pt{110} (a, b) and Pt{100} (c, d) single crystal electrodes in 0.1 M sulphuric acid: before (pink) and after (blue) electrooxidation

(0.85 V); after hydrogenation (red, -0.1 V), and the clean single crystal electrodes CV response (black). Scan rate: 50 mV·s⁻¹.

4.2.2.2 *In situ* SERS studies of 2-pentyne and 4-octyne adsorption at polycrystalline Pt surface

Figure 4.14 shows SER spectra from the platinum surface of the Au@Pt NPs undergoing hydrogen evolution reaction in the presence of a saturated pentyne in aqueous 0.1 M HClO₄ solution. As is shown in **Figure 4.14a**, the broad band between 2850 and 2930 cm⁻¹ was ascribed to the symmetric and asymmetric C–H stretches of the bulk pentyne and its hydrogenated products. The pair of peaks at 2238 and 2305 cm⁻¹ are associated with the C≡C triple bond stretches, although one was much stronger than the other. The peak at 1035 cm⁻¹ was assigned to C–C stretches, while the one at 398 cm⁻¹ was due to C–C≡C–C skeleton vibrations.¹³ There was always a sharp peak at 934 cm⁻¹ due to the perchlorate vibrations (HClO₄ used as the electrolyte) as mentioned earlier. All the peaks were observed as well when the electrode was stepped to the double layer potential (0.4 V, **Figure 4.14b**). However, some extra bands also appeared in the spectra at this potential. The most obvious one was the broad band centred at 1580 cm⁻¹, which was due to the alkenic stretch associated with the di-sigma/pi-bonded surface intermediate. Also, a small band due to the stretch of adsorbed CO on the platinum surface at 2030 cm⁻¹. The corresponding metal-carbon, CO–M and C–M vibrations were signified by the appearance of the band at 490 cm⁻¹. Finally, a slight decrease of all C–H stretch peak intensities at double layer potentials (0.4 V) was seen.

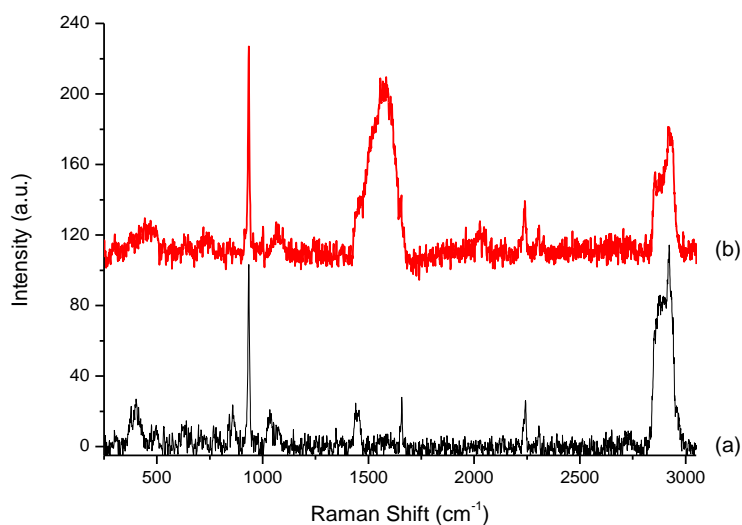


Figure 4.14 SER spectra of 2-pentyne in 0.1 M perchloric acid adsorbed on Au@Pt NPs at (a) HER potential (-0.1 V) and (b) double layer potential (0.4 V).

When 2-pentyne was substituted by octyne, the same SERS experiments were performed and the results are depicted in **Figure 4.15**. As usual, bands due to the bulk octyne were observed. The symmetric and asymmetric C–H stretches of octyne and its hydrogenated products gave rise to a broad band between 2850 and 2965 cm^{-1} . Only one peak for C \equiv C stretches appeared at 2230 cm^{-1} , which was weaker than the one in pentyne. This is because the C \equiv C band is usually weak when there is a degree of symmetry in the molecule.¹³ The peak at 1078 cm^{-1} was assigned to C–C stretches. When hydrogen was present (**Figure 4.15a**), there were hardly any bulk octyne bands present, except the C–H stretches above 2820 cm^{-1} . Instead, a new intense band at 2090 cm^{-1} was observed. It was due to the Pt–H stretch vibrations, which are normally seen only when organic/impurities are absent from the electrolyte. As a large peak due to Pt–H vibrations could be observed from the surface, we deduce that the bulk concentration of 4-octyne was so low that the steady state condition of adsorbed product could not be maintained. That is, the amount of octyne in the bulk solution was so small, it was insufficient to maintain a surface coverage under HER condition. Furthermore, depletion of octyne via hydrogenation also disfavoured subsequent physisorption of alkyne such that even bulk bands are ‘missing’. When the potential was changed to reside in the double layer (**Figure 4.15b**), the Pt–H band completely disappeared, whilst an intense band at 1580 cm^{-1} appeared. Similar to pentyne, it was due to the alkenic

stretches of the surface complex with a di-sigma/pi bond to the surface. Under this condition, some bulk bands of octyne were also observed, such as C≡C stretches at 2230 cm⁻¹ and C–C stretches at 1078 cm⁻¹. The C–H vibrations were also less intense compared to those in the hydrogen evolution situation.

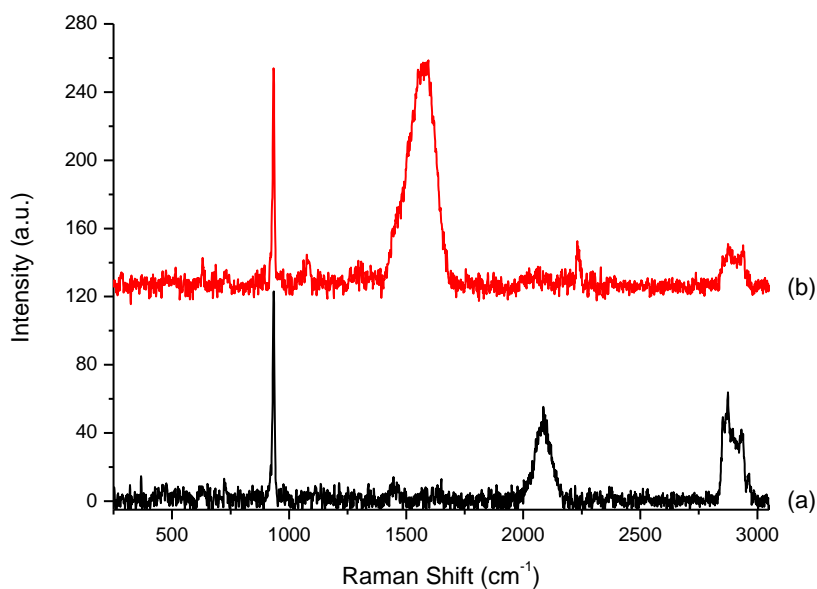


Figure 4.15 SER spectra of 4-octyne in 0.1 M perchloric acid adsorbed on Au@Pt NPs at (a) HER potential (-0.1 V) and (b) double layer potential (0.4 V).

4.2.2.3 *In situ* SHINERS studies of 2-pentyne and 4-octyne adsorption on Pt{*hkl*} single crystal electrodes

In order to determine the contribution of defect sites in forming the di-sigma/pi- surface complex from alkynes, SHINERS was used to elucidate the electrochemical hydrogenation of both pentyne and octyne on platinum single crystal electrodes. First, the SER spectra of pentyne adsorption on a Pt{111} surface is shown in **Figure 4.16**. In both spectra, the band centred at 2920 cm⁻¹ was due to the C–H stretch vibration of the bulk pentyne and its hydrogenated products. Only one band associated with the C≡C triple bond stretches could be observed at 2234 cm⁻¹, with the spectrum collected at 0.4 V (**Figure 4.16b**) showing a slightly more intense 2234 cm⁻¹ peak than at the HER potential (**Figure 4.16a**). A sharp peak at 1649 cm⁻¹, which only

appeared at the HER potential, might be due to the C=C stretching vibrations of *cis* -CH=CH- stretch of the hydrogenated product.¹³ When the hydrogen was absent, the band of this species could hardly be observed. Further evidence of forming this particular product was the appearance of a new band at 730 cm⁻¹ in both spectra. Interestingly, it was not discovered on the surface of Au@Pt NPs. This was assigned as the C-H deformation vibrations of -CH=CH- in *cis*-disubstituted alkene which, in this case, was *cis*-2-pentene.¹³ At the HER potential, the peak at 497 cm⁻¹ was weak, but sharp. This was probably due to the C=C skeletal vibrations of the product. And it was even weaker at the double layer potential. The major difference between the spectra obtained on Pt{111} single crystal electrode surface and Au@Pt NPs surface was that there was no broad band around 1580 cm⁻¹ observed in the former situation. It means the di-sigma/pi-bonded surface intermediate was not formed on the (111) surface. All the bands were associated with the hydrogenated products close to the surface without actually binding to it.

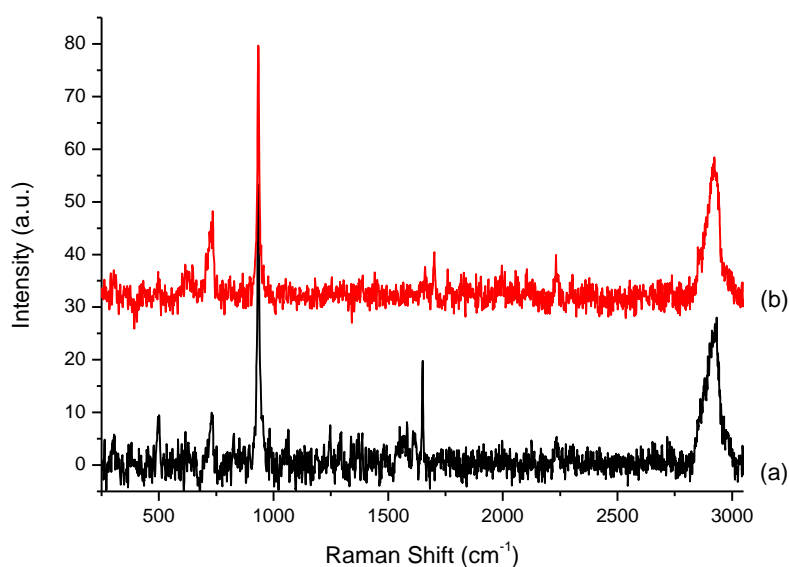


Figure 4.16 SHINER spectra of 2-pentyne in 0.1 M perchloric acid adsorbed on Pt{111} single crystal electrode surface at (a) HER potential (-0.1 V) and (b) double layer potential (0.4 V).

Then, the adsorption of pentyne on a Pt{110} surface was studied by SERS measurements. As is shown in **Figure 4.17**, the regular bands due to bulk alkyne molecules close to the surface were observed. For example, the symmetric and asymmetric C-H stretches of the bulk pentyne and its

hydrogenated products gave rise to a broad band between 2800 and 2950 cm^{-1} . One of bands due to the $\text{C}\equiv\text{C}$ triple bond stretching vibrations was observed at 2234 cm^{-1} as before. The sharp peak at 1649 cm^{-1} , if not buried in the broad band, could still be seen at the HER potential. Moreover, the band at 730 cm^{-1} due to the C–H deformation vibrations of a $-\text{CH}=\text{CH}-$ substituent supported the production of *cis*-disubstituted alkene. Besides, it could be easily noticed that the broad band at 1580 cm^{-1} reappeared in both spectra. It suggested that the di-sigma/pi-bonded surface intermediate was stably adsorbed on the {110} surface. Also, there was CO formed in this process since a band at 2000 cm^{-1} was also observed consistent with atop CO.

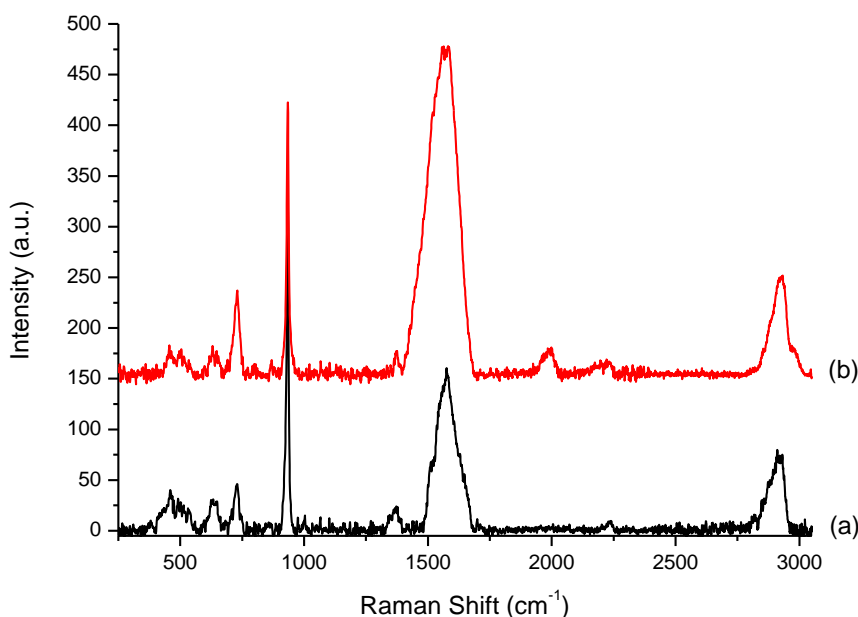


Figure 4.17 SHINER spectra of 2-pentyne in 0.1 M perchloric acid adsorbed on Pt{110} single crystal electrode surface at (a) HER potential (-0.1 V) and (b) double layer potential (0.4 V).

Finally, Pt{100} was investigated in relation to the adsorption of 2-pentyne. Since it was a flat terraced surface, unsurprisingly the spectra obtained at both HER and double layer potentials were similar to the ones on Pt{111} surface (**Figure 4.18 a and b**). Typical vibrational bands appeared as usual, such as the symmetric and asymmetric C–H stretching vibrations between 2850 and 2960 cm^{-1} , the $\text{C}\equiv\text{C}$ triple bond stretches at 2234 cm^{-1} (and maybe 2302 cm^{-1}), the C=C stretching vibrations at 1649 cm^{-1} , the C–H deformation vibrations of *cis* $-\text{CH}=\text{CH}-$ at 730

cm^{-1} , and the C=C skeletal vibrations at 495 cm^{-1} . There were hardly any signs of adsorbed intermediate on the surface except the appearance of a weak broad band at around 1585 cm^{-1} at the double layer potential (0.4 V). This di-sigma/pi-bonded surface intermediate may only survive a little bit under this condition. After roughening the surface electrochemically, not only the intensity of the spectra became stronger, indicating more products were generated; but the broad band at 1580 cm^{-1} appeared, especially at the double layer potential. This was due to the creation of defect sites on the surface made more di-sigma/pi-bonded surface intermediate adsorbed.

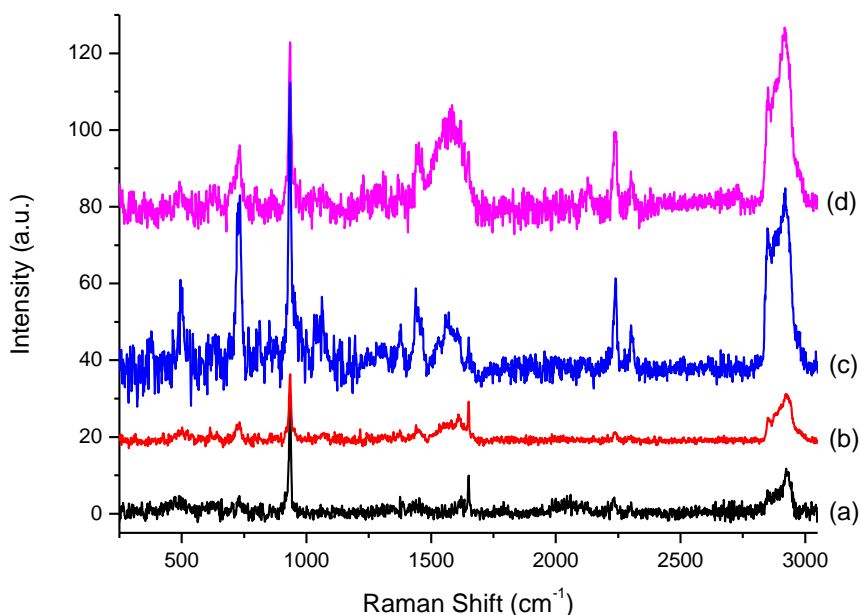


Figure 4.18 SHINER spectra of 2-pentyne in 0.1 M perchloric acid adsorbed on flat (a, b) and roughened (c, d) Pt{100} single crystal electrode surface at (a, c) HER potential (-0.1 V) and (b, d) double layer potential (0.4 V).

To make a comparison with pentyne, octyne was explored by adding it into the electrolyte. Different well defined platinum single crystal electrodes were used as well to study octyne adsorption on the surfaces. First, the SHINERS of octyne adsorption on Pt{111} was studied and the data collected is shown in **Figure 4.19**. It was easy to spot that the bands due to bulk octyne appeared at least in one of the spectra, such as symmetric and asymmetric C-H stretches between

2850 and 2965 cm^{-1} , CH_3 bending vibration at 1450 cm^{-1} , and C–C stretches at 1075 cm^{-1} . The differences between the two spectra at HER and double layer potentials mainly included a huge increase of the band centred at 1580 cm^{-1} in the latter one, which was due to the di-sigma/pi-bonded surface complex formed on the platinum {111} surface. It was more stable when there was no presence of hydrogen, which would usually reduce the alkene to the corresponding alkane. In addition, CO was formed at double layer potential (0.4 V) as suggested by the appearance of the peak at 1990 cm^{-1} . Bulk octyne was adsorbed on the surface in the steady state situation as well because the peak due to C \equiv C stretch vibrations at 2235 cm^{-1} was observed. Most interestingly, a new band between 800 and 900 cm^{-1} appeared. It was assigned as the CCC chain stretching vibrations of octyne, which was not observed on polycrystalline platinum surfaces previously.

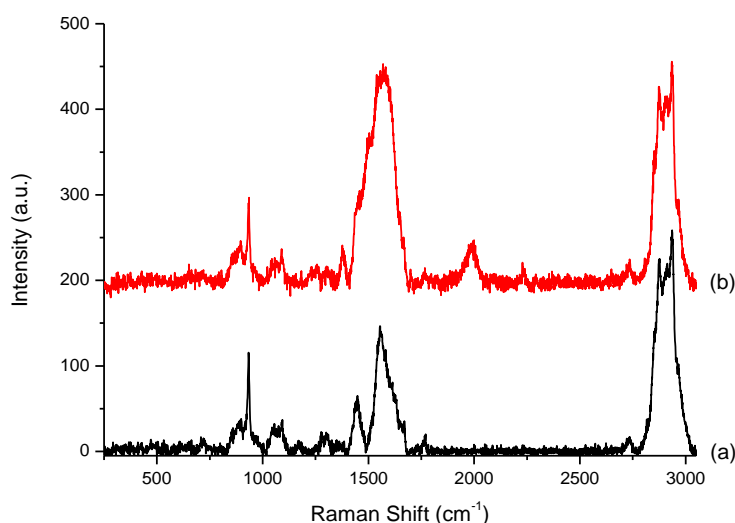


Figure 4.19 SHINER spectra of 4-octyne in 0.1 M perchloric acid adsorbed on Pt{111} single crystal electrode surface at (a) HER potential (-0.1 V) and (b) double layer potential (0.4 V).

On the Pt{110} surface, the peak due to Pt–H vibrations was observed at 2090 cm^{-1} whilst evolving hydrogen on the electrode (**Figure 4.20a**). It was similar to the result obtained using a polycrystalline platinum surface as seen in **Figure 4.15a**. At double layer potentials, CO was formed as signified by the appearance of the peak at 2000 cm^{-1} (**Figure 4.20b**). Therefore, the metal-carbon vibration band at 490 cm^{-1} was assigned to the contribution of the adsorbed CO.

Also, the bulk octyne appeared to be physisorbed on the surface at this potential (-0.1 V) because of the peak at 2235 cm^{-1} associated with the alkyne carbon triple bond stretches. Most interestingly, the band around 1580 cm^{-1} was again seen to increase compared to the HER region at the double layer potentials (0.4 V). Again, the broad band below 900 cm^{-1} due to CCC chain stretches on the surface was observed in both spectra, only it was bigger with the presence of hydrogen.

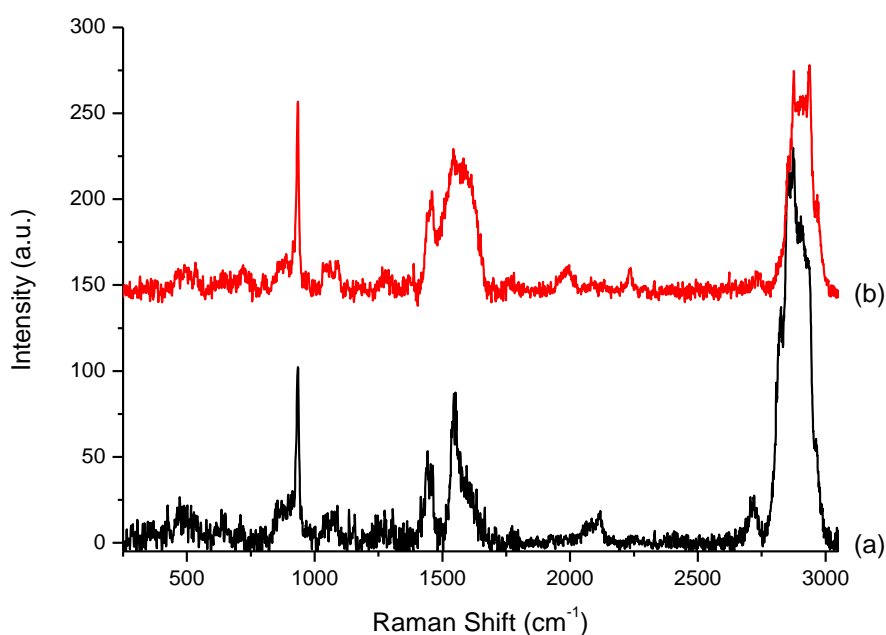


Figure 4.20 SHINER spectra of 4-octyne in 0.1 M perchloric acid adsorbed on Pt{110} single crystal electrode surface at (a) HER potential (-0.1 V) and (b) double layer potential (0.4 V).

The last test of octyne adsorption was carried out on Pt{100} and the results are shown in **Figure 4.21**. Clearly, besides the observation of several common peaks (symmetric and asymmetric C–H stretches between 2850 and 2965 cm^{-1} , CH_3 bending vibration at 1450 cm^{-1} , and C–C stretches at 1075 cm^{-1}), the one due to metal-carbon vibrations at 490 cm^{-1} was quite obvious in both spectra. However, no adsorbed CO was observed as there was no sign of any band appearing around 2000 cm^{-1} in either spectrum. At double layer potentials (0.4 V), the band at 1580 cm^{-1}

was five times the intensity of the one at HER potentials. It suggests that, on (100) terraces, the di-sigma/pi-bonded complex was stably adsorbed much more without the presence of hydrogen and hardly adsorbed when hydrogen was evolved. Meanwhile, the peak due to C≡C stretches was not observed, which suggests that the bulk octyne was not adsorbed on (100) terraces as easily as other surfaces. However, the band due to CCC chain stretches at 850 cm⁻¹ could be observed at under HER conditions but not at the double layer potential region, which meant that there was still octyne adsorbed on the (100) terraces.

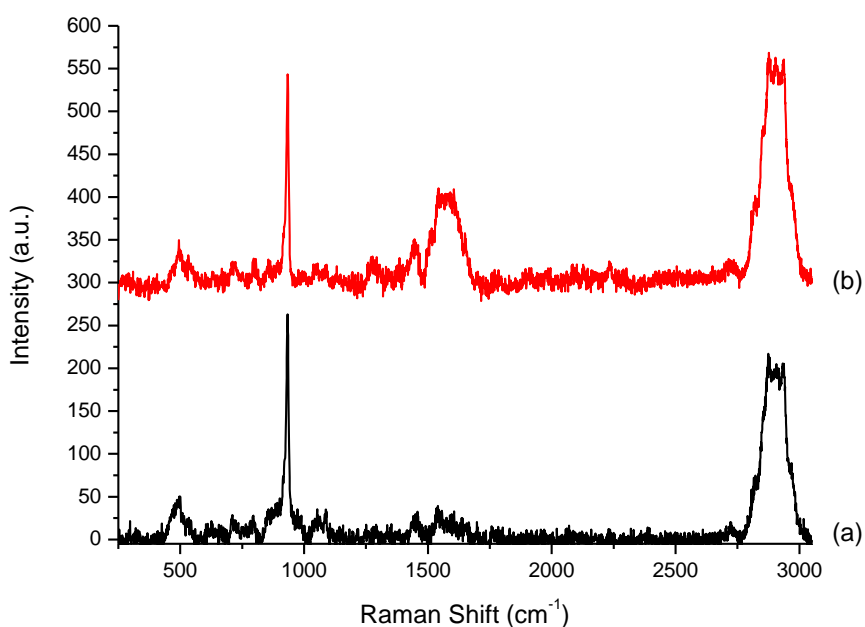


Figure 4.21 SHINER spectra of 4-octyne in 0.1 M perchloric acid adsorbed on Pt{100} single crystal electrode surface at (a) HER potential (-0.1 V) and (b) double layer potential (0.4 V).

4.2.3 Discussion

With CV measurements, all the ‘saturated’ coverages of the irreversibly adsorbed alkyne molecules on platinum surfaces were studied. Differences in this parameter for various Pt{*hkl*} were observed. The main conclusion was that Pt{111} was remarkably resistant to alkyne irreversible adsorption compared to Pt{100} and Pt{110}. For butynediol, the maximum extent of irreversible adsorption was with Pt{100} with 50% of all H UPD sites blocked following

dosing of the surface. For Pt{111}, only a quarter of these sites were blocked. Hydrogen gas evolution was found to be an effective treatment for the removal of any molecular fragments formed but adsorbed CO generated by this required potential excursions to > 0.7 V to completely strip it from the Pt surface. The generation of adsorbed CO is a common intermediate formed on Pt by alcohol containing organic molecules.²⁷ For pentyne and octyne, which are not soluble in water, dosing them on the platinum surfaces was achieved by exposure to neat liquid alkyne. In terms of the blockage of the platinum surface, there were hardly any differences between the {100} and {110} surfaces, with about half of the H UPD sites blocked after such treatment. Interestingly, the only difference in blocking behaviour between octyne and pentyne was observed using Pt{111}. Pentyne covered twice the surface area compared to octyne. Only speculative reasons for this effect may be given. The key difference between Pt{111} and the other Pt surfaces studied seems to be the weaker interaction with alkynes. If adsorption was a balance between alkyne solubility in aqueous media, bulkiness of alkyl groups and the surface adsorption enthalpy, possibly in the case of Pt{100} and Pt{110} overrides any subtle differences in the physical properties of octyne and pentyne. For Pt{111}, the weakness of the surface interaction may allow these physical differences to dominate.

Again, with electrochemical treatments, the hydrogen formed on the surface was found to reductively strip any molecular fragments formed. Hence, under real catalytic conditions, removal of the alkyne from the surface should be facile, only being inhibited should significant amounts of adsorbed CO form which would remain stable unless removed by combination with adsorbed OH to form carbon dioxide.

A key finding of the present study from *in situ* SERS measurements of butynediol is that defect sites appear to be strongly associated with the formation of adsorbed di-sigma/pi-bonded alkenic intermediates following alkyne adsorption at Pt electrodes. No matter it was the Au@Pt NPs surface, or the roughened Pt{111} surface on which defect sites were created, the intermediates showed a preferential adsorption and strong binding. Inspection of the surface Raman spectra also reveals that the C=C stretch band around 1580 cm^{-1} is actually rather broad and probably consists of several overlapping peaks in the range of $1500\text{-}1600\text{ cm}^{-1}$. Interestingly, even for Pt{111} (**Figure 4.9**), the C=C stretch band exhibited a substantial peak width suggesting a variety of bonding configurations associated with the surface intermediate. We suggest that

variations in the angle of tilt between the surface and the plane of the alkene may be responsible for this behaviour.¹⁵ It should also be noted that polymerisation of alkynes at surfaces has been reported²⁸ and it may be that interactions between pi-electrons on a number of adsorbed intermediates could be responsible for this peak-broadening effect. More work is required to elucidate the precise nature of the interaction giving rise to peak broadening. Nonetheless, there is a satisfactory confluence of reactivity, CV and SERS/SHINERS data pointing to the importance of defect sites in controlling hydrogenation selectivity. If defect sites population is controlled, selectivity to alkene is also controlled when alkynes are selectively hydrogenated at platinum catalysts.

In order to compare with the behaviour of butynediol adsorption, the adsorption of butenediol on the surface of Au@Pt nanoparticles was explored. The remarkably similar intermediate band was observed at 1567 cm^{-1} , which strongly suggested a common surface di-sigma/pi-bonded surface intermediate being formed in both the alkyne and alkene surface reactions.

The study of pentyne and octyne adsorption on different platinum surfaces by SERS shared some common findings. On polycrystalline platinum surfaces, there were only di-sigma/pi-bonded intermediates forming at the double layer potentials for both chemicals. The surface complex could hardly survive when hydrogen was evolved on the surface. Especially for octyne, Pt-H species were dominant on the surface (**Figure 4.15a**), attesting to the lack of uptake of octyne on this surface since Pt-H stretches are characteristic of clean Pt. So comparing with pentyne, octyne more weakly adsorbs on the platinum surface.

By looking more deeply at the spectra obtained with pentyne on different single crystal surfaces, one finds that there was hardly any intermediate formed on the {111} and {100} surfaces. However, on the {110} and roughened {100} surfaces, the band associated with the pi-bonded surface intermediate appeared due to the generation of defect sites.

The SER spectra obtained with octyne were not necessarily the same as the ones with pentyne. Since for all different types of surfaces, the intermediate could more or less form on them. Sometimes, the band at around 1550 cm^{-1} was sharp, indicating a specific binding orientation of the surface complex was formed, especially when hydrogen was evolved. Then at the double layer potential, this band became stronger and broader, suggesting that more configurations of

the intermediate could form on all different types of surfaces in a more stable situation. Meanwhile, as octyne is a molecule with a longer chain, the CCC chain stretches were clearly observed in the spectra due to the appearance of a broad band at 900 cm^{-1} .

4.3 Conclusion

The hydrogenation reactivity behaviour of different platinum surface was investigated by combining CV, SERS and SHINERS techniques. Different platinum surfaces in the form of nanoparticles and single crystals were studied. It was shown that alkyne adsorption on Pt defect sites produces a long-lived di-sigma/pi-alkene complex which may undergo further hydrogenation to produce alkane. This complex may form on different surfaces with various orientations. However, depending on the specific molecules, the intermediate may not survive on some surfaces due to the steady state conditions arising from the catalytic reaction whereby adsorption of alkyne and hydrogenative desorption of reaction intermediates determines the overall surface coverage of intermediate as a function of potential.

4.4 References

1. B. Bridier and J. Pérez-Ramírez, *Journal of the American Chemical Society*, 2010, **132**, 4321-4327.
2. B. Bridier, N. Lopez and J. Perez-Ramirez, *Dalton Transactions*, 2010, **39**, 8412-8419.
3. M. García-Mota, B. Bridier, J. Pérez-Ramírez and N. López, *Journal of Catalysis*, 2010, **273**, 92-102.
4. M. Crespo-Quesada, A. Yarulin, M. Jin, Y. Xia and L. Kiwi-Minsker, *Journal of the American Chemical Society*, 2011, **133**, 12787-12794.
5. I. Lee, F. Delbecq, R. Morales, M. Albitzer and F. Zaera, *Nature Materials*, 2009, **8**, 7.
6. D. J. Jenkins, A. M. S. Alabdulrahman, G. A. Attard, K. G. Griffin, P. Johnston and P. B. Wells, *Journal of Catalysis*, 2005, **234**, 230-239.
7. G. A. Attard, K. G. Griffin, D. J. Jenkins, P. Johnston and P. B. Wells, *Catalysis Today*, 2006, **114**, 346-352.
8. J.-F. Li, Z.-L. Yang, B. Ren, G.-K. Liu, P.-P. Fang, Y.-X. Jiang, D.-Y. Wu and Z.-Q. Tian, *Langmuir*, 2006, **22**, 10372-10379.
9. J. F. Li, Y. F. Huang, Y. Ding, Z. L. Yang, S. B. Li, X. S. Zhou, F. R. Fan, W. Zhang, Z. Y. Zhou, Y. Wu de, B. Ren, Z. L. Wang and Z. Q. Tian, *Nature*, 2010, **464**, 392-395.
10. M. Bron and R. Holze, *Surface Science*, 2000, **457**, 178-184.
11. E. Herrero, A. Rodes, J. M. Pérez, J. M. Feliu and A. Aldaz, *Journal of Electroanalytical Chemistry*, 1995, **393**, 87-96.
12. M. I. Batuev, A. A. Akhrem and A. D. Matveeva, *Bulletin of the Academy of Sciences of the USSR, Division of chemical science*, 1960, **9**, 526-528.
13. G. Socrates, *Infrared and Raman Characteristic Group Frequencies: Tables and Charts*, Wiley, 2004.

14. L. Jensen, C. M. Aikens and G. C. Schatz, *Chemical Society Reviews*, 2008, **37**, 1061-1073.
15. J. P. Camplin, J. K. Eve and E. M. McCash, *Physical Chemistry Chemical Physics*, 2000, **2**, 4433-4440.
16. N. R. Avery and N. Sheppard, *Proceedings of the Royal Society of London. A. Mathematical and Physical Sciences*, 1986, **405**, 1-25.
17. P. Zhang, Y.-X. Chen, J. Cai, S.-Z. Liang, J.-F. Li, A. Wang, B. Ren and Z.-Q. Tian, *The Journal of Physical Chemistry C*, 2009, **113**, 17518-17526.
18. R. Foucault, R. L. Birke and J. R. Lombardi, *Langmuir*, 2003, **19**, 8818-8827.
19. J. A. Bennett, G. A. Attard, K. Deplanche, M. Casadesus, S. E. Huxter, L. E. Macaskie and J. Wood, *ACS Catalysis*, 2012, **2**, 504-511.
20. A. Sáez, E. Expósito, J. Solla-Gullón, V. Montiel and A. Aldaz, *Electrochimica Acta*, 2012, **63**, 105-111.
21. A. Björling and J. M. Feliu, *Journal of Electroanalytical Chemistry*, 2011, **662**, 17-24.
22. K. A. Willets and R. P. Van Duyne, *Annual Review of Physical Chemistry*, 2007, **58**, 267-297.
23. Y. Fang, Y. Wei, C. Bai and L.-s. Kan, *The Journal of Physical Chemistry*, 1996, **100**, 17410-17413.
24. Z.-Q. Tian, B. Ren, J.-F. Li and Z.-L. Yang, *Chemical Communications*, 2007, **0**, 3514-3534.
25. L. S. Jung, C. T. Campbell, T. M. Chinowsky, M. N. Mar and S. S. Yee, *Langmuir*, 1998, **14**, 5636-5648.
26. J. C. Hulteen and R. P. Van Duyne, *Journal of Vacuum Science & Technology A*, 1995, **13**, 1553-1558.
27. H. E. Morris, *Chemical Reviews*, 1932, **10**, 465-506.
28. B. Tardy and J. C. Bertolini, *J. Chim. Phys. Phys.-Chim. Biol.*, 1985, **82**, 407-414.

CHAPTER FIVE

Steric Effects in Hydrogenation of Alkynes and the Role of PVP in Promoting Selectivity

5.1 Introduction

SERS has been shown to be a powerful means for determining the orientation of molecules adsorbed on surfaces. According to ‘surface selection rule’ (see section 2.4.5.2), vibrations would be the most intense in the SERS spectrum if they derive their intensities from a large value of α_{zz} (z being the local surface normal). Hence, the geometry of surface compounds plays a significant role in their SERS response in relation to the intensities of individual bands. In particular, a compound which exhibits a planar structure can be characterised in terms of its orientation in space to a metal surface from measurement of the relative magnitude of the intensities of, for example, their C-H stretching bands in SERS.¹

When a molecule adsorbs on a metal surface, steric effects may cause changes of SERS band intensities as well. Steric hindrance occurs when the large size of a substituent group within a molecule prevents adsorption geometries that are normally observed in related molecules containing smaller groups. When the angle between the adsorbed molecule and the metal surface changes, the vibrational bands in SERS change accordingly. For example, in the SERS spectra of aromatic carboxylate acids, there are two typical bands related to the vibrational modes of the carboxylate group. The relative intensity of the $\nu_s(\text{COO}^-)$ band (1390 cm^{-1}) and the $\delta(\text{COO}^-)$ band (850 cm^{-1}) may be different because of the way carboxylates interact with the surface through their π -electrons (two-legged or one-legged geometry, tilt angle).²

Alkyne adsorption on platinum surfaces has already been discussed previously in Chapter Four which highlighted changes in adsorption relating to alkyne chain length. In this chapter, two more alkynes are chosen in order to explore their interactions with different platinum surfaces under various situations. As is shown in **Figure 5.1**, in contrast to the alkynes studied in Chapter Four, both propargyl alcohol (PA) and 2-methyl-3-butyn-2-ol (MeBuOH) contain a terminal H atom rather than alkyl groups at the C1 position. And MeBuOH contains two methyl groups (–

CH₃) at the C3 position while PA contains two H atoms. As a methyl group is larger than hydrogen, this would affect the way that the alkyne molecule interacts with the platinum surface. If the orientation alters, there should be some changes in the SERS reflecting this change in ‘accessibility’ of the alkyne group to Pt atoms in the surface. Therefore, in situ SERS experiments were performed using PA and MeBuOH undergoing hydrogenation on platinum surfaces together with CV to probe coverage and stability of adsorbed intermediates as a function of potential. Difference in behaviour between PA and MeBuOH should reflect the difference in tertiary and primary carbons at the carbon 3 position.

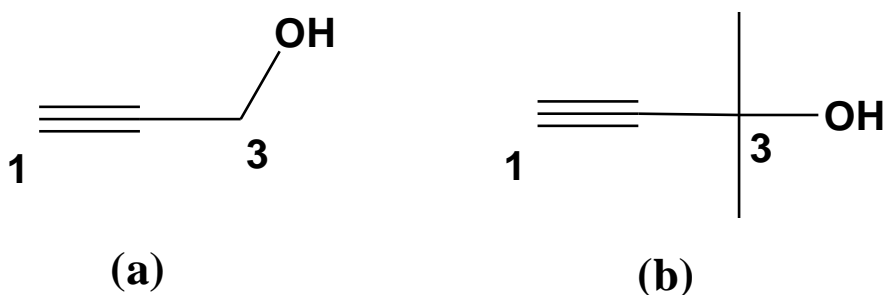


Figure 5.1 Schematic structures of (a) propargyl alcohol and (b) 2-methyl-3-butyn-2-ol.

In addition, the possible influence of polyvinylpyrrolidone (PVP) upon the selectivity of alkyne hydrogenation will be investigated via a series of coadsorption experiments. In particular, changes in the stability of alkyne chemisorbates will be interrogated by both CV and SHINERS under hydrogenating conditions.

5.2 Results and Discussions

5.2.1 CV studies of alkyne adsorption on Pt surfaces

5.2.1.1 CV of propargyl alcohol adsorption on Pt{*hkl*} single crystal surfaces

Propargyl alcohol adsorption on the three basal plane Pt single crystal electrodes was investigated with cyclic voltammetry. The usual preparation procedure outlined in Chapter Four was applied. The flame-annealed and hydrogen cooled electrode was dipped into a small amount of pure liquid propargyl alcohol. Then, after washing with water to remove the excess alcohol, cyclic voltammetry was performed.

Firstly, **Figure 5.2** shows the CVs of Pt{111} single crystal electrodes before and after propargyl alcohol adsorption. It can be seen that only 10% of the Pt{111} electrode surface area was blocked by propargyl alcohol (pink CV) prior to any electrochemical treatment. It indicated that propargyl alcohol weakly adsorbed onto the Pt{111} surface. By applying more positive potentials to the working electrode, some of the irreversibly adsorbed intermediates could be electrooxidised (potential cycles between 0 and 0.8 V). The CV in green suggests that most propargyl alcohol adsorbed on the surface was removed during this procedure. In order to recover the Pt{111} electrode CV response completely, hydrogen was evolved on the surface as potential cycling was carried out within the potential range between -0.1 V and 0.8 V. The red CV with a pair of sharp peaks at 0.44 V signified that the Pt{111} surface was almost as clean as the freshly flame annealed surface after this procedure.

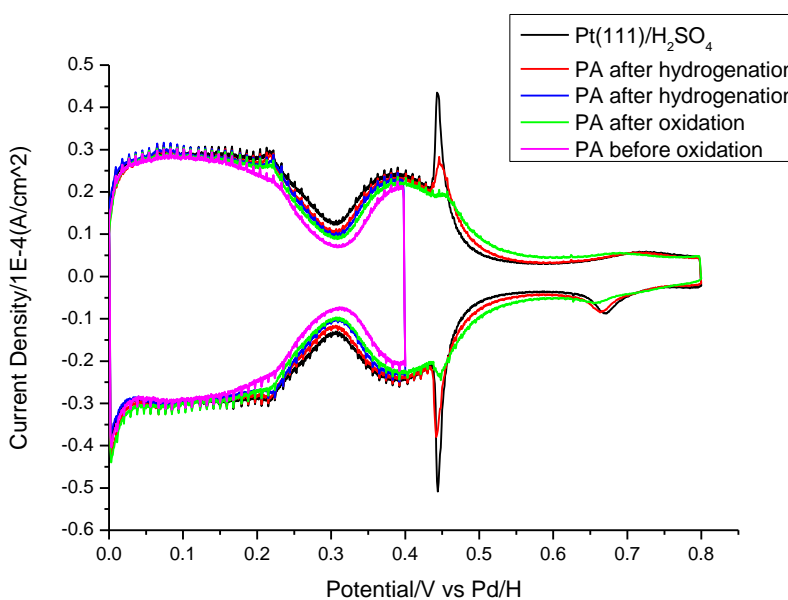


Figure 5.2 Cyclic voltammograms of propargyl alcohol irreversible adsorption on a Pt{111} single crystal electrode in 0.1 M sulphuric acid: before (pink) and after (green) electrooxidation (0.8 V); after hydrogenation (blue and red, different positive potential limits) and the clean Pt{111} CV response (black). Scan rate: 50 mV·s⁻¹.

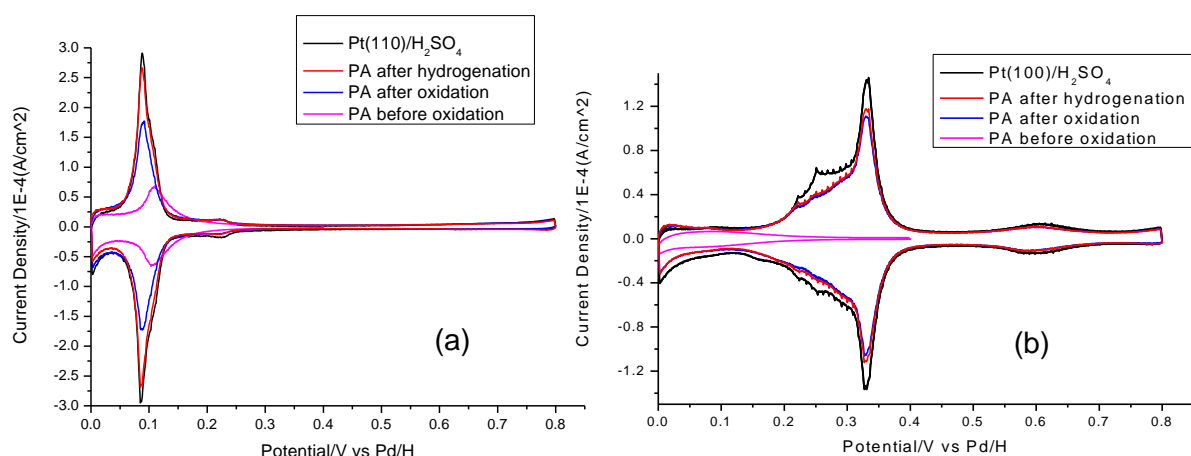


Figure 5.3 CVs of propargyl alcohol adsorption on (a)Pt{110} and (b) Pt{100}single crystal electrodes in 0.1 M sulphuric acid: before (pink) and after (blue) electrooxidation (0.8 V), after hydrogenation (-0.1 V, red), and the clean single crystal electrodes CV response (black). Scan rate: $50 \text{ mV}\cdot\text{s}^{-1}$.

The same dosing procedure was carried out using Pt{110} and Pt{100} single crystal electrodes to explore surface structural differences that could be giving rise to changes in PA adsorption. As is shown in **Figure 5.3**, propargyl alcohol could adsorb much more readily on these two crystal surfaces, with 75% coverage of all hydrogen underpotential deposition (H UPD) sites on Pt{110} and 90% on Pt{100}. In **Figure 5.3a**, the Pt{110} surface could be cleaned by electrooxidation and even recovered to 99% of the freshly flame annealed surface CV response after evolving hydrogen gas. In **Figure 5.3b**, the majority of irreversibly adsorbed species on Pt{100} could be removed via electrooxidation to 0.8 V as usual, but further hydrogenation could not recover the clean Pt{100} CV. Hence, propargyl alcohol or its decomposition products appear to adsorb most strongly on Pt{100}.

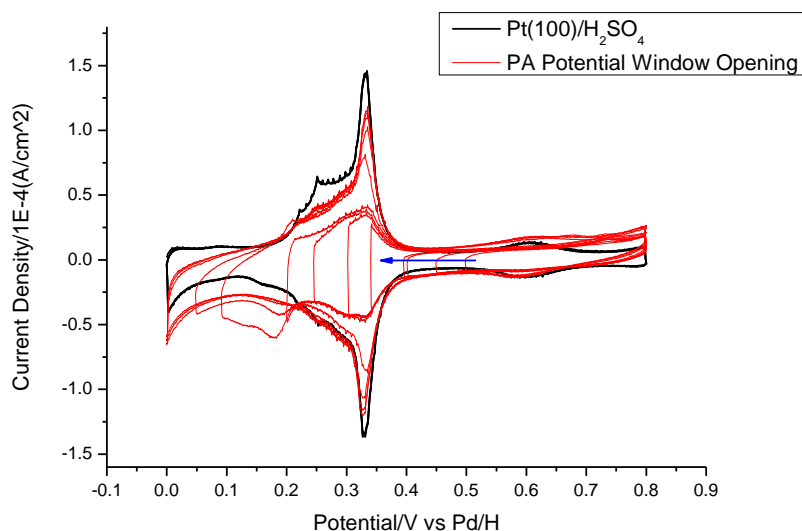


Figure 5.4 CVs of Pt{100} before (black) and after adsorption of propargyl alcohol in 0.1 M sulphuric acid. The red cycles indicate a window opening experiment in the direction of the blue horizontal arrow. Scan rate: 50mV s^{-1} .

Since the Pt{100} electrode surface gave rise to the most significant changes after adsorption of propargyl alcohol, potential window opening experiments were carried out to explore what products might be being generated with electrochemical treatments. As shown in **Figure 5.4**, the potential was scanned from the upper limit (0.8 V) to increasingly more negative potentials followed by scanning in the positive direction. It was discovered that, the double layer capacitance decreased after PA adsorption, indicating molecules had adsorbed on the surface. As the potential was swept more negative and reached into the H UPD region a peak below 0.7 V due to the electrooxidation of CO appeared on the positive part of the sweep cycle. At the same time, more surface sites were becoming available as signified by the increase in H UPD peak intensity. In particular, when the potential was below 0.2 V, a sharp reduction peak in the CV showed up and the (100) terrace sites began to gradually recover. It is suggested that the availability of Pt{100} terrace sites catalysed further reduction of adsorbed fragments of propargyl alcohol and helped clean the surface. In spite of this however, there still remained a residual quantity of adsorbed fragments that could not be removed by evolving hydrogen (as noted in previous experiments with Pt{100} in Chapter Four).

5.2.1.2 CV of 2-methyl-3-butyn-2-ol adsorption on Pt{*hkl*} single crystal surfaces

The adsorption of MeBuOH on Pt{*hkl*} single crystal electrodes was also investigated with cyclic voltammetry. Changes in CV might provide clues relating to differences between MeBuOH and propargyl alcohol adsorption since the bulky tertiary carbon position should dictate greater steric hindrance with the surface compared to adsorption of PA. Again, the CVs of MeBuOH adsorbed on the surface of Pt{111} single crystal electrode are presented first of all.

The pink CV in **Figure 5.5** shows that more than 80% of the Pt{111} surface was blocked by MeBuOH before any electrochemical treatment. This was a significantly larger coverage on Pt{111} compared to all alkynes studied thus far. After potential cycling in the range of 0 ~ 0.8 V, the green CV was obtained. Only about 10% extra of the H UPD surface area was freed up during this process which suggested that MeBuOH was adsorbing quite strongly on the Pt{111} surface. However, the adsorbed molecular fragments could still be removed rather easily by evolving hydrogen gas on the surface, as the red CV with a pair of sharp peaks suggested that more than 95% surface was recovered utilising this approach.

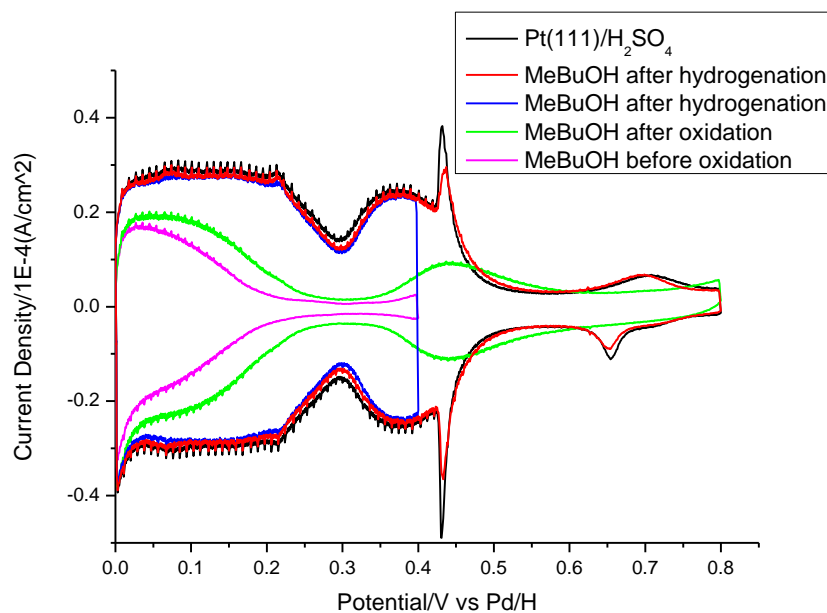


Figure 5.5 CVs of 2-methyl-3-butyn-2-ol adsorption on a Pt{111} single crystal electrode in 0.1 M sulphuric acid: before (pink) and after (green) electrooxidation (0.8 V); after hydrogenation

(blue and red, different positive potential limits) and the clean Pt{111} CV response (black). Scan rate: $50 \text{ mV}\cdot\text{s}^{-1}$.

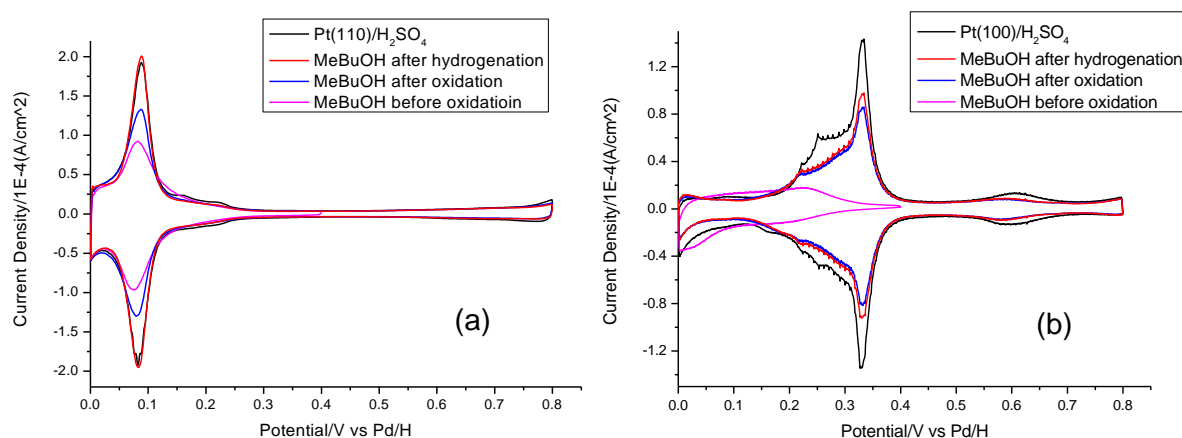


Figure 5.6 CVs of 2-methyl-3-butyn-2-ol adsorption on (a)Pt{110} and (b) Pt{100} single crystal electrodes in 0.1 M sulphuric acid: before (pink) and after (blue) electrooxidation (0.8 V), after hydrogenation (-0.1 V, red) and the clean single crystal electrodes CV response (black). Scan rate: $50 \text{ mV}\cdot\text{s}^{-1}$.

In **Figure 5.6** is shown the result of dosing Pt{110} and Pt{100} single crystal electrodes with MeBuOH and potential cycling between 0 and 0.4 V. The pink CVs in both **Figure 5.6a** and **5.6b** were obtained after this treatment. 70% of the H UPD surface area of Pt{110} was covered by MeBuOH adsorption, whilst 80% of Pt{100} was blocked. For Pt{110}, the majority of the adsorbed molecules were removed by electrooxidation. After hydrogenation, almost all of the surface sites were recovered and the CV of clean Pt{110} was obtained (red CV in **Figure 5.6a**). However, for Pt{100}, a result similar to that of propargyl alcohol adsorption was found with only partial recovery of all H UPD sites after hydrogenation.

To compare with the adsorption of propargyl alcohol on a Pt{100} electrode surface, potential window opening experiments were also carried out with MeBuOH. The same technique described before was applied here and the results are shown in **Figure 5.7**. It can be seen that as the potential became more negative eventually reaching the H UPD region, the electrooxidation of CO was observed at about 0.7 V. More and more CO was electrooxidised because the current increased around 0.7 V in the positive scan of the CV. When the potential reached below 0.3 V,

molecular fragments adsorbed on the platinum surface started to be reductively desorbed resulting in the appearance of H UPD peak intensity. The reason that more CO was being formed was because in parallel with freeing up Pt sites, decomposition of molecular fragments could take place leading to CO formation. A sharp reduction peak below 0.2 V indicated that the adsorbed molecules were hydrogenated when the Pt-H UPD species was present. After a couple of cycles, most of the (100) terraces were freed, which was consistent with behaviour observed previously.

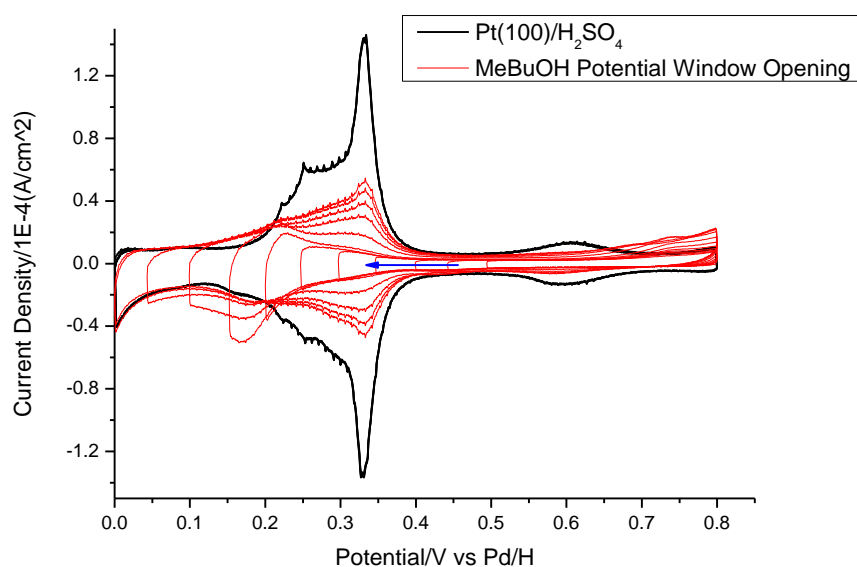


Figure 5.7 CVs of Pt{100} before (black) and after adsorption of 2-methyl-3-butyn-2-ol in 0.1 M sulphuric acid. The red cycles indicate a window opening experiment in the direction of the blue horizontal arrow. Scan rate: $50\text{mV}\cdot\text{s}^{-1}$.

5.2.2 *In situ* SERS studies of propargyl alcohol adsorption on Pt surfaces

5.2.2.1 Polycrystalline Pt surface

For the SERS tests, 0.1 M propargyl alcohol was added to the 0.1 M HClO_4 electrolyte which was passed through the flowcell. First, Au@Pt NPs were applied on the platinum working electrode in order to examine the adsorption of propargyl alcohol on polycrystalline Pt surfaces. As usual, with the control of the potential, *in situ* SERS experiments were carried out and the

spectra obtained are shown in **Figure 5.8**. Some of the peaks in both spectra were readily identified as being due to the bulk propargyl alcohol adsorption on the platinum surface. The peaks at 2881 and 2941 cm^{-1} were assigned as symmetric and asymmetric stretches of C–H bonds respectively. C \equiv C stretching vibrations gave a strong peak at 2122 cm^{-1} , while its skeletal vibrations gave a rather weak peak at 314 cm^{-1} . The band at 1457 cm^{-1} was caused by –CH₂–scissoring vibrations, whilst the one at 921 cm^{-1} was due to C–C \equiv C stretches. The band ascribed to C–O stretches occurred at 1030 cm^{-1} , while its deformation vibrations peak appeared at 557 cm^{-1} . Finally, the peak at 930 cm^{-1} was always observed because of the usage of HClO₄ as the electrolyte (symmetric Cl–O stretch of anion). Comparing the two spectra below, the broad band at 1560 cm^{-1} at HER potential (-0.1 V, **Figure 5.8a**) was much weaker than the one observed at double layer potentials (0.4 V, **Figure 5.8b**). This band, which was due to the alkenic stretches of the di-sigma/pi-bonded surface intermediate, was usually weak in the presence of coadsorbed hydrogen whereas it was much more intense at double layer potentials. Again, as mentioned in Chapter Four, a dynamic steady state situation of adsorption/hydrogenative stripping determines the surface coverage of the di-sigma/pi-bonded surface intermediate. The bands below 500 cm^{-1} are ascribed to the metal-carbon stretches on the surface. In addition, a slight increase of the intensity of C–H stretch peaks at HER potentials, particularly the symmetric stretch at 2881 cm^{-1} relative to the asymmetric stretch at 2932 cm^{-1} , was noted.

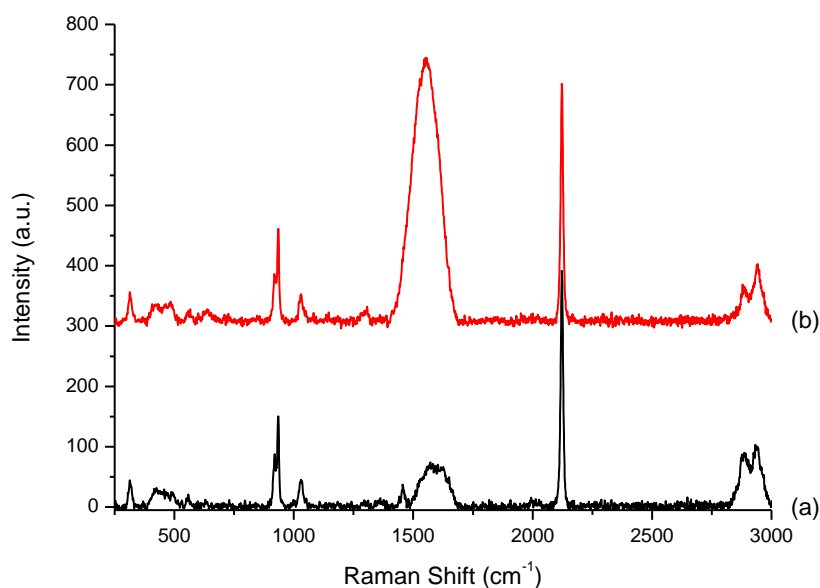


Figure 5.8 SER spectra of 0.1 M propargyl alcohol in 0.1 M perchloric acid adsorbed on Au@Pt NPs at (a) HER potential (-0.1 V) and (b) double layer potential (0.4 V).

5.2.2.2 Pt{*hkl*} single crystal surfaces

Well defined platinum single crystal electrodes were used in order to study the adsorption of propargyl alcohol on different surfaces. Therefore, Pt{111} single crystal electrodes decorated with Au@SiO₂ NPs were utilised as the working electrode. The SHINERS experiments were performed at two different potentials and the results are shown in **Figure 5.9**. Although these two spectra shared common peaks, both of them were dissimilar to the bands obtained on Au@Pt NPs surfaces. First, there was only one broad band appearing at 2930 cm⁻¹ due to C–H stretching vibrations. The symmetric and asymmetric stretches didn't give rise to distinct vibrational frequencies like those observed on the polycrystalline platinum surface. Also, the peak due to C≡C stretches at 2122 cm⁻¹ was rather weak compared to the SERS result on Au@Pt, whilst the C≡C skeletal stretch peak (314 cm⁻¹) could hardly be observed. The band assigned as the alkenic stretches of the di-sigma/pi-bonded surface complex was still observed on this (111) surface, but the intensity was far less than it was on the polycrystalline surface (using the perchlorate peak as a pseudo reference). At double layer potentials (0.4 V), it was slightly more intense than at HER potentials. This means that although more of this the intermediate adsorbed in the absence of hydrogen, it is still present even when the electrode is evolving hydrogen. In addition, CO formation was monitored via the appearance of the peak at 2000 cm⁻¹. Interestingly, a new peak at 1160 cm⁻¹ was discovered in both spectra. This could be possibly assigned as unsaturated –CH₂– in-plane deformation vibrations specific to species adsorbed on terraces rather than defects (hence, it is absent on polycrystalline surface). There was also a small broad band beneath the perchlorate peak. It was assigned to the α -unsaturated C–C stretching vibrations of alkyne again adsorbed on terraces due to its absence in the spectra from polycrystalline surfaces.

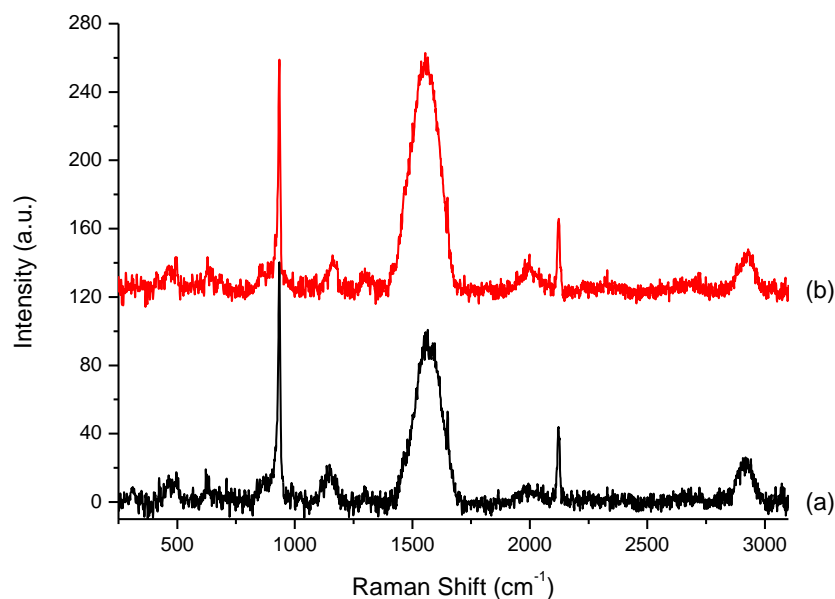


Figure 5.9 SER spectra of 0.1 M propargyl alcohol in 0.1 M perchloric acid adsorbed on Pt{111} single crystal electrode surface at (a) HER potential (-0.1 V) and (b) double layer potential (0.4 V).

The Pt{111} single crystal electrode was then replaced by Pt{110}, and the adsorption of propargyl alcohol explored. **Figure 5.10** shows the SER spectra obtained at two different potentials. Some peaks shown in the figure were similar to the ones with Pt{111}, such as C–H stretches at 2930 cm^{-1} , $\text{C}\equiv\text{C}$ stretches at 2122 cm^{-1} , adsorbed CO vibrations at 2000 cm^{-1} , $-\text{CH}_2-$ in-plane deformation vibrations at 1160 cm^{-1} and metal-carbon stretches below 500 cm^{-1} . However, the intensities of some of the peaks were different when compared to Pt{111}. For example, the alkenic stretches of the di-sigma/pi-bonded surface intermediate were more intense both at HER (-0.1 V) and double layer (0.4 V) potentials with the latter exhibiting greater intensity than the former. Because of the larger amount of the surface intermediate formed, the bulk molecule of propargyl alcohol was found to exhibit less surface adsorption based on the low intensity of the bulk bands. In addition, a broad band underneath the perchlorate peak (930 cm^{-1}) appeared at HER potentials and grew even bigger at double layer potentials. This was due to the α -unsaturated C–C stretching vibrations on the surface. A correlation between the intensity of this band and the di-sigma/pi-bonded surface intermediate band was indicated. Also indicated is

a growth in the intensity of the adsorbed CO feature around 2000 cm^{-1} consistent with the CV results showing that after reductive desorption of adsorbed fragments, pathways that form adsorbed CO become important.

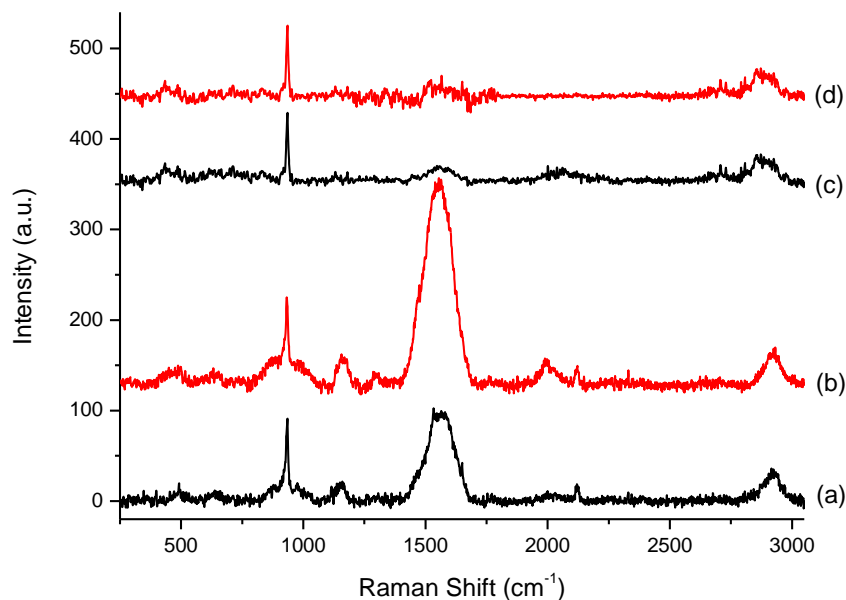


Figure 5.10 SER spectra of 0.1 M propargyl alcohol in 0.1 M perchloric acid adsorbed on Pt{110} single crystal electrode surface at (a) HER potential (-0.1 V), (b) double layer potential (0.4 V); and after hydrogenation in 0.1 M perchloric acid at (c) HER potential (-0.1 V), (d) double layer potential (0.4 V).

Since the adsorption behaviours of propargyl alcohol on different platinum surfaces before and after hydrogenation have been compared with CV, it is noteworthy to make the same comparison with SHINERS. Therefore, after obtaining the spectra of propargyl alcohol adsorbed on the platinum surface, the electrolyte was swapped back to the pure 0.1 M aqueous perchloric acid. The two spectra in **Figure 5.10** (c and d) are examples to illustrate whether or not the adsorbed alkyne layer could survive after hydrogenation. As can be seen in **Figure 5.10c**, when the potential was maintained at -0.1 V, all the bands due to the bulk propargyl alcohol molecules and di-sigma/pi-bonded surface intermediate were eliminated with only the sharp perchlorate anion vibrational band remaining at 930 cm^{-1} . Also, a weak but broad band appearing at 2090 cm^{-1} in

Figure 5.10c suggests that the Pt–H stretching vibration is observed. This Pt–H bond vibration can only be observed on the clean surface undergoing hydrogen evolution. Therefore, it is confirmed spectroscopically that the adsorbed alkyne molecules, together with the surface intermediate on the surface were removed after the hydrogenation treatment. This result corresponds to the CVs obtained previously (**Figure 5.3a**), which indicated that clean surfaces may be recovered after potential cycling after alkyne molecules are adsorbed. In addition, the greater intensity of the di-sigma/pi-bonded surface intermediate for Pt{110} would be consistent with a larger capacity to block H UPD sites afforded to PA adsorbed on Pt{110} compared with Pt{111}. When the potential was changed from -0.1 V to 0.4 V, the band due to the Pt–H stretching vibration disappeared as expected since no hydrogen evolution was occurring (**Figure 5.10d**).

Finally, the adsorption of propargyl alcohol was tested using the surface of a Pt{100} single crystal electrode, and the results are shown in **Figure 5.11**. Despite the regular bands that were observed in all the spectra on different surfaces (C–H stretches at 2930 cm^{-1} , $-\text{CH}_2-$ in-plane deformation vibrations at 1160 cm^{-1} and metal-carbon stretches at 490 cm^{-1}), the peak at 2122 cm^{-1} due to $\text{C}\equiv\text{C}$ stretches could hardly be observed on the (100) terraced surface. This suggests that the bulk PA molecules barely adsorbed on the surface when covered with chemisorbed intermediates with both the bands at 1560 and 930 cm^{-1} being rather intense compared to Pt{111}, suggesting more intermediate molecules were adsorbed on the surface. Even at HER potentials (-0.1 V, **Figure 5.11a**), there was quite a large amount of surface intermediate since the band at 1560 cm^{-1} remained strong. However, it didn't increase much in intensity at the double layer potential (0.4 V, **Figure 5.11b**). In addition, the adsorbed CO vibration at 2000 cm^{-1} and metal-carbon stretches at 490 cm^{-1} were observed, both of which were stronger in the double layer region, as found also using Pt{110} and therefore, the same mechanism of CO formation is proposed.

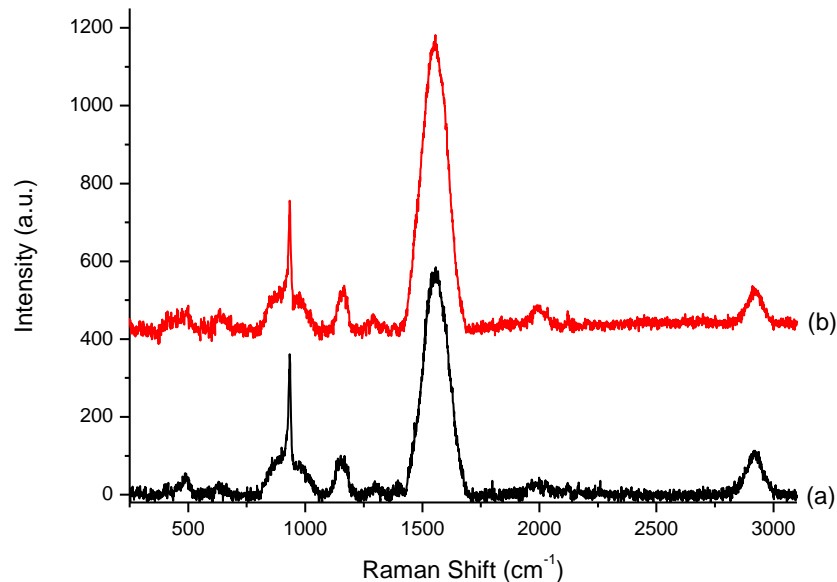


Figure 5.11 SER spectra of 0.1 M propargyl alcohol in 0.1 M perchloric acid adsorbed on Pt{100} single crystal electrode surface at (a) HER potential (-0.1 V) and (b) double layer potential (0.4 V).

5.2.3 *In situ* SERS studies of 2-methyl-3-butyn-2-ol adsorption on Pt surfaces

5.2.3.1 Polycrystalline Pt surface

In this section, MeBuOH was used instead of PA in a repeat of all the experiments carried out with propargyl alcohol, in order to discover what the steric effect of the tertiary methyl groups and the surface selectivity towards the catalytic hydrogenation. First, on the polycrystalline platinum surface, the SERS tests of MeBuOH hydrogenation were performed with H₂SO₄ as the electrolyte. **Figure 5.12** shows the data corresponding to its adsorption at HER (-0.1 V) and double layer (0.4 V) potentials. In both spectra, the bulk bands of MeBuOH were readily distinguished at 2118 cm⁻¹ (C≡C triple bond stretch), 1447 cm⁻¹ (asymmetric CH₃ bend), 1375 cm⁻¹ (symmetric CH₃ bend) and 710 cm⁻¹ (C–H primary alkyne bend). At the HER potential region, new bands appeared which were not ascribable to bulk molecules of MeBuOH. For example, the sharp peak at 1590 cm⁻¹ indicated the formation of a di-sigma/pi-bonded surface complex which has been proposed previously. However, at 20 cm⁻¹ higher than bands observed

using PA, the steric effects of the crowded tertiary methyl groups was clearly perturbing the adsorbed complex relative to PA. In addition, a band at 775 cm^{-1} was observed. This could be associated with a C=C-H out of plane bend of the surface complex. However, the C=C-H stretches above 3000 cm^{-1} (sp^2 C-H stretch) were not observed, which was probably because the surface selection rule played some role in rendering them very weak. When the potential was held at the double layer region, some changes were observed in the spectrum obtained. Extra intensity appeared in the range $1500\text{-}1600\text{ cm}^{-1}$ giving rise to a broad envelope of both pre-existing bands (those at hydrogen evolving potentials) and new features presumably due to alkyne adsorption at the higher coverage. This broad multiplicity of overlapping bands was consistent with both a greater coverage of the surface intermediate forming but also in a variety of adsorption configurations. Astonishingly, the intensity of the C-H stretching peaks decreased at 0.4 V although clearly, based on previous results (and CV) the surface coverage of the intermediate must have increased. A possible reason for this development would be some re-orientation of the adsorbed species, which may also cause the disappearance of the peak at 775 cm^{-1} . In addition, the intensity of the band at 2872 cm^{-1} (C-H symmetric stretch) decreased a lot in the absence of hydrogen, which was similar to the previous situations described in Chapter Four whereby re-orientation of the adsorbed molecule was proposed. Since there was no sign of CO adsorption on the surface, the metal-carbon stretches around 490 cm^{-1} could be ascribed were exclusively to bonding of the surface alkene complex to the platinum surface.

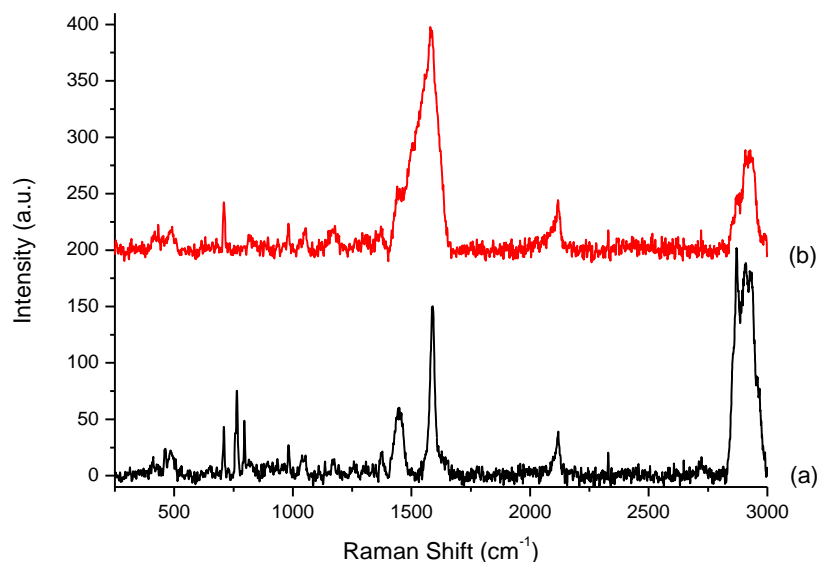


Figure 5.12 SER spectra of 0.1 M 2-methyl-3-butyn-2-ol in 0.1 M sulphuric acid adsorbed on Au@Pt NPs at (a) HER potential (-0.1 V) and (b) double layer potential (0.4 V).

5.2.3.2 Pt{*hkl*} single crystal surfaces

Three well defined platinum single crystal electrodes were then used to explore if there would be any variations for the adsorption of MeBuOH on different surface geometries. The data corresponding to Pt{111} are shown in **Figure 5.13**. Some bulk bands appeared in both spectra (a) and (b), such as C–H stretching vibrations in the range 2820-2980 cm^{-1} , C \equiv C stretches at 2117 cm^{-1} , asymmetric CH₃ bending vibrations at 1437 cm^{-1} , symmetric CH₃ bend at 1374 cm^{-1} , CC–O stretches at 1175 cm^{-1} and C–H primary alkyne bend at 710 cm^{-1} . At the HER potential (**Figure 5.13a**), there was a sharp, prominent peak at 1585 cm^{-1} similar to that exhibited by adsorption on polycrystalline platinum and therefore, ascribable to formation of a di-sigma/pi-bonded surface intermediate. However, at double layer potentials different orientations of the surface intermediate may coexist in this situation since there appeared to be a broad band overlapping with the prominent, sharp peak. If we assume that the ‘sharp’ SERS peak is commensurate with a specific orientation of the adsorbed alkyne on a Pt{111} site, the overlap of the broad band at double layer potentials would be explicable as similar vibrational modes but arising from alkynes adsorbed in a variety of different surface configurations. When the potential

was shifted away from the HER to the double layer region (**Figure 5.13b**), the broad set of bands centred at 1561 cm^{-1} increased in intensity due to this effect. This would be because in this relatively stable situation, the di-sigma/pi-bonded surface complex adsorbed with a larger amount as described previously. In addition, the C–H stretch region ($2820\text{--}2980\text{ cm}^{-1}$) underwent a decrease in its intensity compared to when hydrogen was present. CO adsorption was definitely observed at double layer potentials, if not clearly in the HER region, as signified by the appearance of the band at 2000 cm^{-1} . This means that the metal-carbon stretches around 490 cm^{-1} were partially formed by the presence of adsorbed CO.

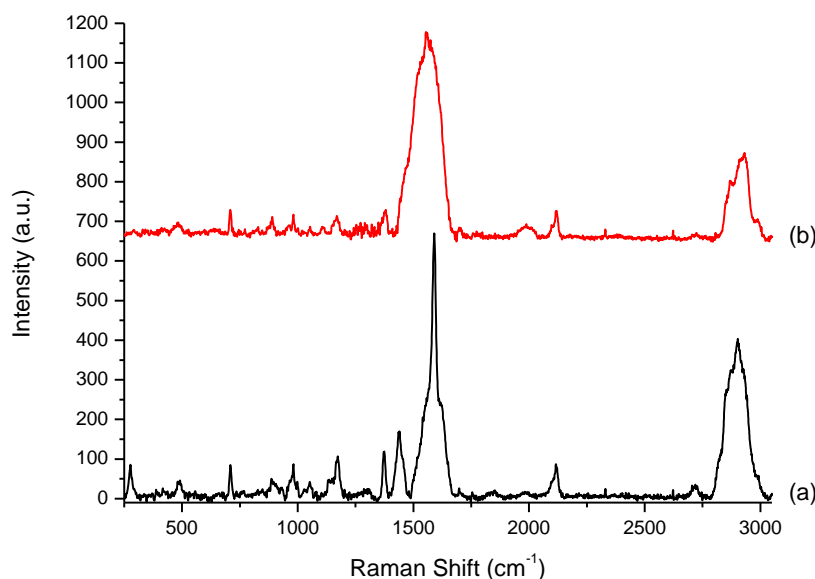


Figure 5.13 SER spectra of 0.1 M 2-methyl-3-butyn-2-ol in 0.1 M sulphuric acid adsorbed on Pt{111} single crystal electrode surface at (a) HER potential (-0.1 V) and (b) double layer potential (0.4 V).

The adsorption of MeBuOH was then tested using a Pt{100} single crystal surface and the results are shown in **Figure 5.14**. Some of the bands due to the bulk molecules adsorbed on the surface were observed in both spectra, and they were similar to the ones obtained with Pt{111}. However, there were also some changes in the shapes and intensities of these bands. For example, the bands due to the C–H stretches showed more details so that the symmetric (2869 cm^{-1}) and asymmetric (2930 cm^{-1}) stretches could be distinguished. The di-sigma/pi-bonded

surface complex was adsorbed on the (100) terraces as well as signified by the band appearing at 1560 cm^{-1} but the band was relatively weak compared to Pt{111}. From the HER potential (-0.1 V , **Figure 5.14a**) to the double layer potential (0.4 V , **Figure 5.14b**), the band didn't increase much in intensity. CO adsorption on the surface was clearly observed as the band around 2000 cm^{-1} appeared in both of the spectra, among which the one in the double layer region was slightly stronger. Therefore, one cannot neglect the CO contribution to the metal-carbon stretches at 490 cm^{-1} .

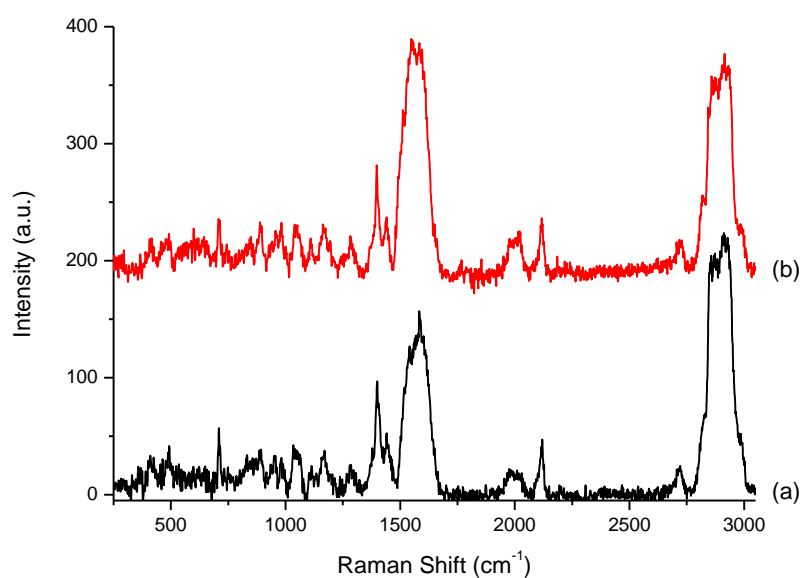


Figure 5.14 SER spectra of 0.1 M 2-methyl-3-butyn-2-ol in 0.1 M sulphuric acid adsorbed on Pt{100} single crystal electrode surface at (a) HER potential (-0.1 V) and (b) double layer potential (0.4 V).

Clearly, the finding that less di-sigma/pi-bonded surface intermediate was being formed (if amount adsorbed was reflected in relative band intensity between different samples) and that its intensity hardly changed when going from the hydrogen evolution potential region to the double layer seems at odds with all other findings and the CV results showing a strong alkyne-surface interaction. The only explanation to reconcile all of these results would be that already Pt{100} achieves full coverage of the di-sigma/pi-bonded surface intermediate at -0.1 V (albeit with a

rather weak absolute intensity) and there are simply no more sites available when moving into the double layer region attesting to the very strong surface-alkyne interaction on Pt{100}.

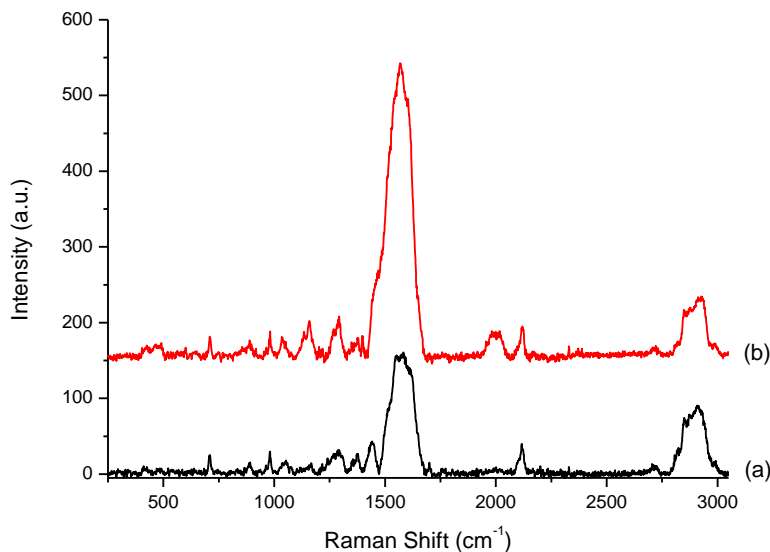


Figure 5.15 SER spectra of 0.1 M 2-methyl-3-butyn-2-ol in 0.1 M sulphuric acid adsorbed on Pt{110} single crystal electrode surface at (a) HER potential (-0.1 V) and (b) double layer potential (0.4 V).

Finally, the adsorption of MeBuOH was explored on a Pt{110} surface to make comparisons with Pt{111} and Pt{100}. In **Figure 5.15**, the symmetric and asymmetric C–H stretches gave rise to C–H stretch vibrations in the range of 2820-2980 cm^{-1} , and as usual the band obtained at the HER potential (-0.1 V, **Figure 5.15a**) was a little stronger than the one at the double layer potential (0.4 V, **Figure 5.15b**). The other bulk bands were also observed in both spectra, such as the C \equiv C stretches at 2119 cm^{-1} , the symmetric and asymmetric CH₃ bending vibrations at 1375 and 1441 cm^{-1} , CC–O stretches at 1175 cm^{-1} and the C–H primary alkyne bend at 710 cm^{-1} . The band due to the alkenic stretches of the di-sigma/pi-bonded surface intermediate at 1560 cm^{-1} was much stronger in the double layer region than at HER potentials. This was consistent with previous findings suggesting a dynamic adsorption/hydrogenative desorption steady state. It is striking that the prominent, sharp band at 1590 cm^{-1} observed with both polycrystalline Pt and Pt{111} is not visible for Pt{100} or Pt{110}. This is probably due to the large width of the band centred at which certainly overlaps the 1590 cm^{-1} state if it was present. Interestingly, CO

adsorption could only be observed at double layer potentials as signified by the bands at 2000 and 490 cm^{-1} .

5.2.3.3 PVP modified Pt surface

Polyvinylpyrrolidone (PVP) is often used as a capping agent for regulating particle size during growth. It has previously been implicated in improved selectivity towards semi-hydrogenation of alkynes.^{3,4} In Attard's recent study⁵, a series of Pt catalysts were tested for their efficacy in the selective hydrogenation of three alkynes. The substrates examined in this work were a symmetric internal alkyne, 4-octyne, an unsymmetrical internal alkyne, 2-pentyne and a terminal alkyne with a polar functionality, 2-methyl-3-butyn-2-ol. The first two were examined spectroscopically in Section 4.2.2. The latter substrate was also used in a study on shape selectivity by Crespo-Quesada *et al.*⁴ where it was observed that decreasing the particles edge/terrace ratio led to an increase in selectivity to alkene. The reason for this was thought to be a reduced rate of deep hydrogenation to the alkane, which was speculated to occur solely over edge sites.

In the present study, a standard 5 wt.% Pt/graphite catalyst reduced at 700 K was examined (in collaboration with University of Birmingham) and modified with two different coverages of PVP. It was demonstrated that PVP selectively blocked defect sites leaving Pt{111} terraces intact, similar to behaviour exhibited by bismuth.⁶ **Figure 5.16** shows the changes in the CV of the sintered catalyst corresponding to the adsorption of PVP. The selective blocking of defect sites by PVP was the key finding, which was signified by the attenuation in the intensity of the two peaks at approximately 0.05 V ({{110} sites) and 0.21 V ({{100} × {111} steps) (Pd/H) with increasing PVP loading. The broad peak centred at 0.40 V associated with Pt{111} terraces was also seen to decrease for PVP adsorbed on Pt{111} but to a lesser extent. In turn it was replaced by an increase in intensity around 0.6 – 0.7 V associated with OH rather than bi-sulphate adsorption at Pt{111} sites (single crystal work is presently being prepared for publication in collaboration with Prof. Shi-Gang Sun at Xiamen University also showing this effect). Although it was difficult to assign the coverage of PVP since the number of Pt sites blocked per PVP polymer was unknown, the residual H UPD peak area (charge) between 0 and 0.3 V relative to the un-dosed catalyst may be used to signify the number of 'free' Pt sites after PVP adsorption. However, after approximately 50% of H UPD sites were blocked, no matter how much PVP was

added, no further attenuation in H UPD charge was observed. Meanwhile, all electrosorption peaks broadened and the double layer capacitance increased. Therefore, in terms of H UPD sites blocked, a coverage of PVP may be determined up to 50% surface blockage before reaching a plateau.

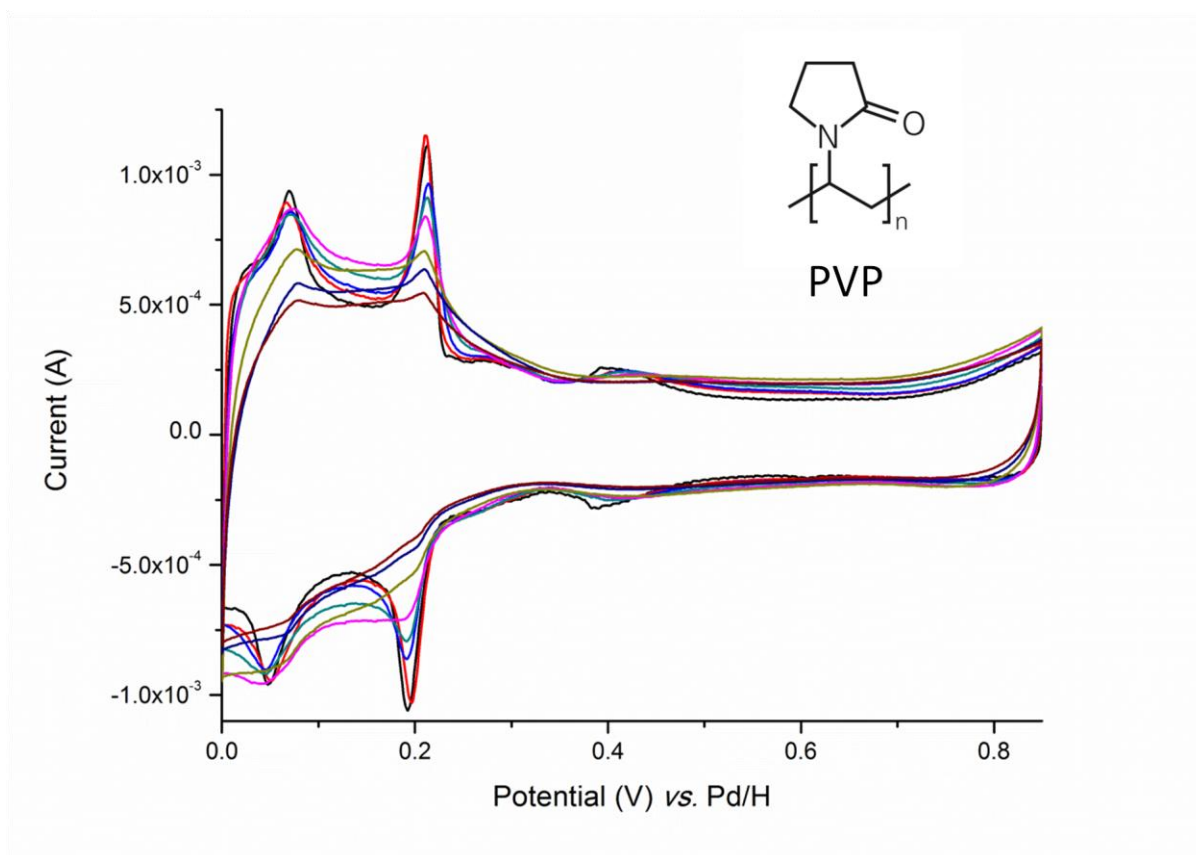


Figure 5.16 Cyclic voltammograms for increasing loadings of PVP on the reduced Pt on graphite catalyst in 0.5 M sulphuric acid. Sweep rate = $50 \text{ mV}\cdot\text{s}^{-1}$. Insert is the structure of PVP.

In order to highlight the extent of defect site blocking, **Figure 5.17** was plotted with the attenuation of the intensity of the $\{100\} \times \{111\}$ defect feature at 0.2 V as a function of PVP amount added to the catalyst. A linear decrease in peak intensity was observed up to 5 mL of PVP added. It was therefore concluded that all defect sites were practically blocked after 5 mL of PVP had been does onto a fixed mass of the catalyst. Both the 10 and 12 mL dosed samples fell into the plateau region of this plot, which represented 2 and 2.4 times the critical amount of PVP associated with defect blocking.

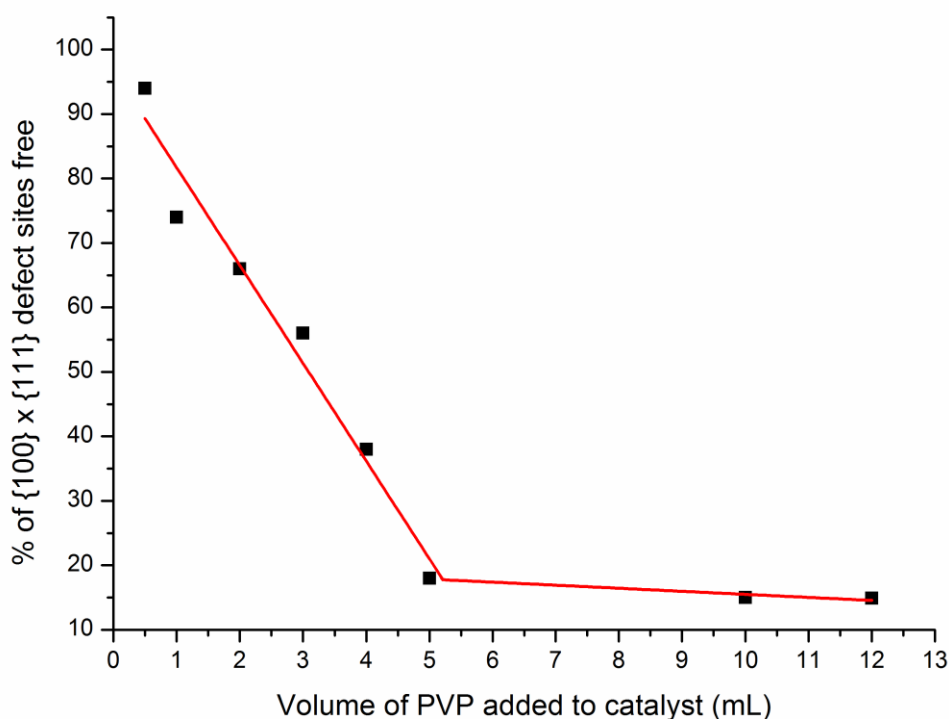


Figure 5.17 Plot of $\{100\} \times \{111\}$ step peak intensity versus volume of PVP dosed. A critical blocking of the defect sites was achieved after 5 mL of PVP was added.

In the light of the catalytic data reported in ref. 5, it was concluded that PVP enhanced the reaction selectivity. Hence, SERS experiments of MeBuOH (because of its ease of solubility in aqueous electrolytes compared to pentyne and octyne) during electrochemical hydrogenation were attempted again using Au@Pt NPs modified with PVP such that all defect sites were blocked according to the CVs in **Figure 5.18**. The SERS data corresponding to MeBuOH hydrogenation in the absence (**a** and **b**) and presence (**c** and **d**) of adsorbed PVP are shown in **Figure 5.19**. As illustrated in **Figure 5.12**, the bulk bands of MeBuOH were assigned in all spectra, such as C≡C triple bond stretch at 2118 cm^{-1} , asymmetric CH₃ bend at 1447 cm^{-1} , symmetric CH₃ bend at 1375 cm^{-1} and C–H primary alkyne bend at 710 cm^{-1} .

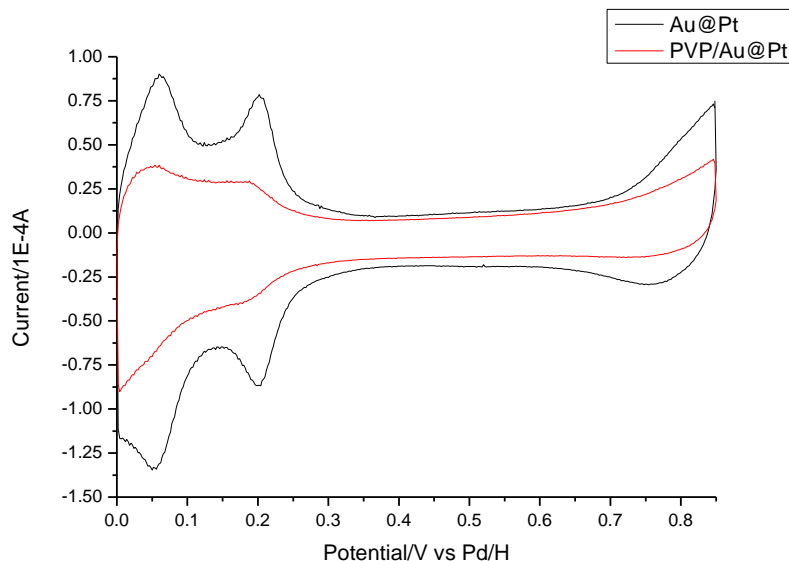


Figure 5.18 CVs of Au@Pt NPs before (black) and after (red) being modified with PVP.

The effect of PVP was investigated by repeating the SERS measurements using a PVP-modified surface. The spectrum of MeBuOH undergoing hydrogen evolution in **Figure 5.19c** was obtained with the PVP-modified surface. It was more or less the same as the spectrum in **Figure 5.19a** except for a slight decrease in the intensity of all peaks. Under HER conditions, the 775 cm^{-1} feature was again noticeable as were the sharp, prominent peak at 1580 cm^{-1} and the C–H stretch peaks at 2872 cm^{-1} . The bands from PVP were very weak in **Figure 5.19c** although a weak feature is observed at 1760 cm^{-1} when PVP was adsorbed (due to protonated amide N–H vibration) in agreement with previous findings by El-Sayed *et al.* who erroneously assigned the also noted the ‘blue shifted’ peak to the C=O stretch of the amide when PVP was adsorbed on silver.⁷ In basic media the 1760 cm^{-1} ‘C=O’ stretch was found to disappear (not shown). It was speculated that the amount of PVP adsorbed was actually just at the detection limit of our spectrometer in spite of an observed stretching frequency of 1760 cm^{-1} .

However, when compared with **Figure 5.19b**, **Figure 5.19d** revealed that a significant inhibition of di-sigma/pi-bonded surface complex occurred following a modification of the surface with PVP. Hence, at double layer potentials where hydrogen was absent, PVP acted to inhibit the uptake of alkyne. In fact, there was little difference between spectrum **5.19c** and spectrum **5.19d** except for the usual decrease in C–H stretch intensity around 2900 cm^{-1} and the disappearance of

the 775 cm^{-1} peak in the absence of hydrogen. Therefore, it was concluded that uptake of alkyne was inhibited by PVP. Furthermore, since uptake of PVP was associated with defects (see CV data), the di-sigma/pi-bonded complex must also be strongly associated with these sites (**Figure 4.7** and **4.10**). Hence, PVP must be blocking these sites leading to an increase in selectivity and a decrease in activity because the di-sigma/pi-bonded complex formation is inhibited at defects and it is this intermediate which ultimately is hydrogenated to form the alkane. The nature of the adsorbed complex in the case of adsorbed MeBuOH was intriguing since it appeared to be quite stable under HER conditions as signified by the intensity of the band at 1580 cm^{-1} (**Figure 5.19 a** and **c**). It is noteworthy also that the other two hydrocarbon alkynes tested gave rise to superior activity and selectivity compared to MeBuOH, with adsorbed PVP only making a moderate change to MeBuOH selective hydrogenation.⁵

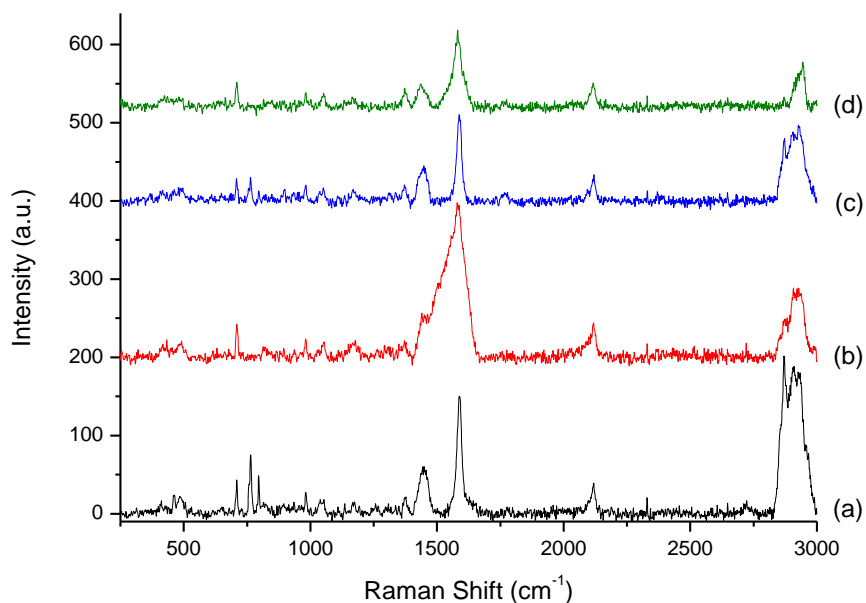


Figure 5.19 SERS of 2-methyl-3-butyn-2-ol (a) at HER (-0.1 V) and (b) double layer potential (0.4 V). (c) Same as (a) except surface dosed with PVP. (d) Same as (b) except surface dosed with PVP. Concentration of 2-methyl-3-butyn-2-ol was 0.1 M in 0.1 M aqueous sulphuric acid.

5.2.3 Discussion

Several factors may influence the interaction, reactivity and orientation of molecular adsorbates at metal electrode surfaces. Here, the molecular structure was the factor to be explored.

The adsorption of propargyl alcohol on the surfaces of different platinum single crystal electrodes varied, with the highest initial coverage found on Pt{100} (90%) and far less coverage on Pt{111} (10%) whereas MeBuOH could cover more than 80% of the Pt{111} surface, which was the same if not larger than the coverage on Pt{100} (~80%) and Pt{110} (70%). Therefore, the main difference between propargyl alcohol and MeBuOH was that MeBuOH may adsorb on all three basal planes effectively, while propargyl alcohol only weakly adsorbed on the (111) surface. Behaviour described here is similar to other molecules adsorbing on Pt{111} such as ethyl pyruvate.⁸ The expectation was that MeBuOH should adsorb more weakly than PA due to the steric encumbrance of methyl groups preventing full interaction of the alkyne substituent with Pt surface atoms.

However, it was found that the weakest adsorption turned out to be propargyl alcohol on the (111) surface whereby no steric hindrance should be observed at all. Two possible explanations may be suggested. The first would be that the strong induction effect by the methyl groups from MeBuOH molecules would push electron density onto the alkyne group making it more reactive with the platinum surface than PA. This electron-rich alkyne group may therefore form a strong bond with metal atoms. Hence, the MeBuOH molecule could adsorb on all three basal faces of platinum quite easily and strongly. Although propargyl alcohol also showed strong adsorption on Pt{110} and Pt{100}, it had a poor coverage on (111). An alternative explanation to this electronic interpretation of surface binding is afforded by a consideration of this increased hydrophobicity of MeBuOH compared with PA, i.e. the presence of extra methyl groups may increase the tendency of MeBuOH to adsorb from the aqueous electrolyte onto the Pt surface and thus override any surface structural effects.

The intensities of SERS signals obtained for the adsorptions of both molecules on each platinum surface were in accord with CV in that the higher the coverage of molecules on the surface (as determined by CV), the stronger the SERS intensity of all bands was found to be. Therefore, the SER spectra of propargyl alcohol adsorbing on the Pt{111} single crystal electrode surface gave

rise to the least intense bands when compared to all other systems investigated. All of the spectra of MeBuOH adsorbing on Pt{*hkl*} surfaces exhibited very strong SHINERS band intensities.

For propargyl alcohol, the di-sigma/pi-bonded complex formed was observed on all Pt surfaces as signified by the appearance of the band at 1560 cm⁻¹. This surface intermediate gave rise to more intense 1560 cm⁻¹ band at double layer potentials than when the electrode was evolving hydrogen. On the (111) and (100) surfaces, the intensity of the band was only slightly stronger at double layer potentials. It is suggested that the weak interaction on Pt{111} of the alkyne molecule would explain this effect whereas the ‘saturation’ of the Pt{100} surface by adsorbed alkyne would manifest itself also as very little change in 1560 cm⁻¹ band intensity at all. It should also be noted that because the (110) surface maybe regarded as more ‘defective’ than the other basal planes due to a mixture of (1x2) and (1x1) surface phases being present after hydrogenation cooling.⁹ According to the previous finding using PVP, the intermediate should preferentially adsorb more on these defect sites. In this regard, it is interesting to note that the biggest difference in 1560 cm⁻¹ band intensity as a function of hydrogen evolution and double layer potential was found on the surface of Au@Pt NPs where defect sites dominate.

However, a more complicated situation is found for MeBuOH. For example, a sharp peak was observed at 1585 cm⁻¹ only appearing on the (111) surface at the HER potential, while on the other surfaces, all the bands centred at 1560 cm⁻¹ were rather broad. Again, on the (110) surface, there was a big change of the band intensity upon moving from HER potentials to the double layer region.

In the case of PVP, selective blockage of defect sites was found using CV of polycrystalline platinum resulting in only Pt{111} terraces being exposed to the reactant. The prominent, sharp peak at 1589 cm⁻¹ was a signature of adsorption at (111) sites and these were the only states resulting from PVP adsorption on the polycrystalline sample according to SHINERS (**Figure 5.19**). At double layer potentials, small increases in intensity around 1560 cm⁻¹ could be discerned but only a fraction of the intensity when PVP was absent.

Several examples in the literature have proved the improvement of alkyne hydrogenation selectivity by dosing the catalyst with organic compounds, including PVP.^{6, 10-17} Crespo-Quesada *et al.* studied the selective hydrogenation of ethyne and explored the behaviour of PVP-modified

Pd catalysts and Pd catalysts in which PVP had been removed using ozone treatments.³ When PVP was removed, they found a huge increase in activity, but a decrease in selectivity towards ethene product. These results match with the present study if defect sites were blocked by PVP. They also used shape-controlled NPs to study the role of defects based on catalytic measurements⁴ and found an increase in selectivity in the hydrogenation of alkynes to alkenes when the ratio of terrace sites to defect sites was increased using nanoparticle shape control. The results in this chapter are in accordance with these findings. However, instead of starting with well-defined Pt NPs, the approach used here was to monitor changes induced by a surface capping agent on a pre-existing Pt catalyst (no particle shape control). This approach affords some advantages in relation to using shape controlled nanoparticles in that technical catalysts of proven catalytic capabilities may be monitored by ‘switching off’ specific adsorption sites (PVP or bismuth¹⁸). Recently, Kwon *et al.*¹⁹ showed the overall selectivity of the hydrogenation of alkynes was determined by the balance of interactions between the nanoparticle Pt catalyst surface and the capping agent/substrate in terms of differential adsorption energetics. By using this approach, one may tune the selectivity. If particular substrates interact with defect sites sufficiently strongly or a large excess of the substrate enables displacement of PVP, the substrate could compete successfully with irreversibly adsorbed PVP for defect sites resulting in a decrease in selectivity. This could also be true for inert site blockers such as bismuth and PVP. However, this effect for bismuth and probably other inorganic additives would be small relative to surface modification by organic ligands. Hence, although it is important to replace toxic metals with more benign adsorbates (like PVP) in heterogeneous selective hydrogenation, one has to ensure that binding is commensurate with the maintenance of good selectivity whilst achieving reasonable activity.

5.3 Conclusion

By studying propargyl alcohol and MeBuOH, the reactivity of platinum surface was once again probed using a combination of CV and SHINERS. A range of particles, including nanoparticles, single crystal and supported particles, was explored. It is proven that alkyne adsorption on Pt defect sites yields a long-lived di-sigma/pi-alkene complex which may undergo further hydrogenation to produce alkane. Alkene selectivity can be increased by blocking defect sites, using PVP or Bi, leaving only Pt{111} terraces available for catalysis. Differential adsorption of

the substrate molecules on different surfaces determines the SERS intensity. Due to the ‘extra’ methyl groups in MeBuOH compared to PA, a variety of adsorption orientations for MeBuOH was deduced based on the SERS response of the adsorbed surface complex. In particular, a singular response for MeBuOH adsorbed on Pt{111} sites is reported that is not observed for propargyl alcohol.

5.4 References

1. M. Moskovits and J. S. Suh, *The Journal of Physical Chemistry*, 1988, **92**, 6327-6329.
2. J. S. Suh and J. Kim, *Journal of Raman Spectroscopy*, 1998, **29**, 143-148.
3. M. Crespo-Quesada, J.-M. Andanson, A. Yarulin, B. Lim, Y. Xia and L. Kiwi-Minsker, *Langmuir*, 2011, **27**, 7909-7916.
4. M. Crespo-Quesada, F. Cárdenas-Lizana, A.-L. Dessimoz and L. Kiwi-Minsker, *ACS Catalysis*, 2012, **2**, 1773-1786.
5. G. A. Attard, J. A. Bennett, I. Mikheenko, P. Jenkins, S. Guan, L. E. Macaskie, J. Wood and A. J. Wain, *Faraday Discussions*, 2013, **162**, 57-75.
6. J. A. Anderson, J. Mellor and R. P. K. Wells, *Journal of Catalysis*, 2009, **261**, 208-216.
7. M. A. Mahmoud, C. E. Tabor and M. A. El-Sayed, *The Journal of Physical Chemistry C*, 2009, **113**, 5493-5501.
8. R. J. Taylor, Cardiff University, 2010.
9. R. Michaelis and D. M. Kolb, *Journal of Electroanalytical Chemistry*, 1992, **328**, 341-348.
10. M. Crespo-Quesada, R. R. Dykeman, G. Laurenczy, P. J. Dyson and L. Kiwi-Minsker, *Journal of Catalysis*, 2011, **279**, 66-74.
11. N. Semagina, A. Renken and L. Kiwi-Minsker, *The Journal of Physical Chemistry C*, 2007, **111**, 13933-13937.
12. C. Evangelisti, N. Panziera, A. D’Alessio, L. Bertinetti, M. Botavina and G. Vitulli, *Journal of Catalysis*, 2010, **272**, 246-252.
13. C. Lange, S. Storck, B. Tesche and W. F. Maier, *Journal of Catalysis*, 1998, **175**, 280-293.
14. C. Lange, D. De Caro, A. Gamez, S. Storck, J. S. Bradley and W. F. Maier, *Langmuir*, 1999, **15**, 5333-5338.
15. N. Semagina, E. Joannet, S. Parra, E. Sulman, A. Renken and L. Kiwi-Minsker, *Applied Catalysis A: General*, 2005, **280**, 141-147.
16. M. G. Musolino, C. M. S. Cutrupi, A. Donato, D. Pietropaolo and R. Pietropaolo, *Journal of Molecular Catalysis A: Chemical*, 2003, **195**, 147-157.
17. M. M. Telkar, C. V. Rode, R. V. Chaudhari, S. S. Joshi and A. M. Nalawade, *Applied Catalysis A: General*, 2004, **273**, 11-19.
18. J. A. Bennett, G. A. Attard, K. Deplanche, M. Casadesus, S. E. Huxter, L. E. Macaskie and J. Wood, *ACS Catalysis*, 2012, **2**, 504-511.
19. S. G. Kwon, G. Krylova, A. Sumer, M. M. Schwartz, E. E. Bunel, C. L. Marshall, S. Chattopadhyay, B. Lee, J. Jellinek and E. V. Shevchenko, *Nano Letters*, 2012, **12**, 5382-5388.

CHAPTER SIX

Adsorption of Ethyl Pyruvate on Platinum Surfaces

6.1 Introduction

Originally, the Orito reaction¹, the enantioselective hydrogenation of methyl pyruvate (MP) to R-methyl lactate over a cinchonidine (CD) modified supported platinum catalyst was reported (**Figure 6.1**). This being the first heterogeneous enantioselective hydrogenation of an alpha-ketoester, it constituted an important advance since utilising heterogeneous catalysts afforded many advantages over homogenous catalytic analogues such as ease of separation and re-use. Subsequently, it was shown that the next number of the homologous series, namely ethyl pyruvate (EP) exhibited identical reaction performance to MP under Orito-type reaction conditions.² Hence, when taken as a pair, numerous *in situ* and *ex situ* techniques have been applied to investigating their surface reactivity including STM^{3, 4}, TPR³, NEXAFS⁵, RAIRS⁶, XPS⁷ together with theoretical methods including DFT^{8, 9}. The adsorption behaviour of MP and EP on Pt{111} surface has been reported by McBreen and Baiker.⁶⁻⁸ Based on all of these studies, four different adsorption modes have been suggested for the alpha-ketoester on platinum:

- 1) An end-on configuration bound via an oxygen lone pair from the ketone, known as η^1 .⁸
- 2) A Pt–O and Pt–C σ -bonded entity with the C–O bond held horizontal to the surface, known as η^2 .⁸
- 3) A flat orientation with the molecular plane parallel to the surface plane involving π -bound states of one or both carbonyls.⁶
- 4) A Pt–O bond from both carbonyls with a delocalized π -orbital between them known as an enediolate.⁷

Multiple adsorption modes of the reactant molecule may exist at the same time, with the η^1 mode being dominant.⁹ If a polycrystalline supported platinum catalyst is used, the Orito reaction itself may be thought of as taking place at numerous surface sites and the key question then becomes which sites are best at promoting enantioselectivity? The adsorption of the substrate remains

obscure unless the different adsorption sites are identified. It is known that there are structure-reactivity relationships in the Orito reaction with superior enantioselectivities resulting from catalysts treatments such as sintering¹, sonication² and coadsorption of site-blocking inert adatoms¹⁰, all the methods either promoting or eliminating specific sites such as terraces or steps. The results from such experiments are rather contradictory with some workers emphasising the presence of (111) terraces as essential for high enantiomeric excesses (*ee*)¹¹ whereas others indicate that loss of defect sites leads to poor *ee*¹².

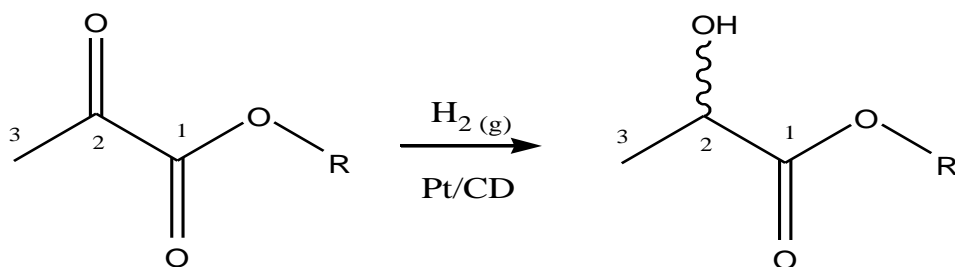


Figure 6.1 Structures of alkyl pyruvate reactants (MP: R = CH₃, EP: R = CH₂CH₃) and the alkyl lactate products (ML and ethyl lactate (EL)).

In this chapter, CV and SERS have been used to explore the characteristics of the adsorption behaviour of EP on both polycrystalline and single crystal platinum surfaces. The purpose was to identify the adsorption geometries of EP on different types of platinum surface arrangements and any surface by-products following hydrogenation. If a side reaction such as the dissociative adsorption of the reactant molecule occurs, these products may also be monitored and used to gain understanding of the catalytic mechanism. With the help of SHINERS, the selectivity and reactivity of certain single crystal sites was determined for the first time. It is worth noting that all of the studies were carried out in an aqueous liquid phase at room temperature rather than in ultra-high vacuum (UHV) so conditions reported here are closer to the *operando* conditions pertaining to the real catalytic reaction system.

6.2 Results and Discussions

6.2.1 CV of ethyl pyruvate adsorption on Pt{*hkl*} single crystal surfaces

CV measurements of the clean, well-ordered low Miller index platinum single crystal electrode surfaces were first recorded. Then, as in Chapters 4 and 5, the substrate EP was introduced by first immersing the electrode into the neat liquid (usually for a few seconds). Excess EP was removed by gently rinsing the electrode with ultra-pure water. Finally, after returning the electrode to the electrochemical cell, the CV experiments of EP adsorption on different Pt{*hkl*} electrodes were performed.

CVs of the Pt{111} single crystal electrode before and after adsorption of EP are shown in **Figure 6.1**. The black CV represents the clean surface of Pt{111}. The main features included a pair of characteristic sharp peaks at 0.44 V which indicated that the surface was clean and that long range surface order was present. After dosing the crystal with EP for five seconds, the blue CV was taken. It showed that about 10% of H UPD surface area was removed with attenuation of the sharp peaks of the so-called butterfly peak. A further small decrease was observed after a further sixty seconds of EP exposure (pink). Although the peaks at 0.44 V disappeared, only a small area of the (111) surface was blocked by EP (85% of H UPD sites free). No oxidation or reduction peaks related to EP decomposition products were observed. However, evolving hydrogen on the electrode at -0.1 V would remove the adsorbed EP fragments and clean the surface. As a result, the red CV showed that after this treatment most of the (111) surface sites in the hydrogen adsorption/desorption region between 0 and 0.3 V, were recovered as well as the sharp anion peak at 0.44 V.

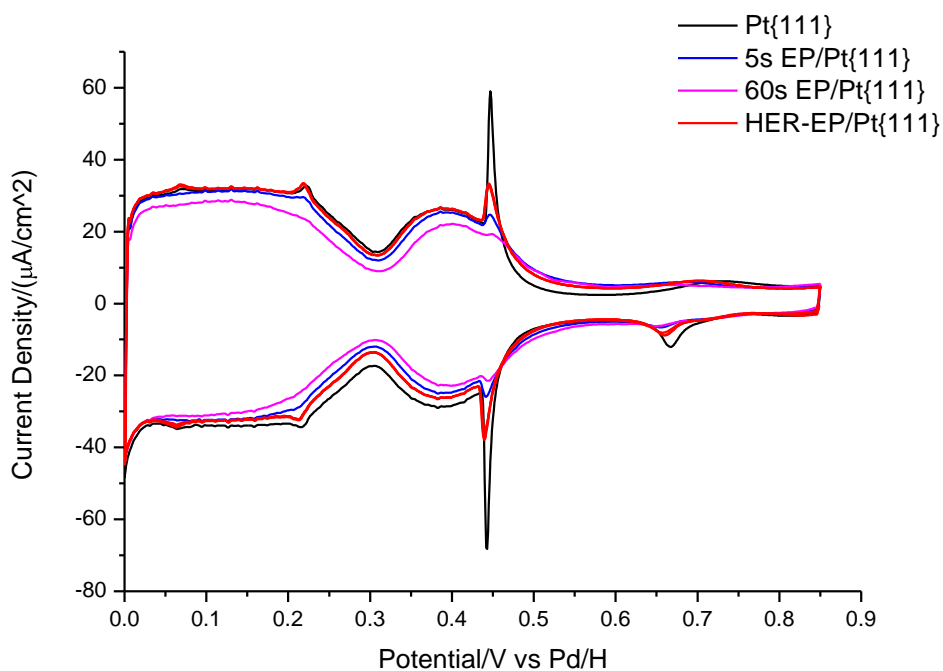


Figure 6.1 CVs of platinum{111} before and after adsorption of EP. Red curve is CV recorded following EP dosing and hydrogen evolution at -0.1 V. Electrolyte = 0.1M H₂SO₄, sweep rate = 50 mV·s⁻¹.

The Pt{110} single crystal electrode CV measurements following dosing of EP are shown in **Figure 6.2**. The peaks at 0.086 V due to H UPD on the (110) terraces were largely attenuated even after dosing the surface with EP for only five seconds. The blockage of the H UPD surface area by EP was as much as 40% after this relatively low exposure time suggesting that Pt{110} is much more reactive towards EP than Pt{111}. A sharp decrease in current density on the negative-going sweep near 0 V indicated the hydrogenative reduction and desorption of the adsorbed EP. The gentle rise around 0.7 V in the positive sweep gave a hint of weak electrooxidation of CO¹³, which was reported previously to be a decomposition product of EP on platinum.¹⁴ Hydrogen evolution on the electrode surface resulted in the majority of the surface H UPD sites being recovered as the peaks in the CV following this treatment nearly overlapped with those of the clean surface.

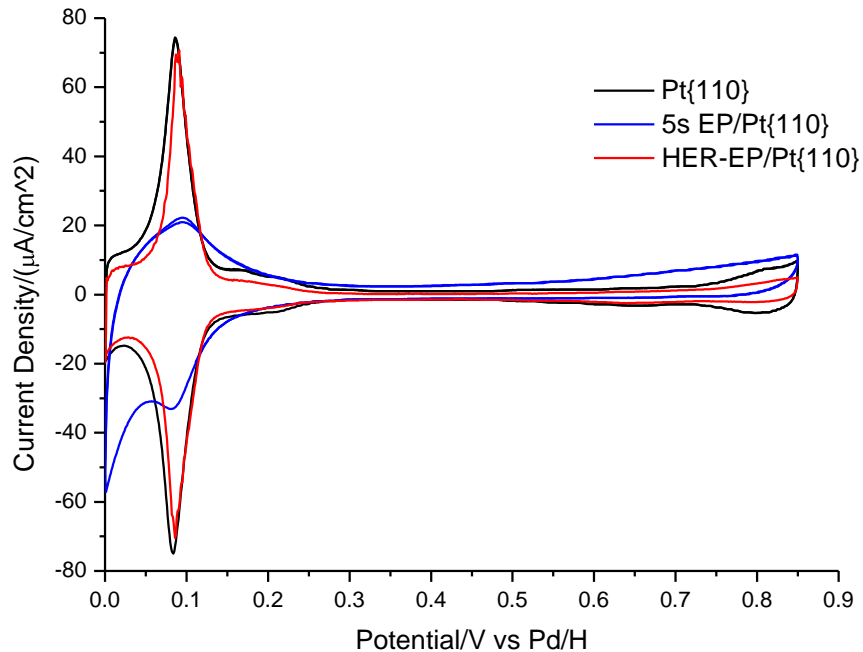


Figure 6.2 CVs of platinum{110} before and after adsorption of EP. Red curve is CV recorded following EP dosing and hydrogen evolution at -0.1 V. Electrolyte = 0.1M H₂SO₄, sweep rate = 50 mV·s⁻¹.

The final single crystal electrode studied was Pt{100} and the CV of the clean surface (black) is shown in **Figure 6.3**. Two characteristic peaks at 0.22 V and 0.32 V representing (100) × (111) step sites and (1×1) – (100) long range order terrace sites respectively are noted.¹⁵ After dipping the electrode into EP for five seconds, the (red) CV in **Figure 6.3** was recorded. The change in the CV profile was remarkable as several new electroadsorption features were revealed. A large reduction in the charge associated with the H UPD region indicated that the surface was blocked by EP. Two thirds of the H UPD surface area was covered with EP, which was the largest coverage among all three single crystal electrodes investigated. Meanwhile, the positive sweep contained a significant peak at 0.74 V, which was ascribed to CO electrooxidation and stripping. Normal potential cycling between 0 and 0.7 V proved effective in the removal of some EP as signified by a small recovery in H UPD electroadsorption sites. However, only by evolving hydrogen on the electrode surface at -0.1 V could the majority of EP be desorbed as shown in the red CV of **Figure 6.3** obtained after the hydrogen evolution treatment. Although the main

features of the clean (100) surface CV profile were recovered, a small H UPD surface area reduction relative to the clean surface was noted and thus it was evident that there were still some EP adsorption species tenaciously held on the surface.

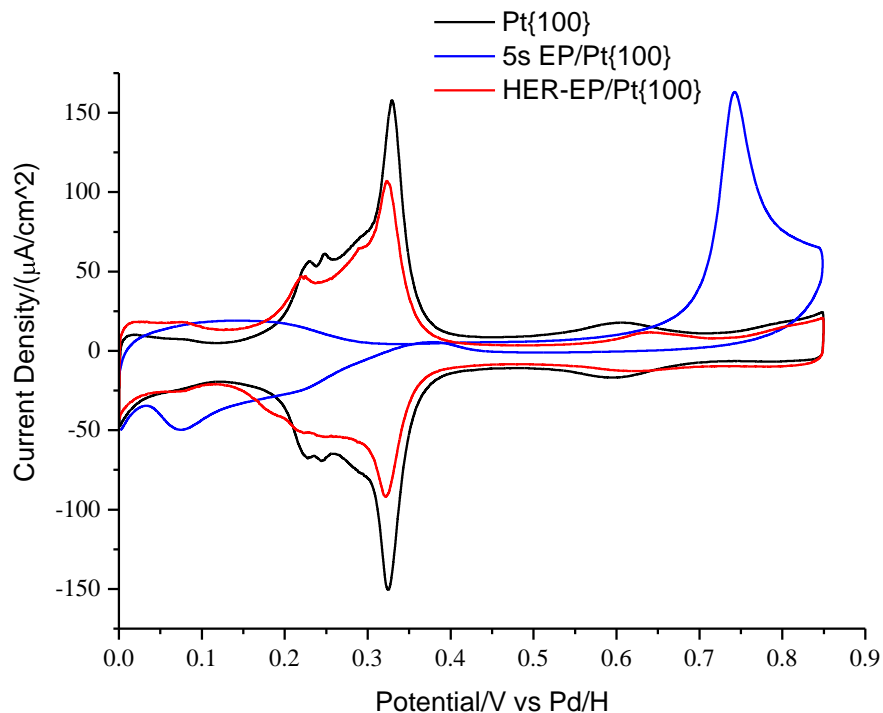


Figure 6.3 CVs of platinum{100} before and after adsorption of EP. Red curve is CV recorded after EP dosing and subsequent hydrogen evolution at -0.1 V. Electrolyte = 0.1M H₂SO₄, sweep rate = 50 mV·s⁻¹.

Finally, potential window opening experiments were carried out in order to establish the potential range in which adsorbed CO was formed. Since the Pt{100} electrode exhibited the most significant changes in its CV after the adsorption of EP, the same technique adopted in Chapters 4 and 5 was applied to Pt{100} and the results are shown in **Figure 6.4**. The potential was scanned from the upper limit (0.85 V) to increasingly more negative potentials followed by scanning in the positive direction. After EP dosing, the double layer capacitance of the electrode was significantly reduced compared to the clean surface proving that adsorption of EP had taken

place. In the first couple of cycles sweeping down to the onset of H UPD, no CO electrooxidation in the subsequent positive going sweep was found. However, sweeping to more negative potentials (< 0.35 V) immediately generated an electrooxidation peak at 0.7 V ascribable to the electrooxidation of adsorbed CO. It grew even bigger when the potential was swept still more negative. A similar mechanism to that proposed for alkynes in Chapters 4 and 5 is suggested whereby upon freeing up metallic Pt sites following EP reductive stripping, residual EP may undergo a dissociative surface reaction generating adsorbed CO as a consequence. Further potential cycling into the H UPD region would reduce still more the coverage of EP molecules and eventually lead to a clean surface. Clearly, based on these measurements, the Pt{100} surface is the most active for generating adsorbed CO from surface EP when free Pt sites are available.

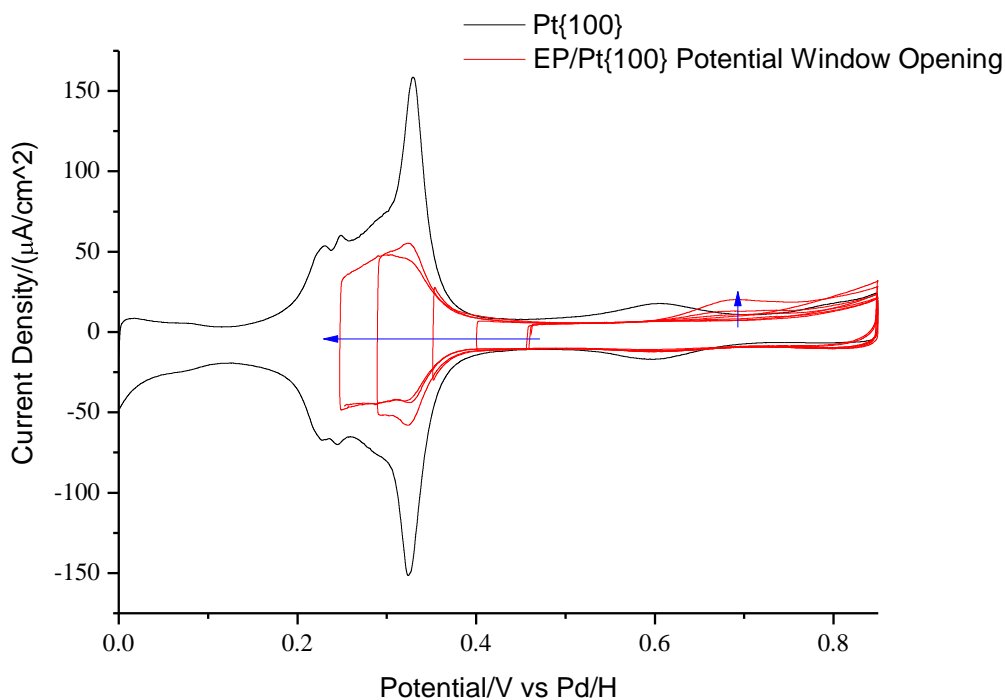


Figure 6.4 CVs of platinum{100} before and after adsorption of EP. The red cycles indicate a window opening experiment (Win-Op) in the direction of the horizontal arrow. Electrolyte = 0.1M H₂SO₄, sweep rate = 50 mV·s⁻¹.

6.2.2 Raman spectra of ethyl pyruvate and its product ethyl lactate

Before carrying out the *in situ* SERS experiments, Raman spectra of neat liquid EP and its hydrogenation product ethyl lactate (EL) were taken as references. The peaks were assigned using standard references and reports¹⁶⁻²², as shown in **Figure 6.5** and **Table 6.1**.

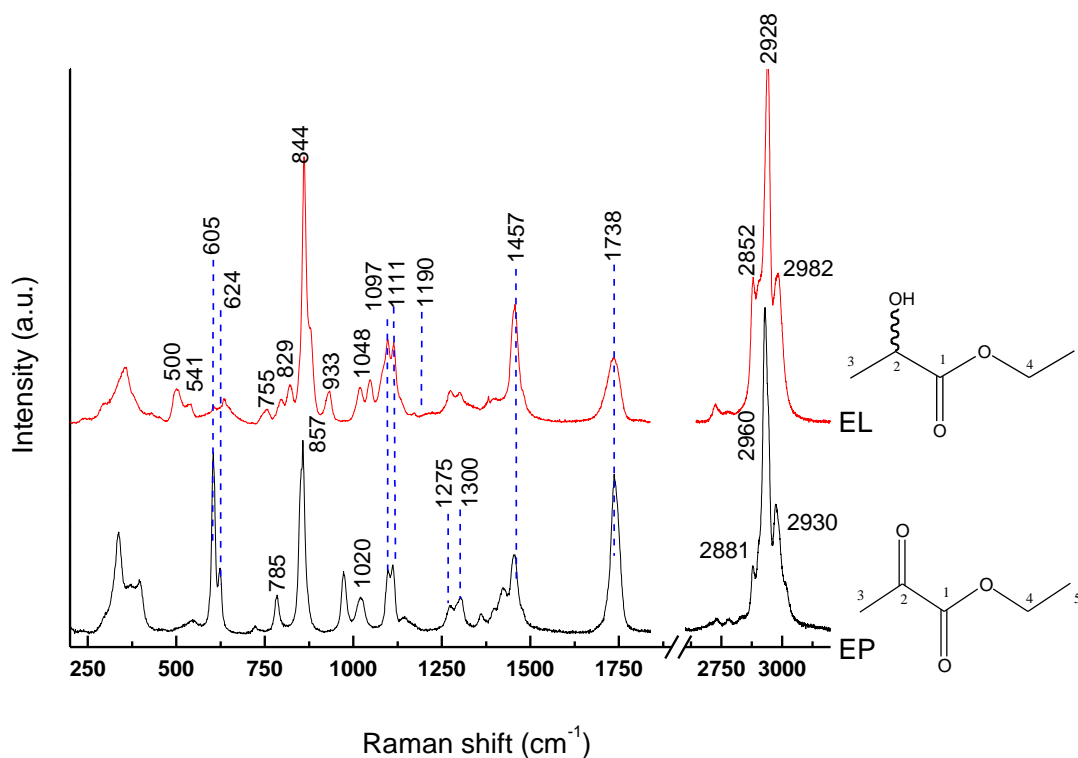


Figure 6.5 Raman spectra of bulk EP (black) and EL (red).

Table 6.1 Band assignments for bulk Raman spectra of EP and EL.²³

Band Position (cm ⁻¹)		Assignment
EP	EL	
3017	2982	va(C ³ -H ₃)
2977	2977	va(C ⁵ -H ₃)
2944	2941	va(C ⁴ -H ₂)
2930	2940	vs(C ³ -H ₃)
2904	2903	vs(C ⁵ -H ₃)
2881	2881	vs(C ⁴ -H ₂)
1738	1738	v(C=O)
1470	1470	δ(C ⁴ -H ₂)
1457	1455	δd(C ⁵ -H ₃)

1423	-	$\delta d(C^3-H_3)$
1399	1382	$\delta w(C^4-H_2)$
1362	-	$\delta s(C^5-H_3)$
1304	1300	$\nu(O-C^4H_2CH_3)$ <i>anti</i>
1273	1275	$\nu(O-C^4H_2CH_3)$ <i>gauche</i>
1111	1114	$\delta r(C^4-C^5H_3)$ <i>anti</i>
1097	1096	$\delta r(C^4-C^5H_3)$ <i>gauche</i>
-	1082	$\nu a(C^1-C^2-C^3) / \delta r(O-H)$
-	1048	$\nu(C^2-C^3) / \delta r(H_3C^3-C^2) / \delta r(C^2-OH)$
1020	1019	$\nu(C^4-C^5H_3)$
972	-	$\nu a(O-C^4H_2-C^5H_3) /$ skeletal
-	861	$\nu(O-C^4) / \delta r(C^5-H_3) / \delta(C^2-C^1-O)$ /skeletal
857	-	$\nu(O-C^4) / \delta r(C^5-H_3) / \delta(C^2-C^1-O)$
-	822	$\nu(C^2-OH) / \delta r(C^3-H_3) /$ skeletal
-	798	$\delta s(C^4-H_2)$
785	-	$\delta r(C^4-H_2)$
-	755	$\delta s(O-C^1-O) / \delta r(C^3-H_3) /$ skeletal umbrella about C^1
624	635	$\delta r(C=O)$
605	605	skeletal $(O-C^1-C^2)$
-	541	$\delta r(C-O)$
-	500	$\delta r(C^2-C^3) /$ skeletal $(O-C^1-C^2)$

6.2.3 SER spectra of EP hydrogenation on Au@Pt NPs surface

Au@Pt NPs were prepared and deposited on the roughened Pt polycrystalline electrode to provide SERS signal. By passing the aqueous H_2SO_4 electrolyte containing dissolved EP through the flowcell, the SER spectra were obtained whilst maintaining the electrode potential in the hydrogen evolution range such that bubble formation was balanced by flow rate to ensure that no impediment to electrolyte flow occurred. In **Figure 6.6**, some familiar bands were observed (black spectrum), including the peaks at 1450, 1302, 1106, 860 and 609 cm^{-1} , which could be assigned as the bulk EP layer adsorbed on the platinum surface. Surprisingly, no feature corresponding to the carbonyl stretches of EP could be discerned. New peaks also showed up in this situation. For example, the peaks at 488 and 2060 cm^{-1} would indicate the presence of on-top carbon monoxide bonded to the platinum surface, which was in agreement with Baiker *et al.*,²⁴ who found that EP undergoes a decarbonylation reaction in the presence of hydrogen on the platinum catalyst and is also in accord with the potential window opening experiments outlined earlier. It can be seen that the peak at 488 cm^{-1} assigned to a Pt-C stretch was much bigger in

size than the peak at 2060 cm^{-1} , suggesting that there was another form of Pt–C bond present at this wavenumber value under hydrogenation conditions. According to Rees *et al.*,²⁵ this is the ‘half-hydrogenated state’ (HHS, **Figure 6.7**), which was proposed as being an intermediate between the ethyl pyruvate and the ethyl lactate product. It was postulated as forming after the rapid addition of the first hydrogen atom to the oxygen atom of EP (with the addition of the second hydrogen atom to the half-hydrogenated Pt–C bond thought to be the rate-determining step of the hydrogenation reaction). The strong peak at 1050 cm^{-1} was due to the presence of C–O stretch of an alcohol, which would be the –OH group formed after hydrogenation of the C=O keto group of EP, thus giving an ethyl lactate-like intermediate. The absence of a keto carbonyl stretch under hydrogenation conditions is therefore explained with presumably, the ester carbonyl stretch being silent due to the surface selection rule.

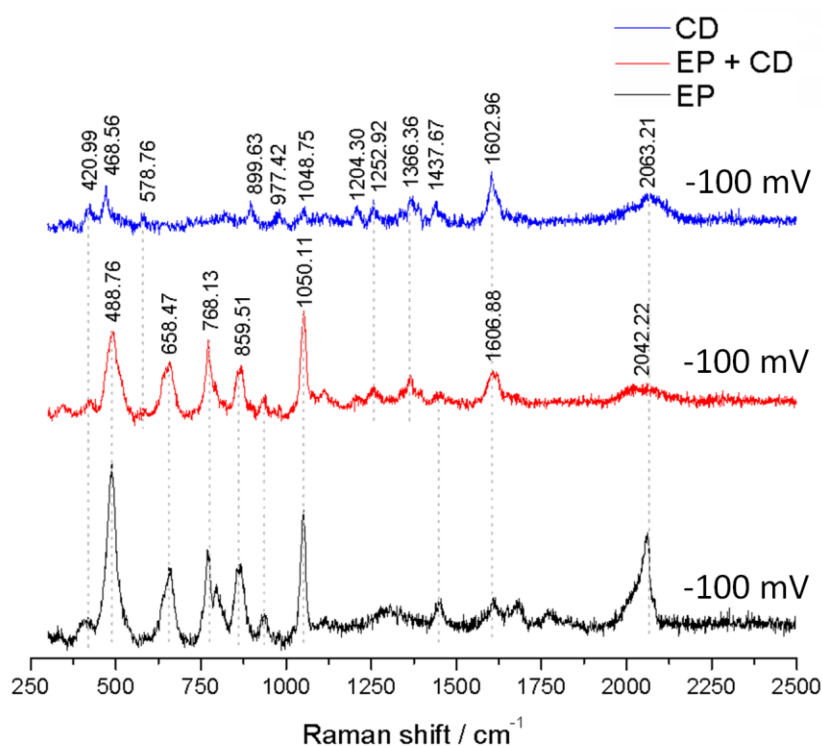


Figure 6.6 SER spectra of 2×10^{-5} M CD (blue), 0.1M EP with 2×10^{-5} M CD (red) and 0.1M EP only (black), **all** under hydrogenation conditions (-100 mV) on Au@Pt NPs in 0.1 M H_2SO_4 .

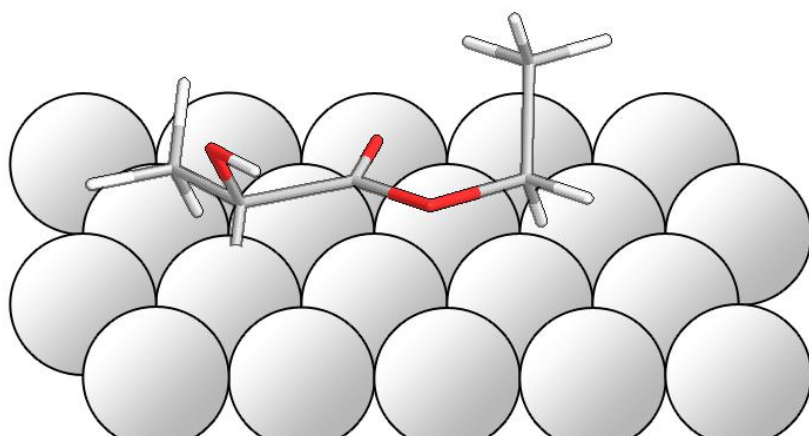


Figure 6.7 Adsorption geometry of the HHS of EP on platinum surface.²³

In the Orito reaction, it is a tremendous challenge to understand the role of the chiral modifier. It has been established that cinchonidine (CD) adsorbs onto the platinum surface via the quinoline ring parallel to the plane of the surface in a ‘flat’ orientation at low concentrations. The mechanism for adsorption in this case was thought to be via the aromatic π states²⁶ (**Figure 6.8a**). At a higher concentration, the quinoline ring becomes tilted with respect to the surface plane and adsorbs through the nitrogen lone pair of electrons and the carbon in the α -position (hydrogen abstracted) to the nitrogen of the quinoline ring, referred to as α -quinolyl²⁷ (**Figure 6.8b**). Other adsorption modes were understood to co-exist, but the flat and α -quinolyl modes were dominant and high *ee* was always correlated with CD lying flat on the Pt surface.²⁶ According to Baiker²⁸, a 1:1 docking mechanism between CD and EP on the surface with hydrogen bonds forming between a protonated tertiary nitrogen of the quinuclidine substituent and the keto carbonyl is thought to hold the EP in the correct enantioface position (together with steric interactions between the chiral pocket formed between CD and the platinum surface) such that hydrogen atoms are added from the Pt surface to the keto carbonyl providing a mechanism for chiral induction. In an alternative model by McBreen, chiral induction also involves a 1:1 docking between CD and EP but in this model, the hydrogen bonding interactions are somewhat different with the hydrogens of the quinolone ring also being activated by the platinum surface to provide sufficient tethering of EP in the correct enantio face configuration for enantioselective via hydrogen bonding for enantioselective hydrogenation to occur. Hence, when CD and EP are

coadsorbed, evidence for hydrogen bonding interactions from SERS would be very useful in confirming if such interactions are actually occurring.

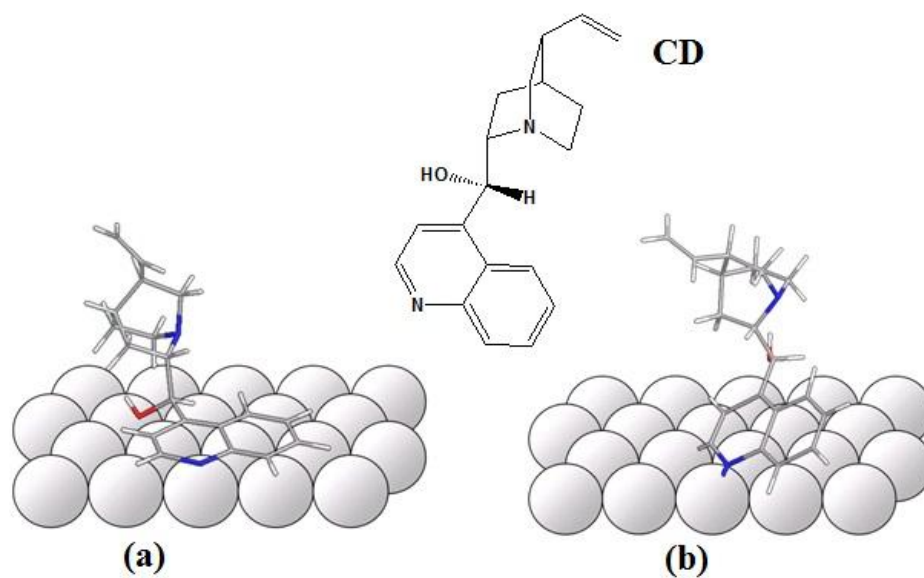


Figure 6.8 Adsorption geometries for CD on platinum in the (a) ‘flat’ orientation and (b) α -quinolyl.²³

When CD was co-adsorbed with EP in the spectroelectrochemical cell, hardly any change in the positions of peaks associated with the HHS were observed save for a small decrease in their intensity. Hence, no new interaction between CD and the HHS could be detected. That is not to say that some differences were observed (red spectrum, **Figure 6.6**). For example, the intensity of the adsorbed CO peak at 2040 cm^{-1} was much reduced upon adsorbing CD and this effect had already been noted by Baiker and co-workers using surface Infra-Red.¹⁴ Hence, CD inhibits decarbonylation. One may speculate that the important ensemble of adjacent Pt sites (as found in the previous CV window opening measurements) is not available since CD prevents such ensembles forming. Instead, the CO stretch was replaced by a broader band due to the vibrational stretching of Pt–H, which was red shifted from 2085 cm^{-1} in the absence of CD to 2063 cm^{-1} when CD is present. This band is observed only when CD is present and was a notable feature of the earlier study²⁹ since a 20 cm^{-1} frequency shift caused by CD to the Pt–H stretch would imply a ‘weaker’ bond making the hydrogen more active (an important feature of the Orito reaction is that reaction rate *acceleration* is observed when CD is added to EP). In the earlier work,

deuterated electrolytes proved that the 2065 cm^{-1} band could be red-shifted to around 1500 cm^{-1} in accordance with expectations based on the increase in reduced mass of the D–Pt versus the H–Pt bond when CD was present. Hence, it was proposed that the chiral modifier competed with the HHS for adsorption sites and created a chiral pocket into which hydrogen could also adsorb and interact with the modifier causing the Pt–H bond to weaken via hydrogen bonding with the tertiary nitrogen atom of the quinuclidine substituent of CD.²⁹ Unfortunately, the key keto carbonyl stretch necessary to identify red shifts in the frequency of the vibration as a consequence of hydrogen bonding could not be observed. In previous gas phase studies of EP²³, this band could be observed but in the aqueous electrolyte it could not. It was suggested that a physisorbed layer of EP was the reason the keto carbonyl stretch could be not observed in this case. Hence, the role of hydrogen bonding interactions could not be clarified based on the present study. It could also be that the lifetime of the keto carbonyl form of EP is very small under hydrogenation conditions and therefore, it cannot be observed. Only the long lived HHS (in which hydrogenation of the keto carbonyl has already occurred) can be observed under *operando* conditions.

6.2.4 SER spectra of EP adsorption on the surface of Pt{*hkl*} single crystal electrodes

6.2.4.1 Pt{111}

In order to specify the contribution of different surface sites towards the hydrogenation of EP, the adsorption of EP on several Pt single crystal electrodes were investigated using the SHINERS technique. The spectrum of EP adsorbed on the surface of a Pt{111} single crystal electrode decorated with Au@SiO₂ NPs is shown in **Figure 6.9a**. The black spectrum represents EP adsorption at the HER potential. The broad band just below 3000 cm^{-1} was due to the C–H stretching vibrations of EP. Together with the C–C–O stretching band at 857 cm^{-1} , O–C–O scissoring vibrational band at 750 cm^{-1} and C=O rocking vibrational band at 649 cm^{-1} , they were all assigned as the bulk EP adsorbed on the platinum surface. The broad band at 1580 cm^{-1} could be associated with a carbonyl stretch of the EP interacting with the Pt surface²⁹ but could equally be due to a small amount of carbonaceous contamination although in this case it is difficult to rationalise its presence after multiple potential cycles into the oxide region (**Figure 6.9b**) which

should certainly remove such species. It is also possible that the band may be ascribed to the C=C stretch of EP in its enolic form⁴ although again, the enol form is reported to be completely destabilised in the presence of adsorbed hydrogen^{30, 31} (see later). The sharp peak at 936 cm⁻¹ arises from the symmetric Cl–O stretch of the perchlorate anion. Differences in the spectra of EP adsorbed on the surface of Au@Pt NPs and Pt{111} in **Figure 6.9a** include a couple of new, intense peaks appearing at 418 cm⁻¹ and at 965 cm⁻¹. These striking features are quite different to those observed on the polycrystalline Pt surface and moreover, vibrational bands ascribable to the HHS are completely absent from the spectrum in **Figure 6.9a**. This suggests that the presence of defect sites might be crucial in order to observe the HHS bands, particularly those at 485 and 1050 cm⁻¹ which corresponded to the Pt–C and C–O stretching vibrations of EP half hydrogenated state. Also, no evidence of CO adsorption on the surface was observed due to the absence of the peak at about 2030 cm⁻¹.

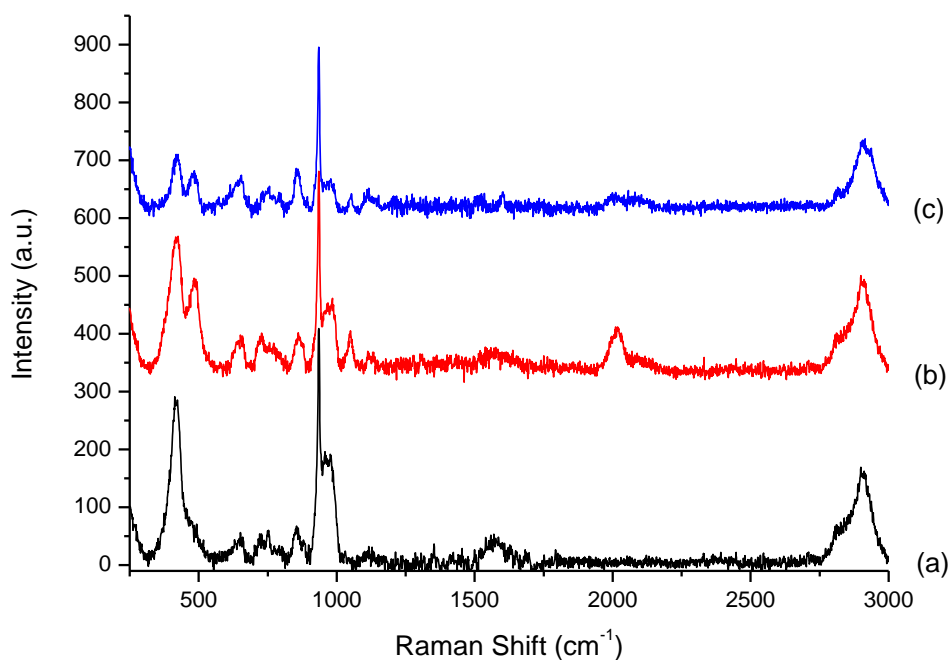


Figure 6.9 SHINER spectra of 0.1 M ethyl pyruvate adsorption in 0.1 M HClO₄ at the HER potential (-0.1V) on the surface of (a) Pt{111}, (b) electrochemically roughened Pt{111}, and (c) electrochemically roughened Pt{111} with the presence of 2×10^{-5} M cinchonidine.

In order to ascertain whether or not this hypothesis was correct, electrochemical surface oxidation (1.2 V vs. Pd/H)/ reduction (0 V vs. Pd/H) potential cycles were carried out to generate defects in the Pt{111} surface.³² In **Figure 6.9b** is shown the SHINERS obtained from a roughened Pt{111} electrode surface undergoing hydrogen evolution. It is evident that two new bands have appeared at 485 and 1050 cm^{-1} ascribable to the generation of the HHS. Additionally, a clear band at 2016 cm^{-1} indicates that decarbonylation of EP is facilitated at the newly generated defect sites but not at Pt{111} terraces alone. Consequently, the intensity of the 485 cm^{-1} peak should consist of contributions from both adsorbed CO and the metal-carbon stretch of the HHS, The initial bands at 418 and 965 cm^{-1} are slightly attenuated after roughening presumably because of the decrease in the number of Pt{111} terrace sites which have now been replaced by surface defects.

Finally CD was co-adsorbed with EP onto the roughened Pt{111} electrode to investigate if any of the surface species formed were influenced by the coadsorbed alkaloid. The spectrum is shown as **Figure 6.9c**. As expected since CD will now occupy Pt surface sites, the intensity of the bands from adsorbed EP were somewhat reduced in magnitude. CD peaks did appear at 1204 and 1603 cm^{-1} but were extremely weak. The main consequence of this small degree of CD adsorption was the reduction of CO band intensity just above 2000 cm^{-1} . Instead, a broad band centred at 2060 cm^{-1} could be discerned associated with Pt–H stretches, which were red shifted because of interaction with CD as described earlier. Besides these changes, no noticeable changes in either relative band intensities or positions were observed as a consequence of EP and CD coadsorption.

6.2.4.2 Pt{100}

The adsorption behaviour of EP was now investigated using Pt{100}. As shown in **Figure 6.10a**, EP adsorption at the HER potential on the surface of Pt{100} gave very similar bands to the ones seen using the Pt{111} surface. The C–H stretches at 2912 cm^{-1} , the C–C–O stretching band at 854 cm^{-1} , O–C–O scissoring vibrational band at 750 cm^{-1} and C=O rocking vibrational band at 649 cm^{-1} were all ascribable to the bulk EP adsorbed layer on the surface. The pair of peaks at 421 and 975 cm^{-1} were clearly due to the same intermediate species found for Pt{111} but this

time adsorbed on the (100) terraces. Since there were no defect sites available on the surface, no bands associated with the HHS of EP were observed.

In order to discover if defect sites on the (100) surface will behave similarly to those for Pt{111} and help facilitate the formation of the HHS of EP, the Pt{100} single crystal electrode was subjected to a series of potential cycles up to 1.2 V (Pd/H). After ten potential cycles, the EP adsorption SHINER spectrum was obtained at the HER potential (**Figure 6.10b**). The appearance of small bands at 485 and 1050 cm^{-1} indicated the formation of the HHS of EP on the defects created. There was also adsorbed CO being formed after creating the defective surface as signified by the appearance of the band at 2014 cm^{-1} . To prove that more defects will make the surface more susceptible to HHS formation, the (100) surface was roughened still further with another twenty potential sweeping cycles being applied. It can be seen that, in **Figure 6.10c**, the bands at 485 and 1050 cm^{-1} became more intense along with the CO band at 2014 cm^{-1} . Meanwhile, the remaining bands reduced in their intensities. As more terraces were roughened and replaced by defect sites, the HHS of EP dominated the spectrum compared to the ‘terrace’ intermediate. After adding CD into the electrolyte containing EP, a spectrum was collected shown in **Figure 6.10d**. Consistent with the previous findings for Pt{111}, besides the appearance of the bands associated with CD at 1600 and 1365 cm^{-1} , the band due to the adsorbed CO was now quenched. Although once again it was shown that CD inhibited the decomposition of EP to CO and promoted the formation of the final product, there was hardly any band intensity discernible at around 2060 cm^{-1} due to the Pt–H stretches. It is interesting to compare the relative intensities of the 1600 cm^{-1} ring stretches of CD on both Pt{111} and Pt{100} in which, for the same bulk CD concentration, a much more intense band is seen for the Pt{100} surface. This could indicate a stronger interaction of CD with the Pt{100} surface under hydrogenation conditions leading to a higher surface CD coverage. Since it is already reported that the quinoline ring of CD is gradually hydrogenated during reaction leading to a weaker binding to Pt and a corresponding loss of $ee^{29,33}$, it may be that this could also be reflected in the structural reactivity differences reported for the Orto reaction. That is, the stronger the interaction of a Pt surface with CD, the superior the enantioselectivity will be afforded.

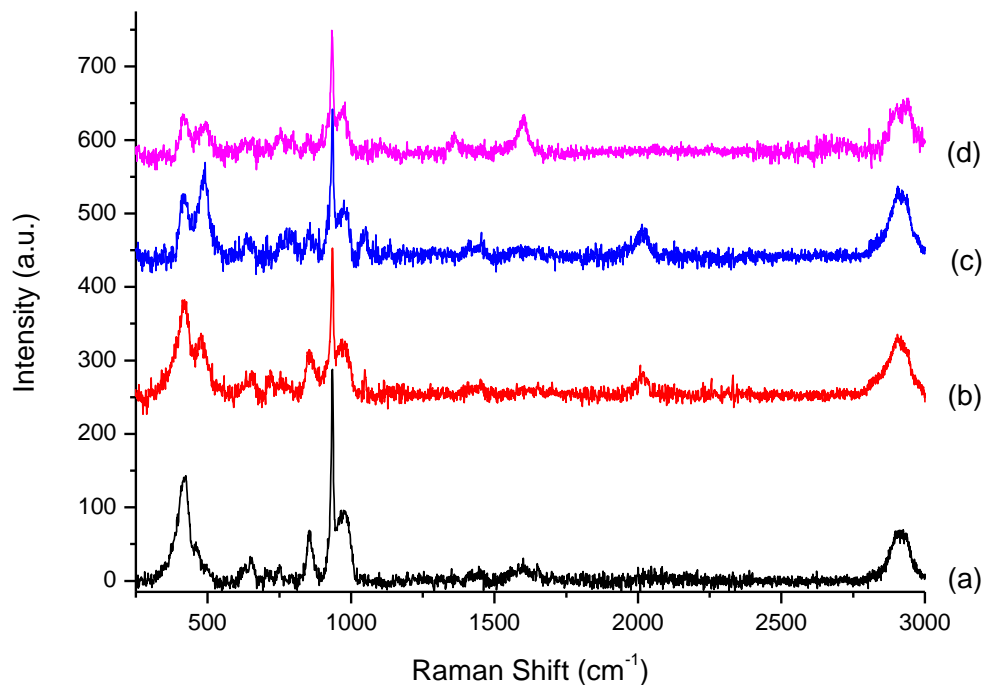


Figure 6.10 SHINER spectra of 0.1 M ethyl pyruvate adsorption in 0.1 M HClO₄ at the HER potential (-0.1 V) on the surface of (a) Pt{100}, (b) slightly roughened Pt{100}, (c) strongly roughened Pt{100}, and (d) strongly roughened Pt{100} with the presence of 2×10^{-5} M cinchonidine.

6.2.4.3 Pt{110}

Interesting results were obtained when EP was adsorbed on the surface of Pt{110} single crystal electrode at the HER potential. As shown in **Figure 6.12a**, the bands of bulk EP appeared at 2906 (C–H stretch), 860 (C–C–O stretching vibrations), 756 (O–C–O scissoring vibrations) and 652 (C=O rocking vibrations) cm^{-1} as usual. However, unlike for Pt{111} and Pt{100}, terrace intermediate bands at 420 and 970 cm^{-1} co-existed with HHS bands at 493 (Pt–C stretches) and 1050 (C–O stretching vibrations) cm^{-1} prior to any roughening by potential cycling. A small band at 2023 cm^{-1} was also observed, which indicated a small amount of CO adsorbed on the surface as well. Both of these observations suggest that Pt{110} is intrinsically defective compared to the other two basal planes. It is interesting to note that Pt{110} actually undergoes a surface

reconstruction from a (1x1) to a ‘missing row’ (1x2) when clean and thermally equilibrated. Hence, 50% of surface atoms have to undergo displacement for this phase transition to occur.³⁴ Recent STM imaging results both under UHV and electrochemical conditions show that depending on the cooling environment following thermal annealing, Pt{110} may contain either pure (1x1) and (1x2) ordered phases or a mixture of both.^{35,36} The cooling ambient used in the present study after flame-annealing generates a mixed phase with numerous defects being present³⁷ and therefore the EP results reported here are entirely consistent with the defective surface produced after flame-annealing and hydrogen cooling.

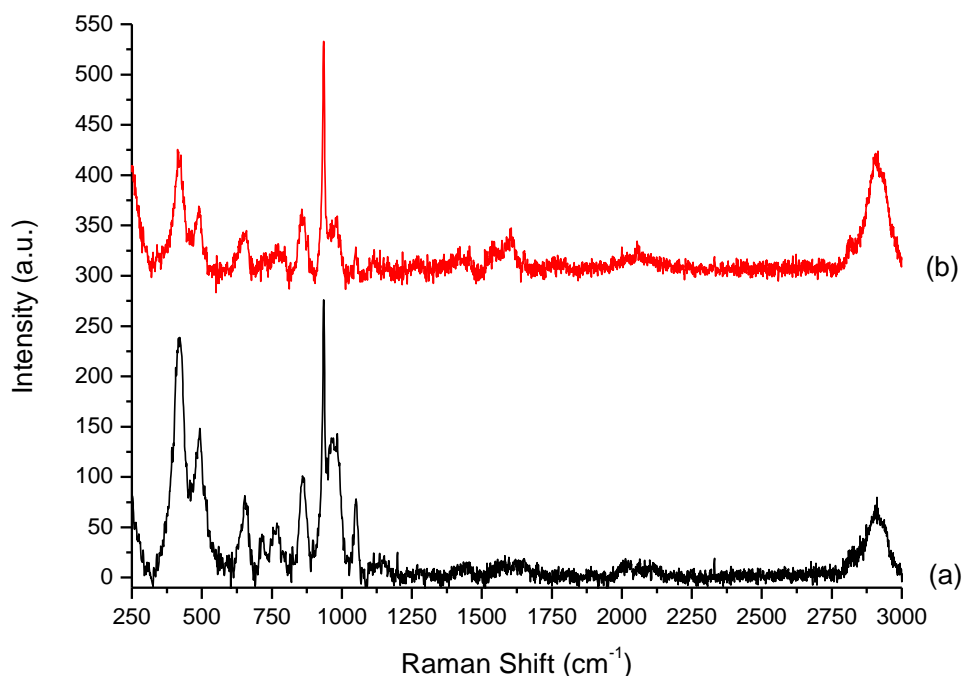


Figure 6.11 SHINER spectra of 0.1 M ethyl pyruvate adsorption in 0.1 M HClO₄ at the HER potential (-0.1 V) on the surface of (a) Pt{110}, and (b) Pt{110} with the presence of 2×10^{-5} M cinchonidine.

In **Figure 6.11b**, CD was co-adsorbed with EP onto the Pt{110} surface resulting in the disappearance of the CO band at 2023 cm⁻¹. Instead, Pt–H (stretching vibration at 2070 cm⁻¹) features were apparent in accordance with results for Pt{111} and Pt{100} and a medium intensity CD quinoline ring stretch at 1600 cm⁻¹, certainly more intense than on Pt{111} but

slightly less marked than observed with Pt{100}. Again, a dichotomy between {111} surfaces and Pt{100}/Pt{110} surfaces is becoming a guiding thread throughout the present studies with a much weaker interaction of substrates on Pt{111} compared to the other basal planes.

6.2.4.5 The influence of the potential on EP adsorption on the Pt{111} surface

It has previously been shown that the HHS of EP only exists at potentials where hydrogen evolution is taking place.²⁵ In the present study, it has further been verified that defect sites are also a prerequisite for HHS formation (and adsorbed CO from decarbonylation of EP). Already, this finding has profound implications for the Orito reaction since the structure-activity relationships associated with this reaction may already be being addressed and future studies using shaped nanoparticles may reveal whether or not the HHS is a necessary intermediate for high *ee* or merely a spectator species. However, so far as the newly discovered terrace intermediate is concerned, questions regarding its stability as a function of potential (and implicitly as a function of hydrogen coverage) has not yet been addressed. Therefore, a series of experiments was undertaken to monitor the stability of the terrace intermediate as a function of potential in order to compare its behaviour with the HHS.

As shown in **Figure 6.12**, the spectrum obtained from EP containing perchloric acid on Pt{111} for the HER potential at -100 mV (vs. Pd/H) gave rise to the characteristic terrace intermediate Raman bands at 420 and 975 cm^{-1} already discussed. With an increase of the potential from the HER region to 0 V it is noted that there is actually a slight increase in the intensity of both of these bands. This is a striking difference to the behaviour of the HHS peaks which would be almost completely attenuated at this potential.²⁹ Hence, the terrace intermediate is already behaving quite differently to the HHS. The slight increase in intensity observed could be due to several factors such as a simple reorientation of the terrace intermediate towards the planar electrode surface or that the rate of hydrogenative desorption of this intermediate is much reduced such that the steady state coverage increases slightly. As the potential increases to 0.1 V, both peaks associated with the EP terrace intermediate are reduced markedly in intensity. Hence, an explanation of this behaviour in terms of relative rates of reduction/adsorption can no longer hold since the intensity of the peaks has decreased. Again, one could invoke a re-orientation of the intermediate such that band intensity decreases or that the rate of formation of this

intermediate is reduced at the more electrooxidising potential (even though H UPD states are still occupied with adsorbed hydrogen).

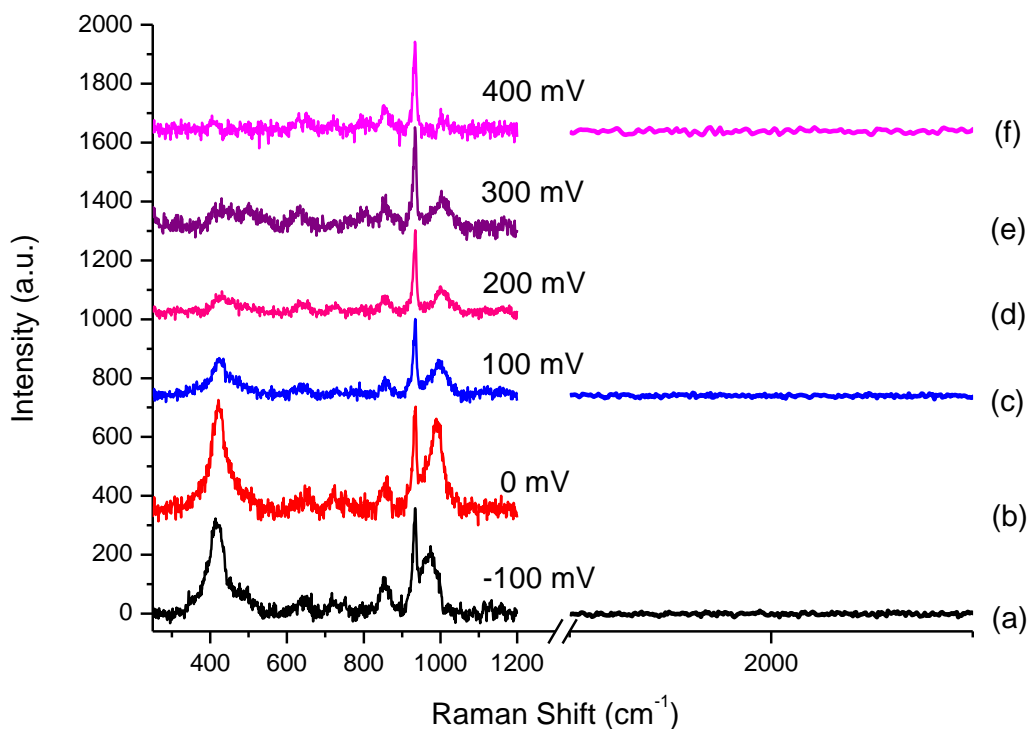


Figure 6.12 SER spectra of 0.1 M ethyl pyruvate adsorption in 0.1 M HClO₄ on Pt{111} at different potentials: (a) -100 mV, (b) 0 mV, (c) 100 mV, (d) 200 mV, (e) 300, and (f) 400 mV vs. Pd/H.

It has been found from CV measurements that for irreversibly adsorbed monolayers of EP, decarbonylation of EP occurs at potentials in the HER and H UPD regions. Therefore, a possible mechanism for the gradual attenuation of the terrace intermediate bands might be that it is slowly being converted into yet another (SHINERS silent) species plus adsorbed CO. However, no concomitant increase in CO intensity (2030 cm⁻¹ wavelength) was observed following exposure to EP at these reducing potentials. Although in the SHINERS experiment, EP was contained within the bulk electrolyte rather than irreversibly adsorbed as in the CV experiments, the absence of a growth in CO bands is astonishing. It could be that the amount of CO produced for Pt{111} is relatively small and because the Raman cross section is also small, the spectrometer

would not yield sufficient sensitivity to detect this adsorbed molecule. However, this is thought unlikely. Hence, the only feasible explanations for the behaviour observed is either that the rate of formation of the terrace intermediate in the absence of a reducing environment is low compared to the rate of desorption or that the orientation of the adsorbed entity changes slowly as a function of potential such that the crucial 418 and 970 cm^{-1} transitions are no longer SERS active due to surface selection rule considerations.

Another aspect of the potential dependence of the SHINERS peaks is that the 970 cm^{-1} feature moves to higher wavenumber within the potential range examined. It is well known that those bonds involving an exchange of positive or negative charge into bonding/anti-bonding orbitals may undergo a Stark shift as a function of potential.³⁸ This may be the case here (in which case the Stark tuning rate would be a rather large 100 cm^{-1}/V and also decidedly non-linear over the range of potential investigated). However, none of the other bands are affected in this way suggesting that whatever their nature, they are not involved in a transfer of charge into bonding/anti-bonding orbitals as a function of potential. A more likely explanation for the shift therefore might be that in one configuration, the vibrational mode is interacting with the surface (steric effect-lower vibrational frequency) whereas in the other mode, the vibration is no longer 'frustrated' by being in contact with the electrode surface platinum atoms (shift to higher frequency).

Therefore, a preliminary interpretation of the spectroscopic data would be that the terrace intermediate is a form of EP bonded to the surface via the lone pairs of electrons on the ketone carbonyl and lying almost parallel to the surface (**Figure 6.13**). In this case, the 418 cm^{-1} band could be well described either as a metal–O stretch or the wagging mode of the ketone carbonyl.¹⁶ The 970 cm^{-1} band would be consistent with the rocking mode of a methyl/C=O substituent according to Socrates.¹⁶ Hence, when this rocking mode impinges close to the surface, a softening of the vibration might be expected. However, as the C=O – metal tilt angle increases such that the EP molecular axis lifts away from the surface, both of these stretches might be expected to change their intensities and the 970 cm^{-1} vibration to shift to slightly higher frequencies. Interestingly, if the terrace intermediate is simply a tilted form of molecular EP it might explain why it is seen at relatively positive potentials compared to the HHS which is a reduced species and will only form in the presence of evolved hydrogen.



Figure 6.13 Schematic changes of the orientation of EP on Pt surface with the increase of the potential.

The only problem with this interpretation is that according to McBreen *et al.*, EP in the absence of hydrogen spontaneously forms chains of EP molecules in their enolic form on Pt{111} at room temperature.⁴ Therefore, can the terrace intermediate be assigned to an enolic form of EP? Several factors mitigate against this interpretation. First, it is reported that the enolic form of EP is completely unstable when coadsorbed with hydrogen and reversibly converts back into its keto form.²⁵ Hence, the stability of the terrace intermediate whilst hydrogen is being evolved would pose a problem in this model. One could argue that in the present study, EP was contained within the bulk electrolyte whereas McBreen's work is carried out in UHV for a monolayer of EP.⁴ Hence, there is no opportunity for the enol tautomer at equilibrium to form via replenishment from the bulk. Another problem would be the absence of certain bands associated with enol formation. Foremost amongst these would be C–H stretches at wavenumbers greater than 3000 cm^{-1} due to the presence of sp^2 hybridised carbon and a C=C stretch around 1580 cm^{-1} . These were not observed. The 970 cm^{-1} band would be consistent with an out of plane C–H vibration of a vinyl ether²³ but it is uncertain how one could then interpret the shift of this band with potential within such a model. Hence, the enol model does not quite fit the data although it would be consistent with observation of surface intermediate bands at potentials positive of the H UPD region because adsorbed hydrogen atoms are absent and according to McBreen *et al.*, should form spontaneously.⁴ The reported EELS data for EP enol formation on Pt{111} do give rise to bands around 400 and 970 cm^{-1} but again also to stretches around 1560 and 3030 cm^{-1} .^{23, 39} It may be that the condensed phase of the aqueous electrolyte may well disrupt the delicate hydrogen bonding interactions necessary to facilitate keto-enol tautomerism in UHV so the enol chains may not actually be forming.

A final and more extreme interpretation of the SHINER spectrum of the terrace intermediate could be that actually, full transfer of charge from the keto C=O to the metal occurs with transfer of a single hydrogen atom to the carbon of the keto carbonyl resulting in an alkoxide species. The product ethyl lactate is then formed when the second hydrogen is transferred to the alkoxide oxygen atom. In this case, the 418 cm⁻¹ peak would also be associated with a metal-oxygen stretch and again the 970 cm⁻¹ band assigned to either a frustrated rocking mode of the methyl substituent interacting with the surface which hardens as tilt angle changes or indeed a C–O stretch of the alkoxide which also shifts both frequency and intensity as the alkoxide tilts as a function of potential. However, this interpretation is rejected based on DFT calculations performed by Bjork Hammer⁴⁰ which showed a large activation energy barrier to addition of the first hydrogen atom to carbon compared to a decrease in energy when the first hydrogen atom was transferred to the oxygen atom of the keto carbonyl.

As the potential was further increased into the double layer range, there was no obvious hint of any EP molecules or any surface derivatives adsorbed on the surface since the SER spectra were generally flat and featureless. This behaviour has also been reported previously using Au@Pt nanoparticles.²⁵ However, once surface OH groups began to form on the surface (electrochemical oxide formation at Pt surface), a new set of peaks began to emerge (**Figure 6.14**). Two peaks started growing more intense at 841 and 1354 cm⁻¹ together with other notable features at 425, 1615 and 1725 cm⁻¹. All of these peaks have been assigned previously to the adsorption of a pyruvate species formed as a consequence of hydrolysis of the ester to form the corresponding acid and alcohol.²³ Hence, the 841, 1354 and 1615 cm⁻¹ peaks are identified as the bending (δ), symmetric stretching (s) and asymmetric (as) stretching vibrations respectively of the carboxylate group adsorbed on the surface.

It was noticed that the $\nu_s(\text{COO}^-)$ band was split into two peaks at 1354 and 1369 cm⁻¹. The 1369 cm⁻¹ peak of the doublet became weaker at higher potentials. Also, with the increase of potential, the two bands at 841 and 1354 cm⁻¹ reached their maximal size and then became smaller as the surface became more covered in surface oxide. Interestingly, no shift in the position of these peaks was observed as a function of potential but between 900 and 1000 mV (Pd/H) their relative intensities changed signifying a change in the orientation and mode of bonding of the carboxylate to the surface from uni- to bi-dentate.⁴¹ In this reference it is demonstrated that when

the CO_2^- group is tilted on the surface by adsorption through both of its oxygen atoms, the $\nu_s(\text{COO}^-)$ and $\delta(\text{COO}^-)$ bands have similar intensity but the $\nu_s(\text{COO}^-)$ band is slightly stronger than the $\delta(\text{COO}^-)$ band. The relative intensity of the $\delta(\text{COO}^-)$ band with respect to the $\nu_s(\text{COO}^-)$ band becomes stronger as the carboxylate group is more strongly tilted away from the surface at more negative potentials (below 900 mV). If the CO_2^- group is adsorbed flat on the surface through π - electrons, the $\nu_s(\text{COO}^-)$ band is much stronger than the $\delta(\text{COO}^-)$ band. Other peaks at 1725 and 445 cm^{-1} may be ascribed to the symmetric stretch of the keto carbonyl group and the metal-oxygen stretch respectively.

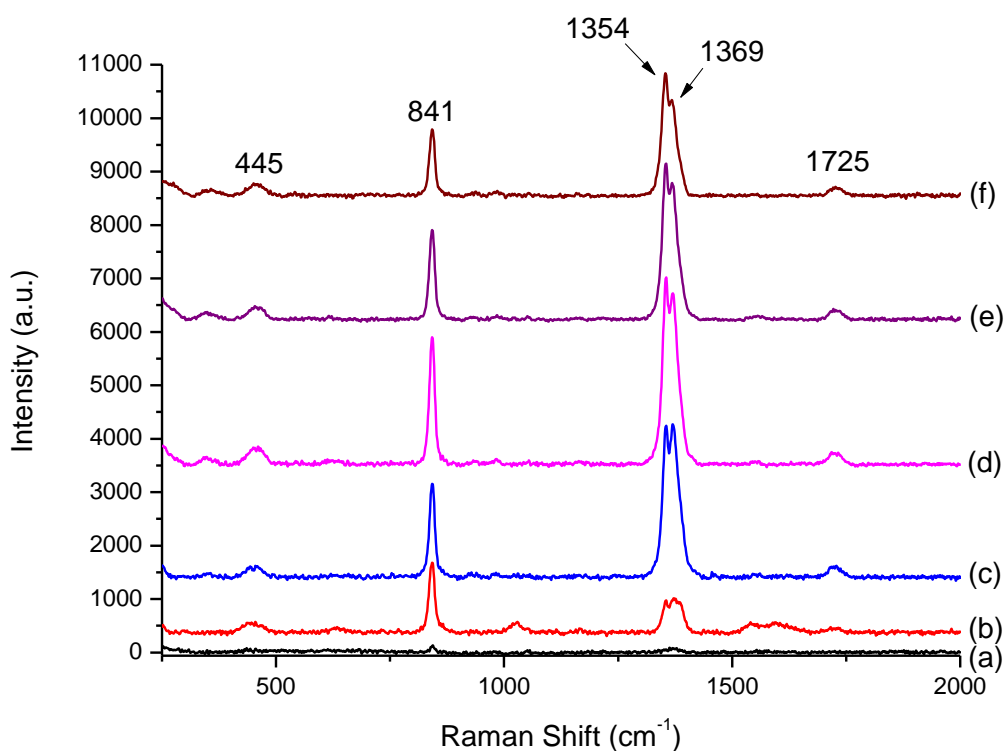


Figure 6.14 SHINER spectra of 0.1 M ethyl pyruvate adsorption in 0.1 M H_2SO_4 on Pt{111} at different potentials: (a) 850 mV, (b) 900 mV, (c) 1000 mV, (d) 1100 mV, (e) 1200, and (f) 1300 mV vs. Pd/H.

Interestingly, two other very weak bands may be discerned at around 650 cm^{-1} and 1580 cm^{-1} . The first of these is clearly the C=O bend of the keto carbonyl accompanying the 1725 cm^{-1} band. The second is more pronounced at more negative potentials (see spectrum (b)) and

disappears by spectrum (f) but could this possibly be due to some enol formation? Clearly, it is a very weak band but its sudden appearance upon shifting potential from 0.85 to 0.9 V certainly rules out a fortuitous carbon contaminant.

6.2.5 Discussion

Figure 6.15 summarises in a single diagram the SHINERS data collected for all of the Pt{*hkl*} surfaces studied together with a typical SER spectrum collected using polycrystalline Au@Pt nanoparticles. The trends discussed are apparent from this montage of data. Two reaction intermediates are identified. The first being the HHS state whose characteristic SER spectrum is shown. Second, a terrace intermediate which has been postulated as being due to an end-on configuration bound via an oxygen lone pair from the keto carbonyl known as η^1 . This species has also been reported as being the dominant species when EP is adsorbed on single crystal Pt{111}⁹ and is confirmed in the present study. Nonetheless, a crucial question to be addressed is how the various intermediates can be linked together in the context of the Orito reaction?

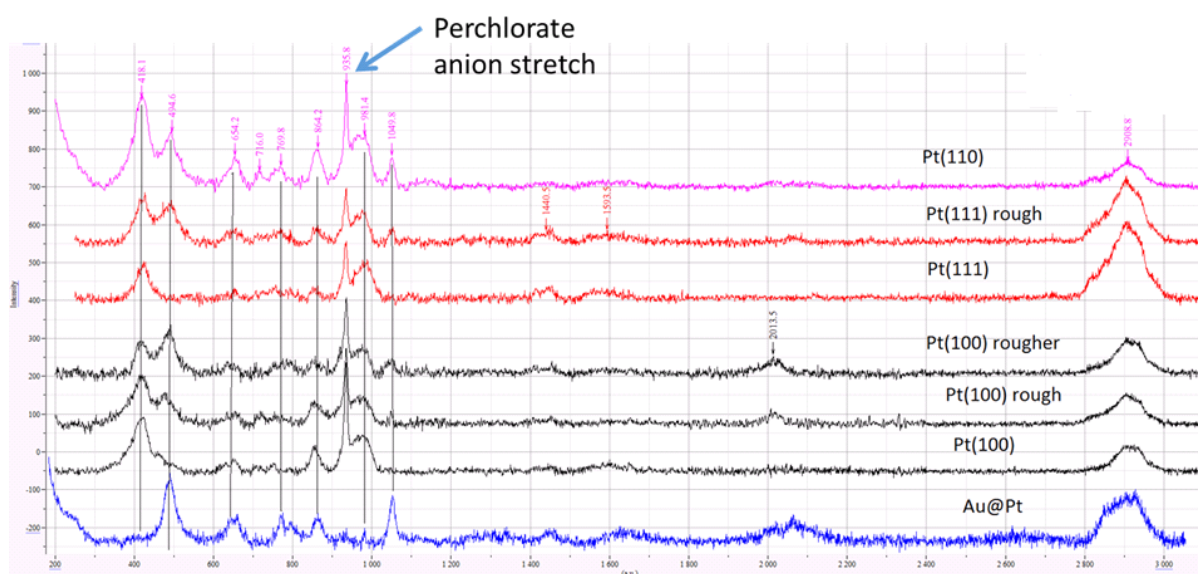


Figure 6.15 Summary of SHINER spectra of EP on Pt{*hkl*} single crystal surfaces studied and SER spectrum of EP on polycrystalline Au@Pt NPs surface.

Figure 6.16 shows a schematic diagram of changes that should be occurring in order to generate the various adsorbed species found in the present study. From **Figure 6.16** it may be seen that a

sequential addition of hydrogen atoms to adsorbed molecular EP results in the final product ethyl lactate. However, when considering the stage at which chiral induction must occur to generate an enantiomeric excess, it is clear that once the HHS is formed (first H addition) then the chirality of EL is already set. Therefore, the HHS so far as chiral induction is concerned, must be a spectator species. Rather, it is at the stage of when the η^1 species is formed that chiral induction needs to take place. This is of course precisely what is speculated following the 1:1 docking models of chiral induction discussed earlier. However, in the present study it was impossible to discern the keto carbonyl stretch and therefore, collect evidence supporting hydrogen bond formation between EP and CD. That chiral pockets of chemisorbed hydrogen on Pt were found when CD was coadsorbed with EP was confirmed. Hence, can one address the question of what type of platinum surface sites might be important for enantioselectivity?

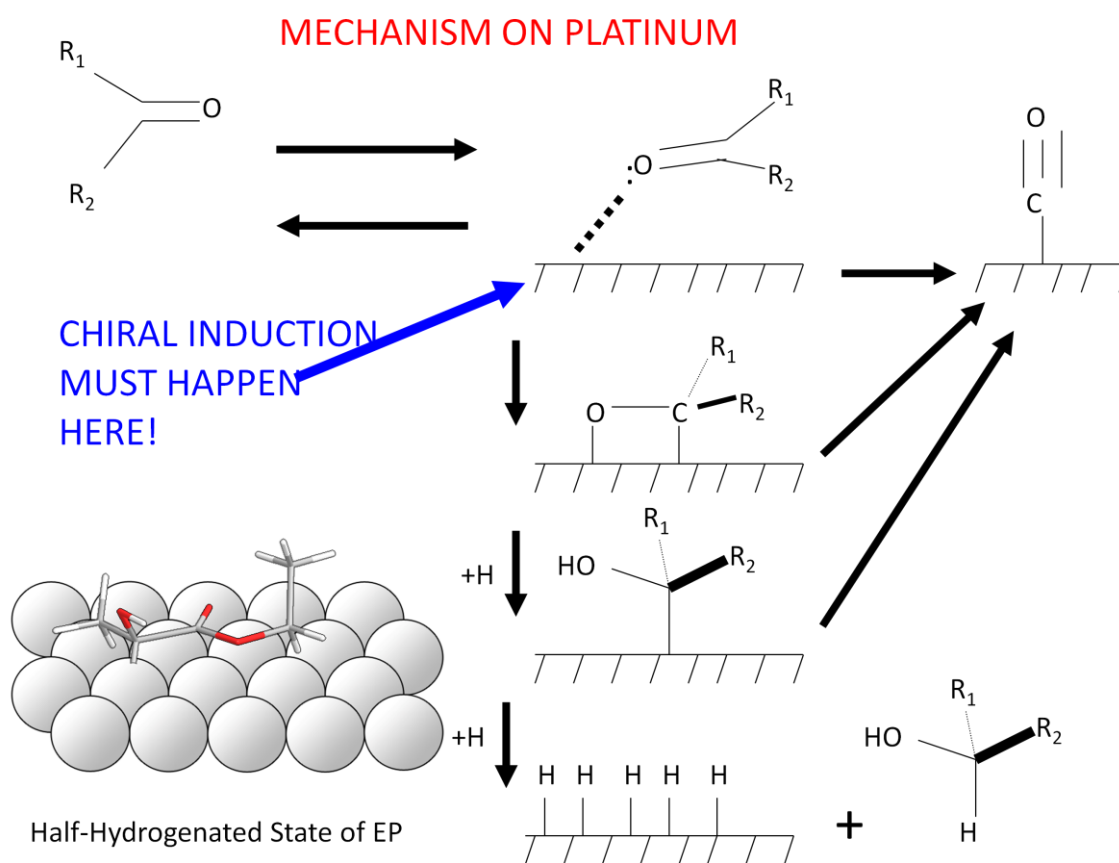


Figure 6.16 Schematic mechanism of ketone reacting on platinum surface.

It has been shown that defect sites catalyse the formation of the HHS and that moreover, the HHS is relatively long lived on the surface. On terrace sites, the HHS is completely absent. Yet we know from CV and SHINERS data that EP is hydrogenated successfully on Pt{*hkl*}. Consequently, if the pathway outlined in **Figure 6.16** is reasonable, it means that if the HHS does form on terraces, its lifetime on the terrace is relatively short. This may be related to a weaker adsorption energy of the HHS on terraces relative to defect/step sites. DFT results from Willock *et al.* demonstrate that this is indeed the case with adsorption energies for the HHS of -90 and -108 kJ·mol⁻¹ for adsorption on Pt{111} and the step of Pt{221} respectively.²³ Interestingly, for the molecular η^1 species the adsorption energies are -60 and -50 kJ·mol⁻¹ for the Pt{111} and Pt{221} step site respectively and hence, the η^1 species is most stable when adsorbed on terraces rather than at steps. According to these calculations though, the HHS should form in preference to the η^1 species on all Pt surfaces. Hence, although the HHS is the most thermodynamically stable entity on both steps and terraces, on steps it is long lived because its adsorption energy is larger than on the terrace so its desorption is slow (and its lifetime long). However, the observation of the η^1 species on terraces rather than the HHS would suggest that an activation energy barrier exists between the two forms but that once overcome, the HHS is rapidly hydrogenated on the terrace compared to the step. DFT calculations by Willock *et al.* are presently underway to confirm this point.

So far as the enantioselective hydrogenation is concerned, clearly the chiral induction carried out by CD must occur before the HHS forms. Hence, based on this hypothesis, one would predict that terrace sites would be beneficial since the η^1 species exhibits a longer lifetime on terraces compared to when interacting with steps (chiral induction would have to be faster than the transformation of the η^1 species into the HHS). This would be in agreement with Baiker's findings¹¹ who used shaped nanoparticles to confirm that terrace sites were superior to defects in promoting enantioselectivity during Orito-type reactions. However, in previous studies by Attard *et al.*, the strategy of selectively decorating the defect sites of a supported 5% Pt on graphite catalysts demonstrated unequivocally that *ee* decreased if defect sites were blocked.⁴² In Baiker's study, it should be noted that defect sites were still present although a correlation was found between increasing *ee* and surface population of terrace sites in the shaped nanoparticle study. Therefore, a reconciliation of these divergent interpretations might be that terraces are necessary for binding both CD and the η^1 species in the correct orientation to favour high *ee* but that the

chiral environment around the quinuclidine substituent ‘overhanging’ or in the vicinity of defect sites could provide an even greater chiral discrimination pathway. The ‘chiral’ pocket created in this way would actually be diastereomeric in nature since defect sites such as kinks may be chiral¹² and combined with the quinuclidine of CD would give rise to two chemically distinct docking positions for EP, namely $+/+$ and $+/-$ where $+$ signifies the handedness of CD and $+$ or $-$ the chirality of the kink site. This model would still place the enantioselective interaction between EP and CD around the defect site however which requires an extremely fast hydrogen transfer from the chiral pocket to the keto carbonyl of EP forming enantioselectively a HHS which is subsequently hydrogenatively desorbed as the chiral product. Clearly, the experiment to be undertaken to prove this conjecture would be to take $\{111\}$ shaped Pt nanoparticles, treat them with Bi to block defect sites and compare *ee* from untreated particles.

As the present study is concerned, discounting the decarbonylation pathway, no major changes in either the wave number or relative intensity of bands could be observed for both of the EP surface intermediates identified following coadsorption with CD. That the adsorbed hydrogen is activated in the presence of CD would suggest a ‘faster’ rate of hydrogenation in the vicinity of CD. Clearly, another factor to be considered is the relative binding of CD at different sites. The present study indicates that under hydrogenating conditions, CD is less stable on Pt $\{111\}$ than on Pt $\{100\}$. Since the surface concentration of CD is an important factor in supporting high *ee* (in that if batch reactors are used, CD needs to be replenished to maintain good *ee* since hydrogenation of the quinolone aromatic system as a function of reaction time renders CD much less strongly bound to Pt²⁸). It is reported that Pt $\{100\}$ shaped nanoparticles are much more active than Pt $\{111\}$ in hydrogenating CD¹¹ in agreement with the much greater binding of CD on the Pt $\{100\}$ surface reported here.

Clearly, the actual mechanism of the Orito-reaction is extremely complex with a subtle balance of many factors determining optimal *ee* (the role even of different solvents should be considered here also). However, the possibilities for influencing the nature of the EP bound states available as a function of surface structure have been highlighted in the present study. In this context, experiments using microfluidic systems whereby EP is hydrogenated on single crystal electrodes would prove invaluable since the actual *ee* of product is obtained after the reaction mixture is collected post reaction. Preliminary measurements to this effect have just started (Attard and

Wirth to be published) and although yields are in excess of 80% EL are feasible, *ee* obtained are rather low (~ 20%). With further optimisation, this may improve and different Pt{*hkl*} compared and this data related to the present SHINERS results.

Taylor has studied the adsorption of the gas phase of EP on polycrystalline platinum surfaces (Au@Pt NPs) with and without the presence of the hydrogen gas.²³ Although the phase of EP changed from liquid to gas, its behaviour is similar in both situations, as the HHS forms on the platinum surface both circumstances. Nevertheless, in future experiments it is worth trying to explore further this aspect by replacing the liquid EP with gas phase EP adsorption on all of the basal planes of the platinum in order to see if the η^1 species forms rather than the HHS.

6.3 Conclusion

EP adsorption on the surfaces of different platinum single crystal electrodes has been studied. New discoveries include the formation of distinct surface species ascribable to adsorbed EP under hydrogenating conditions. The EP HHS, which was found to be a critical intermediate of the hydrogenated product, only forms on the step sites of the platinum surface at the HER potential. However, another new intermediate adsorbate, which is believed to be a η^1 species and is believed to be a precursor of the HHS only forms on the terraces of the surface. As long as there is hydrogen present, no matter if gaseous or electrosorbed, both intermediates form and are stable. In contrast, only the η^1 species can exist at potentials positive of the HER. Both CV and SERS demonstrate that decarbonylation of EP can occur as a side reaction at defect sites. Coadsorption with CD inhibits this side reaction. The exact role of both EP surface intermediates in affording high *ee* is not clear but some speculative reasons suggesting how each may influence overall *ee* are posited. If the HHS is an essential intermediate on the reaction pathway to product, its formation is found to be catalysed at defect sites so an abundance of defect sites might favour activity. However, if the initial transfer of a hydrogen atom is the important enantioselective step, terrace sites might be the most suitable since the η^1 species appears the most long-lived with greater possibility of interacting with hydrogen from the CD induced chiral pocket prior to transfer of the second hydrogen followed by desorption of EL. If the Pt catalyst is oxidised, it is expected that pyruvic acid will be the final product based on the surface stability of the pyruvate species under such conditions according to SHINERS measurements.

6.4 References

1. Y. Orito, S. Imai and S. Niwa, *NIPPON KAGAKU KAISHI*, 1979, **1979**, 1118-1120.
2. X. Li, R. P. K. Wells, P. B. Wells and G. J. Hutchings, *Journal of Catalysis*, 2004, **221**, 653-656.
3. J. M. Bonello, F. J. Williams, A. K. Santra and R. M. Lambert, *The Journal of Physical Chemistry B*, 2000, **104**, 9696-9703.
4. S. Lavoie, M.-A. Laliberté, G. Mahieu, V. Demers-Carpentier and P. McBreen, *Journal of the American Chemical Society*, 2007, **129**, 11668-11669.
5. J. M. Bonello, E. C. H. Sykes, R. Lindsay, F. J. Williams, A. K. Santra and R. M. Lambert, *Surface Science*, 2001, **482-485, Part 1**, 207-214.
6. S. Lavoie, M. A. Laliberté and P. H. McBreen, *Journal of the American Chemical Society*, 2003, **125**, 15756-15757.
7. T. Bürgi, F. Atamny, R. Schlögl and A. Baiker, *The Journal of Physical Chemistry B*, 2000, **104**, 5953-5960.
8. A. Vargas, T. Bürgi and A. Baiker, *Journal of Catalysis*, 2004, **222**, 439-449.
9. E. L. Jeffery, R. K. Mann, G. J. Hutchings, S. H. Taylor and D. J. Willock, *Catalysis Today*, 2005, **105**, 85-92.
10. J. M. Bonello, E. C. H. Sykes, R. Lindsay, F. J. Williams, A. K. Santra and R. M. Lambert, *Surface Science*, 2001, **482-485, Part 1**, 207-214.
11. E. Schmidt, A. Vargas, T. Mallat and A. Baiker, *Journal of the American Chemical Society*, 2009, **131**, 12358-12367.
12. G. A. Attard, *Journal of Physical Chemistry B*, 2001, **105**, 10.
13. E. Herrero, A. Rodes, J. M. Pérez, J. M. Feliu and A. Aldaz, *Journal of Electroanalytical Chemistry*, 1995, **393**, 87-96.
14. D. Ferri, T. Bürgi and A. Baiker, *The Journal of Physical Chemistry B*, 2004, **108**, 14384-14391.
15. O. A. Hazzazi, G. A. Attard, P. B. Wells, F. J. Vidal-Iglesias and M. Casadesus, *Journal of Electroanalytical Chemistry*, 2009, **625**, 123-130.
16. G. Socrates, *Infrared and Raman Characteristic Group Frequencies: Tables and Charts*, Wiley, 2004.
17. S. Lavoie, M. A. Laliberté and P. H. McBreen, *Journal of the American Chemical Society*, 2003, **125**, 15756-15757.
18. M. Castonguay, J. R. Roy, S. Lavoie, M. A. Laliberté and P. H. McBreen, *The Journal of Physical Chemistry B*, 2004, **108**, 4134-4140.
19. Y. Mido, H. Shiomi, H. Matsuura, M. A. Raso, M. V. Garcia and J. Morcillo, *Journal of Molecular Structure*, 1988, **176**, 253-277.
20. J. Wang, M. Castonguay, J. R. Roy, E. Zahidi and P. H. McBreen, *The Journal of Physical Chemistry B*, 1999, **103**, 4382-4386.
21. W. J. Ray, J. E. Katon and D. B. Phillips, *Journal of Molecular Structure*, 1981, **74**, 75-84.
22. X. Yang, Z. H. He, X. J. Zhou, S. H. Xu and K. T. Leung, *Applied Surface Science*, 2006, **252**, 3647-3657.
23. R. J. Taylor, Cardiff University, 2010.
24. D. Ferri, S. Diezi, M. Maciejewski and A. Baiker, *Applied Catalysis A: General*, 2006, **297**, 165-173.
25. N. V. T. Rees, R.J.; Jiang, Y.-X.; Morgan, I.R.; Knight, D.W. and Attard, G.A., *Journal of physical Chemistry C*, 2011, **115**, 1163-1170.
26. Z. Ma, I. Lee and F. Zaera, *Journal of the American Chemical Society*, 2007, **129**, 16083-16090.
27. D. Ferri and T. Bürgi, *Journal of the American Chemical Society*, 2001, **123**, 12074-12084.

28. H. U. Blaser, H. P. Jalett, D. M. Monti, A. Baiker and J. T. Wehrli, in *Studies in Surface Science and Catalysis*, ed. R. K. G. a. A. W. Sleight, Elsevier, Editon edn., 1991, vol. Volume 67, pp. 147-155.
29. R. J. Taylor, Y. X. Jiang, N. V. Rees, G. A. Attard, E. L. Jeffery and D. J. Willock, *The Journal of Physical Chemistry C*, 2011, **115**, 21363-21372.
30. S. Lavoie, M.-A. Laliberté, I. Temprano and P. H. McBreen, *Journal of the American Chemical Society*, 2006, **128**, 7588-7593.
31. P. B. Wells and R. P. K. Wells, in *Chiral Catalyst Immobilization and Recycling*, Wiley-VCH Verlag GmbH, Editon edn., 2000, pp. 123-154.
32. J. Clavilier, R. Faure, G. Guinet and R. Durand, *Journal of Electroanalytical Chemistry and Interfacial Electrochemistry*, 1979, **107**, 205-209.
33. J. L. Margitfalvi, E. Talas and M. Hegedus, *Chemical Communications*, 1999, 645-646.
34. G. Attard and C. Barnes, *Surfaces*, Oxford University Press, 1998.
35. R. Michaelis and D. M. Kolb, *Journal of Electroanalytical Chemistry*, 1992, **328**, 341-348.
36. N. M. Marković, B. N. Grgur, C. A. Lucas and P. N. Ross, *Surface Science*, 1997, **384**, L805-L814.
37. A. Brew and G. A. Attard, *Journal of Electroanalytical Chemistry*, 2014, **Submitted**.
38. J. F. Li, Y. F. Huang, S. Duan, R. Pang, D. Y. Wu, B. Ren, X. Xu and Z. Q. Tian, *Phys Chem Chem Phys*, 2010, **12**, 2493-2502.
39. N. R. Avery, *Surface Science*, 1983, **125**, 771-786.
40. M.-A. Laliberté, S. Lavoie, B. Hammer, G. Mahieu and P. H. McBreen, *Journal of the American Chemical Society*, 2008, **130**, 5386-5387.
41. J. S. Suh and J. Kim, *Journal of Raman Spectroscopy*, 1998, **29**, 143-148.
42. G. A. Attard, J. E. Gillies, C. A. Harris, D. J. Jenkins, P. Johnston, M. A. Price, D. J. Watson and P. B. Wells, *Applied Catalysis A: General*, 2001, **222**, 393-405.

CHAPTER SEVEN

Adsorption of Ethyl Pyruvate on Palladium Surfaces

7.1 Introduction

Under the conditions of the Orito reaction and using CD as a chiral modifier, palladium was reported to give rise to the *S*-enantiomer of EL in excess rather than the *R*-enantiomer as seen with supported platinum catalysts upon hydrogenation of EP.¹ The accepted model accounting for this alternation in handedness (based on deuterium exchange measurements at the methyl group attached to the carbonyl substituent) was the stabilisation of the *enol* tautomer of EP on the palladium surface leading to the hydrogenation of the enolic C=C bond rather than the carbonyl, resulting in the opposite enantioface being exposed during hydrogenation.¹ Based on this premise, one might expect to observe the *enol* spectroscopically under hydrogenating conditions if it was sufficiently long lived. A series of equivalent experiments to those described in section 6.2.4 were therefore undertaken investigating EP adsorption on palladium and palladium modified Pt single crystal electrode surfaces. In this way, differences between platinum and palladium could be observed in the context of reactive surface intermediates under hydrogenative reaction conditions. Such differences may lead to further insights regarding the mechanism of enantiodifferentiation during Orito-type catalytic reactions.

7.2 Results and Discussion

7.2.1 CVs of palladium deposited on Pt{*hkl*} single crystal electrodes

Well defined palladium adlayers were deposited onto platinum single crystal electrodes using the forced deposition method² as described in section 3.5. Typical CVs of palladium modified Pt{111} electrodes in 0.1 M aqueous sulphuric acid electrolyte are shown in **Figure 7.1**. As reported previously,³⁻⁹ it was found that the growth of the first layer of Pd was indicated by the increase in intensity of the sharp peak at 0.17 V in the CV. Theoretically, this peak would reach its maximum intensity if a perfect, epitaxial and pseudomorphic monolayer of palladium on the platinum surface formed.¹⁰ Indeed, based on surface energy and lattice strain considerations¹¹,

thermodynamically stable monolayers of palladium are predicted to form on Pt{111}. In spite of this, experimental results using Auger electron spectroscopy (AES)¹², XPS¹³ and ion scattering¹⁴ show that Pd exhibits a Stranski-Krastanov growth mode in UHV with a single monolayer forming followed by growth of Pd microcrystallites. A more extreme form of this growth mode was determined by Attard *et al.* for rhodium deposition on Pt{111} associated with the greater difference in lattice constant between Pd and the smaller Rh atom.¹⁵ It should be noted that following the forced deposition of palladium, multiple and rapid potential cycles (500 mV/s) between 0 and 0.85 V (Pd/H) are required to generate the sharpest Pd CV features and in fact the evolution of the adlayer may be monitored in this way as a function of time.¹⁶ Electrochemical adlayers formed via multiple potential cycling treatments are always metastable and the CV peaks described below (including the first monolayer 0.17 V feature) will always broaden and decrease in intensity as a function of time unless ‘electrochemically annealed’ using a potential cycling treatment. Because the palladium and platinum terrace CV peaks are well separated it is possible to monitor simultaneously both regions of the CV as a function of palladium dosage. For example, as palladium is deposited, the characteristic bisulphate peaks of Pt{111} terraces at 0.45 V are gradually attenuated. The onset of palladium multilayer formation is signified by the growth of another single peak at about 0.21 V. This peak becomes broader and shifted to more positive potentials with increasing palladium coverage. Also, the peak at 0.17 V due to the first Pd layer begins to decrease once multilayers form since the underlying palladium monolayer is becoming increasingly blocked by second and third layer palladium. With the assumption of palladium adatoms in the second and subsequent layers blocking adsorption in the first layer, the palladium coverages shown in the figure were estimated by calculating the charge integration of the area under each Pd peak.⁶ Such interpretations based on charge have previously been confirmed following *ex situ* measurements using AES.¹² It should be noted in **Figure 7.1** that even after electrochemical annealing, at a fractional surface Pd coverage of 0.9, a small peak at 0.21 V (red CV) confirms the tendency to generate second layer Pd at submonolayer coverages. After hydrogen evolution, the 0.21 V peak would increase still further (not shown) as the metastable Pd monolayer relax back to a less perfect adlayer with a greater surface concentration of multilayer islands. Hence, in subsequent hydrogenation studies, it should be remembered that the Pd adlayer might be susceptible to reconstruction involving the break-up of larger Pd monolayer islands into smaller multilayer islands revealing clean Pt{111} sites.

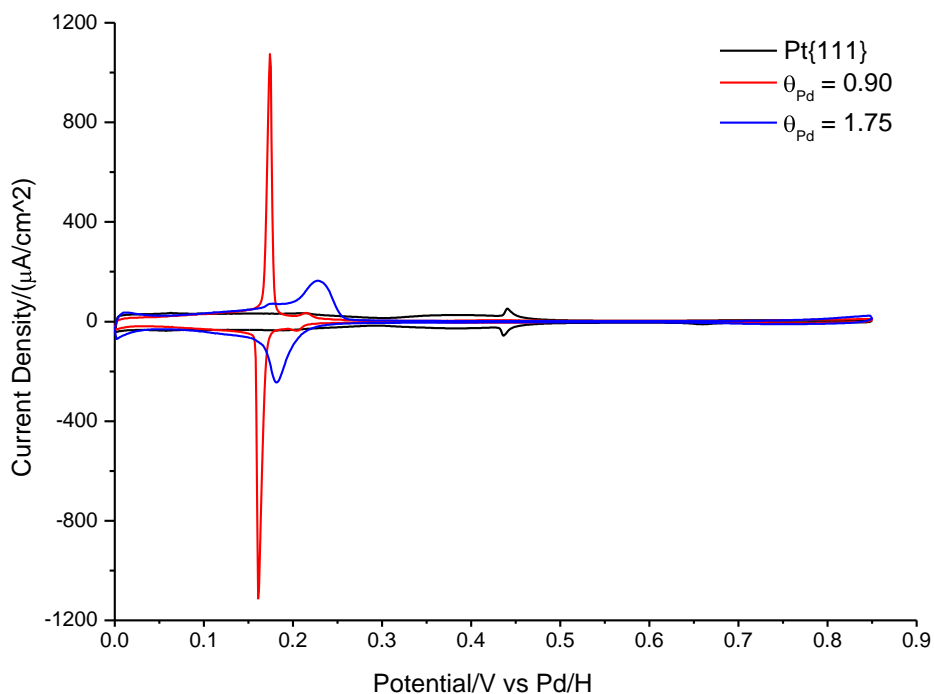


Figure 7.1 Examples of cyclic voltammograms of palladium deposited on a Pt{111} single crystal surface. Electrolyte = 0.1 M H₂SO₄, sweep rate = 50 mV·s⁻¹.

Following these preliminary CV studies on Pt{111}, palladium was deposited on Pt{100} via forced deposition and the results are shown in **Figure 7.2**. As for Pt{111}, clean Pt, single Pd monolayer and multilayer palladium regions of the surface may readily be identified. The H UPD region between 0.2 and 0.35 V in the CV of Pt{100} corresponding to well order Pt{100}-(1x1) terraces was attenuated gradually with the adsorption of palladium. It was found that the peak at 0.35 V due to the (100) terrace maintained its overall structure and shape (not shown in the figure) when palladium was slowly deposited on the surface, which suggested that the wide Pt{100} terraces remained on the Pd covered surface in this situation. Therefore, it was concluded that Pd exhibited island growth during this process in accordance with the attractive lateral interactions found when transition metals are deposited on other transition metals.¹⁷ Further experimental support for this conclusion has been found using *in situ* X-ray scattering data as reported by Ross *et al.*¹⁸ Palladium adsorbed in the first Pd monolayer was signified by the appearance of a sharp electrosorption peak at 0.1 V.^{19,20} Although the maximal intensity of this peak was not as big as the first layer of Pd on Pt{111}, it grew linearly in magnitude as more

Pd adsorbed up to a monolayer. In order to reach this point and ensure that no Pt{100} features were evident, extensive potential cycling was required. Even in this case however, second layer Pd would always be seen at fractional coverages between 0.8 and 1 due presumably to the lower diffusion coefficient exhibited by Pd on the more corrugated Pt{100} surface as opposed to the smoother Pt{111} terrace. It may also be that Pd adatoms adsorbing onto larger Pd islands would require a much larger diffusion length to occupy vacant Pt sites on Pt{100}. Whatever the reason, one always found the formation of second layer palladium commencing before completion of the first, similar to the behaviour of Pt{111} but much more marked. This second and multilayer Pd electroadsorption peak at 0.21 V started growing even when there was only 50% coverage of the Pt surface area by Pd without potential cycling. Interestingly, the peak for the second layer of Pd was sharper on Pt{100} than Pt{111}. This indicated that the second Pd layer on the (100) surface was much more well defined compared to the (111) surface. However, as multilayer palladium formation occurs, one can expect that the peak at 0.21 V will become broader and decrease in intensity with a polycrystalline appearance which indeed is observed. With the increase of the Pd coverage on the surface, the formation of Pd-OH electroadsorption features increased also at 0.8 V. This is quite different behaviour to Pt{111} at the same potential which only showed a small uptake in Pd-OH at similar Pd coverages. It is suggested that both the intrinsic hexagonal geometry of the {111} surface (in sulphuric acid, electrochemical oxide formation only occurs in excess of 1.1 V due to strong blocking by sulphate anions²¹) together with a less defective adlayer would account for these differences. Although it is known that palladium adsorbs oxygenated species more readily than platinum, Alvarez and his co-workers proved that palladium adlayers had a negative impact on the electrocatalytic activity for the electrooxidation of CO on the surface.²² That is, if adsorbed CO was electrooxidised via a Langmuir-Hinshelwood mechanism involving reaction between adsorbed OH and adsorbed CO to form CO₂, the OH adsorbed on palladium exhibited less of a capability of electrooxidising adsorbed CO when adsorbed on palladium. This could have an effect on whether or not adsorbed CO is observed on a palladium surface under reaction conditions using SERS.

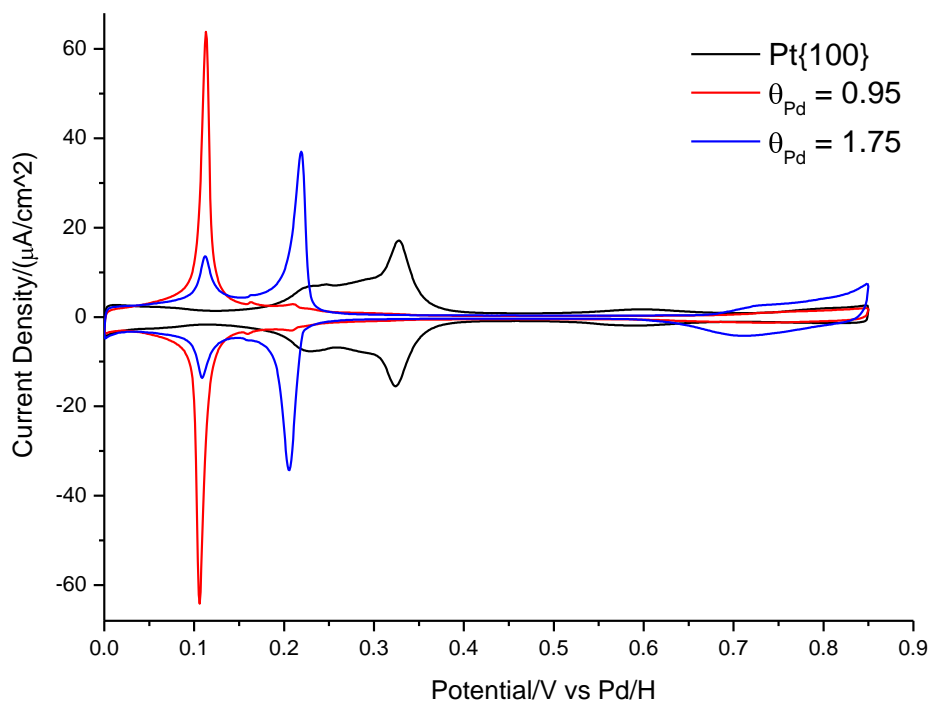


Figure 7.2 Examples of cyclic voltammograms of palladium deposited on a Pt{100} single crystal surface. Electrolyte = 0.1M H₂SO₄, sweep rate = 50mV·s⁻¹.

Finally, **Figure 7.3** shows examples of Pd adsorption on the surface of a Pt{110} single crystal electrode in sulphuric acid. In contrast to the other two basal planes, there was no sharp electroadsorption peak ascribable to Pd adsorption on (110) terrace sites in the H UPD region of the CV. Instead, the charge under this region kept decreasing with increasing amounts of Pd. Eventually, the peak due to Pt{110} sites vanished, replaced by a rather broad peak with a shoulder between 0.1 and 0.23 V. Simultaneously, a broad peak due to Pd-OH formation at 0.75 V was seen growing in the CV profile. The broad appearance of all peaks suggests a rather disordered monolayer structure consisting of small palladium islands. With more than one layer of Pd adsorbed on the Pt surface, both peaks corresponding to Pd-H and Pd-OH would become broader and larger in terms of the area under the curve. Hence, a greater tendency towards the formation of a disordered Pd adlayer of microcrystallites is found as the surface density of platinum atoms decreases. In what follows, EP hydrogenation at palladium and palladium-modified Pt{*hkl*} electrodes will be examined using surface Raman spectroscopy.

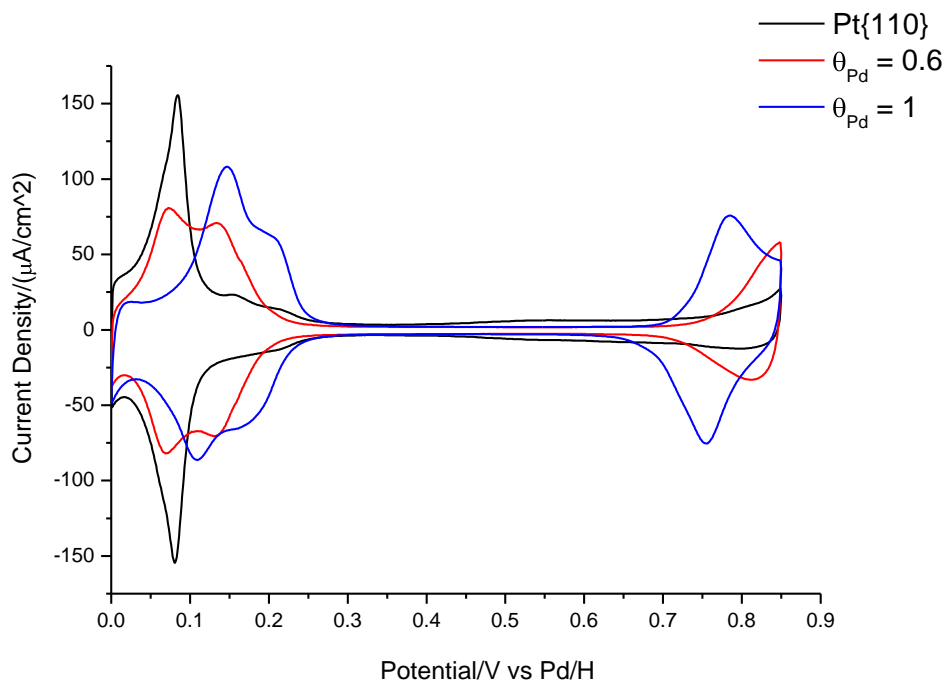


Figure 7.3 CVs of the palladium coverage on the surface of Pt{110} single crystal surface. Electrolyte = 0.1M H₂SO₄, sweep rate = 50mV·s⁻¹.

7.2.2 SERS of EP adsorption on palladium surfaces

7.2.2.1 Polycrystalline palladium surfaces of Au@Pd NPs

SER spectra of 0.1 M EP dissolved in 0.1 M sulphuric acid adsorbed on the Pd surface of the Au@Pd NPs were obtained as a function of potential and the data collected is shown in **Figure 7.4**. According to Taylor, when hydrogen was being evolved on the surface of a Pd electrode, the *enol* form of EP was adsorbed on the Pd surface. As shown in **Figure 7.4a**, it was evident that the observation of the bands at 770 and 979 cm⁻¹ was consistent with the out-of-plane $\delta(\text{C}^3\text{-H}_2)$ vibrational modes of an enol although no bands due to C=C stretches around 1560 cm⁻¹ nor C-H stretches at 3030 cm⁻¹ were present. The peak at 360 cm⁻¹ was assigned by Taylor to the wagging vibration of C²-OH of the adsorbed *enol*-EP. The weak bands appearing at 860 (H₂C-CH₃ stretching vibration), 1200 (C-O stretches), 1332 (C-H₂ bending mode) and 1450 cm⁻¹ (C-H₃ bending mode) were associated with the ester group. Also, due to the decarbonylation of the EP molecules, the band at 1900 cm⁻¹ was assigned to bridge bonded CO adsorbed on the Pd surface.

It should be noticed that compared to polycrystalline Pt surfaces, all the vibrational bands appear rather weak. We shall see later that this is typical behaviour for Pd suggesting that the lifetime of adsorbed species under HER conditions is rather low. It should also be noted that there is absolutely no evidence for bands associated with the HHS at 1050 and 490 cm^{-1} which immediately points to a different reaction mechanism for palladium compared to platinum surfaces when EP is hydrogenated. As the potential changes to more positive values, gradual changes in the spectra are observed with an attenuation in all bands (**Figure 7.4c**) until the double layer potential is reached (**Figure 7.4d**). At this potential (0.43 V), a narrowing in the C–H stretch vibrations at 2925 cm^{-1} together with the appearance of a peak at 1570 cm^{-1} characterise this region. Not only this but the emergence of bands around 840 and 1360 cm^{-1} signify the onset of pyruvate formation adsorbed via the carboxylate group to the surface (see Chapter 6). The bending vibration at 841 cm^{-1} being more intense than the symmetric stretch at 1360 cm^{-1} indicates that as the palladium surface is electrooxidised, the orientation of the pyruvate is such that it is tilted away from the surface.²³ This was also seen during the initial electrooxidation of Pt with the bending vibration at 840 cm^{-1} being more intense than the symmetric stretch at 1360 cm^{-1} .

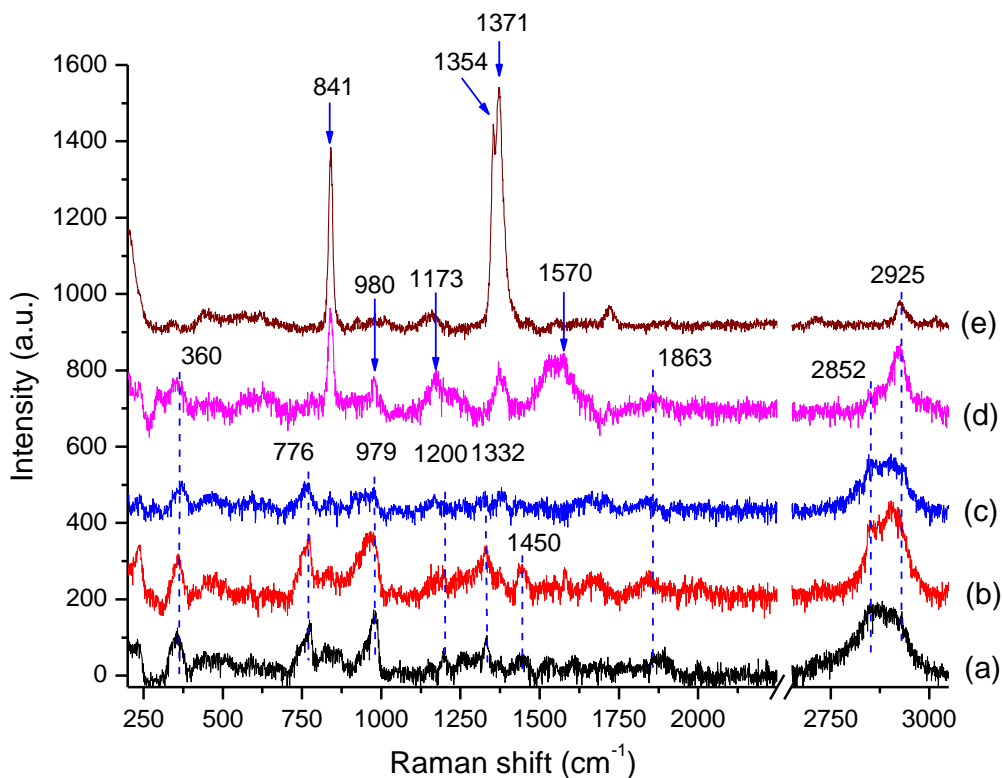


Figure 7.4 SER spectra of EP adsorption on Au@Pd NPs in 0.1 M H₂SO₄ at different potentials (vs. Pd/H reference electrode): (a) -80 mV; (b) 30 mV; (c) 130 mV; (d) 430 mV; and (e) 900 mV.

At 0.9 V, a simple spectrum ascribable to adsorbed pyruvate alone was observed as also seen in Chapter 6 for EP oxidation on platinum. Hence, as more and more electroadsorbed oxygen species form at the more positive potential, they immediately react with EP to generate adsorbed pyruvate and presumably, liberated ethanol both on platinum and palladium. When **Figure 7.4e** is compared with **Figure 6.13d**, both spectra are practically identical with all peaks in **Figure 6.16d** being reproduced in **Figure 7.4e** including the $\nu_s(\text{COO}^-)$ band being split into two peaks at 1354 and 1371 cm^{-1} . Hence, exactly the same mechanism for pyruvate formation is proposed for Pd as for Pt as shown in **Figure 7.5**.

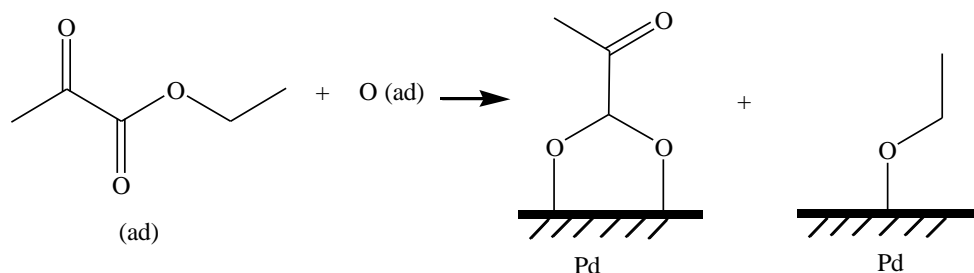


Figure 7.5 EP oxidation scheme on the Pd Surface.

In order to observe specific structural changes ascribable to particular geometric arrangements of the surface atoms, palladium was irreversibly adsorbed on the three basal planes of platinum. In the first instance, and in order to make comparisons with the 2 nm thick palladium films studied using Au@Pd NPs, multilayers of palladium on Pt{*hkl*} were investigated using SHINERS. Following these measurements, single monolayers of Pd on Pt{*hkl*} were studied since it was already well known that such monolayers are electronically quite distinct from either platinum or bulk palladium^{19, 24, 25} and it would be interesting to understand if such changes in electronic properties might be reflected in differing catalytic behaviour.

7.2.2.2 Pd on Pt{110} Palladium multilayer

In **Figure 7.6a** is shown the SHINERS spectrum of EP on a palladium multilayer supported on Pt{110} undergoing hydrogen evolution. Remarkably, hardly any adsorbed species could be observed in the spectrum. This suggests that either the SHINERS particles are not ‘active’ in enhancing the Raman effect or that under such conditions, the palladium multilayer is ostensibly ‘clean’ and that all adsorbed species are short-lived on the time scale of the experiment, perhaps due to the rapidity with which adsorbed intermediates are hydrogenated and subsequently desorbed from the electrode. That the SHINERS effect is in operation may be gleaned from **Figure 7.6b**. Here, at potentials where the palladium surface is electrooxidised, strong bands ascribable to adsorbed pyruvate develop including the $\delta(\text{COO}^-)$ bending mode at 841cm^{-1} and the more intense $\nu_s(\text{COO}^-)$ mode at 1352cm^{-1} , indicating the CO_2^- group was adsorbed in a tilted configuration on the surface via the carboxylate group. Also, the band at 456cm^{-1} (metal-oxygen stretch) and 1722cm^{-1} (C=O stretching mode) of the carbonyl group provided further evidence that a PA product was adsorbed on the surface. There were the only bands that could be observed on the surface in the potential range $-0.1 - 1.2\text{ V}$. The absence of any evidence for enol

formation does raise questions as to whether or not the bands obtained using the Au@Pd nanoparticles were sufficiently weak to be considered part of the spectral background, perhaps due to contamination? At this stage of the study, it was difficult to assert this since the absence of enol peaks could also be purely due to the particular surface arrangement of palladium atoms. However, since multilayers of Pd on Pt{110} are thought to be the most disordered and hence, closest to the polycrystalline surface, the absence of enol features appears strange.

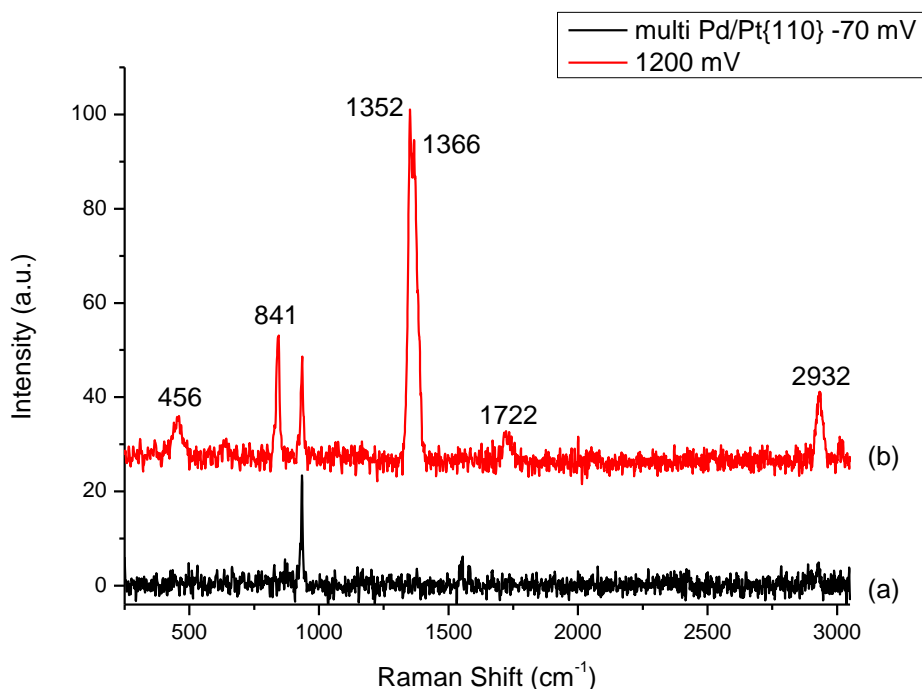


Figure 7.6 SER spectra of EP adsorption on a multilayer Pd modified Pt{110} single crystal electrode in HClO₄ at different potentials (vs. Pd/H reference electrode): (a) -70 mV; and (b) 1200 mV.

7.2.2.3 Pd on Pt{111} *Palladium multilayer*

In **Figure 7.7a** is shown the SHINER spectrum from a Pt{111} electrode modified with multilayers of palladium under HER conditions in contact with an EP containing 0.1 M aqueous perchloric acid electrolyte. As was found with multilayers of palladium on Pt{110}, the spectrum reveals a remarkably clean spectrum with only very weak peaks at 420, 849, 984, 1436 cm⁻¹ and stronger peaks at around 2900 cm⁻¹ ascribable to C–H stretches. The 849, 1436 and 2900 cm⁻¹

peaks may all be ascribed to vibrational modes associated with molecular EP. However, the 420 and 984 cm^{-1} bands are highly characteristic of the tilted keto form of EP bonded to the surface via lone pairs on the keto carbonyl group as outlined in Chapter 6. In Chapter 6 it was emphasised that this species is only formed when terraces are present and this would be consistent with epitaxial growth of Pd on Pt{111} due to each element possessing an almost identical lattice constant.¹¹ However, if this interpretation is correct, it means that the keto form of EP rather than the enol form is stable on Pd under HER conditions which would be in contradiction to experimental findings using deuterium exchange studies.¹ Nonetheless, upon increasing the potential to 0.22 V from the HER region, it is seen that there is an immediate increase in the intensity of the ‘terrace intermediate’ bands and a shift to higher wavenumber in the 984 cm^{-1} band to 997 cm^{-1} in accordance with previous behaviour exhibited by this species on platinum

It is also seen in **Figure 7.7b** that there appears to a rather broad peak at 1580 cm^{-1} which would correspond to an enolic C=C stretch although expected bands at 3030 and 776 cm^{-1} confirming enol formation appear to be absent (the expected 979 cm^{-1} band would be unresolved from the terrace intermediate peak at 997 cm^{-1}). Again, the tricky problem of contamination giving rise to bands in this important region of the spectrum leads to some ambiguity when trying to confirm the presence of enolic species. Nonetheless, the sudden appearance of the 1580 cm^{-1} band at a potential away from when hydrogen is coadsorbed does seem to be in accordance with the known behaviour of the enol. Hence, a tentative interpretation of this effect would be that under HER conditions the enol surface species is completely unstable in that it is readily hydrogenated to form EL whereas in the absence of coadsorbed hydrogen it is stable on the palladium surface.

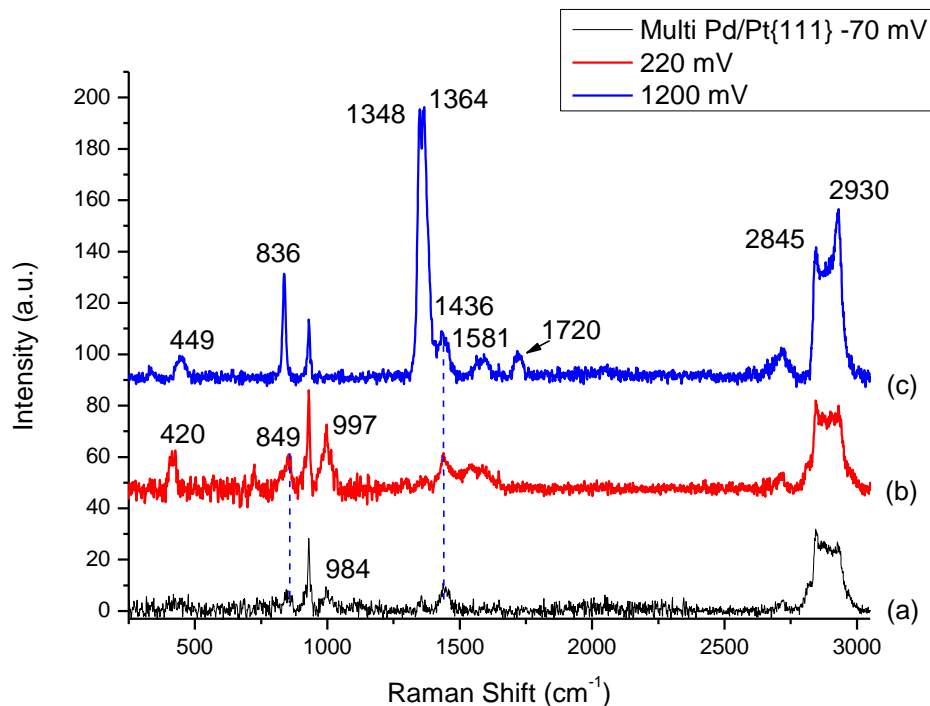


Figure 7.7 SER spectra of EP adsorption on multilayer Pd coated Pt{111} single crystal electrode in HClO_4 at different potentials (vs. Pd/H reference electrode): (a) -70 mV; (b) 220 mV; and (c) 1200 mV.

Finally, the potential was increased to 1200 mV where Pd–O was formed on the surface. As described before, PA would form on the surface at this positive potential. The $\delta(\text{COO}^-)$ band at 836 cm^{-1} and the $\nu_s(\text{COO}^-)$ band at 1348 cm^{-1} were observed (**Figure 7.7c**), which provided evidence of the adsorption of PA in a carboxylate form. Since the $\nu_s(\text{COO}^-)$ band was more intense than the $\delta(\text{COO}^-)$ band, it suggested that the CO_2^- group was adsorbed in a tilted configuration almost parallel to the surface.²³ In addition, the usual 1720 cm^{-1} feature due to the C=O stretching mode together with the metal-oxygen stretch at 449 cm^{-1} were observed but this time, the $\nu_{\text{as}}(\text{COO}^-)$ asymmetric stretch band could readily be discerned also at 1581 cm^{-1} . One final noteworthy feature of **Figure 7.7c** is that the C–H stretch vibration for adsorbed pyruvate is normally a single, sharp feature due to purely CH_3 vibrations (no CH_2 from ethyl ester part of EP). In **Figure 7.7c** a peak at 2845 cm^{-1} is also apparent and this is clearly due to a contaminant not adsorbed on the Pd surface but rather due to being adsorbed on the shell of the SHINERS nanoparticles (remnant of preparation procedure). It should be noted in fact that this part of the

spectrum remains unchanged as potential changes. At 1.2 V, any carbonaceous material would be immediately converted to CO₂ if in electrical contact with the electrode was present. Since the 2845 cm⁻¹ and the smaller 2700 cm⁻¹ feature are seen in all spectra in the figure irrespective of potential (together with what was originally assigned to a bulk EP peak at 1436 cm⁻¹ associated with C–H bending vibrations), it is proposed that alkyl fragments containing CH₂ entities are still bound to the silica shell of the SHINERS particles giving rise to these potential independent species. In spite of this, the clear change from adsorbed fragments of EP which upon electrooxidising the surface generate adsorbed PA can be observed in the spectra. However, it is an extremely demanding process to obtain ‘clean’ SHINERS nanoparticles and a good degree of caution should always be exercised when trying to deduce possible surface mechanistic data when peaks appear to be present in the same form irrespective of potential.

7.2.2.4 Pd on Pt{100} *Palladium multilayer*

According to the spectra in **Figure 7.8**, at the HER potential, EP adsorption on the surface of a Pd multilayer deposited on the Pt{100} surface undergoing HER gave stronger intensities in terms of the bands associated with both surface adsorbed intermediates and bulk EP molecules than any other Pd multilayer surface studied thus far. The bands at 409 and 960 cm⁻¹ would be consistent with those of the terrace intermediate which was described in section 6.2.4. The bands at 775, 856 and 1450 cm⁻¹ were tentatively assigned to being vibrations of *enol*-EP. A shoulder peak at 489 cm⁻¹ was also observed, which would be associated with some form of surface M-C or M-O stretch. Since there was no peak at 1050 cm⁻¹, M-C stretches corresponding to the HHS could be ruled out. Again, due to the absence of bands between 1900 and 2000 cm⁻¹, it is unlikely to be associated with the M-C stretch of adsorbed CO either. Hence, a tentative interpretation might be (although for carbonyl-surface interactions this value would be rather high) that either a keto-carbonyl M-O or enol M-C stretch might account for its presence.

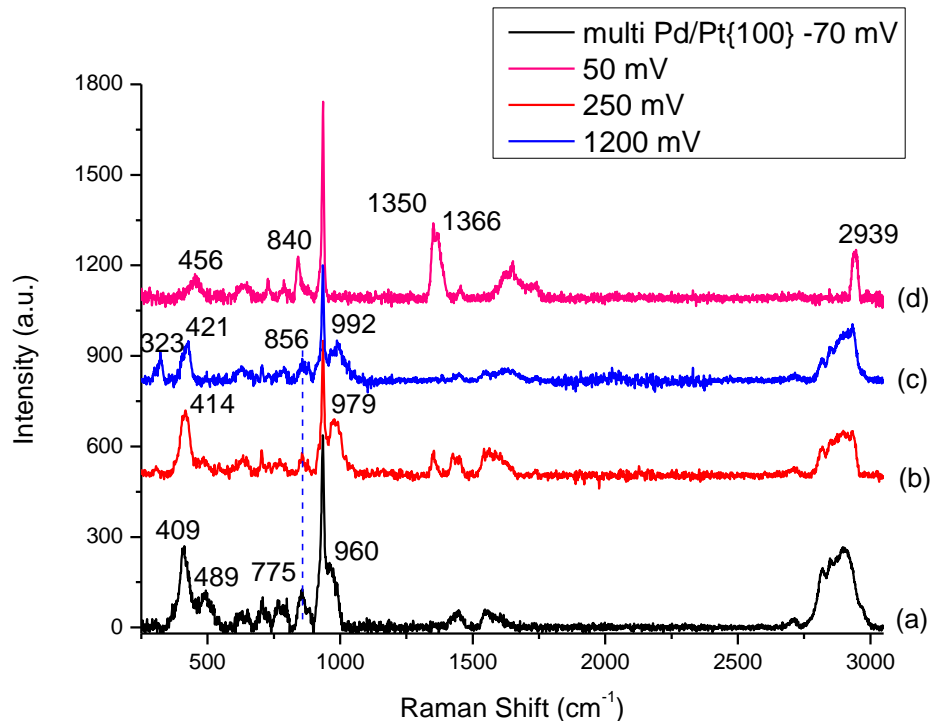


Figure 7.8 SER spectra of EP adsorption on multilayer Pd coated Pt{100} single crystal electrode in HClO_4 at different potentials (vs. Pd/H reference electrode): (a) -70 mV; (b) 50 mV; (c) 250 mV and (d) 1200 mV.

It is astonishing however that so many bands are observed on multilayer Pd under HER conditions when comparison is made with the other Pd multilayer systems. Could it be that in this particular case (and to a lesser extent with Pt{111}) that HER had caused pin-holes to develop in the multilayer film and that the high intensity of Raman bands was because all intermediates are actually formed at Pt sites? As mentioned previously, Pd films are metastable on Pt and it is possible that this would be the case thus affording a consistent explanation for the features observed in the spectra. As potential becomes more positive, it is striking that the changes in all bands reflect precisely those observed for Pt{100} and Pt{111} under the same potential changes. The detail is correct even so far as the blue shift of the 960 cm^{-1} terrace intermediate peak. Given the known surface chemistry of palladium, it seems inconceivable that a keto form of EP could be stable on a palladium surface. Therefore, it is concluded that although the surfaces presented for Pt{111} and Pt{100} modified by multilayers of palladium were those of a pure palladium adlayer, the coverage chosen was insufficient to prevent pin holes forming

revealing the underlying Pt surface and hence the generation of Pt-like species. Based on Au@Pd NP and Pd multilayers on Pt{110}, it is asserted that hardly any surface intermediates should be observed from a pure Pd surface due to their rapid hydrogenation. Rather, all “strong” bands that are observed are originating from Pt sites whereby long lived intermediates may form. In what follows in the next section, it is seen that this effect is even more striking for single Pd monolayers. In **Figure 7.8d**, the usual transformation of EP into adsorbed pyruvate when coadsorbed with electrosorbed oxide is observed. The narrow C–H stretch band at 2939 cm^{-1} signifies that the SHINERS nanoparticles are free of contamination and that no CH_2 alkyl carbons are present at the surface, only the CH_3 attached to the alpha carbon of the pyruvate.

7.2.2.5 Pd on Pt{110} *Palladium monolayer*

In **Figure 7.9**, EP adsorption on a Pd monolayer modified Pt{110} electrode surface was studied using SHINERS. It should be noted that for all of the palladium single monolayer systems studied, it was not possible to examine the formation of pyruvate at high positive potentials. The reason for this was that such high potentials are known to reconstruct the underlying Pt{*hkl*} surface such that terrace features are perturbed and in addition, dissolution of adsorbed palladium can occur.¹⁹ Therefore, spectra confined to the HER and H UPD regions only were collected. In **Figure 7.9a**, a rather complex array of vibrational bands for EP undergoing hydrogenation on Pd/Pt{110} is observed. However, careful inspection reveals that the spectrum is very similar to EP on Pt{110} at HER potentials (**Figure 6.11**) in that the HHS, formed exclusively on Pt defect sites, is giving rise to the bands at 486 and 1044 cm^{-1} whereas the terrace intermediate is responsible for the peaks at 422 and 965 cm^{-1} . It is asserted once again that both of these species are purely associated with Pt surface sites since the HHS has never been observed other than at Pt sites and that the surface chemistry of Pd precludes keto formation under HER conditions.²⁶ Therefore, the Pd adlayer is providing an imperfect covering of the Pt{110} surface such that Pt sites are still available for adsorption. Confirmation of this band assignment may be obtained when the potential is made more positive since the 486 and 1044 cm^{-1} bands disappear (absence of HER hydrogen atoms) and the 965 cm^{-1} band of the terrace intermediates is blue shifted to 995 cm^{-1} as expected. There was possibly signs of *enol*-EP being present on the surface, as revealed by peaks at 777 , 855 and 1450 cm^{-1} and particularly at 1540 cm^{-1} at 0.1 V but save for the latter, these were all very weak bands. Hence, weak or non-existent bands from the Pd

adlayer combined with HHS and terrace intermediate bands originating from free Pt sites fully interprets the spectra shown in **Figure 7.9**.

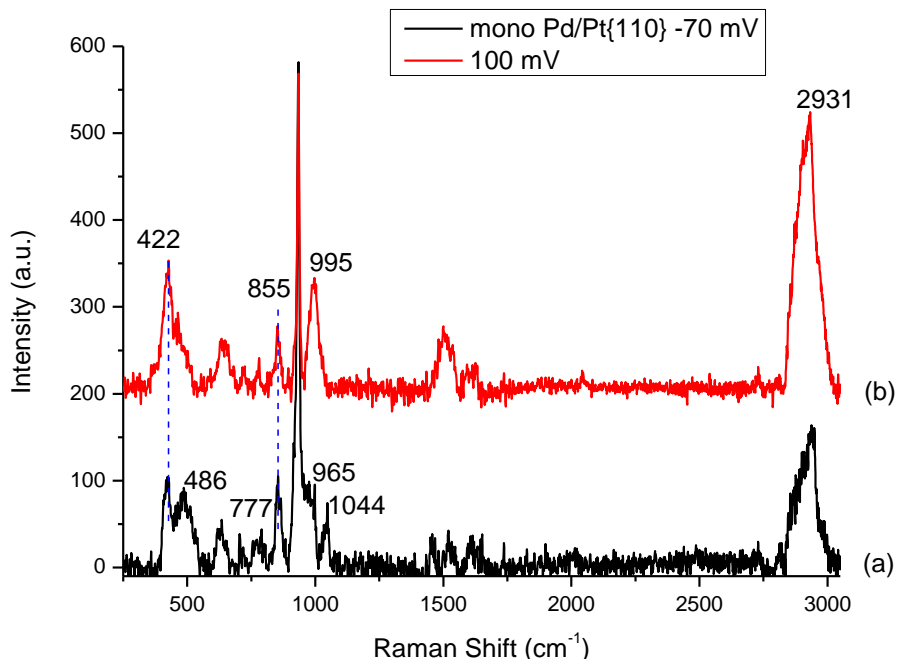


Figure 7.9 SER spectra of EP adsorption on monolayer Pd coated Pt{110} single crystal electrode in HClO_4 at different potentials (vs. Pd/H reference electrode): (a) -70 mV; and (b) 100 mV.

7.2.2.6 Pd on Pt{111} *Palladium monolayer*

After a monolayer of Pd was deposited on the surface of a Pt{111} single crystal electrode, EP adsorption was studied as a function of potential and the corresponding SHINER spectra are shown in **Figure 7.10**. When hydrogen gas was evolved on the surface, the spectrum **Figure 7.10a** was obtained. Similar to the previous results for the Pt{111} electrode outlined in Chapter 6, typical bands due to the bulk layer of EP molecules adsorbed were observed. The broad band between 2848 and 2935 cm^{-1} was due to the symmetric and asymmetric C–H stretching vibrations of EP, together with the C–C–O stretching band at 851 cm^{-1} , O–C–O scissoring vibrational band at 750 cm^{-1} and small C=O rocking vibrational band at 649 cm^{-1} . Besides, the peaks located at 423 and 980 cm^{-1} were found matching with those observed on the Pt{111} surface, which were

associated with tilted keto form of EP with the Pd–O stretch and CH₃/C=O frustrated rock respectively. The latter peak in particular was blue shifted from 965 to 980 cm⁻¹ in accordance with tilting behaviour discussed in Chapter 6. One could argue that the quality (and epitaxy) of the palladium monolayer on Pt{111} should be more perfect than on Pt{110} as found from CV measurements and therefore, if the spectra are to be interpreted as arising solely from adsorption at Pt{111} terrace sites (note the absence of the HHS since no Pt defects are present), why are the bands obtained not very small? For Pd monolayers, electronic structure does not match bulk Pd¹¹ and so it may be that the terrace intermediate may form on Pd{111} terraces of the Pd adlayer. This is possible but unlikely given the almost perfect match of the band wavenumbers with EP on Pt{111} although ultimately, a catalytic hydrogenation experiment using monolayer modified Pd on supported Pt would confirm/refute that enol was still being formed because using CD as modifier, an S-EL excess would be formed. Fortunately, this experiment has been performed.²⁷ Baiker and co-workers prepared Pd-modified Pt supported on alumina catalysts and found that *ee* decreased as a function of Pd coverage and eventually gave rise to an excess of S-EL product rather than R-EL product under Orito-type reaction conditions. Independently of this result, Attard and Alabdulrahman²⁸ used CV to characterise a series of Pd modified 5%Pt on graphite catalysts and found once again a complete loss of *ee* as Pd coverage was increased. Because the growth mode of Pd on this polycrystalline Pt surface was not sufficient to cover all Pt sites, it took a greater amount of Pd than would be required to form a perfect monolayer to fill all Pt sites. Nonetheless, the sharp decrease in *ee* as Pt sites were blocked confirmed that monolayer Pd was generating the opposite enantiomer to Pt sites. Based on both of these pieces of experimental information, it is asserted that EP gives rise to an enol intermediate on palladium and that the keto form would not be stable, even on a Pd monolayer supported on Pt{111}.

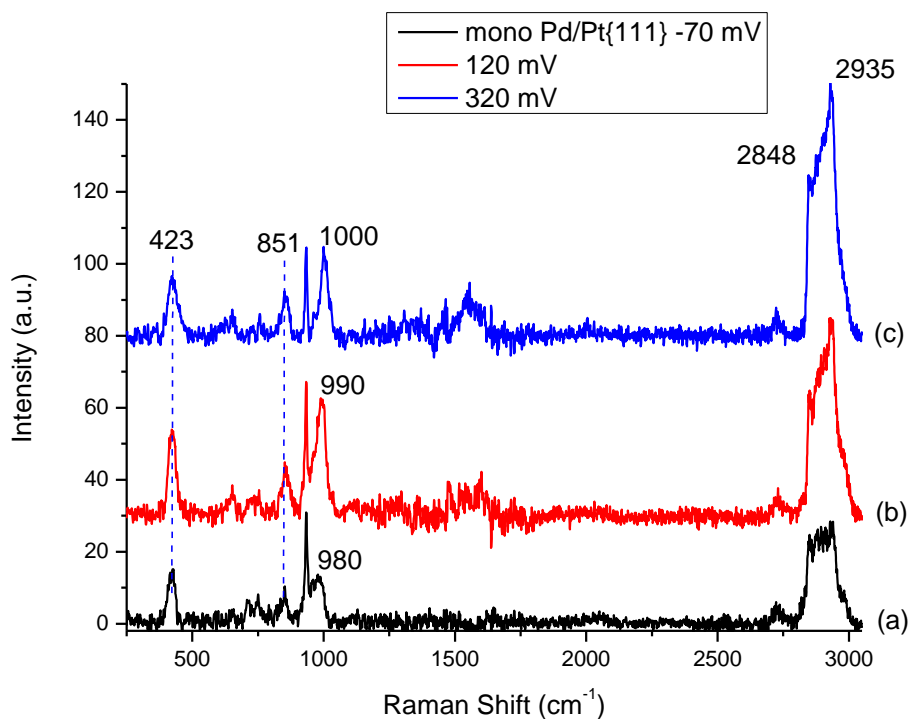


Figure 7.10 SER spectra of EP adsorption on monolayer Pd coated Pt{111} single crystal electrode in HClO_4 at different potentials (vs. Pd/H reference electrode): (a) -70 mV; (b) 120 mV; and (c) 320 mV.

7.2.2.7 Pd on Pt{100} *Palladium monolayer*

A monolayer of Pd was deposited on the surface of the Pt{100} single crystal electrode. SHINER spectra of EP obtained as a function of potential were collected subsequently and are shown in **Figure 7.11**. At the HER potential region (**Figure 7.11a**), besides the observation of the bands due to the bulk EP layer adsorbed on the surface, the peaks corresponding to M–O stretches (420 cm^{-1}) and $\text{CH}_3/\text{C}=\text{O}$ rocking (965 cm^{-1}) may be discerned associated with the presence of the terrace intermediate species. Hence, it is asserted once again that terrace Pt sites are available for reaction with EP due to the instability of the Pd monolayer generating free Pt{100} sites under HER conditions. Again, all peaks were rather weak with prominent bands at 1580 and 1640 cm^{-1} , the latter being due to bulk water bending vibrations.²⁹ A weak band at 777 cm^{-1} was tentatively assigned as the out-of-plane $\delta(\text{C}^3\text{-H}_2)$ mode of the *enol* form of EP due to the presence of what would be a C=C stretch at 1580 cm^{-1} although as mentioned previously,

contaminant peaks often give rise to intensity at this wavenumber value. Other bands present in the spectrum include those at 880, 1350 and 1440 cm^{-1} , which were known to be consistent with molecularly adsorbed EP (ester group). Upon increasing potential, the terrace intermediate band at 965 cm^{-1} shifts to 985 cm^{-1} as expected due to tilting of the keto-EP molecular axis. Since contamination was suspected in this case and knowing that the excursion to 1.2 V will both reconstruct the underlying Pt{100} surface and possibly strip Pd from the surface, a single SHINERS spectrum was collected quickly at this potential in order to see if contaminants could be removed.

As expected, conversion of EP to adsorbed PA was observed (**Figure 7.11c**). The two sharp peaks at 840 and 1354 cm^{-1} were assigned as the $\delta(\text{COO}^-)$ mode and the $\nu_s(\text{COO}^-)$ mode respectively. The latter of these vibrational peaks was only slightly more intense than the former, indicating the CO_2^- group was tilted on the surface by adsorption through both of its oxygen atoms. The bands at 1726 (C=O stretching mode) and 460 cm^{-1} (M–O vibration) of the carbonyl group were also in evidence following formation of PA. However, inspection of the C-H stretch region between 2800 and 3000 cm^{-1} indicated potential independent structure due to incompletely cleaned SHINERS nanoparticles (band intensity between 2800 and 2850 cm^{-1}) rather than a single peak at 2936 cm^{-1} at 1.2 V as would be expected for a pure PA adlayer. Hence, almost certainly (based on lack of potential dependence) the 1437 cm^{-1} (C–H bend), the 2850 cm^{-1} C-H stretch and possibly the 1580 cm^{-1} feature are associated with contamination. In spite of this cautious approach to assigning the bands, the fact that for all Pd surfaces on Pt{*hkl*}, the same behaviour is observed indicates very little structural sensitivity save for terrace and HHS intermediates forming on free terrace and defect Pt sites respectively. Some evidence for enol formation at potentials removed from HER has been obtained but again, Pd sites do not appear to give rise to strong SHINERS peaks due to rapid hydrogenation of all reaction intermediates.

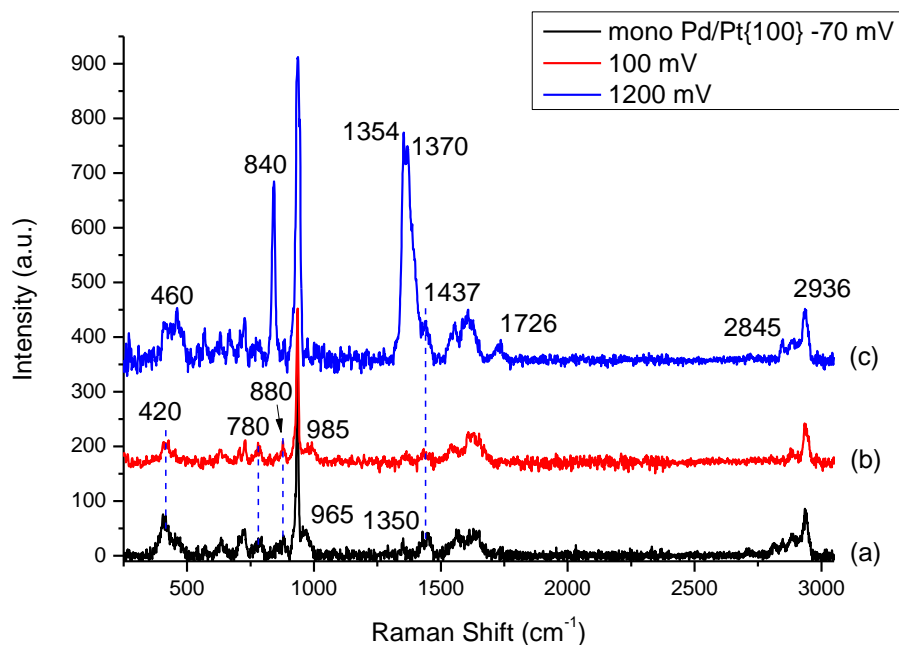


Figure 7.11 SER spectra of EP adsorption on monolayer Pd coated Pt{100} single crystal electrode in HClO₄ at different potentials (vs. Pd/H reference electrode): (a) -70 mV; (b) 100 mV; and (c) 1200 mV.

7.3 Conclusion

Using a combination of CV to characterise the growth of single and multi-layered palladium overlayers on Pt{111} together with SHINERS, the surface intermediates formed during hydrogenation of EP at palladium modified Pt single crystal electrodes have been studied. It is found that unlike platinum, palladium surfaces give rise to very weak SHINERS peaks and in the case of multilayer Pd modified Pt{110}, no features whatsoever are observed until high positive potentials when electrosorbed oxide reacts with EP to generate adsorbed PA. This latter behaviour is identical to that found in Chapter 6 for EP on pure Pt. In fact all of the strong bands observed using Pd modified Pt{*hkl*} are identical to those observed on pure Pt electrodes suggesting reconstruction of the Pd adlayer to reveal Pt subsurface sites. Hence, both the HHS and terrace intermediate formed on Pt are identified but disappointingly, no unequivocal evidence for bands pertaining to EP adsorption on Pd could be identified under hydrogenating

conditions. Reasons for discounting keto intermediate adsorption on Pd are provided based on heterogeneous catalytic studies of supported Pd¹ and Pd modified Pt showing that an enolic form of EP should form on Pd rather than the keto form as found for Pt.³⁰ Clearly, EP hydrogenation on Pd is quite different to Pt particularly in relation to HHS formation and therefore, it is concluded that if a HHS of the enol form of EP does form (at defects or terraces) then it is completely unstable and immediately desorbs as EL. Alkenes are known to hydrogenate at a much faster rate than ketones.³¹ The slower rate of carbonyl hydrogenation and the long-lived keto terrace and HHS on Pt would then be wholly consistent with this catalytic experimental data. Because, no intermediates with Pd surfaces could be observed by SHINERS, coadsorption with CD would prove to be a fruitless exercise in terms of identifying hydrogen bonding or other interactions although a useful future experiment might involve CD adsorption on Pd and its effect on the adsorbed hydrogen. Is the atop H–Pd stretch red shifted in the presence of CD as found with Pt? Does absorption of hydrogen into the palladium lattice allow for observation of a Pd–H atop stretch? It would be very interesting to contrast Rh adsorption with Pd on Pt since Rh is reported to act like Pt in terms of the Orito reaction although exhibiting a somewhat lower overall *ee*.³² From the present study, both HHS and terrace intermediates might well be observed in this case.

7.4 References

1. T. J. Hall, P. Johnston, W. A. H. Vermeer, S. R. Watson and P. B. Wells, in *Studies in Surface Science and Catalysis*, eds. J. W. Hightower, W. N. D. E. Iglesia and A. T. Bell, Elsevier, Editon edn., 1996, vol. Volume 101, pp. 221-230.
2. F. Vidaliglesias, A. Alakl, D. Watson and G. Attard, *Electrochemistry Communications*, 2006, **8**, 1147-1150.
3. L. A. Kibler, A. M. El-Aziz, R. Hoyer and D. M. Kolb, *Angewandte Chemie International Edition*, 2005, **44**, 2080-2084.
4. M. Arenz, V. Stamenkovic, P. N. Ross and N. M. Markovic, *Surface Science*, 2004, **573**, 57-66.
5. G. A. Attard, R. Price and A. Al-Akl, *Electrochimica Acta*, 1994, **39**, 1525-1530.
6. G. A. Attard, R. Price and A. Al-Akl, *Surface Science*, 1995, **335**, 52-62.
7. R. Hoyer, L. A. Kibler and D. M. Kolb, *Electrochimica Acta*, 2003, **49**, 63-72.
8. B. Álvarez, V. Climent, A. Rodes and J. M. Feliu, *Journal of Electroanalytical Chemistry*, 2001, **497**, 125-138.
9. B. Alvarez, J. M. Feliu and J. Clavilier, *Electrochemistry Communications*, 2002, **4**, 379-383.

10. M. J. Ball, C. A. Lucas, N. M. Markovic, V. Stamenkovic and P. N. Ross, *Surface Science*, 2002, **518**, 201-209.
11. K. K. Kolasinski, *Surface Science: Foundations of Catalysis and Nanoscience*, Wiley, 2012.
12. D. J. Watson and G. A. Attard, *Surface Science*, 2002, **515**, 87-93.
13. A. Więckowski, *Interfacial Electrochemistry: Theory, Experiment, and Applications*, Marcel Dekker, 1999.
14. M. J. Ball, C. A. Lucas, N. M. Markovic, V. Stamenkovic and P. N. Ross, *Surface Science*, 2002, **518**, 201-209.
15. G. A. Attard, R. Price and A. Al-Akl, *Surface Science*, 1995, **335**, 52-62.
16. A. A. Al-Akl, Cardiff University, 1997.
17. E. Bauer, *Surface Microscopy with Low Energy Electrons*, Springer, 2014.
18. M. J. Ball, C. A. Lucas, N. M. Marković, V. Stamenković and P. N. Ross, *Surface Science*, 2003, **540**, 295-302.
19. G. A. Attard, R. Price and A. Al-Akl, *Electrochimica Acta*, 1994, **39**, 1525-1530.
20. B. Álvarez, A. Berná, A. Rodes and J. M. Feliu, *Surface Science*, 2004, **573**, 32-46.
21. J. Clavilier, *Journal of Electroanalytical Chemistry and Interfacial Electrochemistry*, 1979, **107**, 211-216.
22. B. Álvarez, A. Berná, A. Rodes and J. M. Feliu, *Surface Science*, 2004, **573**, 32-46.
23. J. S. Suh and J. Kim, *Journal of Raman Spectroscopy*, 1998, **29**, 143-148.
24. T. J. Schmidt, N. M. Markovic, V. Stamenkovic, P. N. Ross, G. A. Attard and D. J. Watson, *Langmuir*, 2002, **18**, 6969-6975.
25. G. A. Attard and A. Bannister, *Journal of Electroanalytical Chemistry*, 1991, **300**, 19.
26. P. B. Wells and R. P. K. Wells, in *Chiral Catalyst Immobilization and Recycling*, Wiley-VCH Verlag GmbH, Editon edn., 2000, pp. 123-154.
27. T. Mallat, S. Szabó, M. Schürch, U. W. Göbel and A. Baiker, *Catalysis Letters*, 1997, **47**, 221-227.
28. A. M. Alabulrahman, Cardiff University, 2007.
29. G. Socrates, *Infrared and Raman Characteristic Group Frequencies: Tables and Charts*, Wiley, 2004.
30. P. Wells and A. Wilkinson, *Topics in Catalysis*, 1998, **5**, 39-50.
31. R. A. W. Johnstone, A. H. Wilby and I. D. Entwistle, *Chemical Reviews*, 1985, **85**, 129-170.
32. S. P. Griffiths, P. Johnston and P. B. Wells, *Applied Catalysis A: General*, 2000, **191**, 193-204.

CHAPTER EIGHT

Conclusion

8.1 Introduction

The surface intermediates formed on different platinum (and palladium) surfaces during selective and enantioselective hydrogenation have been probed using a combination of CV and *in situ* SHINERS (or SERS). A range of different surfaces were examined including nanoparticles, single crystals and supported catalysts. In the first part of the study, several alkyne molecules adsorbing on platinum were investigated in order to rationalise previous heterogeneous catalytic results relating to selective alkyne hydrogenation. The second part of the study concentrated on the hydrogenation of ethyl pyruvate both with and without the coadsorption of the chiral surface modifier cinchonidine. The use of an electrode undergoing the hydrogen evolution reaction provided a convenient source of gaseous hydrogen and the flow configuration of the spectroelectrochemical cell minimised the accumulation of bubbles that would preclude both electrolyte flow and the collection of spectroscopic data. The stability of surface intermediates as a function of alkyne structure was described with a common long-lived intermediate being identified associated with defect sites in particular. In this regard, EP hydrogenation also appeared to form a long lived intermediate associated with adsorption at defect sites whereas, quite different behaviour was originating when planar terraced electrodes were employed. In fact, a notable success of the project has been the first use of SER spectroscopy on single crystal electrodes under *operando* catalytic conditions demonstrating the versatility and applicability of the SHINERS method in catalytic studies. In this chapter, an overview of the conclusions outlined in the previous chapters will be given, followed by a brief discussion in relation to future work.

8.2 Hydrogenation of Alkynes

CV showed that in general, the Pt{111} single crystal surface is the most resistant to irreversible adsorption of alkynes when compared to Pt{100} and Pt{110}. It is asserted that this difference is due to a weaker interaction of alkynes with the more closely packed atomic geometry afforded

by Pt{111} (close-packed surfaces display a lower surface energy than the more open planes¹). In terms of a strong adsorption of MeBuOH even on the Pt{111} surface, a balance between alkyne solubility in aqueous media, bulkiness of the alkyl groups and the surface adsorption enthalpy all must play a part. Electrochemical generation of hydrogen gas may remove almost all of the molecular fragments formed on the Pt surface originating from alkyne adsorption. Adsorbed CO is commonly generated on the surface as a consequence of alkyne adsorption, especially on the more open electrode surfaces.² Removal of adsorbed CO formed in this way requires a potential excursion to at least 0.7 V. A feature of CO generation however was its potential dependence in that for surfaces largely covered by adsorbed molecular fragments, only a weak tendency for the surface decarbonylation reaction was observed. However, after freeing up of Pt sites by reductive stripping of alkyne fragments, CO was found to form at a greater rate demonstrating that adjacent free sites are required for this reaction to occur.

Following the initial CV studies, *in situ* SERS/SHINERS was utilised to explore the molecular components adsorbed on various kinds of platinum surfaces and the detailed interaction between them. The intensities of SERS signals obtained for the adsorption of water soluble molecules on each platinum surface were in accord with CV in that the higher the coverage of molecules on the surface, the stronger the SERS intensity of the bands. The phenomena are different in the case of water insoluble alkyne molecules (2-pentyne and 4-octyne). The reason could be that different molecule adsorption methods were applied. Since CV tests were carried out with a static electrolyte after dosing platinum crystal electrodes from the liquid alkynes, whilst SERS experiments were carried out with a constantly flowing electrolyte with which alkynes were mixed. Nonetheless, the major findings are in common as a di-sigma/pi-bonded complex was observed forming on all Pt surfaces as signified by the appearance of the band in the range of 1500-1600 cm⁻¹. This surface intermediate was more stable at double layer potentials rather than at hydrogen evolution potentials. A steady state involving hydrogenative stripping and adsorption from solution was assumed to rationalise this finding. It was also demonstrated that the long-lived di-sigma/pi-bonded alkene complex prefers to stabilise on Pt defect sites. Previous studies have shown that PVP-modified Pd catalysts used in hydrogenation of ethyne can increase the catalytic selectivity towards ethene product, but with a decrease in activity.³ There is a balance of interactions between the nanoparticle Pt catalyst surface and the capping agent in terms of differential adsorption energetics, which determines the overall selectivity of the

hydrogenation of alkynes.⁴ However, the conclusion of the present study is that the selective blocking of defect sites will prevent the formation of the di-sigma/pi-bonded surface complex and thus, inhibit deep hydrogenation to the alkane, i.e. blocking of defect sites leads to selective hydrogenation.

8.3 Hydrogenation of Ethyl Pyruvate

Ethyl pyruvate has been previously studied on different platinum surfaces using CV by Taylor.⁵ It was shown that EP may adsorb on all basal planes, step and kink sites on platinum surfaces with coverages descending in the order (100)>(110)>(111). The emergence of an irreversible peak at 0.7 V in the positive scan was the most noticeable on Pt{100}. This peak was due to the electrooxidation of adsorbed CO forming from a decarbonylation reaction of EP on platinum.⁶ However, only SERS experiments on polycrystalline Pt surface had been carried out in Taylor's study. In the present study, the Orito reaction on various single crystal Pt surfaces with defined adsorption sites may be approached thanks to the SHINERS technique.

SER spectra of EP adsorption on polycrystalline platinum surfaces have only shown the HHS state. This has been further proven to be associated to the defect sites on Pt surfaces by contrasting the behaviour of polycrystalline and basal plane single crystal electrodes. The EP HHS, which was found to be a critical intermediate of the hydrogenated product, only forms on the step sites of the platinum surface at the HER potential. When the SHINERS method was applied to Pt single crystal electrodes, a new terrace intermediate formed from EP adsorption was discovered. The new intermediate is deduced to be a η^1 species. This species is believed to be a precursor to the formation of the HHS at steps and hence, only forms on the terraces of the surface. As long as there is hydrogen present, no matter if gaseous or electrosorbed, both intermediates form and are stable. In contrast, only the η^1 species can exist at potentials positive of the HER.

The adsorption of EP on different palladium surfaces has also been studied in the present work. Under the conditions of the Orito reaction and using CD as a chiral modifier, palladium was reported to give rise to the *S*-enantiomer of EL in excess.⁷ The accepted model accounting for this alternation in handedness (based on deuterium exchange measurements at the methyl group

attached to the carbonyl substituent) was the stabilisation of the *enol* tautomer of EP on the palladium surface leading to the hydrogenation of the enolic C=C bond rather than the carbonyl, resulting in the opposite enantioface being exposed during hydrogenation. In order to explore the selectivity differences caused by various palladium surface sites, the growth of single and multi-layered palladium overlayers on Pt{*hkl*} single crystal surfaces were characterised. All of the strong bands in the spectra observed using Pd modified Pt{*hkl*} are identical to those observed on pure Pt electrodes suggesting reconstruction of the Pd adlayer to reveal Pt subsurface sites. Hence, both the HHS and terrace intermediate formed on Pt are identified. Disappointingly, no unequivocal evidence for bands pertaining to EP adsorption on Pd could be identified under hydrogenating conditions. Studies of supported Pd and Pd modified Pt showing that an enolic form of EP should form on Pd rather than the keto form as found for Pt.^{7, 8} Clearly, EP hydrogenation on Pd is quite different to Pt particularly in relation to HHS formation and therefore, it is concluded that if a HHS of the enol form of EP does form (at defects or terraces) then it is completely unstable and immediately desorbs as EL.

8.4 Future Work

In the present study, the SHINERS technique has been utilised to explore two major types of reaction with various candidate molecules. By controlling the surface atmosphere simply using cyclic voltammetry, the *in situ* SHINER spectra of the bonding between the molecules and the flat metal surfaces were obtained. However, for all of the reactions being studied, there are still other parameters to be considered so that a few improvements can be made.

For example, one cannot neglect the effect of the temperature on the adsorption of molecules at metal surfaces and the surface interactions between them. For example, could the terrace η^1 species be isolated on a polycrystalline Pt surface at sufficiently low temperatures (i.e. making the transformation rate of the η^1 species into the HHS so slow that an activation energy barrier for the transformation be measured)? Clearly, a low T limit of 273 K pertains in the present experimental apparatus but perhaps UHV studies may be possible? Unfortunately, the high hydrogen pressures and ability to desorb into an aqueous phase would not be available in this case but UHV studies using SHINERS would constitute a whole new branch of surface science with SHINERS replacing for example high-resolution electron energy loss (HREELS) as a probe

of vibrational stretches below 800 cm^{-1} . Higher temperatures would also enable measurements of the stability of the HHS of EP and the di-sigma/pi-bonded complex of the alkyne such that correlations with reaction rate/selectivity and enantioselectivity changes as a function of temperature may be related directly to the relative changes in population of these species as measured by SHINERS. Another future experiment would be to exploit the incredible analytical sensitivity of modern HPLC/NMR equipment in that if the flowing electrolyte could be collected post-reaction and compared with electrolyte before hydrogenation was occurring, real time measurements of selectivity/activity could be made as a function of Pt{*hkl*} electrode being used as the hydrogen generator. Recent measurements by Attard and Wirth [private communication] indeed have demonstrated that this is possible with *ee* changes and product yield as a function of both CD concentration and even R-/S- Pt{*hkl*} surface configuration being observed. This should prove a fruitful area for future investigation of many important heterogeneous catalytic reactions.

Recently, researchers have been looking for different candidates to modify the catalysts in order to achieve novel functions in terms of selectivity. In this study, the adsorption of PVP, bismuth, and cinchonidine *etc.* has been covered as well. Their effects on the reactions have been clearly illustrated. Although it is important to replace toxic metals with cheaper and more benign adsorbates in heterogeneous selective hydrogenation, one has to ensure that binding is commensurate with the maintenance of good selectivity whilst achieving reasonable activity.

The study of enantioselective hydrogenation of EP on different metal surfaces in this project has also raised some questions which need to be solved in the future. Is the atop H–Pd stretch red shifted in the presence of CD as found with Pt? Does absorption of hydrogen into the palladium lattice allow for observation of a Pd–H atop stretch? It would be very interesting to contrast Rh adsorption with Pd on Pt since Rh is reported to act like Pt in terms of the Orito reaction although exhibiting a somewhat lower overall *ee*.

The SHINERS technique has overcome the many drawbacks caused by the traditional SERS approach which previously included a reliance on rough, coinage metal surfaces, the preclusion of interesting, well-defined single crystal metals other than copper, silver and gold and a certain lack of reproducibility in the signal being collected. In the present study, the vibrational bands involved in the interaction between adsorbates and metal surfaces could all be detected by

SHINERS so long as strong attention was paid to surface cleanliness when preparing the SHINERS-modified surface. Therefore, theoretically, any kind of reaction which is heterogeneously catalysed by any metal could be studied if one wants to understand the mechanisms of the processes or the intermediates formed during the catalysis. It is speculated that new types of system may be studied by SHINERS. For example, one may try to mix the Au@SiO₂SHINERS NPs with real catalysts and monitor the reactions occurring on the surfaces of real catalysts under operating conditions. The upper temperature available to the techniques may be constrained by the decomposition temperature of the Au@SiO₂ particles themselves although it appears from recent studies that the sintering of gold is strongly inhibited by encapsulation in silica shells.⁹ If all such problems can be overcome, this novel technique could be applied much more widely in the future.

8.5 References

1. L. Vitos, A. V. Ruban, H. L. Skriver and J. Kollár, *Surface Science*, 1998, **411**, 186-202.
2. H. E. Morris, *Chemical Reviews*, 1932, **10**, 465-506.
3. M. Crespo-Quesada, J.-M. Andanson, A. Yarulin, B. Lim, Y. Xia and L. Kiwi-Minsker, *Langmuir*, 2011, **27**, 7909-7916.
4. S. G. Kwon, G. Krylova, A. Sumer, M. M. Schwartz, E. E. Bunel, C. L. Marshall, S. Chattopadhyay, B. Lee, J. Jellinek and E. V. Shevchenko, *Nano Letters*, 2012, **12**, 5382-5388.
5. R. J. Taylor, PhD Thesis, Cardiff University, 2010.
6. D. Ferri, T. Bürgi and A. Baiker, *The Journal of Physical Chemistry B*, 2004, **108**, 14384-14391.
7. T. J. Hall, P. Johnston, W. A. H. Vermeer, S. R. Watson and P. B. Wells, in *Studies in Surface Science and Catalysis*, eds. J. W. Hightower, W. N. D. E. Iglesia and A. T. Bell, Elsevier, Editon edn., 1996, vol. Volume 101, pp. 221-230.
8. P. Wells and A. Wilkinson, *Topics in Catalysis*, 1998, **5**, 39-50.
9. C.-H. Lin, X. Liu, S.-H. Wu, K.-H. Liu and C.-Y. Mou, *The Journal of Physical Chemistry Letters*, 2011, **2**, 2984-2988.